Terms and Conditions of Use of Digitised Theses from Trinity College Library Dublin

Copyright statement

All material supplied by Trinity College Library is protected by copyright (under the Copyright and Related Rights Act, 2000 as amended) and other relevant Intellectual Property Rights. By accessing and using a Digitised Thesis from Trinity College Library you acknowledge that all Intellectual Property Rights in any Works supplied are the sole and exclusive property of the copyright and/or other IPR holder. Specific copyright holders may not be explicitly identified. Use of materials from other sources within a thesis should not be construed as a claim over them.

A non-exclusive, non-transferable licence is hereby granted to those using or reproducing, in whole or in part, the material for valid purposes, providing the copyright owners are acknowledged using the normal conventions. Where specific permission to use material is required, this is identified and such permission must be sought from the copyright holder or agency cited.

Liability statement

By using a Digitised Thesis, I accept that Trinity College Dublin bears no legal responsibility for the accuracy, legality or comprehensiveness of materials contained within the thesis, and that Trinity College Dublin accepts no liability for indirect, consequential, or incidental, damages or losses arising from use of the thesis for whatever reason. Information located in a thesis may be subject to specific use constraints, details of which may not be explicitly described. It is the responsibility of potential and actual users to be aware of such constraints and to abide by them. By making use of material from a digitised thesis, you accept these copyright and disclaimer provisions. Where it is brought to the attention of Trinity College Library that there may be a breach of copyright or other restraint, it is the policy to withdraw or take down access to a thesis while the issue is being resolved.

Access Agreement

By using a Digitised Thesis from Trinity College Library you are bound by the following Terms & Conditions. Please read them carefully.

I have read and I understand the following statement: All material supplied via a Digitised Thesis from Trinity College Library is protected by copyright and other intellectual property rights, and duplication or sale of all or part of any of a thesis is not permitted, except that material may be duplicated by you for your research use or for educational purposes in electronic or print form providing the copyright owners are acknowledged using the normal conventions. You must obtain permission for any other use. Electronic or print copies may not be offered, whether for sale or otherwise to anyone. This copy has been supplied on the understanding that it is copyright material and that no quotation from the thesis may be published without proper acknowledgement.

EXPERIMENTAL INVESTIGATIONS IN TURBOMACHINERY NOISE-SOURCE IDENTIFICATION

IAN DAVIS

Department of Mechanical & Manufacturing Engineering

Parsons Building

Trinity College

Dublin 2

Ireland

January 2014

A thesis submitted to the University of Dublin in partial fulfilment of the requirements for the degree of Ph.D.

Thesis 10222

Declaration

I declare that this thesis has not been submitted as an exercise for a degree at this or any other university and it is entirely my own work.

I agree to deposit this thesis in the University's open access institutional repository or allow the library to do so on my behalf, subject to Irish Copyright Legislation and Trinity College Library conditions of use and acknowledgement.

Ian Davis, January 2014

Abstract

The exact contribution of each of the various core-noise sources within modern turboshaft engines to the noise radiated from the engine exhaust and into the surrounding environment is poorly understood. The objective of the E.U. FP-7 TEENI (Turboshaft Engine Exhaust Noise Identification) project was to better characterise the specific contributions of each core noise-source to this exhaust noise. Sources of core noise include direct combustor noise generated by the unsteady heat release at the combustor stage, broadband turbine noise, periodic turbine noise and flow-noise. Core noise also contributes significantly to the exhaust noise in modern turbofan engines during approach.

One of the key avenues of investigation for the TEENI project was to assess the efficacy of various coherence-based noise-source identification techniques for application in a full-scale turboshaft engine. Such techniques require several acoustic measurements to be made at the noise-sources of interest. These techniques were first tested using a small-scale experimental rig constructed at the Department of Engine Acoustics at the German Aerospace Centre (DLR) in Berlin, Germany. The objective of these tests was to examine the effectiveness of both pre-existing and novel methods of noise-source identification, using the small-scale experimental rig as a simplified representation of a real turboshaft engine. The relative strengths and weaknesses of several pre-existing techniques are discussed, before a novel method of noise-source identification is introduced which identifies the relative contributions of two noise-sources to the specific acoustic modal content measured at a given axial location. This novel method combines both the advanced techniques of modal decomposition and coherence analysis, and represents a significant advancement on pre-existing methods.

Scattering of noise was also observed during the small-scale TEENI experiments. This scattering occurs when noise propagates through (and interacts with) a rotating rotor.

This is a frequent occurrence in aeroengines, where for example downstream-travelling rotor-stator blade-pass tones or low-frequency combustor noise will propagate through several additional rotating compressor/turbine stages. This causes acoustic energy to be scattered at sum and difference frequencies relative to the incident noise. Both scattering of tonal and narrowband noise was observed in the DLR tests, however this scattering only occurs above some critical frequency. Not enough relevant experimental data was gathered for an in-depth study of this scattering of noise to be made however, so a second bench-top experimental rig was designed at TCD. A literature review was conducted, and it was found that this sum and difference scattering is predicted by existing analytical theory. The acoustic modal content of the scattered noise is also predicted. However, no experimental validation of this theory had previously been undertaken. Furthermore, this existing analytical theory has been restricted to scattering of tonal noise, as opposed to broadband or narrowband noise. Finally, some recent literature has suggested that the interaction between the incident noise and the rotor may be non-linear in nature, but further work was needed to verify this.

Experimental tests were undertaken using the bench-top rig at TCD to validate that the various elements of the experimental rig operate as desired. This experimental rig was designed to overcome the limitations of the DLR rig which had prevented a detailed study into frequency scattering of noise. Further tests were then undertaken, applying both single-microphone spectral analysis and modal analysis in order to characterise both the incident and scattered noise. Scattering of tonal and narrowband noise was investigated, with parameters such as rotor-stator geometries, source frequencies, spectral bandwidth of the incident noise and the modal content of the incident noise modified between tests. The experimental results not only validate the existing analytical theory, but also demonstrate scattering of non-tonal noise.

A relationship is found between the onset of significant scattering of noise and the cut-ons of certain acoustic mode orders. This is demonstrated for both tonal and narrowband noise, and it is shown that noise scattering can be predicted given the blade (and vane) counts of the rotor (and stator) stages, the rotational speed of the rotor, and the modal content of the incident noise. It is further demonstrated herein that incident noise and scattered noise can overlap if the spectral bandwidth of the incident noise is wide enough,

raising the possibility of the distribution of acoustic energy across frequency and mode order being significantly affected for broadband noise propagating through a rotor.

Finally, non-linear coherence analysis of this scattering of noise demonstrates the quadratic nature of the underlying interaction which causes sum and difference scattering to occur. Any coherence-based noise-source identification techniques made between measurements upstream and downstream of a rotor (turbine) stage will fail if the propagation path between measurements is not linear, and therefore sum and difference scattering is not just an issue of spectral scattering of noise, but a possible cause of erroneous noise-source identification as well.

Acknowledgements

I would like to first and foremost thank Dr. Gareth Bennett for his guidance through out my research these past five years. His dedication, professionalism and experience were invaluable, and he was always available to offer a helping hand or a gentle shove when I needed it. I look forward to collaborating further in the future.

Much of my research has been undertaken in co-operation with, and partly funded by, the E.U. FP-7 project TEENI under EU commission grant agreement 212367. Through the various consortium meetings and experimental test campaigns I attended I was fortunate enough to collaborate with leaders in the fields of aeroengine acoustics, instrumentation design and aeroengine manufacturing. In particular I would like to thank Ulf Tapken, Benjamin Pardowitz and Philip Kausche at The Department of Engine Acoustics in the Institute of Propulsion Technology of the German Aerospace Centre (DLR) located in Berlin, Germany. Not only did they undertake the TEENI small-scale test campaign at their research facility, but also provided invaluable advice and guidance in designing my bench-top rig at TCD.

Speaking of the bench-top experimental rig – it would not have been possible without the amazing technical staff at the Department of Mechanical & Manufacturing Engineering. I would like to think Michael, Seán, Gabriel and Alex in the workshop who turned my Creo Elements models into reality, and also John Gaynor for the continuing I.T. support.

Finally, I would like to thanks all my family and friends who supported me through the past four years. In particular I wish to thank my mother, Sally, and my father, George, for always supporting my education from Junior Infants through to postgraduate level. I would also like to express my love and gratitude to the ever patient and kind Louise, who would have me killed if she didn't get a special mention!

Contents

List of Figures

Nomenclature

Symbols

Symbol	Units	Description
f_{samp}	Hertz (Hz)	Sampling frequency of data acquisition
R	Metres (m)	Duct outer radius
kR	–	Helmholtz number
q	–	Sum/difference scattering harmonic
m	–	Azimuthal mode index
n	–	Radial mode index
G_{ii}	Pa^2/Hz	Auto-spectral density function of signal i
G_{ij}	Pa^2/Hz	Cross-spectral density function between signals i and j
$i \cdot j$	–	Part of signal i not correlated with signal j
$i : j$	–	Part of signal i correlated with signal j

Acronyms

Term	Description
COP	Coherent output power
SE	Signal enhancement
CSA	Conditional spectral analysis
BPF	Blade-pass frequency
TAM	Targeted azimuthal mode
SPL	Sound-pressure level

Chapter 1

Introduction

1.1   Motivation for Research

As the airline industry continues to grow, the noise emitted from aircraft has been a grow-ing concern with regards to noise pollution, which has been reflected in E.U. directives on aircraft noise such as directive 2002/30/EC. Historically, jet noise has been the focus of most investigation [1]. Such research has lead to the implementation of high bypass-ratio engine types, chevrons at the jet nozzle, and a clearer understanding of the mixing mech-anism of the hot jet exhaust (core), bypass stream (fan), and ambient air have all resulted in a significant reduction in this noise. Core noise refers to the noise emanating from the unsteady heat release of the combustion process, as well as the individual rotor-stator stages of the turbines, and indirect combustion noise generated by the rapid acceleration of entropy inhomogeneities from the combustor through the turbine stages. As jet noise has decreased, the focus has begun to shift to the contribution of core noise radiated from aircraft engines. Core noise consists of both tonal and broadband noise. Core noise is the dominant noise source in engines with little or no jet noise, such as turboshaft engines e.g. helicopter engines. Recent EU funded projects such as Friendcopter and **TEENI** (**T**urboshaft **E**ngine **E**xhaust **N**oise **I**dentification) have focused on the characterisation and hence strategic reduction of core noise emanating from the turboshaft engines used in helicopters. Core noise is also a significant contributor to the noise radiated from turbofan engines during the approach and taxiing of aircraft, when jet velocities are low.

In modern helicopter turboshaft engines, the core noise generated by the combustor and turbine stages dominates the sound radiated from the engine exhaust. Identification of the specific contributions of the combustor and each rotor-stator stage to the core noise is impeded by the lack of available space and the complex duct geometry within the engine for the location of acoustic sensors, as well as very high temperatures. The TEENI project commenced in 2008 with the objective to characterise the broadband noise emanating from turboshaft engine exhausts, and attribute the measured far-field noise in specific spectral ranges to specific core noise-sources within the engine. Figure 1.1(a) shows how, prior to the TEENI project, little is understood of the respective contributions of each noise-source to the noise radiated from the engine exhaust. Many aspects of the generation, transmission and propagation of the various stages within an

aeroengine are poorly understood, particularly their respective contributions to the sound pressure levels of the noise radiated to the far-field. The objective of the TEENI project was to identify the contributions of various core noise-sources to far-field measurements [2]. A hypothetical example of this enhanced understanding as a result of the TEENI project in shown in Figure 1.1(b).

Coherence-based techniques of noise-source identification techniques are well suited to acoustic testing inside turboshaft engines. As the amount of space is severely limited, only a few reference sensors may realistically be located close to each source location. Coherence-based noise-source identification techniques apply the correlation functions estimated between a number of pairs of microphones. The relative contribution of one or more noise-sources to the total noise at a measurement location of interest can then be calculated. The first reported application of such a technique was the coherent output power technique applied by Halvorsen and Bendat [3]. This technique uses a pure (zero extraneous noise) source measurement as an input in order to identify the contribution of this source to the total noise at an output measurement. More sophisticated methods which use more than a single pair of microphones have been developed more recently. These techniques may be applied in situations where a pure source measurement is unavailable, or the reference sensors measure more than one source, subject to certain restrictions. Such techniques include the three-microphone signal enhancement technqiue of Chung [4] and the five-microphone conditional spectral analysis technique of Hsu and Ahuja [5]. A detailed discussion of the formulation of several such techniques is presented in Chapter 4.

Rotor-stator BPF tones propagating downstream in an aeroengine will interact with the rotating blades and stationary stators of the various stages of turbomachinery. This interaction can result in scattering of noise at sum and difference frequencies with respect to the incident noise. Crucially, this scattering has been demonstrated in recent literature to occur not only for tonal noise, but also narrowband (band-limited broadband) noise [6]. This may explain some of the low-frequency acoustic energy found in far-field measurements which cannot be associated with any specific noise-source within the engine, as energy from upstream noise-sources (*e.g.* direct combustor noise) could be scattered in frequency. With reference to Figure 1.1, it may also be possible for the high-frequency
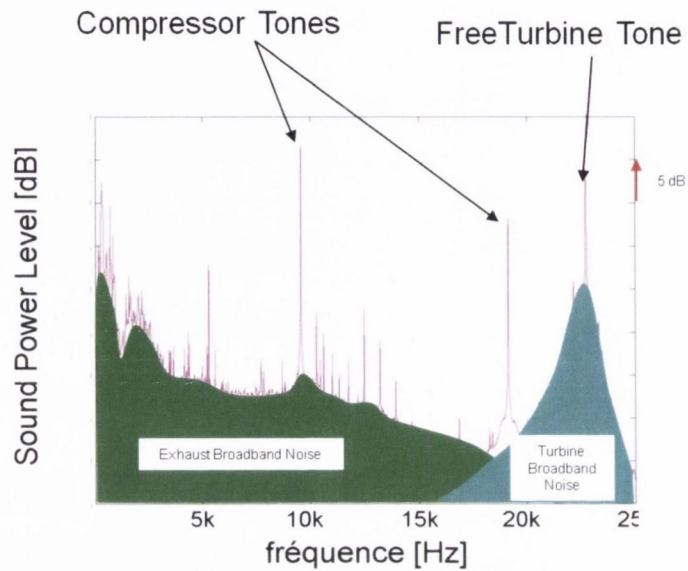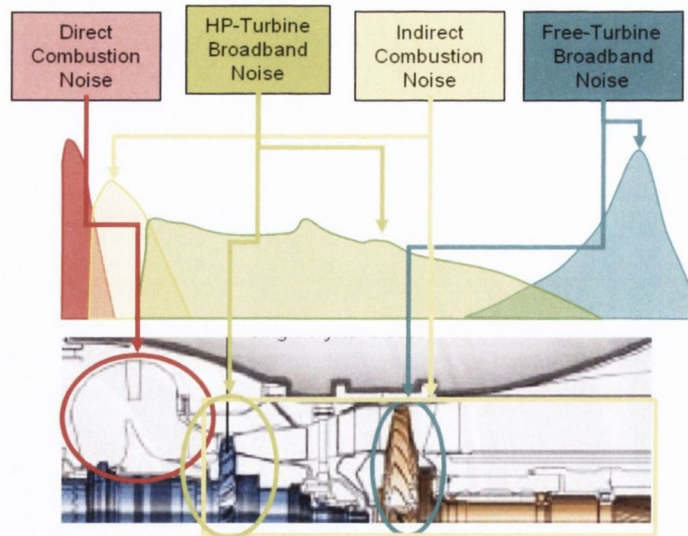
Figure 1.1: TEENI project aims. (a) Shows that prior to TEENI, little is known about the contributions of core-noise sources within turboshaft engines to the broadband noise radiated from the engine exhaust. (b) Shows the objective of TEENI, which is to identify the specific contributions of these core noise-sources to the exhaust broadband noise. A *hypothetical* output from the project is shown [2].

turbine broadband noise to be scattered to lower frequencies, perhaps contributing to the lumps of broadband noise in the range $0Hz$–$2000Hz$. This a concern for studies such as TEENI, which aims to characterise the broadband noise emanating from turboshaft engine exhausts, as some low-frequency noise may not be attributed to a specific core noise-source within the engine using traditional coherence-based methods. Low frequency noise is also attenuated less by atmospheric absorption, and therefore propagates long distances more effectively [7]. The possibility of sum and difference scattering affecting the far-field spectral distribution of acoustic energy in this way would have a significant impact on environmental noise considerations of aeroengine design, and was therefore identified by the author as a key avenue of investigation within the TEENI project.

Sum and difference scattering of noise is an issue for the application of noise-source identification techniques which make the assumption of a linear propagation path between source and receiver, as sum and difference scattering has been suggested as being a non-linear interaction between the downstream propagating noise and rotating turbomachinery. Frequency scattering will furthermore have an impact on the effectiveness of any installed acoustic liners, as noise may be scattered outside the frequency range for which the liner design is effective. Previous analytical theory also suggests that the modal content of the noise at any scattered frequencies will also be affected by the scattered noise [8, 9]. This will further reduce the effectiveness of any liners if they have not been optimised for the acoustic modes excited by the scattered noise. Furthermore, any liners installed upstream of any turbine stages at which scattering occurs will not mitigate the scattered noise. If the scattering mechanism is well understood however it may be possible to eliminate the factors which cause such scattering to occur, therefore eliminating the need for mitigation methods such as acoustic liners.

1.2 Scope and Objectives of Thesis

The aim of the author's research is to contribute in a meaningful way to the research into turbomachinery noise source identification; namely, to better understand the contribution of each noise-source in the engine to the sound radiated from the engine exhaust. The work undertaken is closely linked to the research undertaken as part of the EU FP7 project

TEENI, of which TCD (Trinity College Dublin) was a partner. Figure 1.1 demonstrates how the TEENI project aims to better characterise the contribution of the specific noise generation mechanisms present inside a turboshaft engine to the broadband noise radiated from the engine exhaust. The author was actively involved in the work of TEENI from October 2009 until the project's completion in June 2013.

In December 2009, a major test campaign was undertaken at the engine acoustics branch of DLR (German Aerospace Agency) located in Berlin, Germany. This experimental rig was designed to simulate the key acoustic elements of a turboshaft engine. The experimental parameters were set according to the requirements of both DLR and TCD for research into methods of noise-source identification. This test campaign was completed in February 2010, and the experimental tests generated data for a wide variety of test points. Parameters such as the number of noise sources and type of noise generated (tonal, narrowband or broadband) and the modal content of this noise were changed between test points. This provided a substantial data set in order to investigate noise generation in a turboshaft engine and novel techniques of noise-source identification.

During the Berlin tests, sum and difference scattering of noise through the rotor-stage was observed. An example of this observed scattering is shown in Figure 1.2. Narrowband noise generated by several loudspeakers, shown as NBN, has been scattered by the rotor at sum and difference frequencies of the blade-pass frequency (BPF) of the rotor. It was observed over several narrowband tests that this scattering occurs at high frequencies, but not lower frequencies, as highlighted in Figure 1.3. Not enough relevant data was generated in the Berlin tests to investigate this scattering phenomenon in-depth, therefore a second experimental rig was designed at TCD specifically to investigate noise scattering effects. This experimental set-up was designed in a similar manner to the experimental rig at DLR, with two noise-source regions; a rotor-stator stage and a loudspeaker array. Over both these experimental investigations, this thesis focuses on two main research investigations of turbomachinery noise with the following objectives:

1. to improve existing techniques of noise source identification, by combining modal theory with existing techniques. These techniques only require a few sensors located close to the noise sources of interest, and are therefore very useful for real turboshaft

engine applications where the duct geometry is complex and the available space for the location of acoustic sensors is limited.

2. to gain a better understanding of a specific mechanism of noise propagation in a turboshaft engine. This mechanism involves the interaction between a rotor stage and noise propagating from upstream of the rotor through the rotor, and results in sum and difference frequency scattering which will affect the spectral distribution of acoustic energy and modal content of the noise propagating out the engine exhaust.
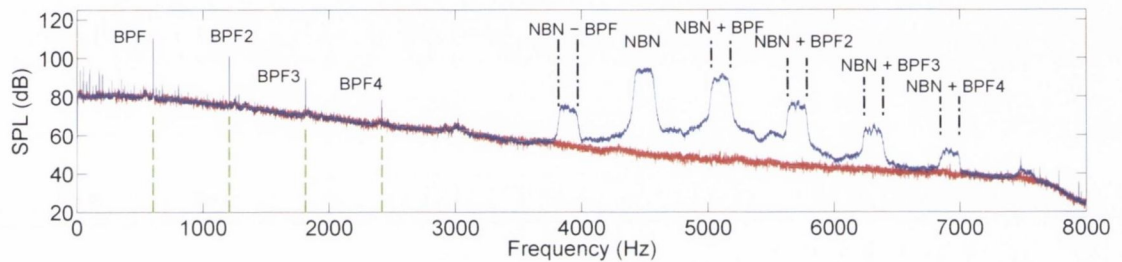
Figure 1.2: Scattering of narrowband noise (NBN) generated by an array of loudspeakers due to interaction with a rotating rotor. This noise was acquired by a microphone downstream of the rotor-stator stage. Noise is scattered at frequencies of NBN plus or minus multiples of the blade-pass frequency (BPF) of the rotor.
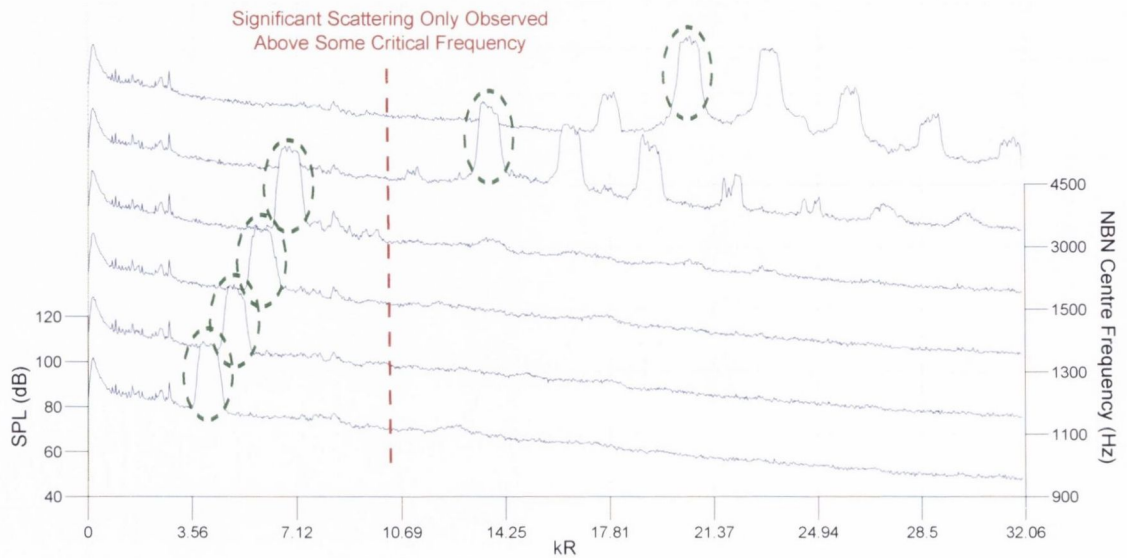
Figure 1.3: Waterfall plot of several test cases similar to that shown in Figure 1.2. The x-axis shows the dimensionless frequency range and the y-axis is the sound pressure level of the measured noise. Each spectra shows a different test case where NBN has been generated by the loudspeaker array at a different centre frequency, as denoted in the z-axis. The NBN generated by the loudspeaker array is circled in green in each case.

1.3 Outline of Thesis

This thesis consists of seven chapters. In Chapter 2, the fundamental theory of the generation, propagation, and radiation of noise in turbomachinery is reviewed. Turbomachinery noise occurs in a ducted environment, and therefore the fundamental theory of duct acoustics is also presented in this chapter. Acoustic analyses of ducted environments are generally enhanced by knowledge of the amplitudes of the cut-on acoustic modes inside the duct. Chapter 3 reviews pre-existing methods of modal decomposition. These decomposition techniques use combinations of several in-duct acoustic pressure measurements to estimate these acoustic modal amplitudes. Finally, the limitations and benefits of a modal decomposition method using a single ring of microphones flush-mounted to an inner duct wall, as used in the experimental tests discussed in Chapter 6, is discussed.

As part of the TEENI project, an experimental study was undertaken on both classic (*i.e.* already published) and novel techniques for identification of noise in turboshaft engines. A test campaign was undertaken at DLR in Berlin, Germany using a small-scale

representation with a simplified geometry of a real turboshaft engine with two noise-source regions representative of the noise-sources inside the engine. Reference sensors were located close to both noise-source regions, and banks of microphones were installed to allow a modal analysis to be performed at two axial locations in the duct. Coherence-based noise-source identification techniques were applied using this test rig for the identification of the noise generated by both noise-source regions. The theory, test procedure and results from applying these techniques are discussed in Chapter 4. The efficacy and limitations of these techniques is then discussed, and a case of noise scattering which would adversely affect the performance of such techniques is highlighted.

Chapter 5 discusses the design of the second experimental rig used in the test campaign undertaken at TCD to investigate the sum and difference scattering of noise as it interacts with rotating turbomachinery, as previously observed in the tests in Chapter 4. Limitations in the frequency range in which modal analyses could be performed and a large number of rotor blades prevented an in-depth investigation to be undertaken using the DLR test data, necessitating the new experimental rig. A brief literature review is presented which underlines the lack of previous experimental research that focuses on this specific type of noise scattering. The experimental set-up is of a similar basic design to the DLR rig, with two ducted noise-source regions used as a basic analogy to the acoustics inside a real turboshaft engine. Numerical models of aspects of the rig's design are presented, and experimental results are also shown that verify each aspect of the experimental rig operates as intended.

The subsequent results from experimental investigations using the TCD rig of scattering of both tonal and narrowband (band-pass filtered broadband) noise are summarised and discussed in Chapter 6. A relationship is found between the onset of significant scattering of noise and the cut-ons of certain acoustic mode orders. This is demonstrated for both tonal and narrowband noise. It is shown that noise scattering can be predicted given the blade (and vane) counts of the rotor (and stator) stages, the rotational speed of the rotor, and the modal content of the incident noise. Chapter 7 assesses the overall contribution of this thesis, and discusses possible future research topics which arise from the results presented herein.

Chapter 2

Theory of Duct Acoustics and Turbomachinery Noise Generation

2.1   Pressure Field in a Hard-Walled Cylindrical Duct

In the following approach to the acoustics inside a duct, the duct is approximated as being a cylinder of infinite length. The resulting differential equations can then be solved by separation of variables, leading to an eigenvalue problem that can be solved to give the duct propagation modes. For an infinite length duct with superimposed mean flow $\vec{U}$, the pressure, $p = p(r, \theta, x, t)$, can be expressed in cylindrical coordinates as a solution to the homogeneous convective wave equation:

$$\frac{1}{c^2}\frac{D^2 p}{Dt^2} - \frac{\partial^2 p}{\partial x^2} - \frac{1}{r}\frac{\partial}{\partial r}\left(r\frac{\partial p}{\partial r}\right) - \frac{1}{r^2}\frac{\partial^2 p}{\partial \theta^2} = 0 \tag{2.1}$$

The substantive or material derivative describes the rate of change of a quantity as it moves through a space- and time-dependent velocity field, and is defined as:

$$\frac{D}{Dt} = \frac{\partial}{\partial t} + \vec{U}\frac{\partial}{\partial x}$$

The solution is found as a combination of the characteristic functions of Equation 2.1 each of which satisfy specific boundary conditions. The derivation of this separation of variables solution can be found in the literature [10–12], given the following assumptions:

- Flow is an incompressible medium with negligible temperature gradients.

- The mean flow, $U = (U_x, 0, 0)$, is stationary with time.

- The axial mean flow profile and duct cross-sectional area are invariant in the axial direction.

- The mean temperature and density are stationary with time.

Åbom [13] and others demonstrate that the solution to the convective wave equation can be given by a linear superposition of modal terms:

$$p(x, r, \varphi) = \sum_{m=-\infty}^{\infty}\sum_{n=0}^{\infty}[A_{mn}^{+}e^{-jk_{mn}^{+}x} + A_{mn}^{-}e^{-jk_{mn}^{-}x}]f_{mn}(r)e^{jm\varphi} \tag{2.2}$$

where A_{mn}^+ and A_{mn}^- are the complex modal amplitudes, k_{mn}^+ and k_{mn}^- are the axial wavenumbers, and m and n are the azimuthal and radial mode indices respectively. The + and - superscripts refer to the direction relative to the flow, with the convention that positive is in the direction of the mean flow. For the case of a hard-walled acoustic boundary condition, an orthogonal eigensystem is formed, with the modal shape factor described by:

$$f_{mn}(r) = \frac{E_m(\sigma_{mn} r / R)}{\sqrt{N_{m,n}}} \tag{2.3}$$

where E_m is the characteristic function describing the radial pressure distribution as discussed in Section 2.1.1, and σ_{mn} is the associated hard-walled eigenvalue. R is the outer duct radius. In order to satisfy orthogonality, a normalisation factor is calculated by:

$$N_{mn} = 2\pi \int_0^R E_m^2(\sigma_{mn} r / R) r\, dr = \pi R^2 (E_m^2(\sigma_{mn}) - E_{m-1}(\sigma_{mn}) E_{m+1}(\sigma_{mn})) \tag{2.4}$$

This transforms the orthogonal mode eigensystem into an orthonormal mode eigensystem. A mean flow can be accommodated for in the formulation of the axial wavenumbers which is a function of σ_{mn} and the free-field wave number, k.

$$k_{mn}^{\pm} = k \frac{-M_x \pm \alpha_{mn}}{\beta^2} \tag{2.5}$$

where

$$\alpha_{mn} = \sqrt{1 - \left(\frac{\beta \sigma_{mn}}{kR}\right)^2} \tag{2.6}$$

and

$$\beta = \sqrt{1 - M_x^2} \tag{2.7}$$

2.1.1 Radial Pressure Distributions for Annular and Circular Ducts

For an annular duct, the pressure distribution across the radius is given by:

$$p_m(r) = \sum_{n=0}^{\infty} a_{mn} p_{\mu}(r) = a_m \sum_{n=0}^{\infty} a_n p_n(r) = \sum_{n=0}^{\infty} a_{mn} E_{mn}^{\eta}(k_{mn}^{\eta} r) \qquad (2.8)$$

$$E_{mn}^{\eta} = E_{mn}^{\eta}(k_{mn}^{\eta} r) = E_{mn}^{\eta}(b k_{mn}^{\eta} r/b) = E_{mn}^{\eta}(k_{mn}^{\prime \eta} r') \qquad (2.9)$$

See Tyler and Sofrin [14], for example, for similar reasoning. The characteristic E function is given in the range $a \leq r \leq b$ by the following combination of Bessel functions:

$$E_{mn}^{\eta}(k_{mn}^{\eta} r) = J_m(k_{mn}^{\eta} r) + Q_{mn}^{\eta} Y_m(k_{mn}^{\prime \eta} r) \qquad (2.10)$$

where a is the duct inner radius, b is the duct outer radius, and η is the hub-to-tip ratio (a/b). J_m and Y_m are the Bessel functions of the first and second kind respectively, of order m.

The characteristic numbers $k_{mn}^{\prime \eta}$ and Q_{mn}^{η} are found from the roots of the following simultaneous equations, which arise from the boundary condition that the pressure gradient at the duct walls must be zero:

$$J_m'(k') + Q_m^{\eta} Y_m'(k') = 0 \qquad (2.11)$$

$$J_m'(\eta k') + Q_m^{\eta} Y_m(\eta k') = 0 \qquad (2.12)$$

where J' and Y' denote the derivatives of the Bessel functions of the first and second kind respectively with respect to r.

The radial mode shapes for an annular duct are shown in Figure 2.1 with a hub-to-tip ratio $\eta = 0.25$. The first four m orders are shown. As η decreases, higher-order radial modes are biased towards the hub. This has the consequence that as η is increased, the cut-on frequency of higher-order radial modes is increased. Modal cut-ons are discussed in further detail in Section 2.2. Similar plots are presented in the works of Tyler and Sofrin [14] and Moore [15].
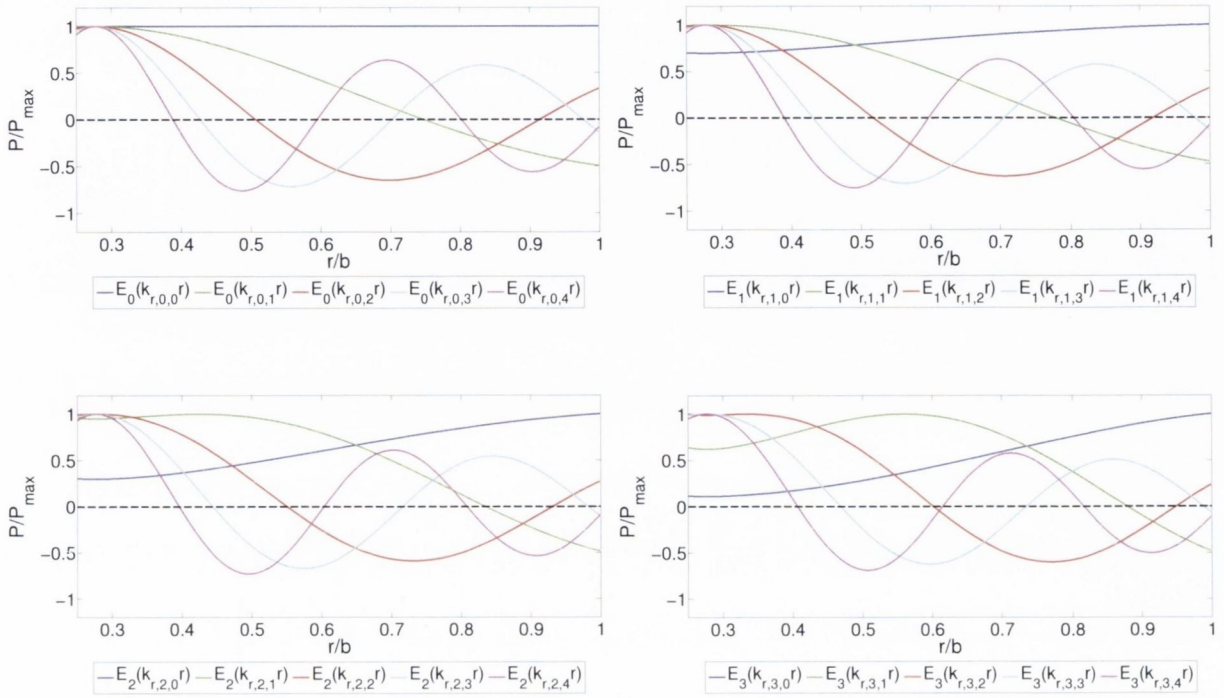
Figure 2.1: Radial pressure distributions for an annular cross-section duct for Bessel functions of order 0-3, $\eta = 0.25$, at a specific azimuthal angle.

For a duct with a circular cross-section ($a = 0$), the existence of the Bessel function of the second kind is in violation of the boundary conditions. The characteristic function in this case is therefore given by:

$$E_{mn} = J_m(k_{mn}r) \tag{2.13}$$

For the boundary condition that the pressure gradient at the duct wall is zero for the case of a duct with a circular cross-section:

$$J'_m(k_{mn}r) = 0 \tag{2.14}$$

The radial mode shapes for a circular duct are shown in Figure 2.2. The first four m orders are shown.
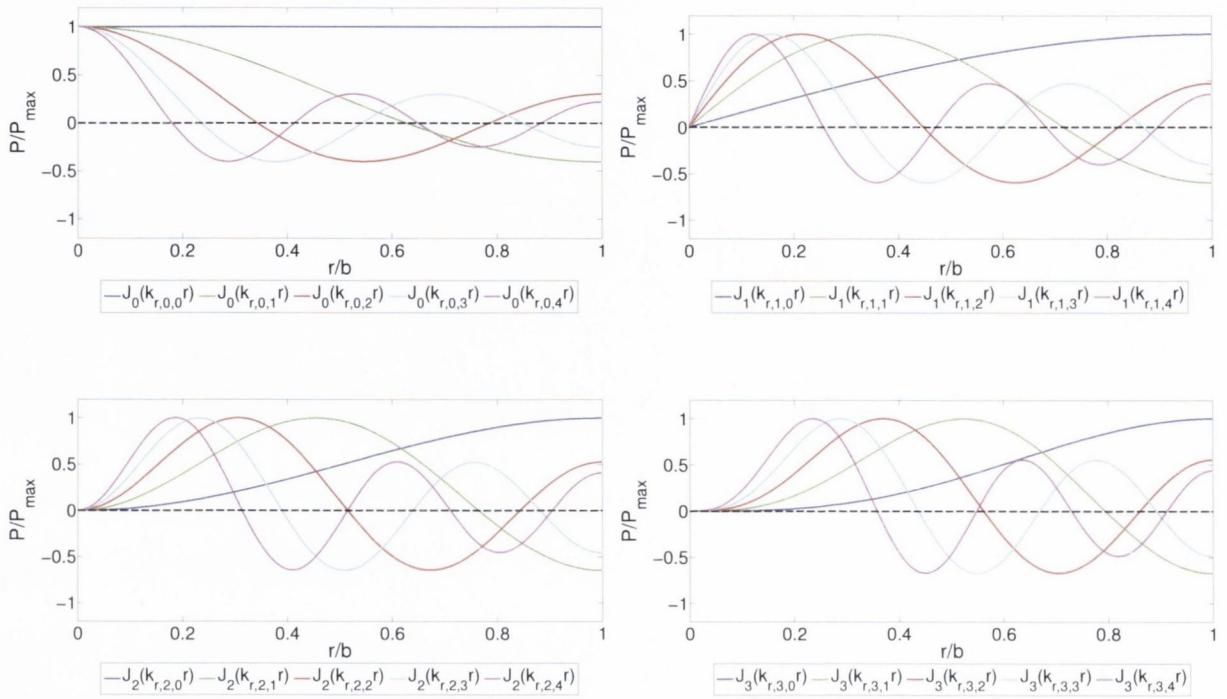
Figure 2.2: Radial pressure distributions for a circular cross-section duct for Bessel functions of order 0-3, at a specific azimuthal angle.

2.2 Acoustic Modal Propagation

In Section 2.1, it was demonstrated that for a hard-walled cylindrical duct of infinite length, the acoustic pressure in the duct can be considered as the linear superposition of infinite many acoustic modal amplitudes (see Equation 2.2). The acoustic modes of propagation arise as eigenvalue solutions to the Equations 2.11, 2.12 and 2.14 outlined in Section 2.1.1. A full overview of the eigenvalue solution can be found, for example, in Eversman [12]. The behaviour of these modes can be better understood by considering the axial wavenumber, as defined in Equation 2.5. For:

$$(1 - M^2)\left(\frac{\sigma_{mn}}{kR}\right)^2 < 1 \tag{2.15}$$

the values of $k_{mn}^{\pm}$ are real. If $k_{mn}^{\pm}$ is complex, the resulting modes will be attenuated with axial distance, and will decay in amplitude exponentially. These evanescent modes have no acoustic energy associated with them [16]. Such acoustic modes are said to be "cut-off". The cut-off ratio for a particular acoustic mode order is given by (see for example Rice [17]):

$$\zeta_{mn} = \frac{kR}{\sigma_{mn}\sqrt{1 - M^2}} \tag{2.16}$$

When the cut-off ratio ζ_{mn} is greater than one for a particular mode order at a particular frequency, the mode will propagate with very little attenuation in a duct. These modes are said to be "cut-on". Several cut-on modes can co-exist at a particular frequency if their respective cut-off ratios are greater than unity. Equations 2.15 and 2.16 highlight the dependence of the cut-on of acoustic modes on the Helmholtz number, kR. As kR is increased, more higher-order modes are cut-on in a duct of radius R. Furthermore, the eigenvalue σ_{mn} is dependent on the cross-sectional geometry of the duct, as discussed in Section 2.1.1. The cut-on frequency of a given mode in a given duct will therefore vary depending on the duct geometry, as well as the mean flow velocity, ambient temperature, and ambient pressure. Any swirling mean flow will also modify the cut-on behaviour of the acoustic modes, with this modification depending on whether or not they contra-rotate relative to the flow swirl direction. Golubev and Atassi [18] investigated the effect of a mean swirl velocity on the behaviour of acoustic mode propagation, and found that a normal mode analysis will reduce to a non-linear eigenvalue problem. Numerical simulations are required in order to analyse the behaviour of both cut-on and evanescent modes in the case of a swirling flow.

In many scenarios where duct acoustics are being investigated, such as in an aero-engine, the frequency range of interest commonly extends above the cut-on frequency of several of these higher-order acoustic modes. Knowledge of the constituent modal amplitudes for each cut-on mode is useful for determining the propagation process of sound in the duct, and can also be used to help identify the relative contributions of noise sources in the duct to this propagating noise (as applied in Section 4.3). Certain sources of noise, such as the periodic interaction between rotor-stator stages, have specific modal content associated with them i.e. the dominant acoustic modes at these periodic frequencies can be predicted. Several studies have also used acoustic modal theory to study fan noise [19, 20], compressor noise [9, 21] and combustor noise [22].

For a hard-walled duct, the eigenfunction which describes the acoustic mode shape in the (r, θ) plane is given by:

$$\Psi_{mn}(r,\theta) = E_{mn}^{\eta}(k_{mn}r)e^{(im\theta)} \tag{2.17}$$

The dependence of the characteristic E function on η in Equation 2.17 can be dropped for the case of a circular cross-section. This eigenfunction has been plotted for the case of a circular cross-sectioned duct by Bennett [23]. Figure 2.3 plots these eigenfunctions for the case of an annular cross-sectioned duct for a range of (m, n) mode orders, with a hub-to-tip ratio $\eta = 0.25$.
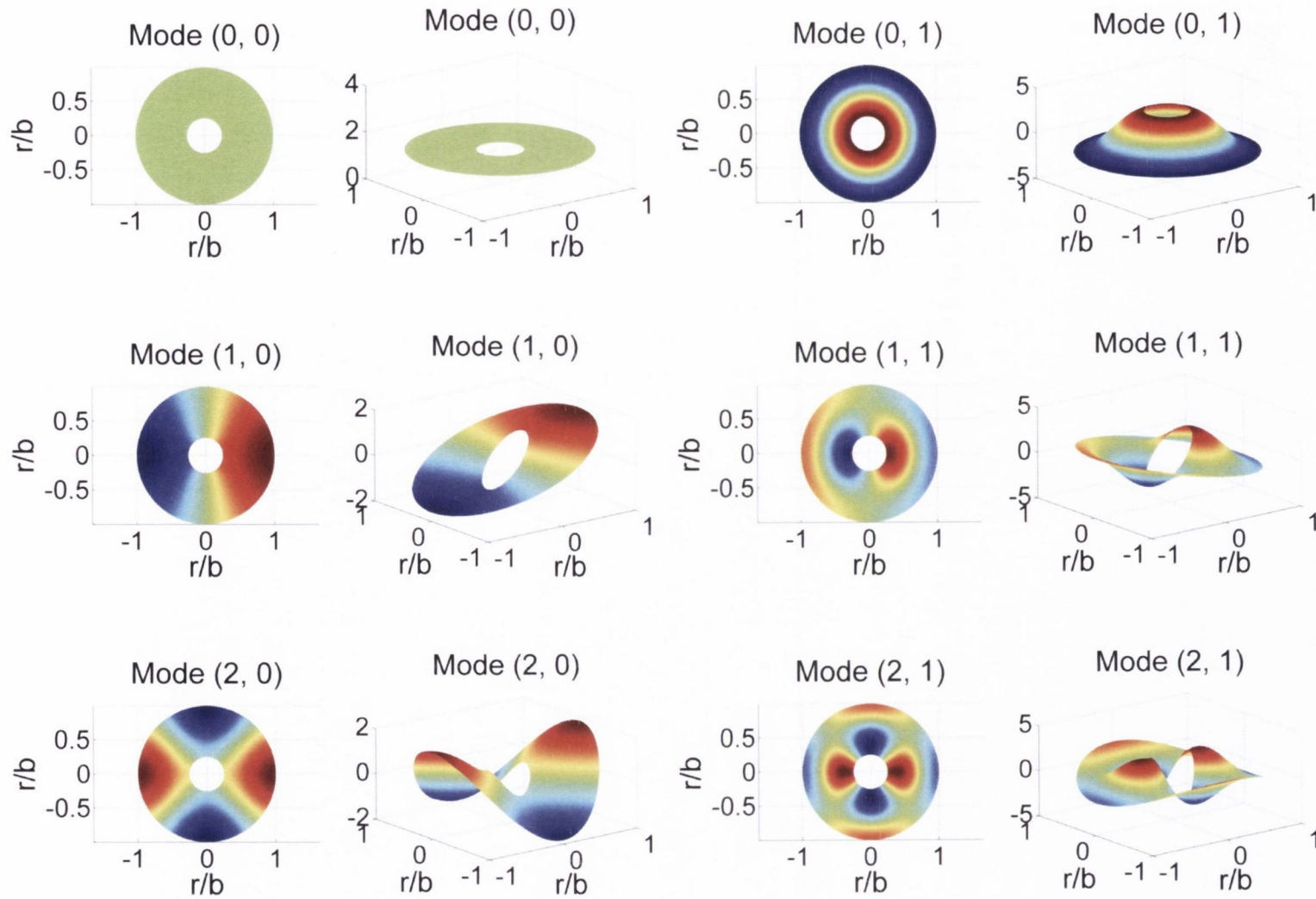
Figure 2.3: Acoustic mode shapes for an annular cross-sectioned duct, $\eta = 0.25$.

2.3   Acoustic Transmission Through Area Discontinuities

For the case of one-dimensional (plane) wave front transmission with zero mean-flow, as occurs in ducted geometries at low frequencies, the acoustic pressure in a finite length duct can be represented simply by the superposition of forward and backward travelling waves:

$$p = Ae^{-jkx} + Be^{jkx} \tag{2.18}$$

where A is the amplitude of the forward-travelling wave and B is the amplitude of the backward-travelling wave. For transmission through an area discontinuity, as occurs in aeroengines as well as in mufflers and other common ducting systems, the transmissibility and reflection of the acoustic waves through the discontinuity is of great interest. Area discontinuities can be used to limit acoustic transmissibility and therefore act as passive mufflers. For a sudden contraction or expansion, the reflection coefficient for a forward-travelling plane wave is given by:

$$R = \frac{S_2 - S_1}{S_2 + S_1} \tag{2.19}$$

where S_1 is the cross-sectional area of the duct prior to the contraction/expansion and S_2 is the cross-sectional area after the contraction/expansion. No acoustic power is lost, but sound is reflected due to the change in the characteristic impedance (Y_0) between the two cross-sectional areas. In order to better improve the transmission through a change in cross-sectional area, a gradual change in cross-sectional area with axial-distance is required. Conical, exponential or hyperbolic expansions/contractions allow better matching of characteristic impedances. More detail on the specific impedances inside these various horn geometries can be found in Morse [24].

At a given axial location in a uniform duct, the specific acoustic impedance is given by:

$$\zeta(x) = \frac{p(x)}{v(x)} = Y_0 \frac{Ae^{-jkx} + Be^{jkx}}{Ae^{-jkx} - Be^{jkx}} \tag{2.20}$$

At the end of a duct, the geometry will commonly terminate by one of three different way: with a closed end, with an open end, or with an anechoic termination. For a rigid closed end termination, the specific impedance will tend towards infinity, meaning that all incident noise will be reflected. Levine and Schwinger [25] studied the affects of sound radiation from an unflanged duct into hemispherical space, and made an empirical fit for the values of both the amplitude of the reflection coefficient $|R|$ and the end correction δ. The magnitude of the reflection coefficient is dependent on frequency, and drops monotonically as the Helmholtz number (kR) is increased.

When designing experimental tests for duct acoustics investigations, it is often necessary to eliminate reflections at one or both end(s) of the duct. This is necessary for establishing causal links between noise-source regions and output measurements within the duct through correlation analysis, for example. Acoustic horn theory can be applied to design an anechoic termination which will eliminate reflections at the duct end(s) by matching the characteristic impedance of the inside of the duct with that of the surrounding environment. For wave propagation through a diverging geometry, the change in acoustic pressure is described by Webster's formula:

$$\frac{\partial p'}{\partial x^2} + \frac{d[\ln(S(x))]}{dx}\frac{\partial p'}{\partial x} = \frac{1}{c_0^2}\frac{\partial^2 p'}{\partial t^2} \tag{2.21}$$

As well as designing anechoic terminations, horn theory can also be applied in order to better match the characteristic impedances at area discontinuities within a duct. This is useful in the design of waveguides for transmitting noise from loudspeakers into test ducts, see for example the experimental set-up shown in Section 4.2.

2.4   Rotor-Stator Noise Generation in Aeroengines

The key noise-source regions in the core region of a typical aeroengine can include the compressor, combustor and turbine stages. An example of the locations of these regions is shown in Figure 2.4 for a typical turboshaft engine. The rotor-stator stages of the compressor and turbines are sources of both tonal and broadband noise. Advances in turbofan engines have resulted in high bypass-ratio engines, which have reduced the effect of jet noise. During approach and when taxiing, turbomachinery noise is a highly significant

noise-source in such engines, as shown graphically in Figure 2.5. The relative contribution of core noise-sources to the total noise radiated from aircraft has also increased in modern aeroengines, as illustrated in Figure 2.6. In turboshaft engines, where jet noise is negligible due to low exhaust velocities and there is no bypass stream, turbomachinery noise dominates the noise radiating from the engine exhaust. Figure 2.5 demonstrates that the rotor-stator stages of the turbine contribute significantly to the broadband noise from the engine exhaust, and dominate the total core noise. Tonal noise generated by periodic interactions at these turbine stages will also contribute significantly to the total engine tonal noise.
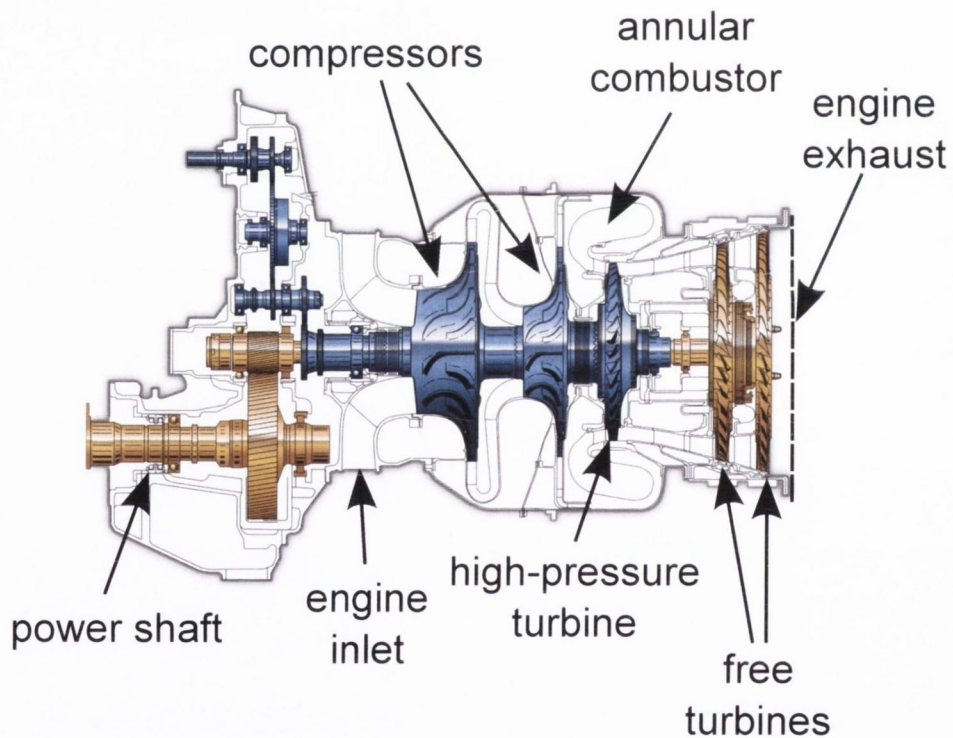
Figure 2.4: Schematic of an Ardiden 1H1 helicopter engine.

For a ducted rotor rotating at a subsonic tip speed, a typical acoustic pressure spectrum taken close to a rotor-stator stage will consist of a broadband noise floor, with tonal peaks at the blade-pass frequencies of the rotor. The blade-pass frequency tone of a rotor results from the steady pressure field generated by the periodic rotation of the rotor blades, forming a lobed pressure pattern which propagates axially in the duct as a travelling wave with a fixed circumemferential speed [14]. The shape of this lobed pressure pattern,
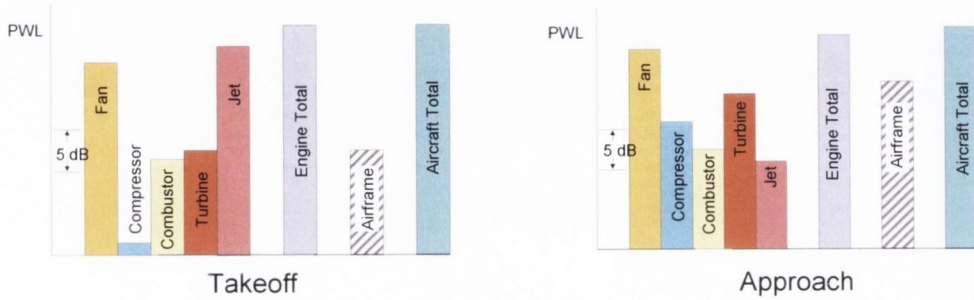
Figure 2.5: Relative power levels of aircraft noise sources at takeoff and approach. Reproduced from Astley *et al.* [1].
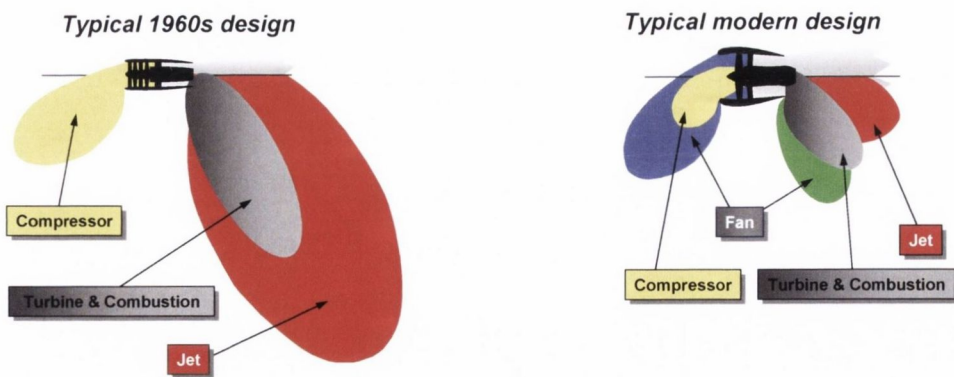
Figure 2.6: Engine noise sources: 1960s versus a modern design. Reproduced from Astley *et al.* [1].

when examined in a cross-sectional view of the duct at a given axial location, will vary depending on the blade geometries of the rotor *e.g.* blade pitch angle, camber. The blade-pass frequency of a rotor and its harmonics are given by:

$$\text{BPF} = h \left(\frac{NB}{60} \right) \tag{2.22}$$

where N is the rotational speed of the rotor in rpm, B is the number of rotor blades, and h is a positive integer which refers to the BPF harmonic. Tones may be observed for a rotor rotating with subsonic tip speeds at certain rotor shaft harmonic frequencies ($iN/60$) if there is an imbalance in the shaft, where i is a positive integer. At supersonic tip speed, tonal peaks at all shaft frequencies will appear in the spectrum. These multiple pure tones are referred to as "buzz-saw" noise. As a consequence of the lobed shape of the pressure pattern generated by its blade-pass frequency (BPF) and harmonics, only certain azimuthal mode orders will be excited by the rotor at these frequencies. For a rotor with B blades, a B-lobed pressure pattern will be generated at the fundamental BPF. Expanding for each subsequent h BPF harmonic, an hB lobed pressure pattern will be generated. The azimuthal mode order generated, m, is therefore given by:

$$m = hB \tag{2.23}$$

This analysis was also extended by Tyler and Sofrin [14] for the case of a rotor interacting with a stator, a common interaction in aeroengines. The stator vanes are used to divert the angular components (swirl) of the rotor wake in the axial direction, increasing fan hydrodynamic performance. The resulting pressure field given by the interaction of the rotor pressure field with a stator containing V vanes is give by:

$$p_{mn} = V a_{mn} \cos(m\theta - hB\Omega t + \phi_{mn}) \tag{2.24}$$

where m is restricted to

$$m = hB - kV \qquad\qquad k = \cdots -2, -1, 0, 1, 2 \cdots \tag{2.25}$$

The interaction field at each h rotor BPF harmonic is the infinite superposition of rotating pressure patters, each rotating with an angular velocity of $hB\Omega/m$ radians per second where Ω is the angular speed of the rotor.

For the case of rotor-alone noise, neglecting the presence of any nearby stator stages, the dominant sources of noise are the interaction between inlet boundary layers/distortions with the fan and fan self noise. Fan self-noise is caused by airfoil trailing-edge noise, separation stall noise, laminar boundary layer shedding noise, tip vortex formation noise and trailing-edge vortex shedding noise. Brooks *et al.* [26] use a semi-empirical approach in order to get an overview of these noise generating mechanisms. Glegg [27, 28] discusses these noise source mechanisms for a single airfoil by examining blade surface unsteady pressure distributions. These works contains a large list of references to work in the field of rotor self-noise. Predictions of fan broadband noise have made large steps forward in recent years, due to an increased interest as treatment of fan tonal noise has improved. Simulations of fan broadband noise are an area of continuing study, as more sophisticated numerical and CAA (computational aeroacoustic) codes are being developed. The recent E.U. FP-6 project PROBAND has better characterised the broadband noise-source mechanism generated by rotors (specifically fan noise in turbofan engines), using fundamental experiments in conjunction with advanced CFD to provide a deeper insight into the flow physics in the source regions [29].

In the chapter by Groeneweg *et al.* [30], it is stated that fluctuating pressures, whose phase or trace speed is supersonic relative to an observer, will radiate sound to that observer. Vortical disturbances, or gusts, are the origins of such fluctuating pressures on blade rows of a rotor. The fluctuating normal force per unit span of a blade, F_2, is given by:

$$F_2 = \pi \rho_o U_r a_2 c \exp[i(k_3 y_3 - k_1 U_r t)]\eth(\dot{k_1}, k_3, M_r) \tag{2.26}$$

The co-ordinates here are aligned such that y_1 is along the blade chord and y_2 is in the direction of the upwash. ρ_o is the ambient density, c is the blade chord, and U_r is the velocity of convection of the gust relative to the blade chord. $\eth$ is the response function for the gust of wavenumber k convecting at U_r. For special conditions with respect to

airfoil geometry and flow type (compressible or incompressible), solutions for ∂ exist in the literature [31–36].

Periodic interactions between rotor blades and stationary stator vanes excite infinite many spinning modes at every blade-pass harmonic, as stated in Equation 2.25. Cut-on modes generated by this mechanism will propagate in the duct. The strength of these interaction effects can be reduced by increasing the spacing between the rotor blade and stator vane rows, but this will in turn reduce the hydrodynamic efficiency of the stator. Judicious choice of the number of rotor blades and stator vanes can help ensure that most of the lower order modes, which are most likely to be cut-on at the blade-pass frequencies, are not generated as per Equation 2.25. In the next chapter, a method of exciting specific azimuthal modes using an array of monopole sources is discussed, which could simulate a fan BPF tone for example. Methods for decomposing the acoustic pressure field at a given axial location in a duct into its constituent modal amplitudes using arrays of microphones are also discussed.

Chapter 3

Acoustic Modal Analysis and Generation

Modal analysis techniques allow the specific modal content at a given axial location in a duct to be determined. Generally, these techniques use a large number of acoustic pressure measurements taken by microphones arranged at a range of axial, azimuthal and radial locations, in conjunction with steering vectors describing the physics of modal transmission in a duct, to estimate the complex modal amplitudes. Each acoustic mode describes a specific way in which noise can propagate in a duct, and therefore knowing the amplitudes of these acoustic modes gives a more complete understanding of the transmission of sound, and hence allows better mitigation of this noise using active noise control (ANC) methods or through passive attenuation using acoustic liners. In this chapter a range of modal decomposition techniques are reviewed, and a technique for modal analysis using multiple microphones flush-mounted to the duct inner wall and applied in the experimental test results analysed in Chapters 4 and 6 is discussed. Finally, the theory of targeted mode generation is shown. Targeted mode generation uses several circumferentially spaced noise sources, and can be used to generate tonal noise with a dominant targeted azimuthal mode (TAM) at this tonal frequency. Analytical simulations are used to demonstrate the effectiveness of this technique.

3.1   Overview of Modal Decomposition Techniques

Early studies in modal analysis include the theoretical work of Dyer [37], who considered a source that is "completely random in space" in a hard-walled circular duct. Dyer concluded in his analysis that subject to certain parameters all acoustic modes present in the duct above their respective cut-on frequencies will carry equal energy. Morfey [38] furthered Tyler and Sofrin's discussion on these rotating pressure patterns, or azimuthal modes. Morfey further investigated the transmission of higher-order acoustic modes in axisymmetric ducts, and established a relationship between the mode intensity and the mode amplitude and impedance. Mugridge [39] presented a method for identifying the rotating acoustic modes which may be generated at a rotor stage using time and space correlations between two pressure transducer signals. These transducers are traversed circumferentially around the duct at specific axial and radial location inside the duct. This technique allows the mode orders present to be identified and their relative contribution to

the total BPF noise to be assessed. Comparisons were also made by the author between theoretical and experimental mode directivity patterns based on these results. Moore [15] proposed both integration and least-squares matrix inversion methods in order to identify the modal content for both artificial and experimental scenarios, for periodic signals. These techniques allow the relative contributions of several cut-on modes to the noise radiated at a specific axial location in a duct to be assessed. Such techniques of decomposing the sound field in a duct into its specific modal constituents are known as modal decomposition techniques. Other similar direct modal decomposition techniques exist in the literature [40–43], however many make assumptions on the type of signal present in the duct.

Yardley [44] formulated a modal analysis technique using an array of flush-mounted microphones spaced both circumferentially and axially. Åbom [13] introduced a novel method of modal decomposition which uses the transfer function between pairs of microphones, provided the duct eigenfunctions and eigenvalues are known. Unlike many previous modal decomposition techniques in the literature, Åbom's proposed technique does not require a priori assumptions on the signal type present in the duct. Furthermore, this modal decomposition technique allows the content of the modes travelling in both axial directions to be found, hence allowing both the incident and reflected modal content to be identified.

Holste and Neise [45] used rakes of sensors to determine the modal content radiated from a CRISP (Counter Rotating Integrated Shrouded Propfan), which is a novel turbofan configuration used in high bypass ratio engines. A sensor rake located at a single axial location contains several microphones spaced radially. Data is acquired, and the rake is then rotated azimuthally. Data is then acquired at this new azimuthal location. This process is repeated for a full revolution of the sensor rake, and the azimuthal modal content of the pressure field at this axial location is resolved by:

$$\hat{p}(r, \theta, x, \omega) = \sum_{m=-\infty}^{\infty} A_m(x, r, \omega)e^{jm\theta} \tag{3.1}$$

This is a reformulation of Equation 2.2, where the complex circumferential mode distribution is shown in isolation. The sampling time by the microphones in the sensor rake is

synchronised with the trigger signal used to control the rotor's rotation.

Enghardt *et al.* [46] proposed a modal decomposition scheme using equi-azimuthally-spaced wall-mounted sensors only, as opposed to sensor rakes, to decompose the pressure field into its specific modal amplitudes. This form of modal decomposition is far easier to implement in a real aeroengine due to the practical space constraints, and reduces sensor contamination as the wall-mounted sensors do not interact with the flow through the engine. Using computer simulations the authors theorised that the radial modal content could also be decomposed by measuring the sound field at different axial locations as well as different azimuthal positions. The wall mounted sensor configuration was compared experimentally with the results for a sensor rake, and found to agree well. The radial modal analysis (RMA) technique was also tested and found to measure the radial modes as predicted. A similar investigation to Holste and Neise [45] was undertaken by Enghardt *et al.* [47] using sensor rakes for radial mode analysis. Tapken and Enghardt [48] further assessed the radial mode analysis technique by undertaking a numerical study on the effects of frequency, sensor location, and flow conditions such as the presence of swirl. From the results of this study, the authors made suggestions on optimum sensor spacings and potential causes of poor signal conditioning in RMA data analysis.

Bennett [23] implemented a modal decomposition technique based closely on the methods of Åbom [13] and Yardley [44], whereby an array of microphones is mounted flush to the inner duct wall. The sensors in this array are equally spaced azimuthally and axially. The characteristics and advantages of this technique are:

1. incident and reflected modes can be identified;

2. a mean flow can be accommodated;

3. a frequency response function technique may be employed;

4. radial, as well as azimuthal, modes can be identified;

5. duct-wall flush-mounted microphones only are used for the decomposition;

6. the decomposition is performed for all frequencies not only at the BPF and harmonics;

7. data is acquired at all measurement locations simultaneously.

From the formulation of the acoustic pressure in a hard-walled duct given by Equation 2.2, this modal decomposition technique is undertaken in two stages. More detail on both stages can be found in the technical report by Åbom [49]. In the first stage an azimuthal decomposition is carried out using microphones located circumferentially around the duct as follows:

$$p_{l,k} = \sum_{m=1-M}^{M-1} h_{m,k} e^{[jm\theta_l]} \quad \text{where} \quad \begin{array}{l} k = 0, 1....2N - 1 \\[4pt] l = 0, 1, ...2M - 1 \end{array} \tag{3.2}$$

$$\theta_l = \frac{2\pi l}{2M - 1}$$

where M and N are the number of azimuthal and radial modes cut-on at the frequency of interest. l and k refer to the azimuthal and axial microphone indices respectively. This stage may be repeated at several axial locations in order to decompose these modes into both the radial modes and their incident and reflected components:

$$h_{mk} = \sum_{n=0}^{N-1} [A_{m,n}^+ e^{-jk_{m,n}^+ x} + A_{m,n}^- e^{+jk_{m,n}^- x}] f_{m,n}(r) \tag{3.3}$$

Using a process of matrix pseudo-inversion, a least-squares solution can be found for the above equation to estimate the complex modal amplitudes. The first part of the technique requires two measurements per azimuthal wavelength $(2\pi/m)$, analogous to the Nyquist sampling criterion. $2M$ sensors are therefore required to be located azimuthally, where M is the maximum azimuthal mode to be decomposed. This places an upper frequency limit at which this technique can be applied for a given amount of acoustic sensors. Holste and Neise [45] make similar conclusions, and also state that aliasing is possible when not enough sensors are located per cut-on mode. An example of the full expansion of this modal decomposition procedure can be found in Chapter 7 of Bennett [23] for a specific experimental set-up.

The matrix inversion step will be more robust as the system is further over-determined *i.e.* with more microphone measurements per cut-on mode. Castres and Joseph [50] investigated the robustness of the matrix pseudo-inversion step of a modal decomposition

scheme whose least-squares solution minimises $||\hat{\mathbf{p}} - \mathbf{Da}||$, where $\mathbf{p}$ is a matrix of complex acoustic pressure measurements, $\mathbf{D}$ is a directivity matrix describing the physics of acoustic modal propagation, and $\mathbf{a}$ is a matrix of estimated modal amplitudes. The pseudo-inversion step undertaken in the modal decomposition techniques such as Åbom's outlined above are highly sensitive to errors at modal cut-on frequencies due to an ill-conditioned directivity matrix, which is a particular issue at high frequencies when modal cut-ons are grouped close together. A method is described by Castres and Joseph to increase matrix inversion robustness by regularisation, but this must be used as a compromise with the accuracy of the solution.

Recently, Enghardt *et al.* [51] have investigated modal analysis for broadband noise in a duct, where sound will propagate in a duct with energy spread over all cut-on modes. Two techniques were proposed: the first, BBMA I, makes use of the spectral cross-correlations between one reference sensor and all other sensors in a sensor array. This technique was first suggested in another paper by Enghardt [52]. This method assumes that all mode orders present in the duct are mutually uncorrelated. The choice of reference microphone has a marked effect on the resulting mode amplitudes deduced with this technique. The second method, BBMA II, applies a beamforming algorithm, and then decorrelates in order to ascertain the mode correlation factors. Comparison of results using both techniques have shown that BBMA II is more robust in the presence of background noise *e.g.* flow noise. The method of Åbom and adopted by Bennett has also been applied to analyse the modal amplitudes of broadband noise by Davis and Bennett [53], and has been shown to be useful in both tonal and broadband noise studies.

3.2   Targeted Azimuthal Mode Excitation

In active noise control (ANC) studies for ducted noise, the aim is generally to reduce the noise emitted from noise sources in the duct (such as fan BPF noise) by generating additional noise using one or more loudspeaker(s) which destructively interferes with this unwanted noise, and hence reduces the noise emitted from the duct into the surrounding environment. At higher frequencies, several higher-order modes may be cut-on. In such cases, many noise sources such as fan BPF noise have specific modal content associated

with them, thus the dominant acoustic modes can be predicted. In these situations, several loudspeakers spaced azimuthally can be used to excite a specific azimuthal acoustic mode, which will then interact with and reduce the noise generated at the fan BPF [54]. If a single ring of noise sources is used, a specific azimuthal mode can be targeted. Using several axial rings of noise-sources a specific radial mode can be targeted. Aside from ANC applications, targeting of specific modes is useful in order to investigate the scattering of acoustic modes for example, as investigated in Chapter 6.

To demonstrate the effectiveness of targeted mode generation an analytical study is presented. For a single point monopole source in a hard walled annular flow duct, the frequency-domain Green's function for a duct with an axial irrotational mean flow must satisfy:

$$(\nabla^2 - M_x^2 \frac{\partial^2}{\partial x^2} - 2ikM_x\frac{\partial}{\partial x} + k^2)G(x,y) = -\delta(x-y) \tag{3.4}$$

and for a hard-walled boundary condition:

$$\frac{\partial G}{\partial n} = 0 \tag{3.5}$$

where n is a unit vector normal to the surface of the duct. Following the formulation of Goldstein [32], the sound pressure generated at position (x, r, φ) due to a single monopole source with volume velocity $q_0 = v_0 A$ located at $(x_{q0}, r_{q0}, \varphi_{q0})$ can be expressed as:

$$\begin{aligned} p(x,r,\varphi|x_{q0},r_{q0},\varphi_{q0}) &= -j\omega\rho q_0 g(x,r,\varphi|x_{q0},r_{q0},\varphi_{q0}) \\ &= q_0 \frac{\rho c}{2} \sum_{m=-\infty}^{\infty} \sum_{n=0}^{\infty} \frac{J_m(\sigma_{mn}r/R)J_m(\sigma_{mn}r_{q0}/R)}{\alpha_{mn}N_{mn}} e^{-im(\phi-\phi_{q0})}e^{-ik_{mn}^{\pm}(x-x_{q0})} \end{aligned}$$

$$\tag{3.6}$$

where q_0 is the source volume velocity, ρ is the density and c is the speed of sound of the propagation medium. R is the duct radius. $J_m(\cdot)$ is the Bessel function of the first kind, of order m. σ_{mn} is the eigenvalue, $k_{mn}^{\pm}$ is the axial wavenumber and N_{mn} is the normalisation factor of the (m,n) acoustic mode. x, r and φ are the axial, radial and circumferential locations of the receiver location of interest and x_{q0}, r_{q0} and φ_{q0} are the axial, radial and circumferential locations of the monopole source. Equation 3.6 provides
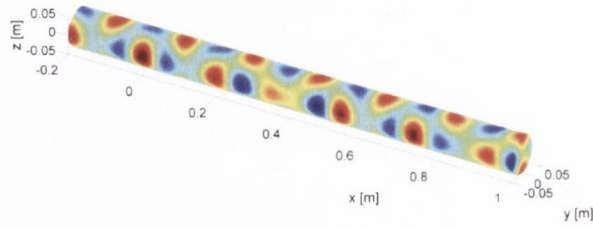
Figure 3.1: Analytical simulation of pressure field generated by a single monopole source located at $x = 0$, $\theta = 0$, $kR = 3.5$. The real part of the complex pressure field is plotted.

the pressure distribution in an (infinite) circular duct as a function of frequency generated by this monopole source. Figure 3.1 shows the pressure field generated in a $1.2m$ length section of circular duct of radius $R = 0.05m$ by a single monopole source located at ($x = 0$, $\theta = 0$, $r = R$). For this case, all duct modes are excited.

Specific azimuthal modes can be targeted by locating multiple monopole noise sources around the circumference of a duct at a fixed axial location and adjusting the phases between the sources as follow:

$$q(\theta_l) = q_m e^{im\frac{2\pi l}{S}} \tag{3.7}$$

where S is the number of monopole sources, l is an index from 1 to S for each monopole source, q_m is the source strength and m is the targeted azimuthal mode (TAM) being excited by the monopole source array.

To demonstrate this targeting of specific azimuthal modes, analytical simulations were undertaken using the theory outlined above. The total acoustic pressure field generated by multiple sources is found through superposition of Equation 3.6 for each source. In Figure 3.2, 15 monopole sources have been equally spaced in the circumferential direction at an axial location $x = 0$. Each monopole source is located at a radial position $r = R$, where R is the radius of the simulated test duct. The real part of the complex pressure field, as found by superposition of Equation 3.6 for each source, is plotted. Each source is of the same strength, generating a tone at $kR = 3.5$ with the phase of each source adjusted as per Equation 3.7. For the left, right and bottom subplots respectively the targeted azimuthal modes are $TAM = 0, 1, 2$. It is apparent from these pressure field plots that the targeted modes dominate, evident by the planar distribution of acoustic pressure excited when $TAM = 0$, and the spiral pressure field patterns indicative of higher-order
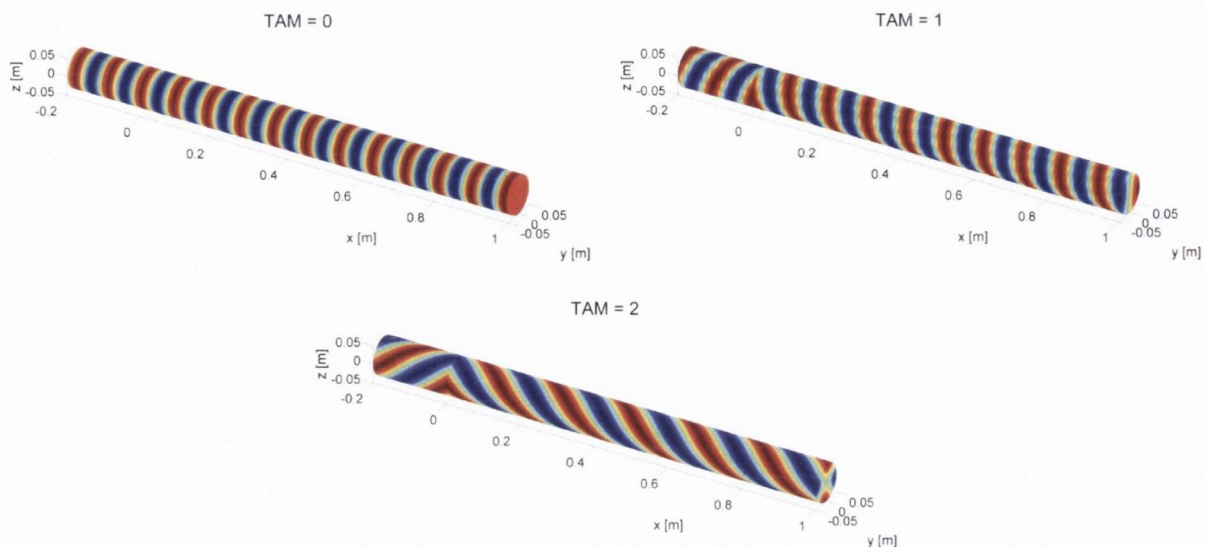
Figure 3.2: Analytical simulation of pressure field generated by targeted mode excitation using 15 circumferentially-spaced monopole sources located at $x = 0$, $kR = 3.5$. The $m = 0, 1, 2$ azimuthal modes have been targeted. The real part of the complex pressure field is plotted.

azimuthal mode propagation when $TAM = 1, 2$.

In order to verify that the targeted mode dominates in each case, a modal decomposition can be performed by interrogating discrete nodes in the complex pressure field and applying a modal decomposition scheme using this data. The radial modal decomposition applied by Bennett and discussed in Section 3.1 was used to find the radial modal amplitudes at an axial location $x = 0.7$. Sixty-four pressure measurements were used, each taken from nodes located at $r = R$ in four axial rings located at $x = 0.7, 0.75, 0.8, 0.85$. Each ring of sixteen nodes is equally spaced in the azimuthal direction around the periphery of the duct. This is analogous in a real experiment to taking microphone measurements using microphones flush-mounted to the wall of the test duct. The focus of this investigation is to target specific azimuthal modes, and therefore the azimuthal mode amplitudes are presented from this radial mode analysis.

When a single monopole source generates noise, all cut-on duct modes are excited and propagate in the duct, as illustrated at a frequency $kR = 3.5$ in Figure 3.3. This modal analysis was performed for the test case shown in Figure 3.1. This modal analysis procedure was repeated for a range of kR values in Figure 3.4, which demonstrates that roughly equal acoustic energy is carried per cut-on acoustic mode, with the test case
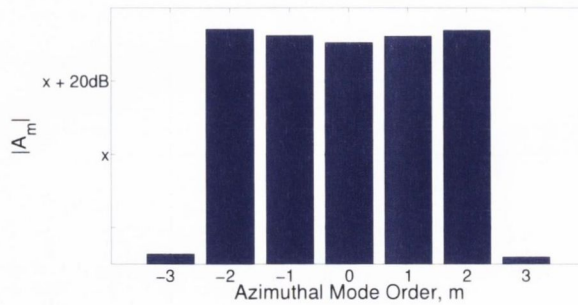
Figure 3.3: Azimuthal modal analysis of pressure field generated by a single monopole source located at $(x = 0, \theta = 0, r = R)$, $kR = 3.5$.
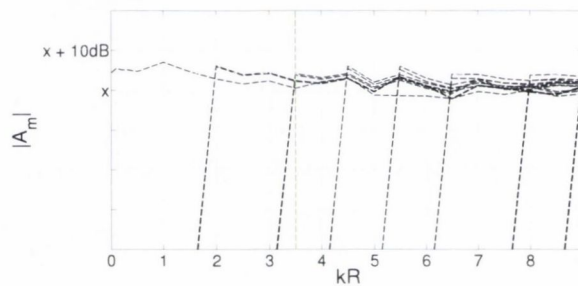
Figure 3.4: Azimuthal modal analysis of pressure field generated by a single monopole source located at $(x = 0, \theta = 0, r = R)$, for a range of frequencies.

shown in Figure 3.3 indicated with a green-dashed vertical line.

The azimuthal modal amplitudes found from modal analyses when three different azimuthal modes are targeted using 15 monopole sources are shown in Figure 3.5. These results were found for the test cases shown in Figure 3.2, and prove that the targeted azimuthal modes dominate the acoustic pressure field. The targeted azimuthal modes dominate by around $30dB$ in each case. This modal analysis is extended for a range of kR values in Figure 3.6, with the green-dashed vertical lines indicating the test cases plotted in Figure 3.5. These figures show that the targeted azimuthal modes dominate for all analysed frequencies above the respective cut-ons of each azimuthal mode. The $m = 0$ mode is excited below the cut-ons of the targeted azimuthal modes for the $TAM = 1$ and $TAM = 2$ test cases. The amplitude of the $m = 0$ mode rapidly decays above the cut-on of the $m = 1$ mode in both cases. No higher-order azimuthal modes are excited above their respective cut-ons aside from the targeted modes.

When performing modal analyses using microphones flush-mounted to the duct wall,
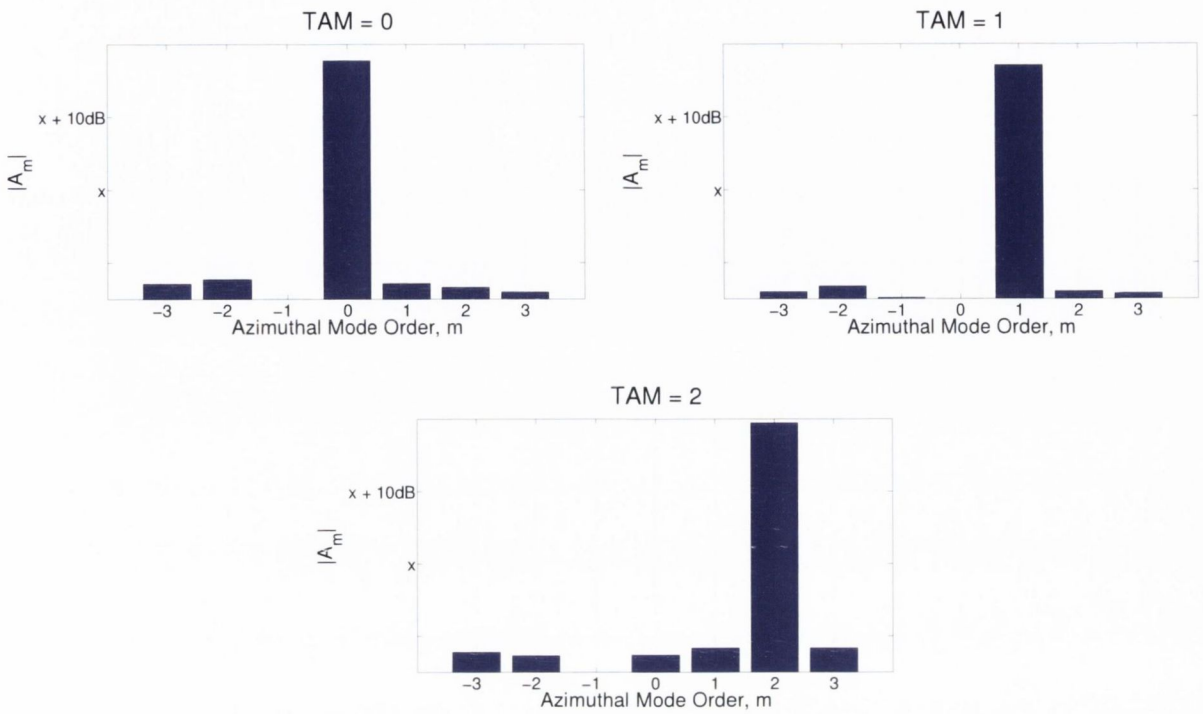
Figure 3.5: Azimuthal modal analysis of pressure field generated by targeted mode generation using 15 circumferentially-spaced monopole sources located at $x = 0$, $kR = 3.5$. The $m = 0, 1, 2$ azimuthal modes have been targeted.
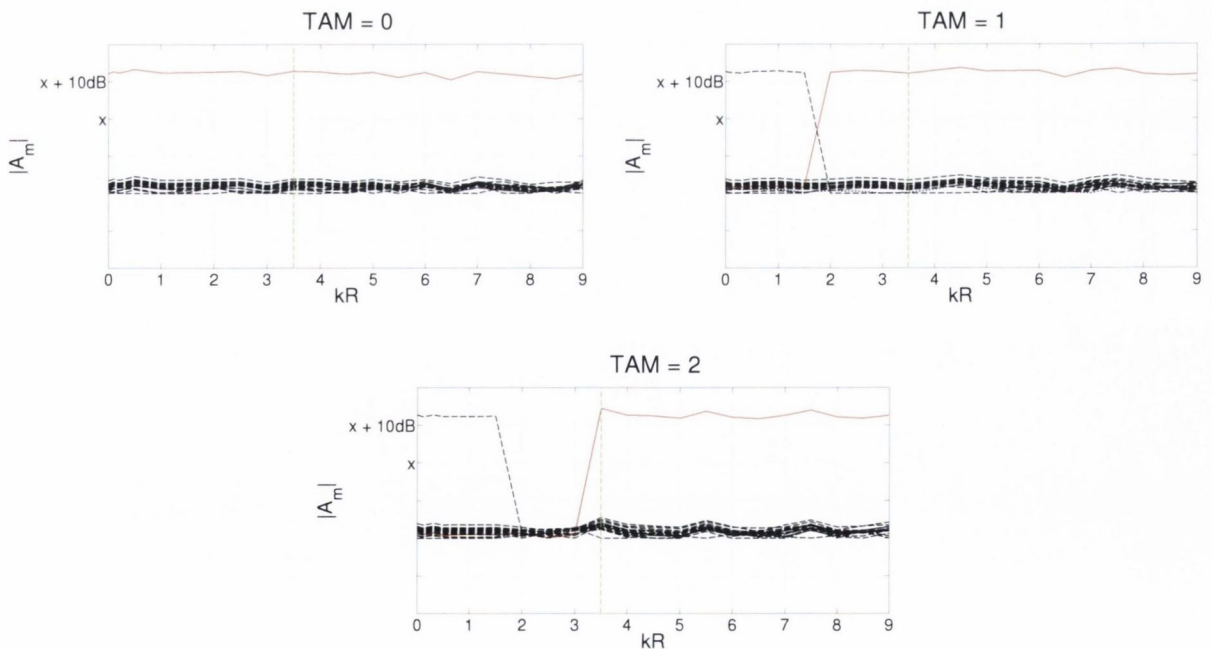
Figure 3.6: Azimuthal modal analysis of pressure field generated by targeted mode generation using 15 circumferentially-spaced monopole sources located at $x = 0$, for a range of frequencies. The $m = 0, 1, 2$ azimuthal modes have been targeted, with the targeted azimuthal mode plotted in red.

it is necessary to make two acoustic measurements per azimuthal wavelength in order to accurately identify each azimuthal mode amplitude. When exciting specific azimuthal modes using monopole sources flush-mounted to the duct wall, it would follow from similar reasoning that the targeted azimuthal mode will be successfully excited when the number of noise sources is greater than double the number of azimuthal wavelengths of the mode being targeted, as per the Nyquist criterion. In order to investigate if this is the case, the test procedure used to calculate the modal amplitudes at $x = 0.7$ in Figure 3.5 was repeated for a range of frequencies and numbers of monopole sources. The azimuthal modal amplitudes were estimated for each test point. Of particular interest is the dominance of the targeted mode, which was quantified by subtracting the level of the most dominant non-targeted mode from the targeted mode. When the targeted mode is not dominant, and hence the mode generator is not effective, this quantity will drop below zero. This quantity will be denoted Δ_{TAM}.

Figure 3.7 shows for selected targeted azimuthal modes (TAM) the values of Δ_{TAM} for a range of dimensionless frequencies (kR) and numbers of monopole sources. The monopole sources are equally circumferentially-spaced around the duct at $x = 0$, $r = R$ in each test case. Each sub-figure plots kR on the x-axis. Each coloured element gives the Δ_{TAM} value measured when N_{SRC} monopoles target a specific TAM at a specific test frequency. When the elements are dark blue it indicates that Δ_{TAM} has dropped below zero, and therefore the mode targeted by the monopole array does not dominate *i.e.* the mode generator is ineffective.

These results show that in order to target a given TAM effectively at cut-on, $n_{SRC} >$ $2 \times$TAM monopole sources are required *i.e.* more than two sources are required per azimuthal wavelength, which matches the Nyquist criterion for digital signal processing. In order for the array of sources to remain effective at higher frequencies, an additional noise-source is required for each additional cut-on azimuthal mode.
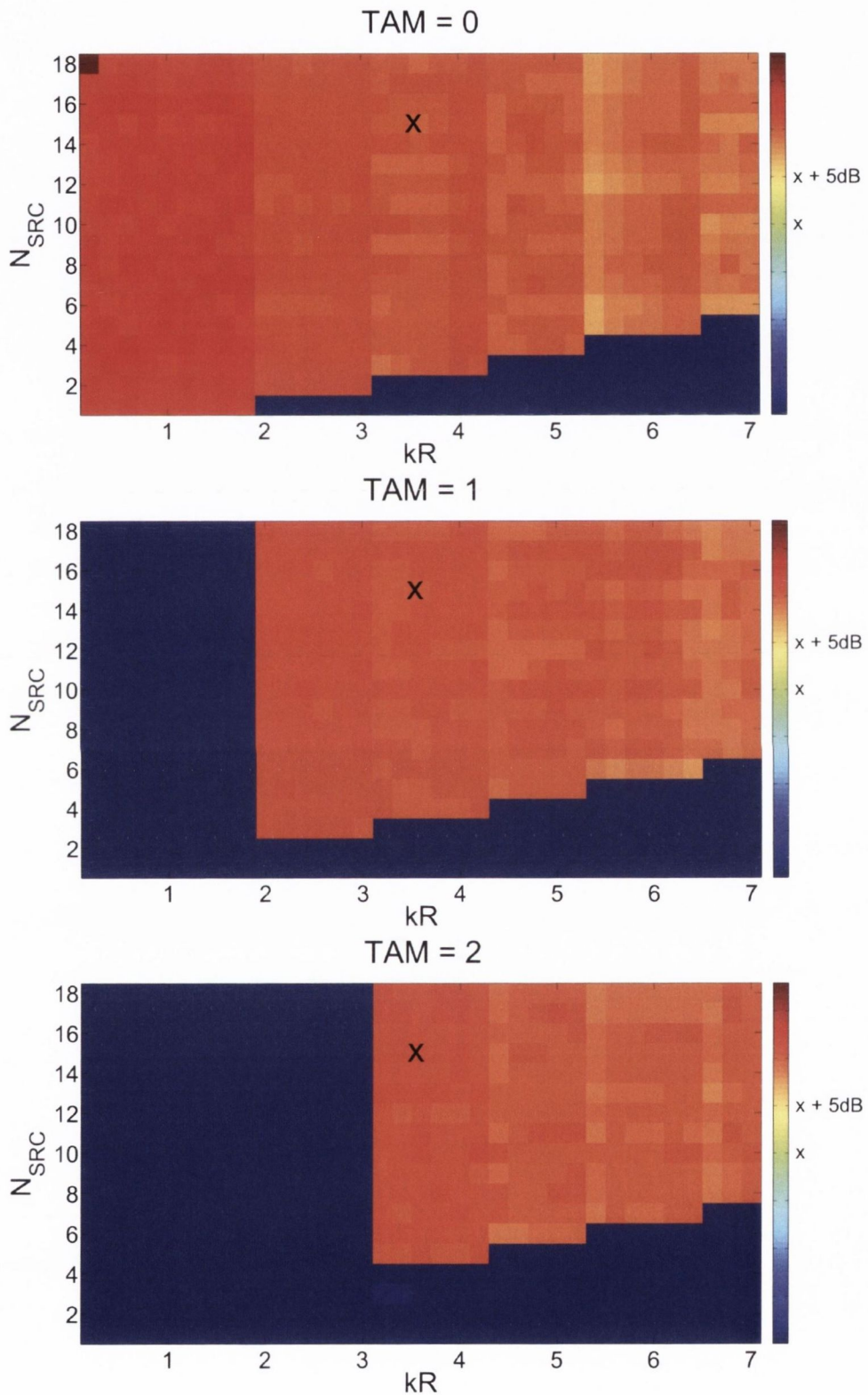
Figure 3.7: Azimuthal modal analysis showing effectiveness of targeted mode generation using a varying number of circumferentially-spaced monopole sources. The colour of each element shows the dominance in dB of amplitude of the targeted mode, as found by a modal analysis performed at $x = 0.7$. Dark blue elements indicate that the targeted mode is not dominant.

3.3   Error Analysis of Single-Ring Azimuthal Modal Decomposition

The modal decomposition technique of Åbom, as outlined in Section 3.1, can be used to decompose the pressure field at a given axial location inside a duct in order to estimate the constituent modal amplitudes. Depending on the number of rings of sensors used, it is possible to identify higher-order azimuthal or radial modes, with or without axial directionality *i.e.* separating out the incident and reflected components.

Using a single ring of sensors, it is possible to identify specific azimuthal modal amplitudes as per Equation 3.2, but without directional information or the ability to separate on radial mode order. Using four rings of sensors it is possible to identify the specific radial mode amplitudes up to and including the cut-on of the $n = 2$ radial mode with directionality. Both methods require at least two sensors per cut-on azimuthal mode in each axial ring of microphones. It is evident that more rings of sensors are desirable, as it allows more information to be discerned regarding the specific modal content within the duct. However, in certain experimental scenarios it is not possible to locate more than a single ring of sensors due to a lack of available sensors, DAQ channels, or space within the duct. Full-scale aeroengines are a particular challenge for acoustic sensor measurements due to the lack of space for sensor measurements and hostile environments with high fluctuating temperatures and flow speeds. Furthermore, in situations where one end of the test duct terminates anechoically and the effect of reflections can be discounted, directional information may be unnecessary. Finally, information on the radial mode amplitudes may simply be unnecessary when for example analysing the targeted azimuthal modal generation results in Section 3.2.

In the experimental tests undertaken in Chapters 6 the number of available channels and microphones was limited, and therefore a modal decomposition was undertaken using a single ring of sensors. In order to investigate the impact of having only a single ring of sensors instead of multiple rings, both analytical and experimental investigations was undertaken and are presented in the proceeding sections. In both investigations the results from a single-ring azimuthal modal analysis are compared to the results from a multiple-ring radial modal analysis, with the multiple-ring analysis used as a benchmark to assess

the error levels in the single-ring analysis.

3.3.1   Analytical Investigation

In the experimental tests undertaken in Chapters 5 and 6, the pressure field at a specific axial location of a circular duct was decomposed into the specific azimuthal modal amplitudes. As the sensors were all located at a single axial and radial location, it is prudent to consider the errors resulting from application of this technique when compared to a more thorough modal analysis using sensors at multiple axial locations. Using multiple rings of sensors, a radial modal analysis may be performed. In order to directly compare the modal amplitudes estimated from a multiple-ring radial modal analysis ($|A_{(m,n),RMA}|$) with the amplitudes estimated from a single-ring azimuthal analysis ($|A_{m,AMA}|$), the radial modal amplitudes are summed into azimuthal modal amplitudes as follows:

$$|A_{m,RMA}| = \sum_{n=0}^{N_m} |A_{(m,n),RMA}| \tag{3.8}$$

where N_m is the largest-order radial mode cut-on for each corresponding m azimuthal mode at any frequencies of interest.

Analytical tests were performed using the hard-walled, circular duct theory outlined in Equation 3.6. The parameters of the analytical tests were matched to the experimental set-up with the duct radius $R = 0.05$. A single monopole noise-source is located at (0,0,0). As demonstrated in Figure 3.4, a single monopole noise source will excite all duct modes that are cut-on in the duct.

Table 3.1 lists the locations of each receiver used to perform both single-ring and multiple-ring modal analysis procedures. More sensors were used in each axial ring in the multiple-ring modal analysis in order to ensure high accuracy in the analysis. It is assumed in the study that the large number of receivers used in the multiple-ring modal analysis will lead to very accurate results, therefore offering a benchmark with which the single-ring results can be compared. Twenty-five receivers located at $x = 2.148$ were used to decompose the modes in the single-ring analysis, matching the experimental set-up. The test frequency range was also matched to the experiments; 2048 test frequencies were investigated in the range 0–13000Hz, giving a frequency resolution of 6.35Hz in the

Table 3.1: Locations of sensors for comparison of modal analysis methods

Modal Analysis Method	x	φ	r
$A_{m,AMA}$	2.148	$2\pi/25{:}2\pi/25{:}2\pi$	R
$A_{m,RMA}$	2.148:0.06:2.568	$2\pi/50{:}2\pi/50{:}2\pi$	R

analysis.

The two azimuthal amplitude estimates $|A_{m,AMA}|$ and $|A_{m,RMA}|$ are shown across all test frequencies in Figure 3.8. Both results have been plotted on the same y-axis scale. These figures show the expected propagation behaviour of a single noise monopole noise-source in a circular duct, with all modes excited above their respective cut-on frequencies. Above their cut-ons each mode carries close to equal energy, with the amplitude of each azimuthal mode increasing as more radial modes are cut-on. Large increases in amplitude are observed at the cut-on of each azimuthal and radial mode, such as the large spike at $kR = 3.83$ for the $m = 0$ mode which corresponds to the cut-on of the (0,1) radial mode. Despite both methods generating similar results, some variation in amplitude is observed. This difference in sound pressure level is isolated in the blue spectra shown in Figures 3.9 and 3.10. As the $|A_{m,RMA}|$ estimate is assumed to be highly accurate, this difference in sound pressure level gives the magnitude error of the single-ring estimate $|A_{m,AMA}|$. This error is generally bound between $-2dB$ and $2.5dB$, with higher errors of up to $4dB$ observed close to modal cut-ons. This error generally decreases for each azimuthal mode as the frequency is increased above its cut-on frequency.

In real experimental investigations, some degree of extraneous noise is expected in any microphone measurements. This noise could arise from structural vibrations at the measurement location, flow-noise due to the hydrodynamic interaction between the microphones and the fluid flow through the duct, or electrical noise in the microphone signal. The impact of such extraneous noise, assumed to be uncorrelated between all measurements, was thus investigated for the single-ring analysis method. Of particular interest was the impact of such noise on measurement of the $m = 0$ mode, as the equal distribution of acoustic pressure with azimuthal angle raises the possibility of all microphones at a single axial and radial location measuring an acoustic node at certain frequencies. It is possible that, with the addition of extraneous noise, the signal-to-noise ratio will

significantly decrease in such situations, causing the error in the modal estimate to rise.

To asses the impact of extraneous noise on the single-ring modal estimate, the complex frequency-domain pressures at the locations listed in the $A_{m,AMA}$ row of Table 3.1 were transformed into the time-domain. Gaussian noise was then added to each time-domain signal, with the magnitude of this extraneous noise a function of the standard deviation of the time-domain signals. The resulting signals with added noise were transformed back into the frequency-domain, and the single-ring azimuthal modal analysis was performed using these complex pressures. This was repeated for 250 averages, simulating ensemble averaging of a real experimentally-acquired signal. The resulting modal amplitudes ($|A_{m,AMA,noise}|$) were then compared with $|A_{m,RMA}|$ as before in order to asses any additional errors introduced by the addition of extraneous noise. The modal amplitudes $|A_{m,RMA}|$ were calculated using the clean (no noise added) pressure signals $i.e.$ the same $|A_{m,RMA}|$ estimate was used as plotted in Figure 3.8.

The difference in sound pressure levels of each azimuthal mode against frequency are plotted for two added-noise cases in the red and green spectra in Figures 3.9 and 3.10. These spectra can be compared with the blue (noise-free) spectra to asses the impact of the added on the single-ring modal estimates $|A_{m,AMA}|$. Some increase in the errors is noted, however these errors still remains low at frequencies other than modal cut-ons, and the change in error levels is only of the order of $1dB$ even when the higher level of noise has been added. The ensemble averaging procedure has reduced the affect of this additive noise such that it is insignificant. Interestingly, no spikes in the error of the $m = 0$ mode are observed, suggesting that measurement of acoustic nodes by all microphones is not an issue.

The error analysis presented in this appendix has demonstrated that, even in the presence of significant levels of extraneous noise, the single-ring azimuthal analysis technique gives an accurate estimate of the azimuthal modal amplitudes for the case of an infinite duct when reflections are non-existent. This verifies the single-ring technique's suitability for application in experimental tests where reflections have been greatly reduced using anechoic terminations.
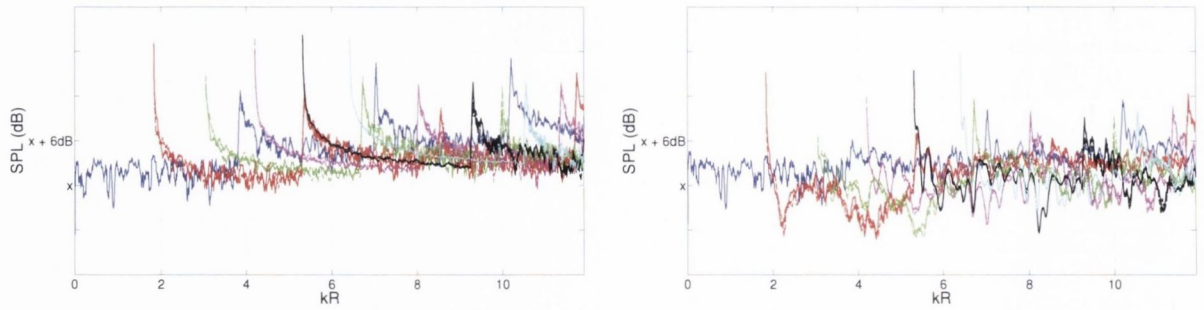
Figure 3.8: Azimuthal modal amplitudes estimated using multiple rings of sensors ($A_{m,RMA}$, right) and a single ring of sensors ($A_{m,AMA}$, left).
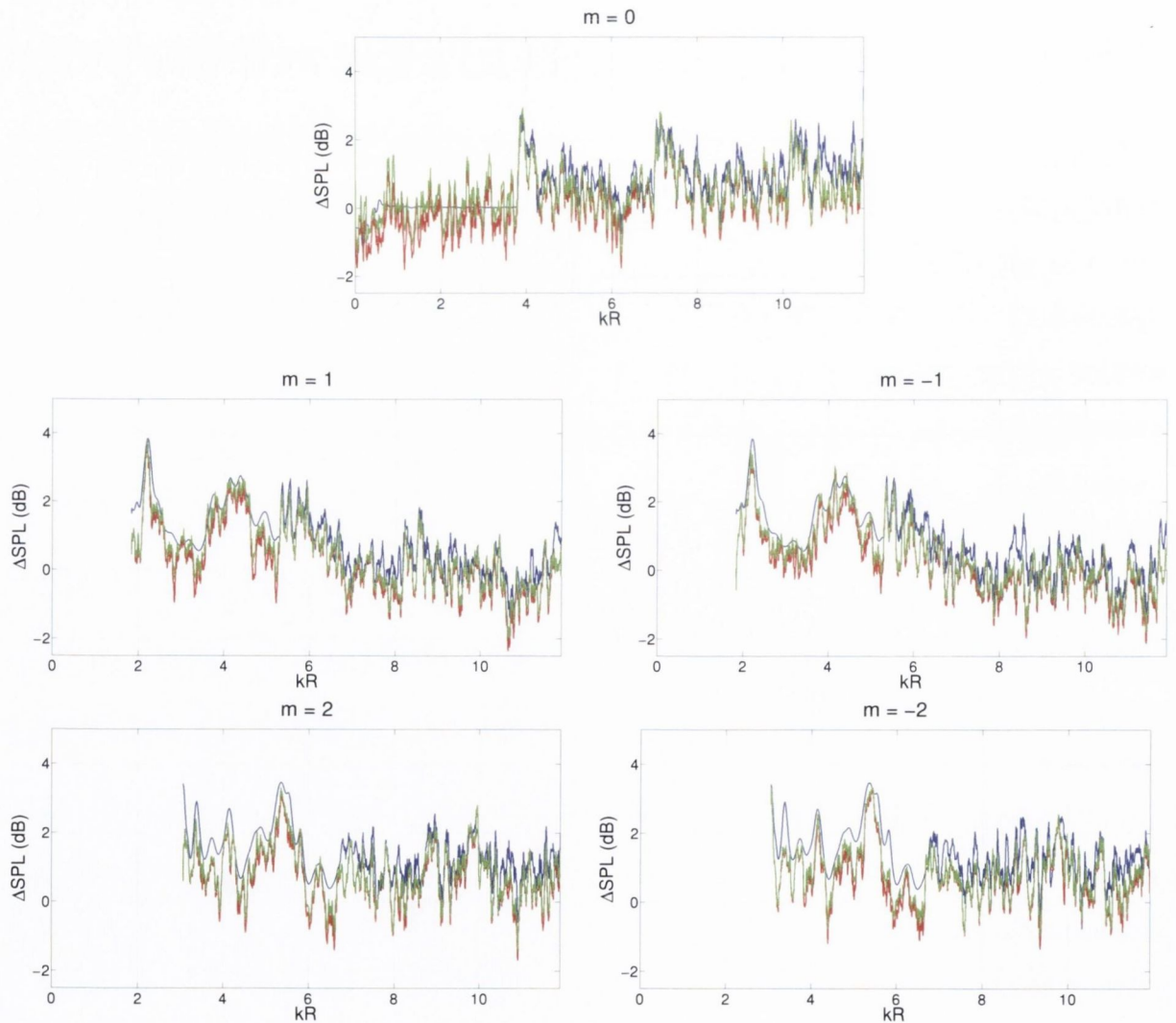
Figure 3.9: Difference in sound pressure levels of azimuthal mode estimates $A_{m,RMA}$ and $A_{m,AMA}$. Uncorrelated noise of magnitudes 5% and 20% of the time-domain signal standard deviation have been added to the $A_{m,AMA}$ estimate in the green and red cases respectively.

44
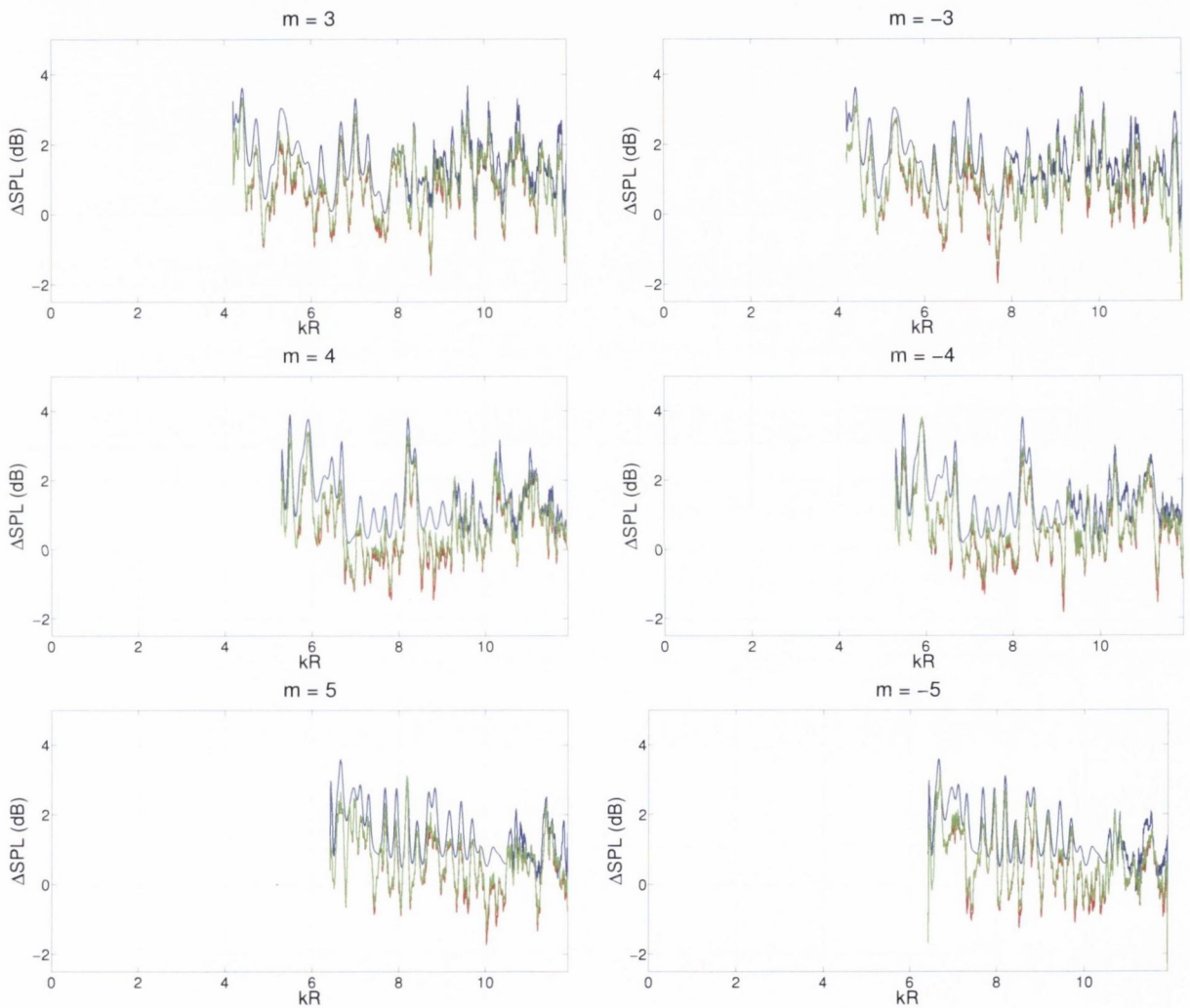
Figure 3.10: Difference in sound pressure levels of azimuthal mode estimates $A_{m,RMA}$ and $A_{m,AMA}$. Uncorrelated noise of magnitudes 5% and 20% of the time-domain signal standard deviation have been added to the $A_{m,AMA}$ estimate in the green and red cases respectively.

3.3.2   Experimental Investigation
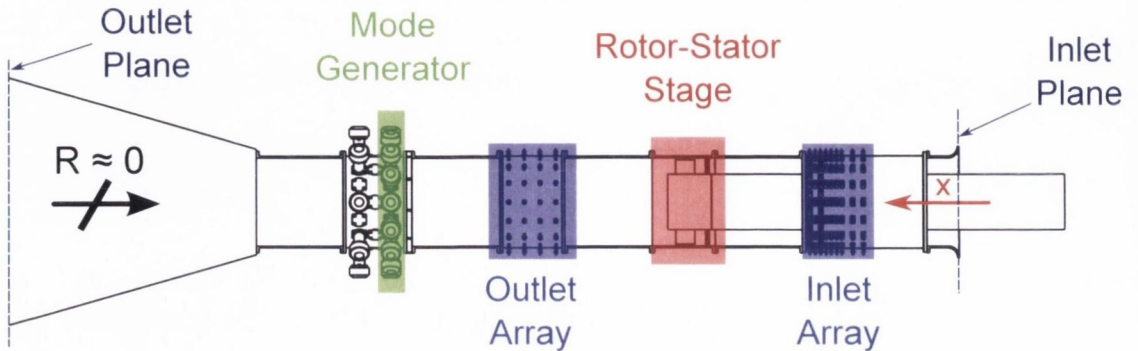
Figure 3.11: Experimental set-up for modal decomposition technique tests.

The experimental set-up used to test a single-ring modal analysis against a multiple-ring modal analysis technique is shown in Figure 3.11, and discussed in greater detail in Section 4.2. The experimental rig located at the engine acoustics branch at DLR, Berlin, has two noise-source regions; a rotor-stator stage and a loudspeaker array. The rotor-stator stage represents a turbine stage in a real aeroengine, and the loudspeaker array can simulate many possible core-noise sources. Two banks of sixty-four microphones, each containing four axial rings with sixteen microphones in each, are used to perform modal analyses at two axial locations in the duct. The inlet sensor array is located at an annular duct section, whereas the outlet array is located at a circular duct section.

In the test scenario investigated, the rotor is rotating at a fixed rotational speed, and the resulting noise measured by each microphone in both sensor arrays. The loudspeaker array generates no noise. This procedure was repeated for rotor speeds of 1500rpm and 3000rpm, giving a BPF of $605Hz$ and $1210Hz$ respectively. Two modal analyses were performed at the rotor BPF for each rotational speed tested using the outlet array of microphones. Weak or no reflections are anticipated of this tonal noise, as the rotor noise propagates in the positive x-direction through the outlet array (where the modal analyses are performed) to the outlet plane, where the duct terminates anechoically.

In the first analysis, a modal decomposition was performed using one of the four rings of microphones. This allows an azimuthal modal analysis to be performed without directionality. This azimuthal analysis was performed using each of the four rings of sixteen sensors individually, giving four azimuthal modal amplitude estimates. A radial modal

analysis was also performed using all sixty-four microphones, which gives an estimate of the radial modal amplitudes with directionality. The results from each single-ring azimuthal modal analysis were then compared to the radial modal analysis performed using four rings of sensors for both rotor speed test cases.

This study primarily focuses on the error levels, as measured by the difference in sound pressure levels between the results from the four-ring radial modal decomposition technique and the single-ring azimuthal decomposition technique. The rotor only test case was selected as the anechoic termination will greatly reduce reflections. As the single-ring technique can not separate out the incident and reflected components, the presence of significant acoustic reflections is anticipated to result in significant error levels in any modal estimates.

Figure 3.12 shows the incident and reflected modal amplitudes at the fan fundamental BPF for two fan speeds, as estimated by the four-ring radial modal analysis technique at the outlet array. The reflected modal amplitudes are generally around 20–$30dB$ lower than the incident amplitudes, suggesting a modal reflection coefficient of around 0.03–0.1. However, modes just above cut-on have much higher reflection coefficients at both BPF frequencies; close to 0.9 in the case of the $m = \pm 4$ modes when the rotor rotates at 3000rpm. The anechoic termination is therefore only effective at reducing reflections for modes well above their respective cut-on frequencies. The modal content of a rotor-stator BPF tone can be predicted using Tyler-Sofrin theory (see Equation 2.25) using the rotor blade and stator vane counts. The rotor-stator in this experimental set-up has 24 blades and 5 vanes, which theory predicts will excite the $m = -1$ and $m = 4$ at the BPF tone. The rotor-stator interaction in fact excites infinite possible azimuthal modes, however only the $m = -1$ and $m = 4$ are cut-on at the BPF at the higher rotational speed. Only the $m = -1$ mode is cut-on at the lower rotational speed. The results in Figure 3.12 would indicate that the $m = -1$ mode does dominate the measured acoustic pressure field at the outlet array at the BPF as expected, for both rotor speeds.

The levels of normalised error ϵ measured between the incident modes, as estimated by the four-ring radial modal analysis, and the modal amplitudes as estimated by the single-ring azimuthal modal analyses, are presented in Figure 3.13. The levels of error between the single-ring estimates and the four-ring estimate of the incident modal amplitudes are
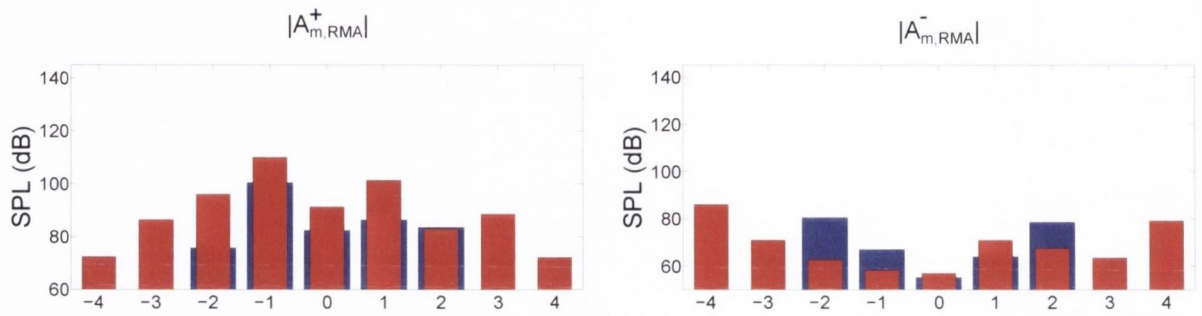
Figure 3.12: Incident (left) and reflected (right) azimuthal modal amplitudes estimated at the fan blade-pass frequency using a radial modal analysis technique performed at the outlet sensor array for two fan rotational speeds; 1500rpm (blue, BPF $= 605Hz$) and 3000rpm (red, BPF $= 1210Hz$).

generally low, of the order of 0.1–0.2. The errors are far higher at the highest cut-on mode orders in all cases, which is anticipated due to the high reflections of these mode orders at the outlet plane of the duct. This would further demonstrate that provided reflections are kept low, a single-ring analysis perform well. This error is significantly larger at mode orders where large reflections have been measured in Figure 3.12.

The objective of the experimental study undertaken in this section has been to investigate the applicability of a single-ring azimuthal modal analysis technique, which may be necessary when the number of available sensors, number of available DAQ channels and/or available space within the test duct is limited. It was thought, prior to these tests, that bias errors due to axial variations of modal amplitudes in the duct would adversely affect any modal estimates using a single-ring of sensors. It was found however that such a technique is suitable if modal reflections are low, as it was found that the azimuthal modal estimates closely matched the robust four-ring technique in such a case. The single-ring azimuthal modal analysis technique was applied in experimental tests outlined in Chapters 5 and 6.
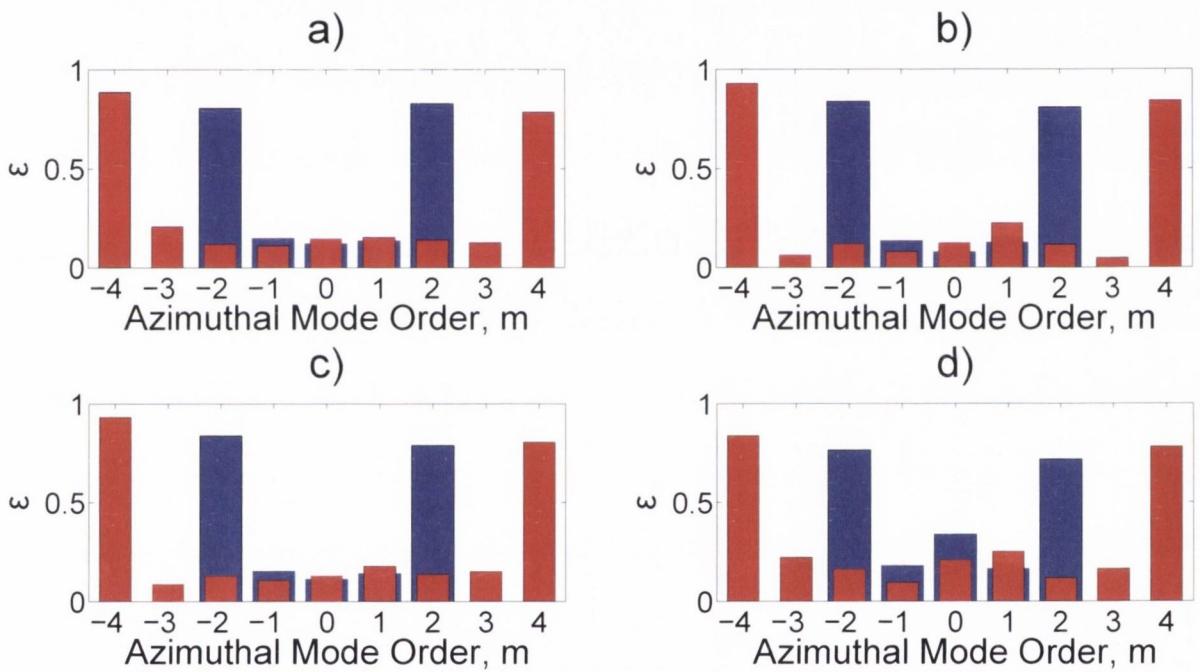
Figure 3.13: Normalised error ϵ between the incident azimuthal modal amplitudes shown in Figure 3.12 and the azimuthal modal amplitudes estimated using four single rings of sensors located at $x = 2726, 2786, 2846, 2906$, shown in sub-figures a)–d) respectively.

Chapter 4

Coherence-Based Noise-Source Identification Techniques

4.1   Theory and Background

Many pre-existing techniques of coherence-based noise source identification exist in the literature. These methods of noise source identification utilise several acoustic pressure measurements both close to the source(s) of interest and in the far-field. The aim of these techniques is to identify the relative contributions of these noise-sources to the noise radiated at the far-field locations of interest. These techniques are therefore useful for applications in aero- and turboshaft engines, where for example the relative contributions of the various turbomachinery noise sources to the noise radiated at the exit plane of the engine could be identified.

Consider the scenario depicted in Figure 4.1 which shows the cut-away schematic of a typical turboshaft engine. Two of the possible core noise-source regions within the engine (downstream of the compressor) have been simplified to two source regions; S_1 and S_2. S_1 is a turbine and S_2 is a combustor. Several reference sensors are located close to both noise-source regions in order to obtain accurate source measurements. Few sensors are used due to the lack of available space within the core duct of the engine. Coherence-based noise-source identification techniques can be used to identify the contribution of the noise generated by these noise sources to the sound radiated to a far-field location of interest, usually in the environment outside the engine. Several such techniques are investigated in the following chapter.

The magnitude-squared or ordinary coherence function is the principal tool used in all these techniques. The coherence function of two time-domain signals $x(t)$ and $y(t)$ can be found by first transforming blocks of the signals into the Fourier domain, giving $X(f)$ and $Y(f)$. The power-spectral densities ($G_{xx}(f)$ and $G_{yy}(f)$) and cross-spectral density ($G_{xy}(f)$) of these Fourier domain blocks can then be formed. The dependence on frequency will be dropped from this point on for succinctness. By averaging these auto- and cross-spectra over many signal blocks, the coherence function between $x(t)$ and $y(t)$ can be found by:

$$\gamma_{xy}^2 = \frac{|G_{xy}|^2}{G_{xx}G_{yy}} \leq 1 \qquad (4.1)$$

It should be noted that the all spectral functions outlined herein are in reality statistical
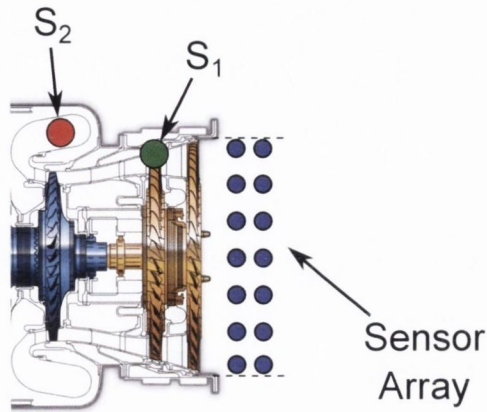
Figure 4.1: Simplified representation of acoustics inside a turboshaft engine duct. Noise is emitted by S_1 and S_2, which represent a turbine and combustor stage respectively, and propagates in the duct. When the turbine is rotating, a flow is induced in the duct.

estimates of real spectral functions estimated using a finite number of samples, and as such these functions should be denoted by $\hat{G}_{xx}(f)$, $\hat{G}_{yy}(f)$ and $\hat{\gamma}^2_{xy}$ to reflect this. Being statistical estimates, they are subject to errors. The extent of these associated uncertainties depend on a number of signal processing parameters and other factors discussed in Appendix C.5.

If the coherence function is greater than zero but less than unity, one of three possible physical situations exist:

1. Extraneous noise is present in the measurements.

2. The system relating $x(t)$ and $y(t)$ is not linear.

3. $y(t)$ is an output due to input $x(t)$ as well as other inputs.

4.1.1   Coherent Output Power (COP)

Figure 4.2 shows a single-input/single-output model where both input $x(t)$ and output $y(t)$ measurements have been made. The input measurement, which could be an acoustic source measurement for example, measures the true input (noise-source) $u(t)$ as well as extraneous noise $m(t)$. Such extraneous noise in uncorrelated with $u(t)$. The output measurement, which could be a far-field acoustic measurement for example, measures the

noise-source's contribution $v(t)$ to the output measurement, as well as extraneous noise $n(t)$.
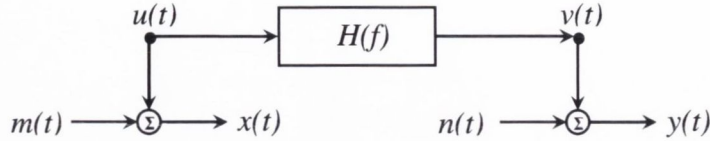
Figure 4.2: Single input/output (SISO) model with added extraneous noise at both input and output.

Consider the case where a pure source time-domain measurement $x(t)$ is available (pure meaning that no extraneous noise, such as additional noise sources, is measured by this sensor *i.e.* $m(t) = 0$). An output measurement $y(t)$ is available which measures this source as well as extraneous noise $n(t)$ (which could include other uncorrelated sources). The contribution of the source measured by $x(t)$ to the noise measured by $y(t)$ is given in this case by:

$$G_{vv} = G_{yy}\gamma_{xy}^2 \qquad (4.2)$$

where $v(t)$ is the contribution of the source measured by $x(t)$ to $y(t)$. This result is known as the coherent output spectrum, and was first reported by Halvorsen and Bendat [3]. With reference to the scenario shown in Figure 4.1, and given that a pure source measurement is available at S_2 (the combustor), the coherent output power technique model would be represented as shown in Figure 4.3. $y(t)$ could be a measurement in the duct, or a far-field measurement outside of the turboshaft engine.

This simple technique is very useful in situations when $m(t) = 0$, providing a measurement of a single noise-source's contribution to any far-field location of interest. For the example shown in Figure 4.3 the technique is applied to identify the contribution of direct combustor noise to an output measurement of interest. However, if extraneous noise is present in the source measurement ($m(t) \neq 0$), the coherent output spectrum is affected as follows:

$$G_{v'v'} = G_{yy}\gamma_{x'y}^2 = G_{vv}\frac{G_{xx}}{G_{xx} + G_{mm}} \leq G_{vv} \qquad (4.3)$$
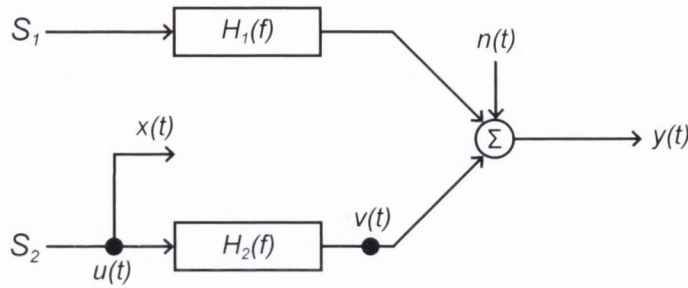
Figure 4.3: Coherent output power model for scenario shown in Figure 4.1 with a pure source measurement of S_2.

i.e. the technique will underestimate $v(t)$. In the scenario shown in Figure 4.1, and given that $x(t)$ in this instance is a measurement at the source S_1 (the turbine), the COP model will be as shown in Figure 4.4. As the turbine induces a flow in the duct, the source measurement $x(t)$ in this case will measure both S_1 and extraneous noise $m(t)$. For the scenario shown in Figure 4.1, this induced flow will generate flow noise. This flow noise is caused by noise sources distributed in the turbulent fluid, and also the hydrodynamic interaction between the fluid flow and the pressure sensor. This flow noise will contribute to this extraneous noise, and assuming that no other noise sources are present in the test duct, could be the main contributor of extraneous noise not correlated between the sensors.

The COP technique has been applied for aeroengine noise-source identification by Karchmer *et al.* [21,55,56] for direct combustor noise identification. By instrumenting a static turbofan engine with internal as well as far-field microphones, the authors estimated the radiation pattern of direct combustor noise to the far-field from the engine exhaust.

4.1.2 Signal Enhancement (SE)

Unlike the COP, which requires a pure measurement of the source of interest without extraneous noise, Chung [4] developed a technique for extraneous noise rejection at the input requiring a minimum of three measurements. This technique can therefore be applied when a pure measurement at the source is not possible, provided this extraneous noise is uncorrelated between each measurement. Such extraneous noise could be flow noise for example. The source measurements at each of the three output measurements
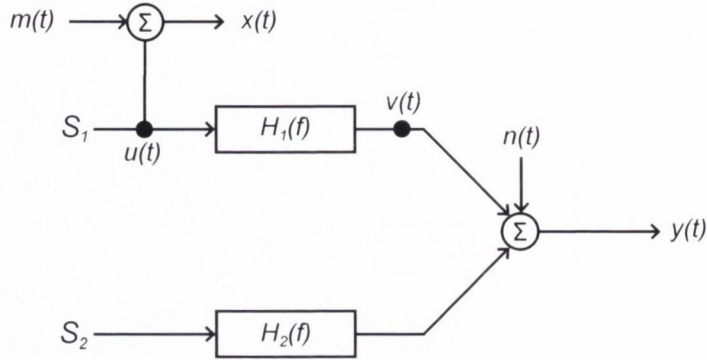
Figure 4.4: COP model for scenario shown in Figure 4.1 with source measurement at S_1. The presence of extraneous flow noise at the inlet measurement will diminish the efficacy of the technique, as shown in Equation 4.3

must be mutually correlated. The desired spectra can then be found using these equations (shown for one sensor only as an example):

$$G_{v_1 v_1} = G_{y_1 y_1} \frac{|\gamma_{y_1 y_2}||\gamma_{y_1 y_3}|}{|\gamma_{y_2 y_3}|} = \frac{|G_{y_1 y_2}||G_{y_1 y_3}|}{|G_{y_2 y_3}|} \tag{4.4}$$

$$G_{n_1 n_1} = G_{y_1 y_1} - G_{v_1 v_1} \tag{4.5}$$

With reference to Figure 4.1, and given that three sensors ($y_1(t)$, $y_2(t)$ and $y_3(t)$) measure source S_1 plus uncorrelated extraneous noise, the SE model will be as shown in Figure 4.5. The possible presence of S_2 in the extraneous noise $l_k(t)$ terms is shown, as the sensors located at S_1 will also measure S_2's contribution to the noise at these locations. If this is the case, the measurement of the contribution of S_2 must be uncorrelated between each sensor, in which case S_2 will be measured as uncorrelated noise and will not contaminate the results.

Shivashankara [57] applied this technique to separate out the contributions of fan, core, and jet noise in a high-bypass turbofan engine to the noise measured at a far-field receiver of interest. More recently, Nance [58] applied the signal enhancement technique to separate out the contributions of both small-scale and large-scale turbulence to the total jet noise radiated from an aeroengine exhaust.
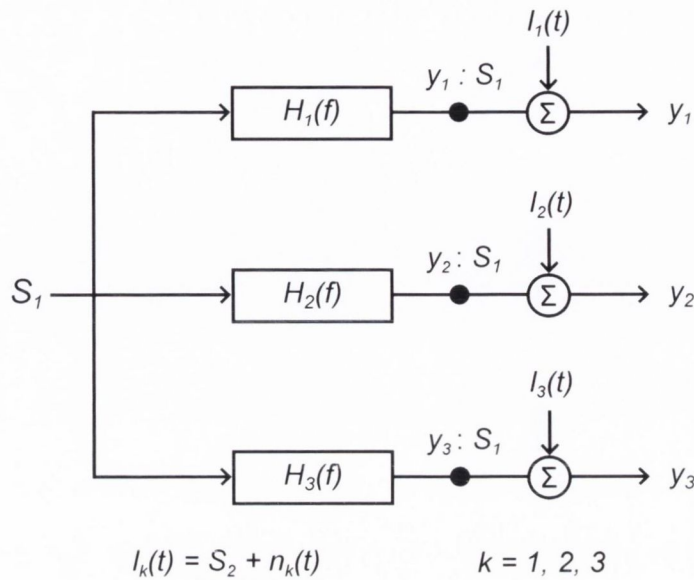
Figure 4.5: Signal enhancement model for scenario shown in Figure 4.1 with three measurements of S_1 plus additional uncorrelated extraneous noise.

4.1.3   Conditional Spectral Analysis (CSA)

One of the limitations of the SE technique is that for measurement locations within the same pressure field, the technique may only be applied when there is a single correlated source between the records. Minami and Ahuja [59] discuss the errors resulting from using the signal enhancement technique when two sources, as opposed to only one source, are measured with extraneous noise. For the situation where there are only two correlated sources, and a pure measure of one of them is attainable, the COP and the SE techniques may be used in conjunction with each other and conditional spectral analysis to success-fully identify both sources and the extraneous noise. This approach was presented by Hsu and Ahuja [5].

The CSA model for the scenario shown in Figure 4.1 is shown in Figure 4.6(a). In this scenario, a pure source measurement is available at S_2, but not at S_1. The first stage consists of separating out the part correlated with the measurable source (S_2) using the COP technique, and thus identifying its contribution. The second stage uses a partial coherence formulation of the SE technique on the residual to remove the extraneous noise, as demonstrated in Figure 4.6(b). Assuming a pure measurement of source S_2 is available, only four microphones are required, with this source measurement used as an

input. The other three microphones measure a combination of contributions from both source S_1 and S_2. In the case that a pure measurement of S_2 is not available, two sensor measurements can be used at S_2 instead of a single measurement. It is required that these microphone measurements measure S_2 and uncorrelated extraneous noise only, and that this extraneous noise is uncorrelated between all sensor measurements. This is the basis for the five-microphone CSA technique.

a) Stage 1 using the C.O.P. technique

b) Stage 2 using the S.E. technique on the residual
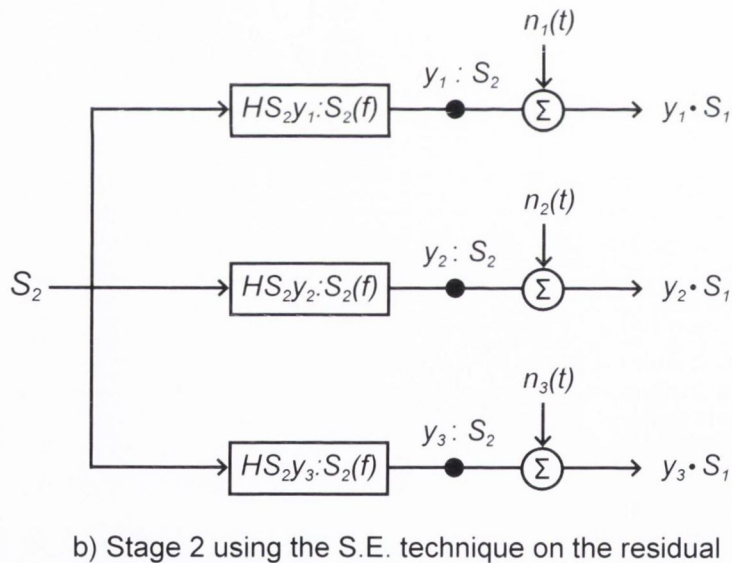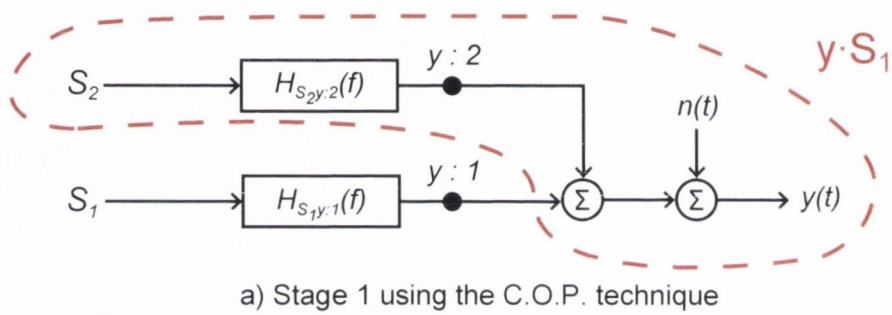
Figure 4.6: Conditional spectral analysis model for scenario shown in Figure 4.1.

Figure 4.7 shows the five-microphone CSA model for the test scenario described in Figure 4.1. It should be noted that microphone measurements $y_4(t)$ and $y_5(t)$ are such that they measure the single source S_2 and uncorrelated noise only. The other three output sensors can be located anywhere, provided their measurements of S_1 and S_2 are correlated with one another. The source spectra G_{kk} and G_{vv} can be found using the following equations (for $y_1(t)$ only, with dependence on frequency not shown for brevity):
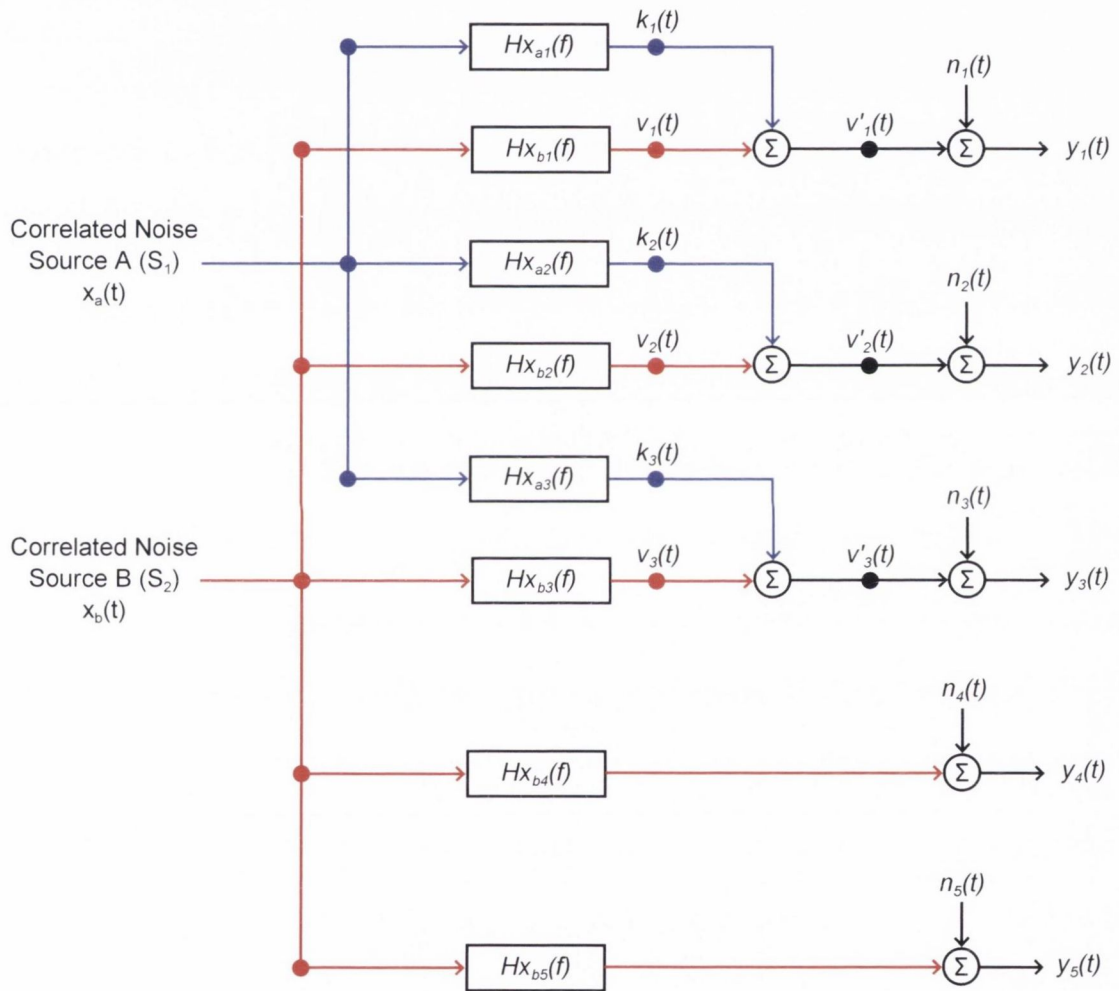
Figure 4.7: Five-Microphone CSA Technique Model for scenario shown in Figure 4.1.

$$G_{k_1 k_1} = \frac{\left| G_{y_1 y_2} - \frac{G_{y_1 y_4} G_{y_5 y_2}}{G_{y_5 y_4}} \right| \left| G_{y_1 y_3} - \frac{G_{y_1 y_4} G_{y_5 y_3}}{G_{y_5 y_4}} \right|}{\left| G_{y_2 y_3} - \frac{G_{y_2 y_4} G_{y_5 y_3}}{G_{y_5 y_4}} \right|} \tag{4.6}$$

$$G_{v_1 v_1} = \frac{G_{y_1 y_4} G_{y_1 y_5}}{G_{y_4 y_5}} \tag{4.7}$$

The five-microphone CSA technique is ideally suited for the two noise-source test scenario shown in Figure 4.1 and discussed through-out this section. The benefit of this CSA technique is that it allows the contributions of two-noise sources to the total noise at a measurement location of interest to be identified, even if both noise-source measurements are correlated across all five output measurements. The COP and SE techniques discussed in this section have only been suitable for noise-source identification of a single correlated source, and this more advanced CSA technique therefore presents a significant advancement on these techniques. Bennett and Fitzpatrick [60] discuss further the relative merits and limitations of various coherence-based noise-source identification techniques.

4.1.4 Novel Modal CSA Technique

As well as reviewing several existing or classical techniques of noise source identification, this study also proposes and investigates a novel technique for identifying the contribution of two noise sources to the noise measured at a sensor of interest. The technique proposed is an enhancement of the five-microphone conditional spectral analysis technique discussed in Section 4.1.3, in order to identify the contribution of two mutually uncorrelated noise-sources to the modal content estimated at a location of interest.

The underlying method follows from the fact that the auto- and cross-spectra used to formulate the G_{kk} and G_{vv} spectra in the five-microphone technique can be calculated using the complex Fourier domain signals of the original time-domain signals $x_1(t)$–$x_5(t)$. Given that $x_1(t)$–$x_5(t)$ are microphone measurements of the acoustic pressure with time, the Fourier transformed signals $X_1(f)$–$X_5(f)$ are the complex acoustic pressure spectra with frequency. Modal decomposition, an advanced technique that uses an array of acoustic sensors to determine the specific modal amplitudes at the sensor array, can be used to determine the complex acoustic pressure of any cut-on acoustic mode in a duct at a given

frequency. Several such techniques are discussed in Section 3.1. It is therefore proposed that one of the complex pressure signals $X_1(f)$–$X_5(f)$ can be replaced by the complex pressure signal of a specific mode travelling in a given direction in the test duct, $A_{mn}^{\pm}$. For the two-source case, this technique could therefore be used to identify the contribution of both sources to the modal amplitudes measured at the sensor array.

With reference to Figure 4.1, the modal content of the noise radiated from sources S_1 and S_2 could be identified at the sensor array using one of the modal decomposition technique outlined in Section 3.1. The complex modal amplitudes of any mode order (m,n) which is cut-on in the frequency range of interest can then be found. The azimuthal index m of any mode to be decomposed must also be less than or equal to $s/2$, where s is the number of sensors per ring. These complex pressure sequences can be used to generate auto-spectra of each (m,n) mode by simply multiplying the complex amplitude of the mode by its complex conjugate. Similarly, cross-spectra can be formulated on a modal basis.

The complex acoustic pressure of each mode decomposed can be used as an output measurement, shown in place of Y_3 in Figure 4.8, in the five-microphone technique. Since the five-microphone technique uses the cross-spectra between five sensor measurements, one of these sensors can be replaced by the complex modal amplitude of a mode of interest. The time-domain measurement signals y_1, y_2, y_4 and y_5 are transformed into the frequency domain, giving the complex pressure signals Y_1, Y_2, Y_4 and Y_5. The five-microphone technique can therefore be used to identify the contributions of sources S_1 and S_2 to the modal amplitudes at the location where the modes have been decomposed, using the auto- and cross-spectra between these five complex pressure measurements as per Equations 4.6 and 4.7. This technique can be used to identify how much acoustic energy each source contributes at a specific mode order over a frequency range of interest. This method could therefore be applied in a real turboshaft engine to identify the contribution of noise sources inside the engine to the modal sound pressure levels at the engine exhaust, allowing a better understanding of the propagation of the sound from noise source to engine exhaust. This information can be used to optimise the design of acoustic liners to attenuate this sound field.
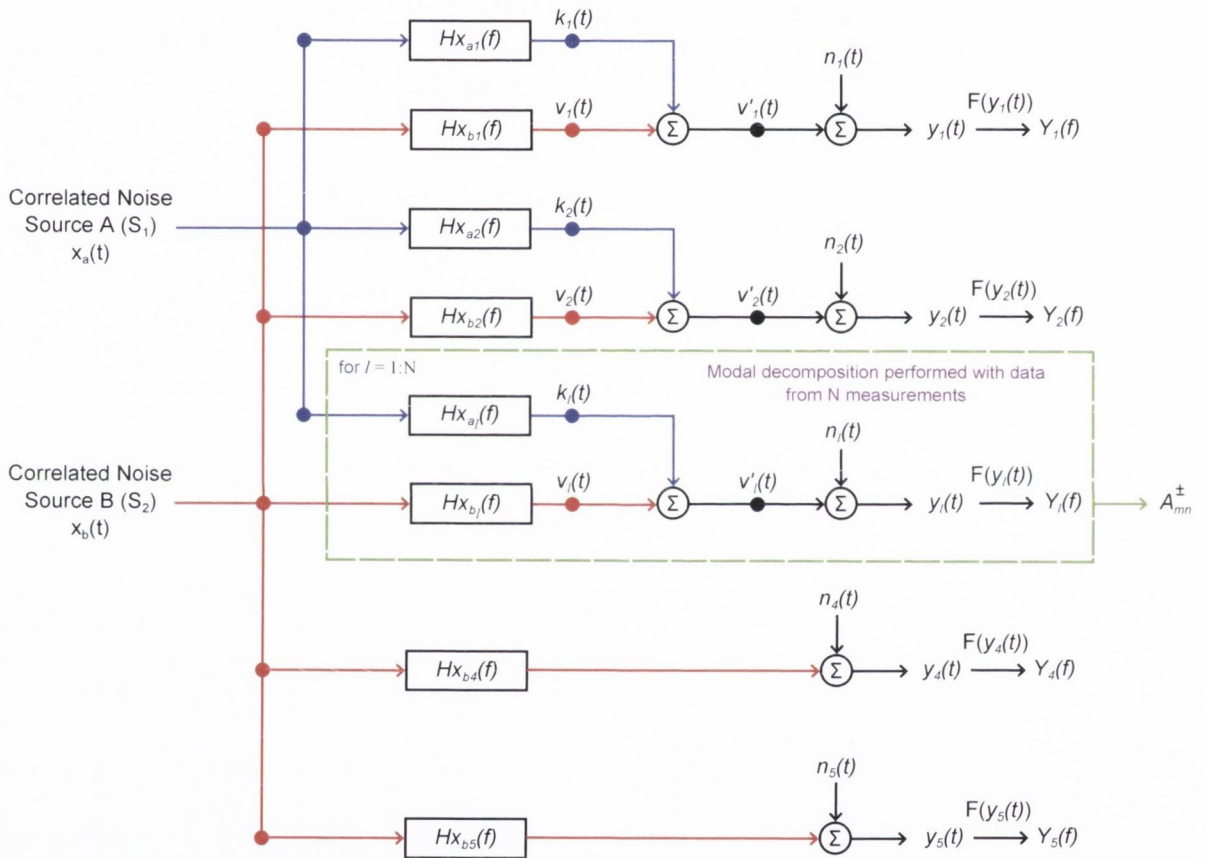
Figure 4.8: CSA modal five-microphone technique model for scenario shown in Fig. 4.1. Measurement $Y_3(f)$ has been replaced by $A_{mn}^{\pm}$, the complex modal amplitude of the (m,n) mode.

4.2   TEENI Small-Scale Experimental Rig

As part of the TEENI project, a test campaign was undertaken at the DLR engine acoustics branch in Berlin, Germany. This experimental set-up was used to investigate the techniques outlined in Section 4.1 and the novel technique outlined in Section 4.1.4. The rig was designed to model the key acoustic elements of a turboshaft engine on a smaller-scale. The test set-up was kept as simple as possible in order to verify the techniques of interest for use in a future full-scale test campaign.

The noise-source regions are a single rotor-stator stage and an array of several loud-speakers which can be used to generate broadband, tonal or narrowband noise. A schematic of the rig design is shown in Figure 4.10. When the rotor rotates, an axial-flow is induced in the positive x-direction. By varying the parameters of these noise-source regions, a wide variety of different test scenarios were investigated, allowing the classical techniques discussed in Section 4.1 to be tested for scenarios of noise-source identification in turbomachinery. At the inlet of the duct, the duct cross-section is annular, with a hub-to-tip ratio $\eta = 0.56$. The hub terminates at the rotor-stator stage, and the duct cross-section is circular beyond this point. The outer radius of the duct is $0.25m$ along its entire length. The duct terminates anechoically at the downstream end, with an anechoic termination designed as per international standard ISO/FDIS 5136.

The rotor-stator stage consists of 24-bladed rotor and a 5-vane stator. The rotor has a maximum rotational speed of 3200rpm. The hub-to-tip ratio, η, is 0.6 at the rotor stage. The rotor blades have a solidity (chord-to-pitch ratio) of 2.3. The solidity of the stator vanes is 0.4. The rotor speed was controlled using a trigger signal sent to a motor control.

The mode generator array consists of a total of 32 loudspeakers in 3 axial rings. Each loudspeaker source is mounted in a conical horn section, which acts as a waveguide between the loudspeaker source and the test duct, as demonstrated in Figure 4.11. Each ring of sources is equi-azimuthally spaced, as shown in Figure 4.12. As well as varying the number of active sources at each test point, the amplification factor of the noise sources can be adjusted. The signal type can also be adjusted. In the TEENI test campaign, three signal

---

[1]Figures created by Ulf Tapken, Benjamin Pardowitz and Philip Kausche at the Engine Acoustic facility at the Institute of Propulsion Technology of the German Aerospace Centre (DLR) located in Berlin, Germany
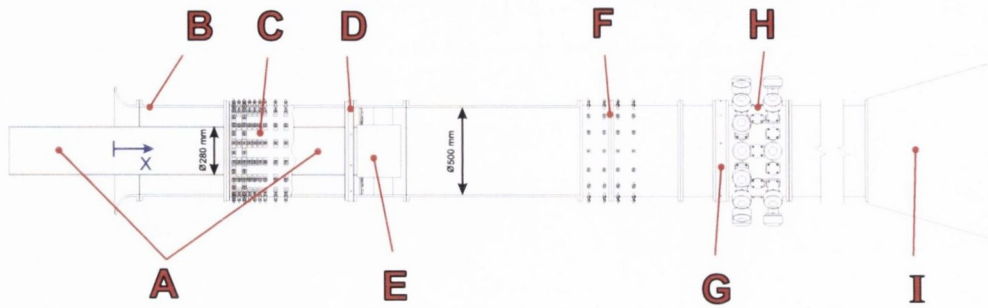
A: hub
B: inlet duct
C: inlet array
D: ring with reference sensors
E: rotor-stator stage
F: outlet array
G: ring with reference sensors
H: mode generator
I: anechoic termination

Figure 4.9: Schematic of experimental rig at DLR used to investigate coherence-based noise-source identification techniques[1].
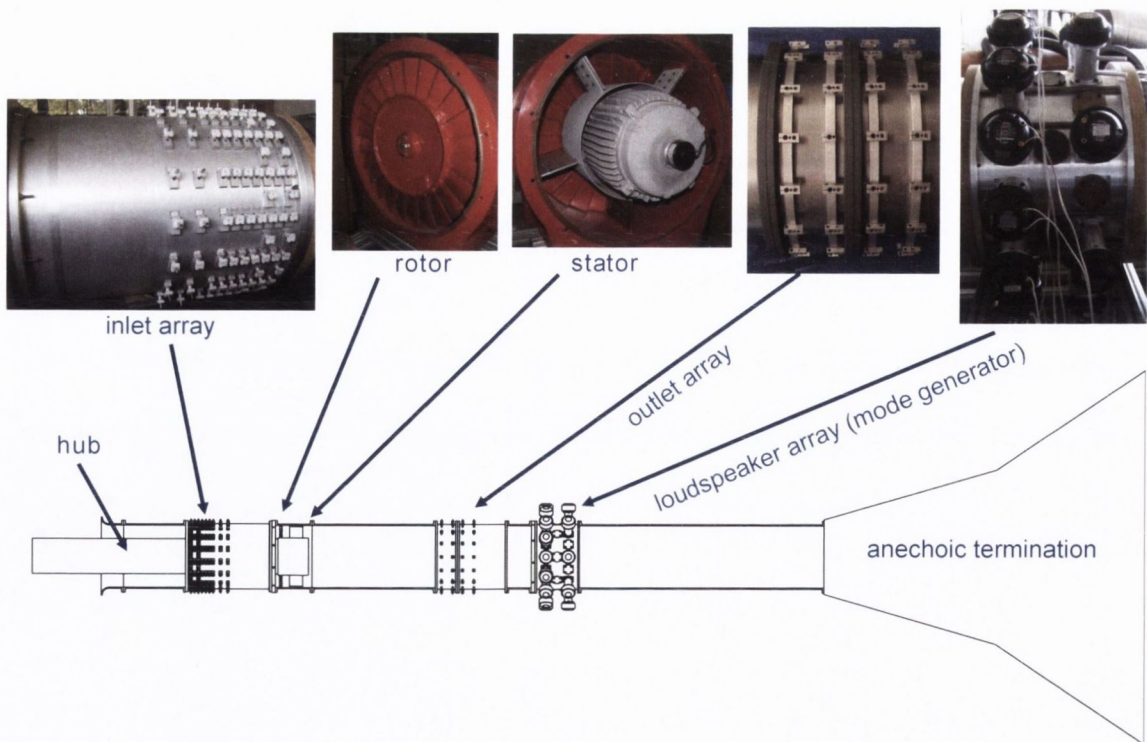
Figure 4.10: Photographs showing key elements of the experimental rig at DLR used to investigate coherence-based noise-source identification techniques[1].
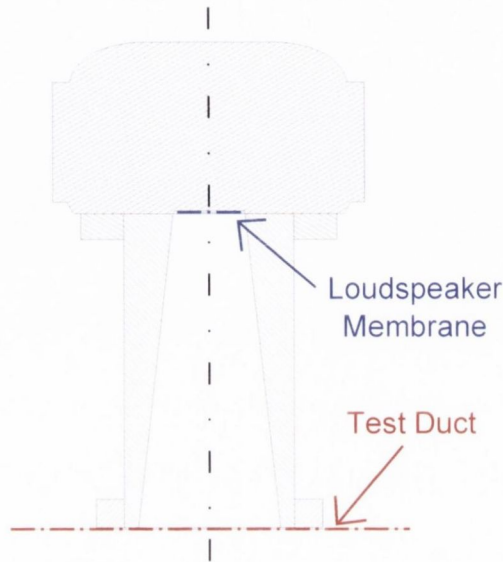
Figure 4.11: Conical waveguide connecting each loudspeaker source in the mode generator array to the test duct[1].
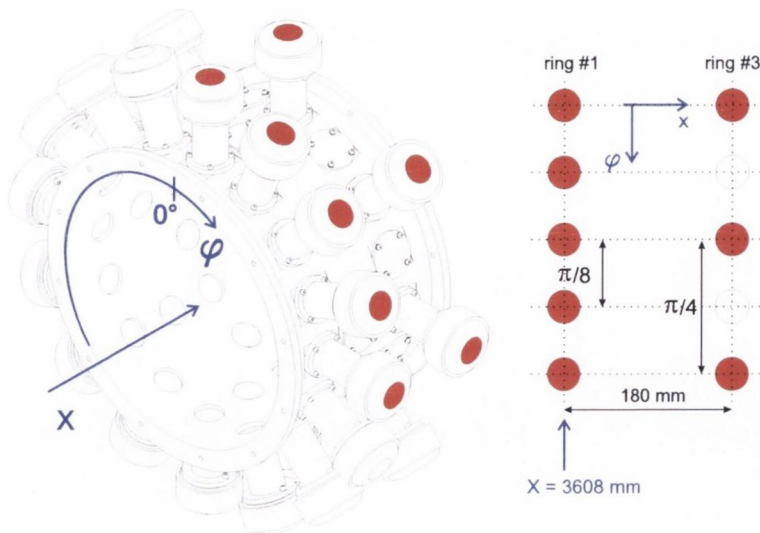
Figure 4.12: Distribution of loudspeakers in mode generator array shown in Figure 4.10[1].
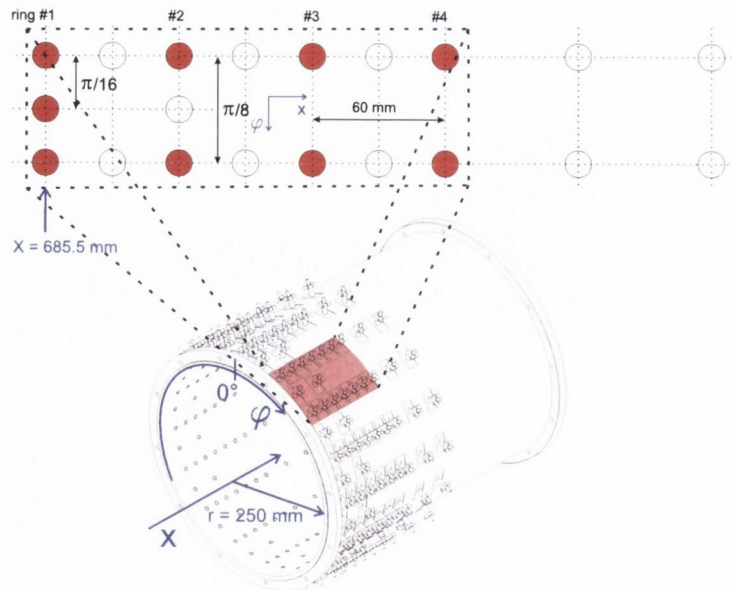
Figure 4.13: Location of microphones assembled in the inlet array shown in Figure 4.10[1].
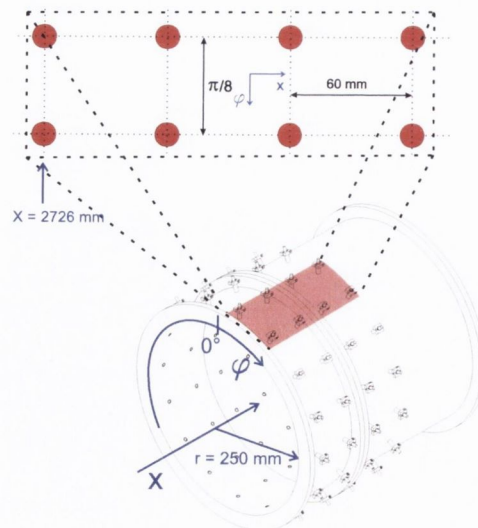
Figure 4.14: Location of microphones assembled in the outlet array shown in Figure 4.10[1].

types were used: tonal, broadband, and narrowband (band-pass filtered broadband).

Data was acquired across 256 independent DAQ channels using in-house hardware and software at a sampling frequency of $16kHz$. G.R.A.S. Sound and Vibration condenser-type 40BP microphones were used to acquire the acoustic pressures at the two banks of sensors (inlet and outlet). The inlet array is located at the hub of the rig. All microphone sensors were flush-mounted to the inside of the test duct wall. The locations of the sensors in both sensor arrays are shown in Figures 4.13 and 4.14. The inlet bank contains 80 microphones, with 3 axial rings of 16 microphones and another axial ring of 32 microphones. The outer bank consists of 64 microphones divided into 4 axial rings. Reference sensors were also located through-out the duct close to the loudspeaker array and rotor-stator stage, as illustrated in Figure 4.15. Of particular note are sensors 1–6 located at the rotor-stator stage and sensors 10 and 11 located within one of the loudspeaker cones.
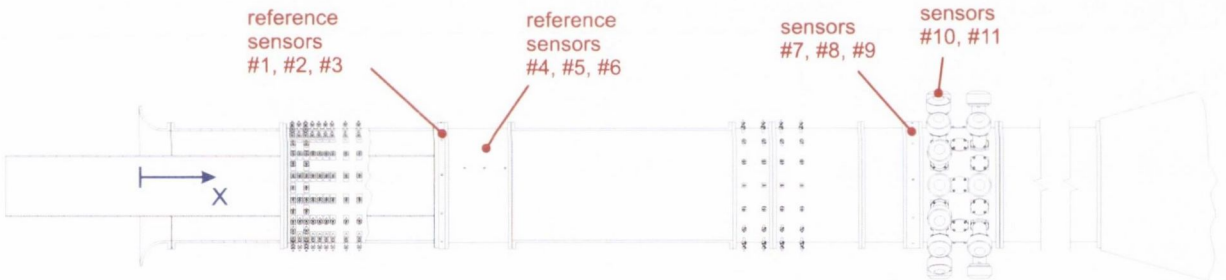
Figure 4.15: Reference sensor locations in DLR experimental rig.

The two banks of sensors can be used to perform an acoustic modal analysis at both axial locations. The modal analysis technique of Åbom [13], as applied by Bennett [6] and discussed in Section 3.1, was used in these experiments. Using four rings of sensors, a full radial modal decomposition of both the incident and reflected acoustic modes may be performed. Due to the sensor requirements for the modal decomposition technique, a full radial modal analysis may be performed up to a frequency of $2100Hz$ at the inlet bank and $1600Hz$ at the outlet bank. The difference between these two maximum frequencies is due to the change of cross-sectional geometry from an annular duct to a cylindrical duct, which affects the cut-on frequencies of the higher-order radial acoustic modes.

4.3   Experimental Results

4.3.1   Classic Techniques

The following test results demonstrate the relative effectiveness of each technique discussed in Section 4.1 when applied to a two-source test scenario, with data acquired during the TEENI test campaign using the experimental rig described in Section 4.2. Two noise-source regions are present. With reference to Figure 4.10, the first of these noise-source regions is the rotor rotating at 1500rpm, which will be referred to as S_{rot}. A single loudspeaker located at the mode generator generating broadband noise is the second noise-source region, and will be referred to as $S_{LS,bbn}$. The key test case investigated has both sources S_{rot} and $S_{LS,bbn}$ present; test case 1 in Table 4.1. Two other test cases; one with $S_{LS,bbn}$ only and the other with S_{rot} only, are used as benchmarks for the analysis of the efficacy of all noise-source identification techniques tested. These are test cases 2 and 3 shown in Table 4.1.

The objective of this test campaign is to assess the relative efficacy of several pre-exisiting coherence-based noise-source identification technique to the total noise measured by a sensor in the inlet array located at ($x = 0.685m$, $\theta = 0°$, $r = R$) for test case 1, using several reference sensors located through-out the test duct. This sensor could represent a sensor at the exhaust of a real turboshaft engine or a far-field measurement, and will be referred to simply as the *inlet sensor* from this point onwards. The SPL spectra measured by this sensor for all three test cases are presented in Figure 4.16. The frequency range investigated was restricted from $750Hz$ to $2000Hz$. This frequency range was selected so that spectra can be presented with fine detail visible in the results. The first harmonic of the rotor BPF at $1210Hz$ is also captured in this range, and therefore its impact on the effective application of each technique can be discussed. Finally, the full-scale engine tests will also focus on a similar low frequency range.

Table 4.1: Test cases investigated in order to test classic coherence-based noise source identification techniques

Test Case	$\mathbf{S}_{rot}$	$\mathbf{S}_{LS,bbn}$
1	Rotating at 1500rpm, BPF at $605Hz$	Generating BBN
2	–	Generating BBN
3	Rotating at 1500rpm, BPF at $605Hz$	–
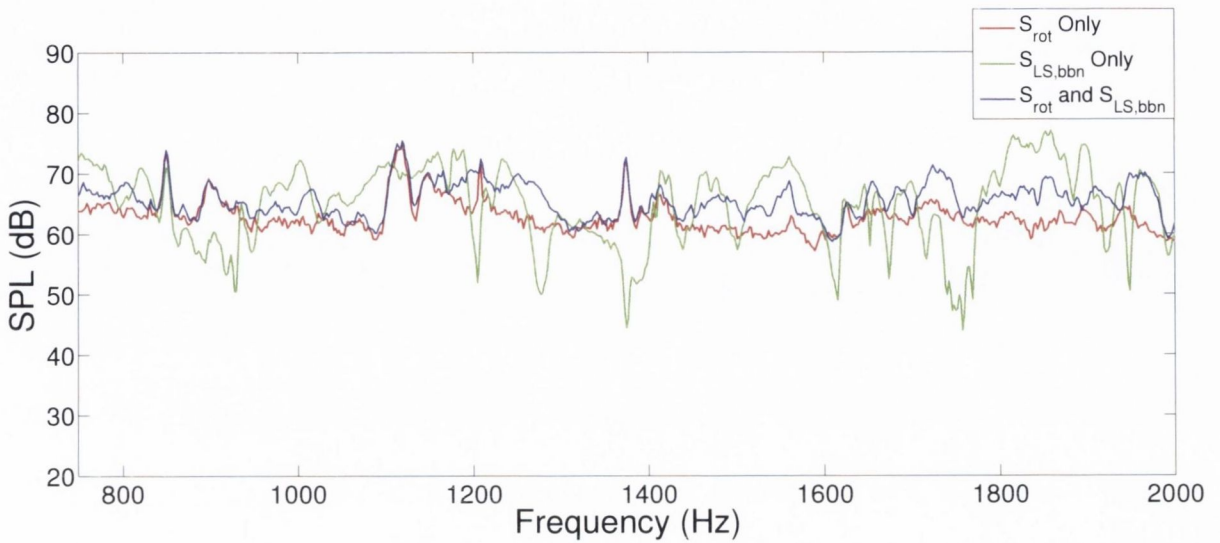
Figure 4.16: Auto-spectra of inlet sensor measurement for three test cases listed in Table 4.1.

The COP method was first investigated in order to identify the contribution of $S_{LS,bbn}$ to the total noise measured by the inlet sensor for test case 1. The COP model shown in Figure 4.3 assumes no noise at the input *i.e.* a pure source measurement. The input measurement x in this case was taken from a sensor inside the active loudspeaker cone (sensor #10 in Figure 4.15). This sensor provides an accurate source measurement of $S_{LS,bbn}$ as the SPL spectrum measured for test case 2 dominates that measured for test case 3 by around $30dB$ for all frequencies (see Figure 4.17). The output measurement, y, is taken from a sensor at the inlet bank of sensors. These sensor positions are shown in Figure 4.18. The G_{vv} spectrum therefore shows the contribution of $S_{LS,bbn}$ to the noise at this inlet sensor, according to the model shown in Figure 4.3.

Since the source $S_{LS,bbn}$ dominates the noise measured inside the loudspeaker cone, the contribution of source S_{rot} at the inlet sensor is identified as extraneous noise for test case 1. The COP result, shown in Figure 4.19, is compared with the SPL spectrum for the inlet sensor when only $S_{LS,bbn}$ is present (test case 2 in Table 4.1). This latter spectrum is used as a benchmark to examine the effectiveness of the COP result. The COP method is shown to be effective by the fact that these spectra match very well for all frequencies, demonstrating the usefulness of the technique when a pure source measurement is possible.

In the results shown in Figure 4.19, the coherent output power result was compared with the auto-spectrum measured at the inlet sensor with only $S_{LS,bbn}$ present. This auto-
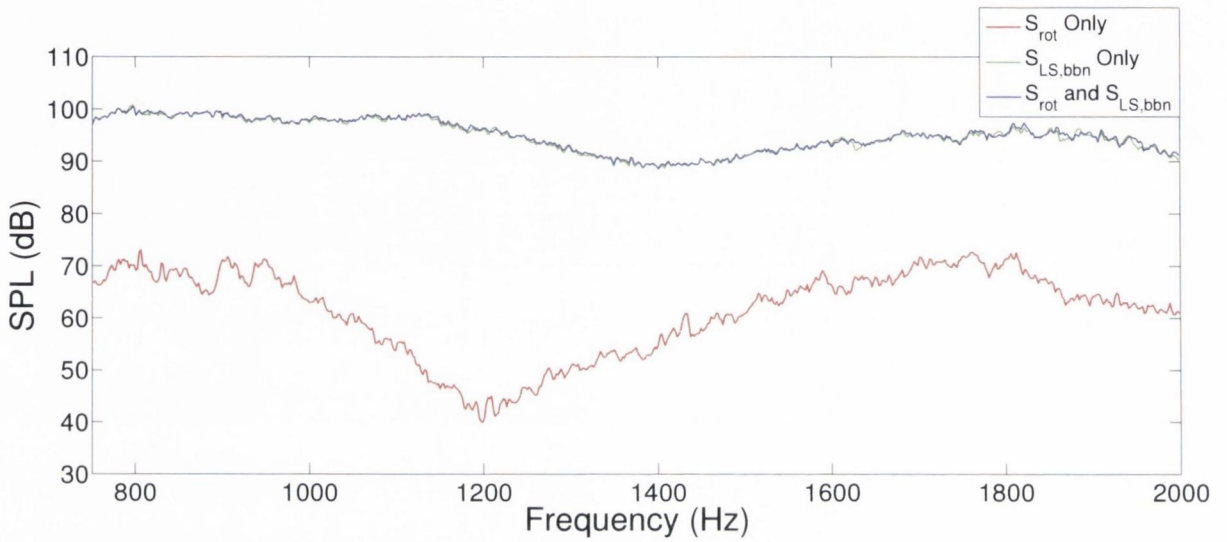
Figure 4.17: Auto-spectra of acoustic sensor measurement located in the cone of a loudspeaker for the three test cases listed in Table 4.1. The loudspeaker is active in test cases 2 and 3.
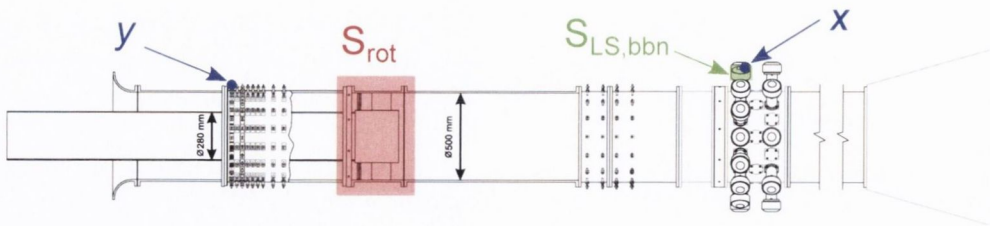
Figure 4.18: Locations of sensor measurements for identification of $S_{LS,bbn}$'s contribution to the noise measured at y using the coherent output power technique.
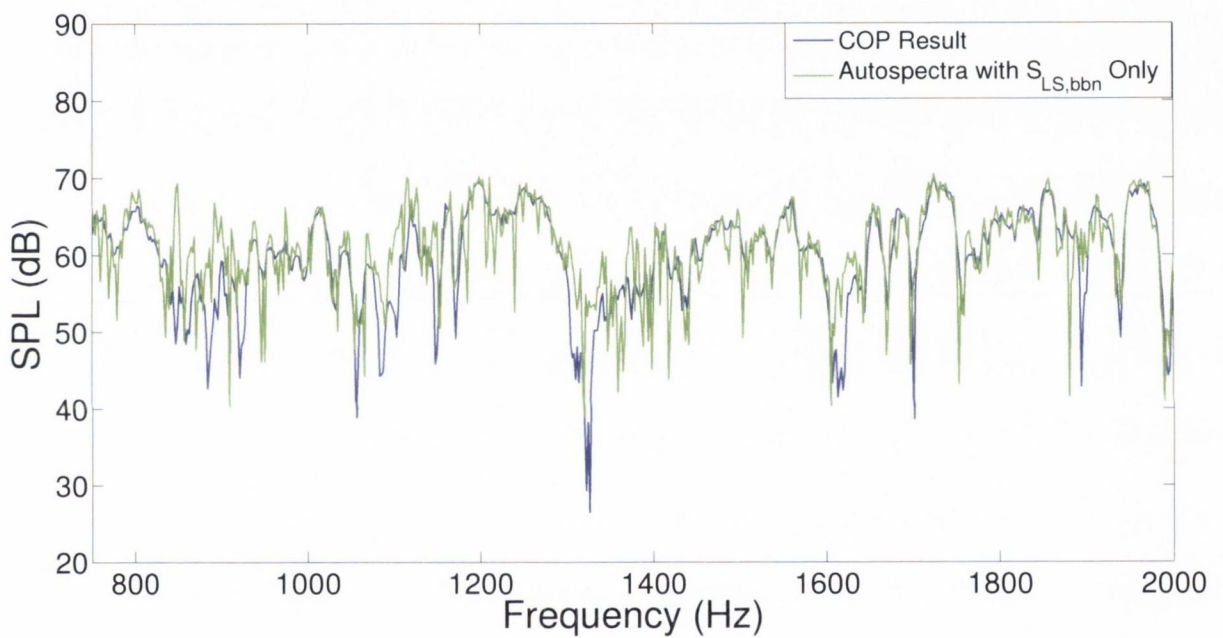
Figure 4.19: Coherent output power results for identification of contribution of $S_{LS,bbn}$ to the noise measured at the inlet sensor with both sources on (test case 1). The blue spectrum shows the coherent output spectrum found using the measurement from a sensor in the loudspeaker cone as the source measurement, and the inlet sensor as the output measurement. The auto-spectrum measured at the same sensor for test case 2 is shown in the green spectrum for comparison.

spectrum was a convenient benchmark for evaluating the success of the COP technique. A similar benchmark was required to show the auto-spectrum at the same inlet sensor with S_{rot} only present – test case 3 in Table 4.1. However, due to the presence of flow-noise induced in the test duct when S_{rot} is present, a raw auto-spectrum at the inlet sensor will contain the contribution of S_{rot} and any flow noise present. In order to give an accurate spectrum showing the contribution of S_{rot} only without flow noise contaminating the results, Chung's [4] signal enhancement method of flow-noise rejection was used to provide a suitable benchmark. The signal enhancement technique was applied using three sensors at the inlet bank for test case 3, removing the uncorrelated flow noise and isolating the contribution of S_{rot} to the inlet sensor of interest. Hence a flow-noise removed spectrum was found which could be used as a benchmark for comparison for any technique's results in identifying the contribution of S_{rot} to the inlet sensor measurement. A comparison between noise measured at the inlet sensor for test cases 1 and 3, and also for test case 3 with flow-noise removed as per the signal enhancement method outlined above, is shown in Figure 4.20.
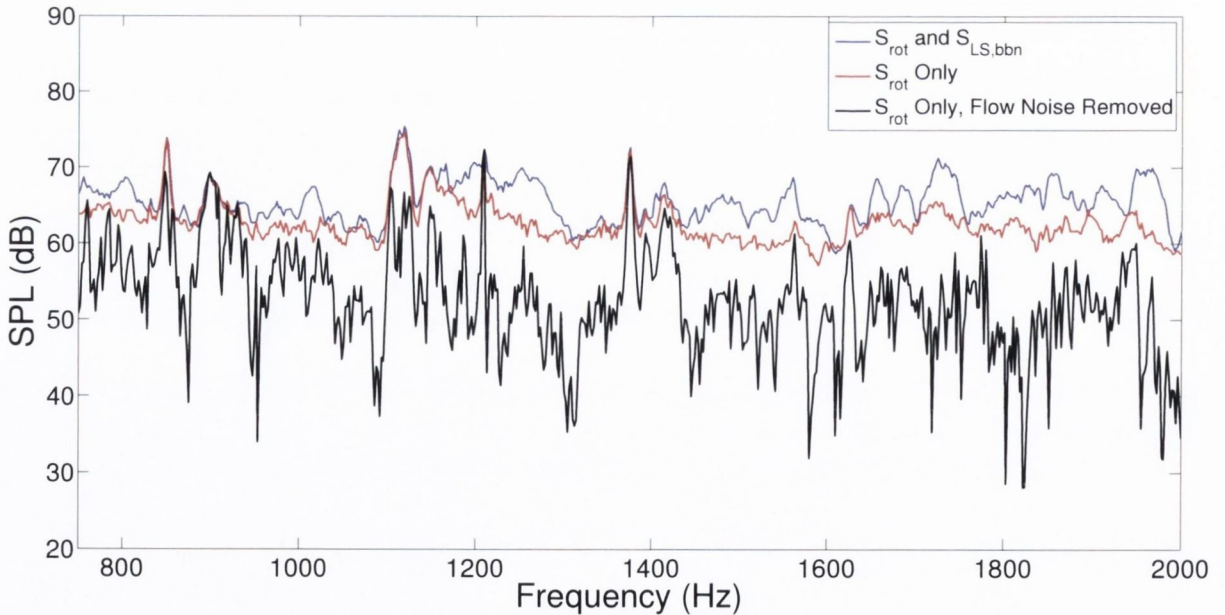
Figure 4.20: Auto-spectra of the inlet sensor measurements for test cases 1 and 3 listed in Table 4.1, as well as the output spectrum from application of the signal enhancement technique for test case 3 which removes the contribution of extraneous flow-noise to the measurement of S_{rot}.

The coherent output power technique was used to attempt to identify the contribution

of S_{rot} to the noise measured at the inlet sensor for test case 1. The locations of the sensors used are shown in blue in Figure 4.21. In this case, an accurate identification of the noise-source's contribution to the inlet sensor is not anticipated due to the presence of flow-noise at the source measurement. The result of applying the COP technique in this test scenario is shown in Figure 4.22. This COP result, shown in blue, matches the green benchmark rotor-stator noise at the inlet sensor quite accurately, however two main issues can be identified. The first is that the tonal peak at the first harmonic of the BPF at $1210Hz$ has not been identified in the G_{vv} spectrum. Secondly, the sound pressure level is overestimated by several dB at certain frequencies, such as in the range $1700Hz$–$2000Hz$, which would contradict the expected result that the coherent output power would drop with the presence of uncorrelated noise at the input measurement (see Section 4.1.1).
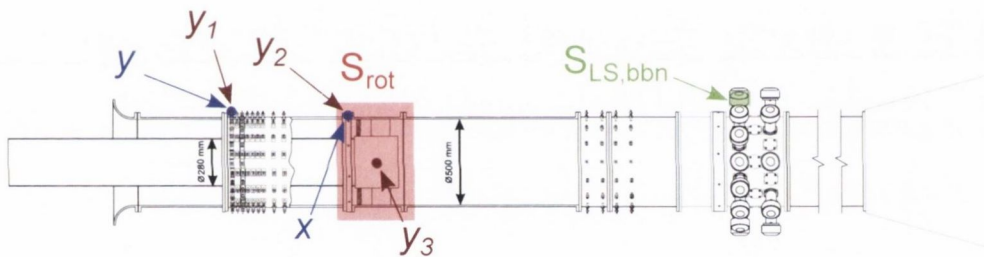
Figure 4.21: Locations of sensor measurements for identification of S_{rot}'s contribution to the noise measured at y. The sensors used for the coherent output power technique are shown in blue. The sensors used for the signal enhancement technique are shown in red. The aim of both techniques is to identify the contribution of S_{rot} to the noise measured by a sensor at the duct inlet – shown as sensor y for the COP technique and y_1 for the SE technique. This is the same inlet sensor in both cases.

Due to the presence of uncorrelated extraneous noise at any measurements of source S_{rot}, the COP technique is unsuitable, and more sophisticated methods are needed. The signal enhancement technique can be used when no pure measurement of the source of interest is available, provided any additional extraneous noise is uncorrelated between each sensor measurement. The locations of the three sensors used in the SE technique are shown in Figure 4.21. Both sensors y_2 and y_3 are located very close to the rotor in order to give an accurate source measurement. The aim of this technique is to accurately identify the contribution of S_{rot} to the noise measured at y_1, which is the same sensor measurement as was used as y in the coherent output power technique *i.e.* the inlet sensor. The result
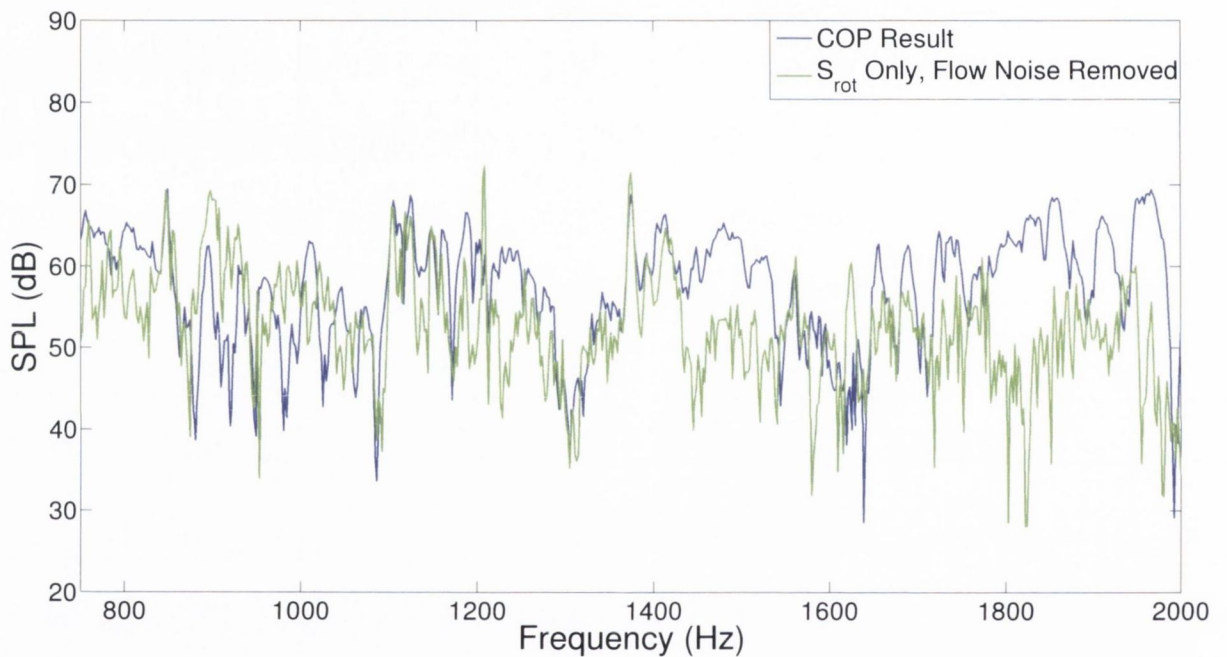
Figure 4.22: Coherent output power result for identification of contribution of S_{rot} to the noise measured at the inlet sensor for test case 1. Sensor positions are shown in Figure 4.21. The blue spectrum shows the coherent output result found using the measurement from a sensor near the rotor-stator as the source measurement, and the inlet sensor as the output measurement. The flow noise-removed spectrum at the same inlet sensor with S_{rot} only is shown by the green spectrum for comparison.

from application of the signal enhancement technique is shown in the red spectrum of Figure 4.23. A similar result is seen with the signal enhancement technique as with the coherent output power technique. The signal enhancement technique was expected to give a result uncontaminated by the uncorrelated flow noise, however in reality it overestimates the flow noise-removed spectrum even more than the COP result. The first harmonic of the BPF tone at $1210Hz$ has however been clearly identified in this case, which is a significant result.
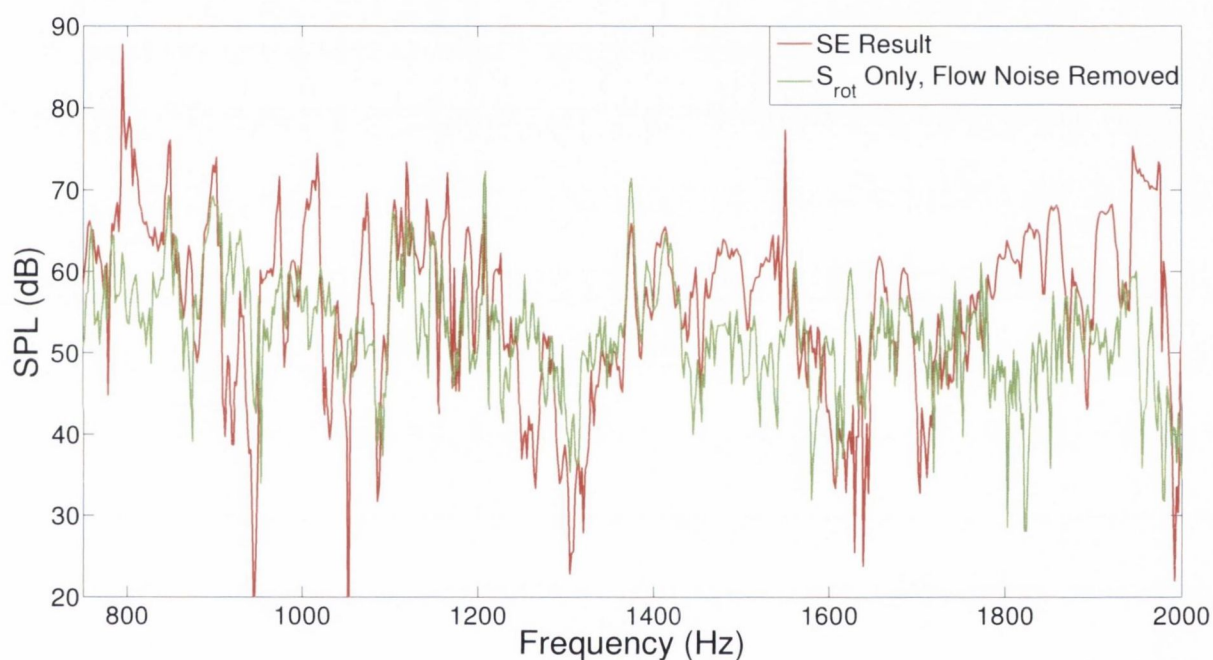
Figure 4.23: Signal enhancement result for identification of contribution of S_{rot} to the noise measured at the inlet sensor for test case 1. Sensor positions are shown in Figure 4.21. The red spectrum shows the signal enhancement result at the inlet sensor using two sensors close to the rotor-stator and the inlet sensor. The flow noise-removed spectrum at the same inlet sensor with S_{rot} only is shown by the green spectrum for comparison.

Both the COP and SE results presented in Figures 4.22 and 4.23 have overestimated the actual contribution of S_{rot} to the noise measured by the inlet sensor for test case 1. This discrepancy could be explained by the presence of a second correlated source ($S_{LS,bbn}$) at the source measurements used in both techniques. If this is the case, the COP and SE results give an estimate of a mixture of both sources S_{rot} and $S_{LS,bbn}$ to the inlet sensor, despite all sensors used as source measurements being located close to the rotor. Given the presence of a second correlated source, a more accurate model of the

noise-source contributions to the sensors used in both the COP and SE techniques for this test scenario will be as shown in Figure 4.24.

Figure 4.25 shows the auto-spectrum of the reference sensor used as a source measurement y_2 in the SE technique and x in the COP technique for test cases 1–3. Since S_{rot} is the dominant source at the sensors close to the rotor-stator, the techniques still give a good qualitative measurement of the shape of the S_{rot} contribution for test case 1, however the additional measurement of $S_{LS,bbn}$ by the reference sensors leads to the over-estimation of S_{rot}'s quantitative contribution. These results have demonstrated that care must be taken when applying both the COP and SE techniques to ensure that a second correlated noise-source is not measured in the source measurements. However, despite the presence of this second correlated noise-source, a reasonably good qualitative approximation of the contribution of S_{rot} to the inlet sensor for test case 1 has been made.
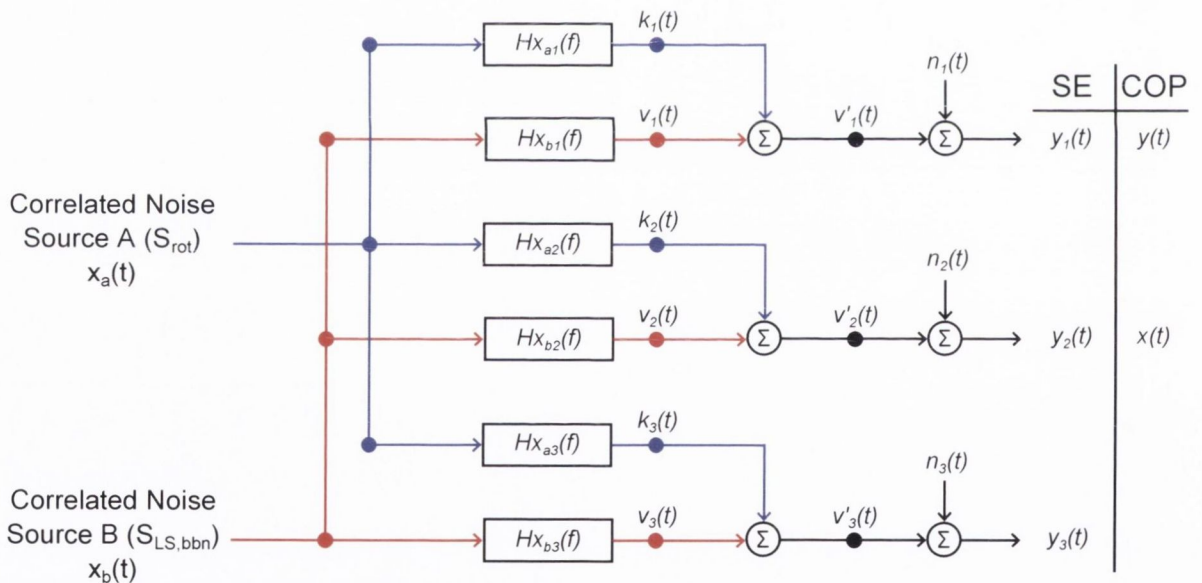
Figure 4.24: Model for identification of the contribution of S_{rot} to the noise at the inlet sensor using the COP and SE techniques. The presence of a second correlated source causes the techniques to fail to accurately identify the contribution of S_{rot} to the inlet sensor.

In order to decouple both correlated noise-sources present in test case 1, a partial coherence formulation is required. The five-microphone conditional spectral analysis technique developed by Hsu and Ahuja [5] and discussed in Section 4.1.3 is a technique which applies the partial coherence formulation given by Bendat and Piersol [61] to separate out
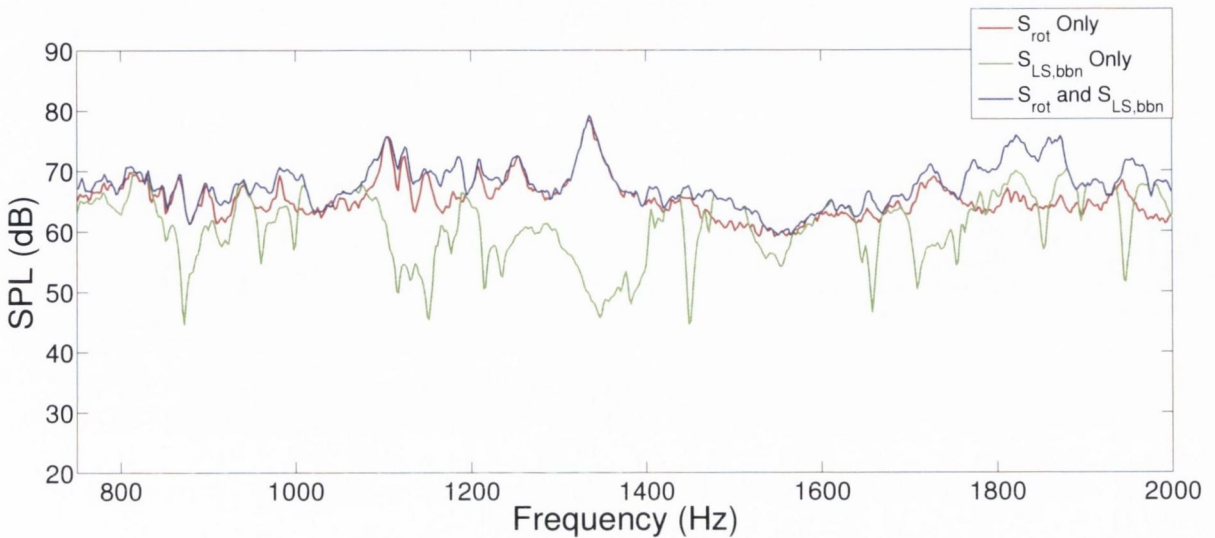
Figure 4.25: Auto-spectra of acoustic sensor measurement used as y_2 in the application of the signal enhancement technique and x in the coherent output power technique shown in Figure 4.21. This figure shows the relative sound pressure levels of S_{rot} and $S_{LS,bbn}$.

the contributions of two sources. A model of this technique is shown in Figure 4.7. Two source measurements are required which must measure one correlated source only, but can accommodate extraneous noise, provided this extraneous noise is uncorrelated with the noise measured at any other sensor. In this case, the source measurements are taken from two reference sensors inside the same loudspeaker cone, giving two source measurements of $S_{LS,bbn}$ (y_4 and y_5). The locations of these measurement signals are shown in Figure 4.26. The other three sensors are located close to the rotor-stator (y_1 and y_2) and at the inlet array (y_3).

The five-microphone CSA technique gives three spectra of interest for each measurement y_{1-3}, as collated in Table 4.2. The G_{vv} spectrum identified in test case 1 is compared with the $S_{LS,bbn}$ measurement made in test case 2 in Figure 4.27. The results match very well, demonstrating that the technique has worked effectively, as the COP technique did in Figure 4.19. The G_{kk} spectrum identified in test case 1 is compared with the S_{rot} measurement made in test case 3 (with flow-noise removed) in Figure 4.27. The results in this case again match very well, unlike the previous attempts using the COP and SE methods shown in Figures 4.22 and 4.23. The partial coherence formulation has allowed the contributions of both correlated noise-sources to be identified, which is a significant advancement.

Deductive thinking would suggest that the noise spectra, which contain any noise present in the raw G_{yy} spectra not accounted for by the G_{vv} and G_{kk} spectra, will identify the contribution of flow noise to the inlet sensor measurement. Other sources of extraneous noise, such as electrical or numerical noise, are assumed to be less significant. The contribution of flow-noise at the inlet sensor was found by applying the SE technique for test case 3 with two other measurement from the inlet array *i.e.* using the same method to remove the contribution of flow-noise in Figure 4.20. This identified noise spectrum found in test case 3 was then compared with the noise spectrum identified by the five-microphone CSA technique (G_{nn}) for test case 1. This result is shown in Figure 4.29, and both spectra again match very well for all frequencies investigated.

Table 4.2: Spectra found through application of the five-microphone CSA technique for test case 1 using the sensors shown in Figure 4.26

Spectrum	Noise Identified
G_{yy}	All Noise Measured at Inlet Sensor for Test Case 1
G_{vv}	$G_{yy} : S_{LS,bbn}$
G_{kk}	$G_{yy} : S_{rot}$
G_{nn}	$G_{yy} \cdot S_{LS,bbn} \cdot S_{rot}$
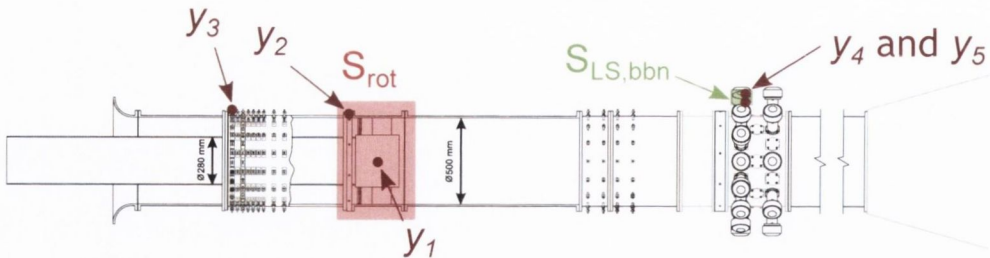
Figure 4.26: Locations of sensor measurements for identification of $S_{LS,bbn}$ and S_{rot}'s contribution to the noise measured at y_3, using the five-microphone conditional spectral analysis technique.

The partial coherence formulation underpinning this technique has successfully decoupled both sources, and accurate spectra have been obtained showing the contributions of both sources to the noise at a sensor of interest. Furthermore, given that only two sources are present, the contribution of an additional uncorrelated noise has been identified. Such uncorrelated noise in a real turboshaft engine could be flow noise. In the case of Figure 4.27, the result closely matches the COP result in Figure 4.19. This is due to the fact
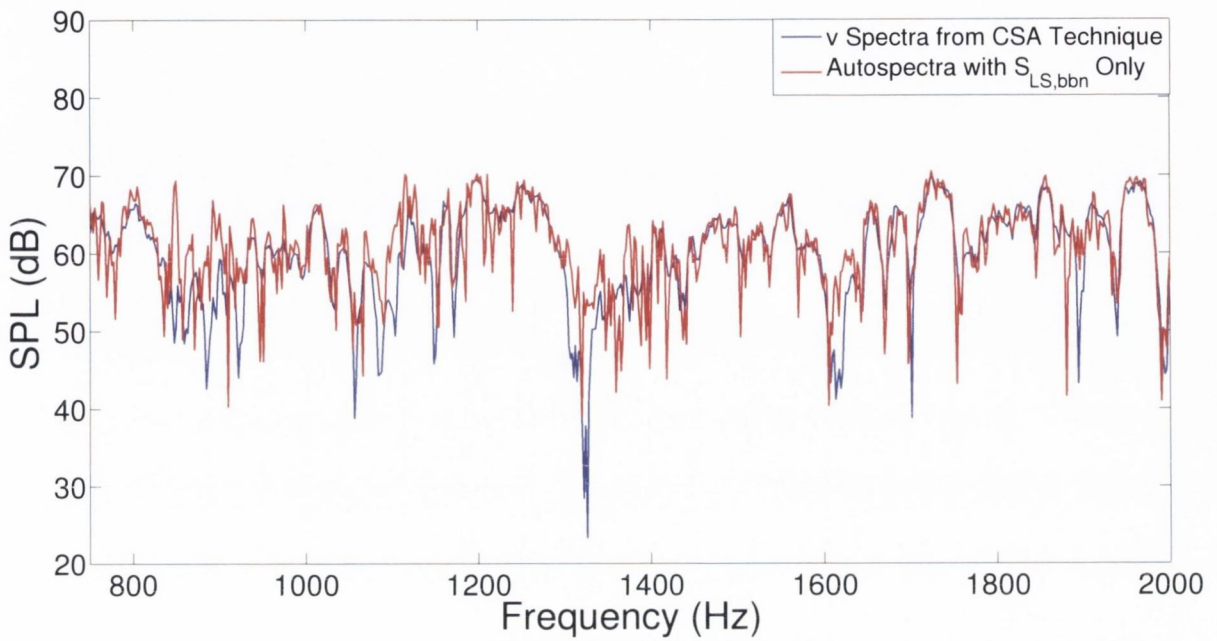
Figure 4.27: Results for identification of $S_{LS,bbn}$'s contribution to the noise at the inlet sensor using the five-microphone CSA technique.
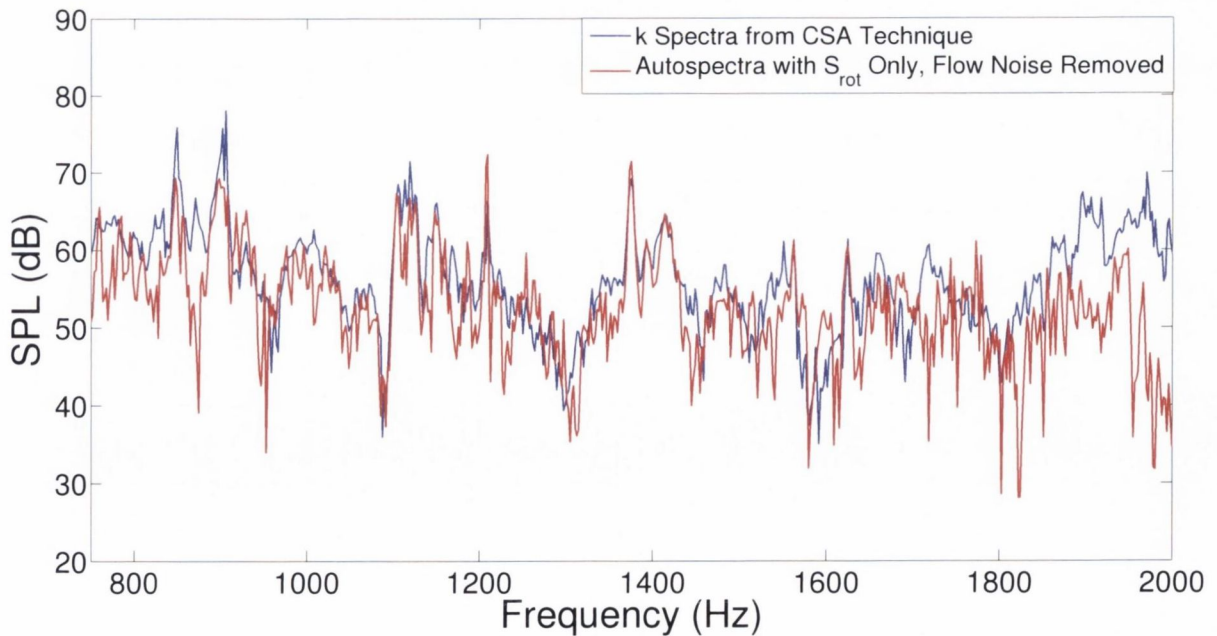
Figure 4.28: Results for identification of S_{rot}'s contribution to the noise at the inlet sensor using the five-microphone CSA technique.
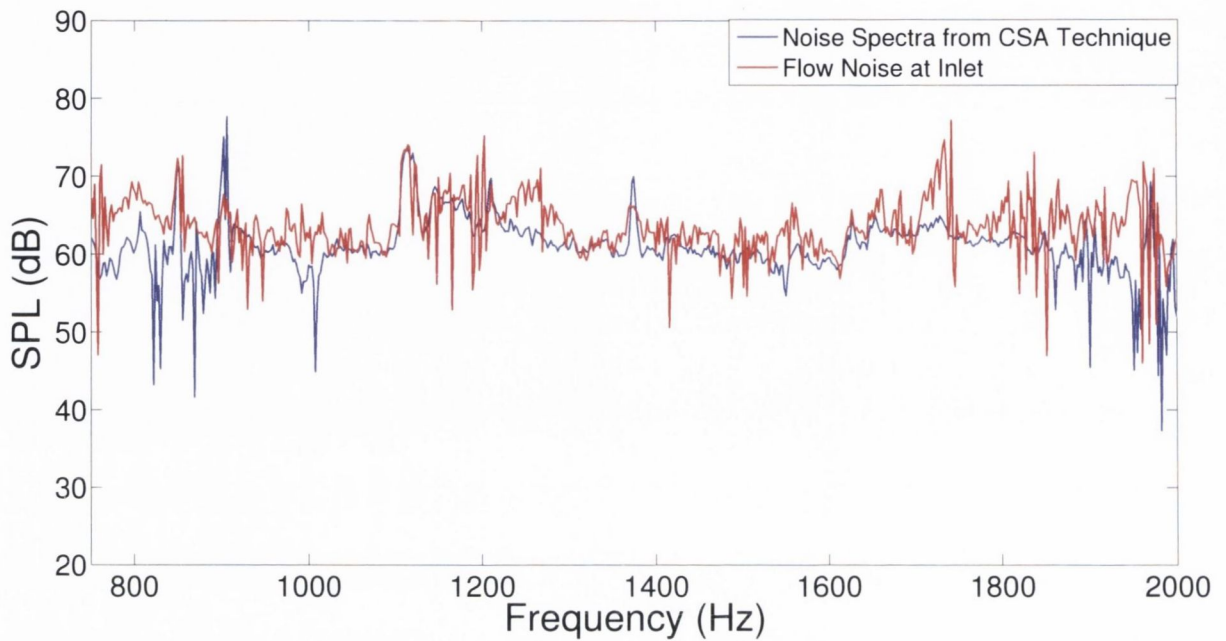
Figure 4.29: Results for identification of the hydrodynamic flow noise induced by the inlet sensor using the five-microphone CSA technique.

that the five-microphone CSA technique utilises the COP technique in its first stage, as discussed in Section 4.1. It is therefore crucial that the microphones used as measurements y_4 and y_5 are located such that they measure one source and uncorrelated noise only. If this requirement is not met, the technique will fail.

4.3.2 Modal CSA Technique

In order to test this new technique (outlined in Section 4.1.4), the modal amplitudes at the inlet sensor array were first estimated using the radial modal decomposition scheme of Åbom (see Section 3.1) for test cases 2 and 3. This gives the specific contribution of each source region to the amplitudes of the modes measured when both noise sources are present in test case 1. These amplitudes were used as the benchmark to test the modal CSA technique's performance.

As with the classic five-microphone CSA technique results discussed in Section 4.1.3, five output measurements are required for the modal CSA technique. Two of these outputs must measure one of the sources without measuring the other source of interest, and any additional extraneous noise measured by these sensors must not be correlated with any other output measurements. The same sensor measurements y_1, y_2, y_4 and y_5 were used

as in the classic CSA technique for testing the novel CSA technique enhanced with modes. The sensor measurement y_3 was replaced with a complex modal amplitude decomposed at the inlet sensor bank. These sensor positions are shown in Figure 4.30. The Fourier transform is taken of the time-domain measurements y_1, y_2, y_4 and y_5, giving the frequency domain signals Y_1, Y_2, Y_4 and Y_5. The complex signal $A_{mn}^{\pm}$, which is the complex modal amplitude of the (m,n) mode travelling in the positive or negative x-direction, is used as measurement Y_3. All five outputs Y_1–Y_5 are complex frequency-domain measurements of the acoustic pressure. By calculating the auto- and cross-spectra of these signals by ensemble averaging and applying Equations 4.6 and 4.7, a total of nine spectra can be determined. These spectra are $G_{v1-3v1-3}$, $G_{k1-3k1-3}$ and $G_{n1-3n1-3}$. By examining the G_{v3v3}, G_{k3k3} and G_{n3n3} spectra, the technique can be used to identify the contribution of both noise-source regions to the modal amplitude $A_{m,n}^{\pm}$ for test case 1.
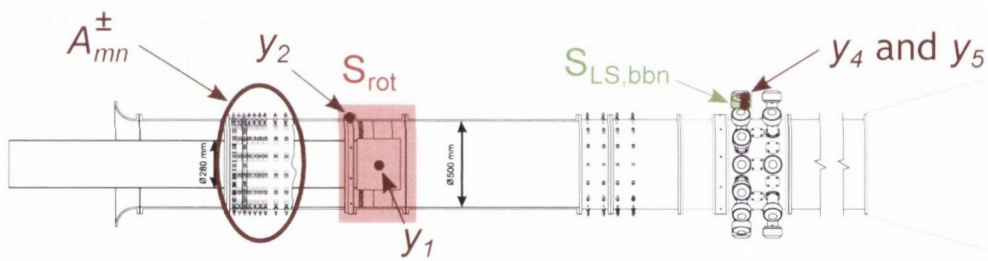
Figure 4.30: Locations of output measurements used in the modal CSA technique. The aim of this technique is to identify the contribution of S_{rot} and $S_{LS,bbn}$ to the amplitudes of the modes travelling in the negative x-direction, as measured by a bank of sensors at the duct inlet – shown as $A_{m,n}^{-}$.

Figure 4.31(a) shows the decomposed radial modal amplitudes at the inlet sensor array when a single loudspeaker generates broadband noise *i.e.* test case 2. Figure 4.31(b) shows the decomposed modal amplitudes with the rotor rotating at 1500rpm *i.e.* test case 3. At most frequencies the highest-order cut-on modes dominate slightly in both test cases. The rotor generates higher levels of broadband noise at lower frequencies than the loudspeaker. For the case of the rotor noise shown in Figure 4.31(b), the tonal peaks at multiples of $605Hz$ corresponds to the blade-pass frequency of the rotor and its harmonics. These modal amplitudes are measured for modes travelling in the negative x-direction *i.e.* travelling away from both sources and towards the inlet plane of the duct.

In order to test the modal CSA technique for the case of two broadband noise sources,

the same test case as was used to investigate the classic techniques was examined. This is test case 1 in Table 4.1. The (2,0) mode was selected for investigation using the modal CSA technique. Any cut-on mode in the frequency range tested ($200Hz$–$2100Hz$) could have been selected. $2100Hz$ represents the upper frequency limit of modal decomposition at the inlet of the test duct, given that there are 16 sensors per ring in the sensor array. The modal decomposition technique also allows the radial modal content of the pressure field to be decomposed with directionality (see Section 3.1), so $A_{2,0}^{+}$ or $A_{2,0}^{-}$ could be chosen as the modal amplitudes of interest. $A_{2,0}^{-}$ was chosen as this represents the amplitude of the (2,0) acoustic mode travelling away from the noise sources, towards the inlet plane of the test duct.
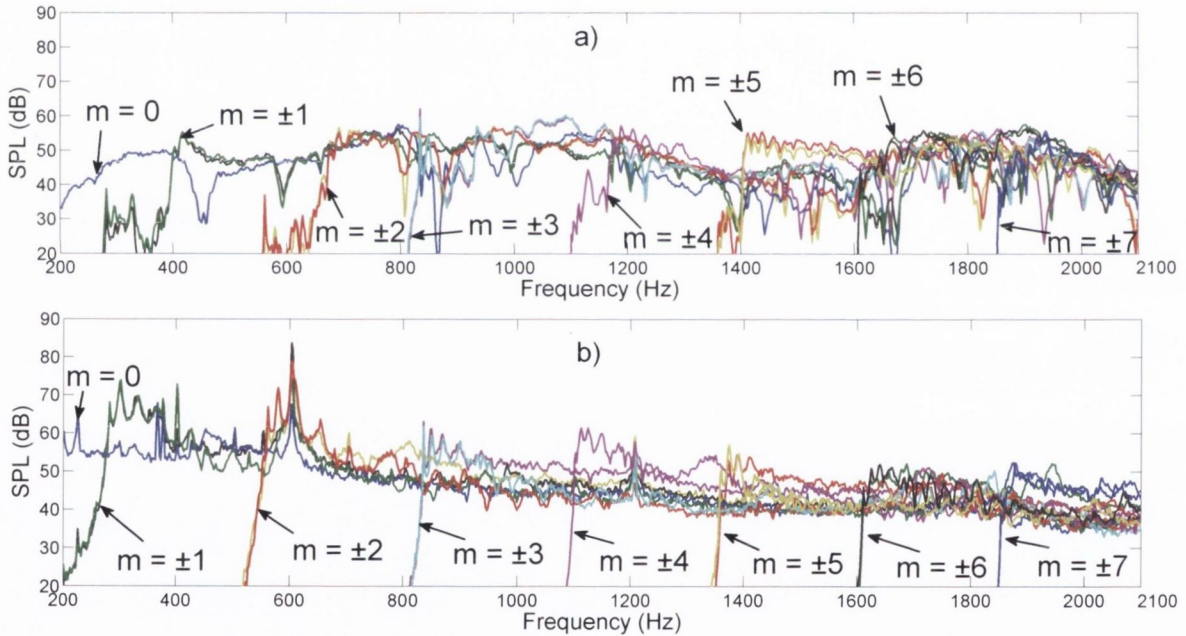
Figure 4.31: Spectra of modal amplitudes decomposed at the inlet sensor bank for all modes cut-on in the frequency range of interest for test cases 1 and 2. The modes are travelling in the negative x-direction *i.e.* away from both sources and towards the inlet plane of the test duct (see Figure 4.10). Sub-figure(a) shows the modal amplitudes measured when $S_{LS,bbn}$ is active – test case 2. Sub-figure(b) shows the modal amplitudes measured when S_{rot} is active – test case 3.

As discussed in Section 4.1, the five-microphone CSA technique is formulated in two stages. The first stage uses the coherent output technique. The complex modal amplitude $A_{2,0}^{-}$ measured at the inlet sensor bank was used as measurement Y_3 in the modal CSA technique. With reference to Figure 4.8, the G_{k3k3}, G_{v3v3} and G_{n3n3} identified using the

modal CSA technique are of interest. Correlated noise source B shown in Figure 4.8 will in this case refer to the contribution of $S_{LS,bbn}$ to $A_{2,0}^-$, due to the fact that measurement Y_4 and Y_5 measure $S_{LS,bbn}$ and extraneous noise only. Similarly, correlated noise source A refers to the contribution of S_{rot}.

Each spectrum identified using the modal CSA for test case 1 are listed in Table 4.3. The modal spectra shown in Figure 4.31 provide benchmarks of the contributions of both $S_{LS,bbn}$ and S_{rot} to the modal amplitudes measured in test case 1, which are then compared with G_{v3v3} and G_{k3k3} respectively in order to analyse the effectiveness of the modal CSA technique.

Table 4.3: Spectra found through application of the five-microphone modal CSA technique for test case 1 using the sensors shown in Figure 4.30

Spectrum	Noise Identified
G_{y3y3}	$A_{2,0}^-$
G_{v3v3}	$G_{y3y3} : S_{LS,bbn}$
G_{k3k3}	$G_{y3y3} : S_{rot}$
G_{n3n3}	$G_{y3y3} \cdot S_{LS,bbn} \cdot S_{rot}$

The G_{v3v3} spectrum is compared to the (2,0) modal amplitude measured when only $S_{LS,bbn}$ is present (test case 2) in Figure 4.32. The blue spectrum shows the modal amplitude decomposed when both noise sources are present; $A_{m,n}^\pm$ in Figure 4.8. The green spectrum shows the modal amplitude decomposed when only the loudspeaker is present. The red spectrum shows the contribution of $S_{LS,bbn}$ to the modal content decomposed at the inlet, as identified using the CSA technique. This result can be compared to the green spectrum to verify the efficacy of the technique. The results are very positive, with both spectra matching well for all frequencies above modal cut-on at $563Hz$. The technique overestimates the modal amplitude around the blade-pass frequency of $605Hz$, most likely caused by y_4 and y_5 measuring some of the blade-pass frequency acoustic energy generated by the rotor which propagates in the duct, violating the assumption that they measure $S_{LS,bbn}$ and extraneous noise only. However, it should be noted that although some of this BPF energy is being measured incorrectly in this result, the measured BPF tone is $20dB$ below the actual BPF, which is a factor of 10. The overall result is therefore still very positive.

Due to the presence of flow-noise introduced into any in-duct sensor measurement
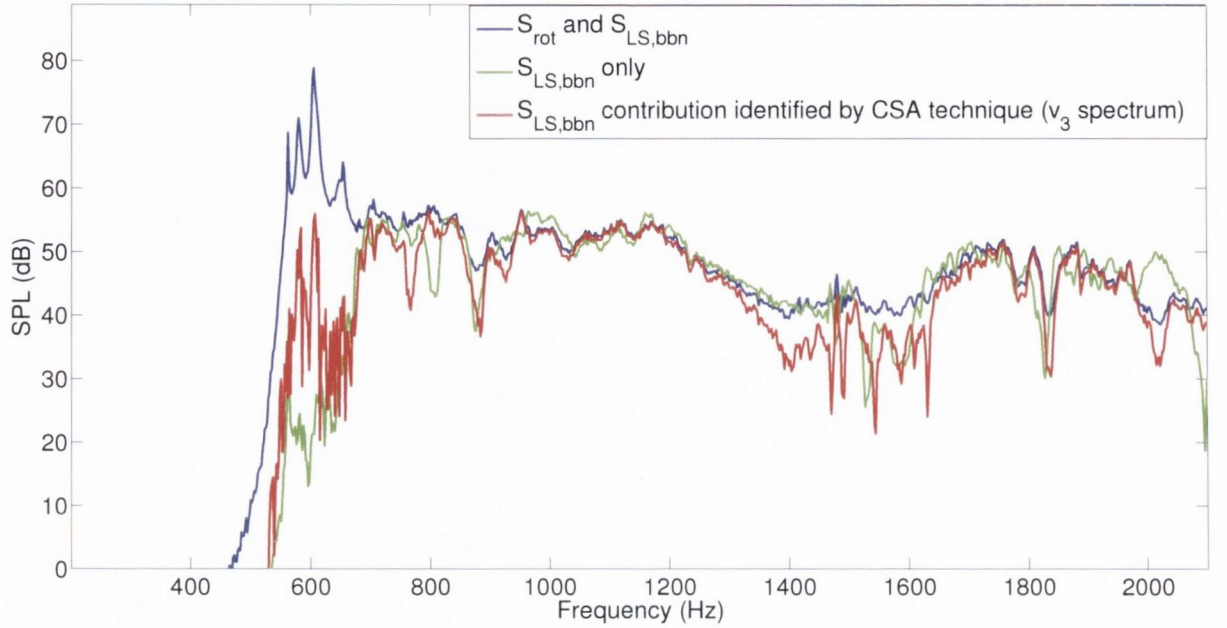
Figure 4.32: Spectra of the $A_{2,0}^{-}$ mode when both S_{rot} and $S_{LS,bbn}$ are present, shown in the blue spectrum (G_{y3y3}), and the spectra of the same mode order when $S_{LS,bbn}$ is present in isolation, shown in the green spectrum. The red spectrum shows the contribution of $S_{LS,bbn}$ to the amplitude of this mode order identified when both sources are present (G_{v3v3}).

when S_{rot} is present, the G_{kk} spectrum identified by the non-modal five-microphone CSA technique was compared to a flow-noise removed spectrum, see Figure 4.28. This flow-noise removed spectrum was found by applying the signal enhancement technique using the inlet sensor of interest and two adjacent sensors for test case 3. A similar approach is proposed for the modal CSA technique in order to separate the contributions of flow-noise and S_{rot} to the modal amplitudes measured when S_{rot} is the only noise-source. This provides a more suitable benchmark for comparison with the results found from applying the modal five-microphone CSA technique.

The modal amplitudes identified at the inlet sensor array for test case are shown in Figure 4.31(b). In the modal decomposition technique 64 sensors are used, however there are an additional 16 sensors in the inlet sensor bank that are not to perform this modal analysis. Two of these unused sensors were used to remove the contribution of extraneous noise to the decomposed modal content in order to find the flow-noise removed modal amplitudes, through application of the SE method. The model for the SE method in this case is shown in Figure 4.33. The SE technique removes any noise uncorrelated between

the modes and the two sensor measurements, so the contribution of extraneous flow-noise to these modal amplitudes is isolated and can be compared to the noise spectrum identified by the modal CSA technique for test case 1 (G_{n3n3}). Furthermore, the flow-noise removed modal spectra from test case 3 can be compared to the G_{k3k3} spectrum identified by the modal CSA technique for test case 1.
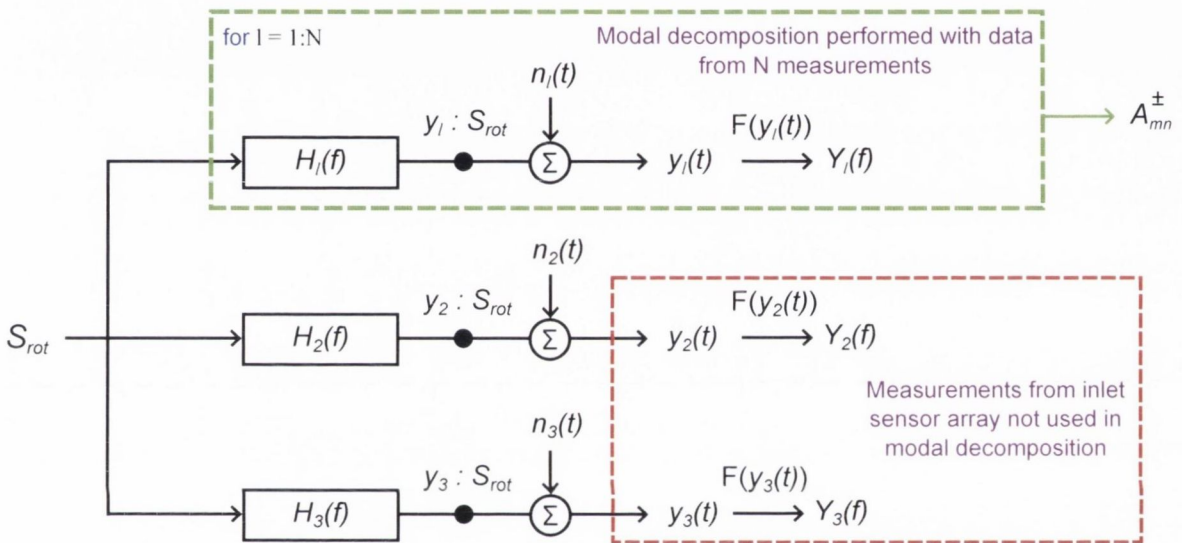
Figure 4.33: Signal enhancement model for removal of flow-noise from the modal amplitudes found for test case 2.

The G_{k3k3} spectrum is compared to the $A_{2,0}^{-}$ modal amplitude measured when only S_{rot} is present (test case 3, with flow noise removed) in Figure 4.34. The blue spectrum again shows the G_{y3y3} spectrum. The green spectrum shows the modal amplitude decomposed when only rotor noise is present (test case 3), with flow-noise removed using the signal enhancement technique. The red spectrum shows the contribution of S_{rot} to the modal content decomposed at the inlet, as identified using the CSA technique, when both $S_{LS,bbn}$ and S_{rot} are present (test case 1). The technique works extremely well in this case. The accurate identification of the tonal peak at the rotor BPF at $605Hz$ is a particularly good result. This is to be expected, as the tonal energy at the blade-pass harmonics will propagate with high coherence in the test duct, hence the accurate result at these frequencies. At frequencies other than the BPF, the shape of the identified rotor noise

spectrum matches the shape of the rotor broadband noise quite well, with a discrepancy from the actual rotor broadband noise of around $3dB$ at frequencies where the rotor broadband noise is significant. When the rotor broadband noise drops below around $30dB$, the identified contribution of the rotor is less accurate due to the low signal-to-noise ratio as the loudspeaker ($S_{LS,bbn}$) dominates at these frequencies.
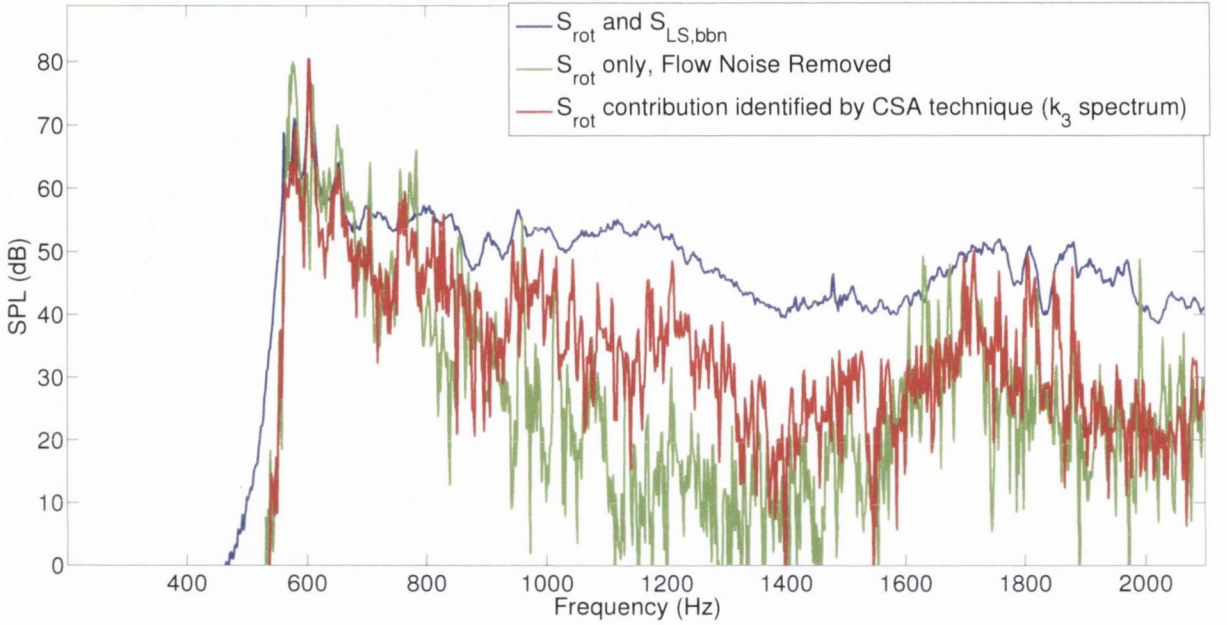
Figure 4.34: Spectra of the $A_{2,0}^{-}$ mode when both S_{rot} and $S_{LS,bbn}$ are present, shown in the blue spectrum (G_{y3y3}). The spectrum of the same mode order when S_{rot} is present in isolation, with flow noise removed using the signal enhancement technique, is shown in the green spectrum. The red spectrum shows the contribution of S_{rot} to the amplitude of this mode order identified when both sources are present (G_{k3k3}).

Figure 4.35 shows the G_{n3n3} spectrum in red, which is the contribution of extraneous noise to the amplitude of the $A_{2,0}^{-}$ mode decomposed at the duct inlet. This spectrum will contain any extraneous noise such as any flow noise present in the measurements. As explained above, the contribution of extraneous flow-noise to these modal amplitudes can be compared to the identified noise spectrum found by applying the signal enhancement technique for test case 3. This noise spectrum will identify the contribution of extraneous noise, such as flow noise and any ambient noise present in the tests. This spectrum is shown in green. As in the non-modal CSA technique, the extraneous flow noise identified by both the modal CSA technique when both sources are present and the signal enhancement technique when S_{rot} is present in isolation match well for all frequencies.

As noted at the beginning of this chapter, all spectral measurements (auto-spectral densities, cross-spectral densities and coherences) made using experimentally-acquired time records are in fact estimates of real functions, and are therefore subject to both variance and bias errors. All coherence-based noise-source identification techniques applied herein use combination of these spectral estimates, and these errors therefore propagate when applying these techniques. These errors are generally dependent on the coherence between the pairs of microphones, the number of averages in the ensemble, the frequency resolution of the estimated spectral functions, and the signal-to-noise ratios of the noise-source measurements. It is necessary to quantify this uncertainty in order to verify the effectiveness of each technique. Such an error analysis has been performed in Appendix C.5.
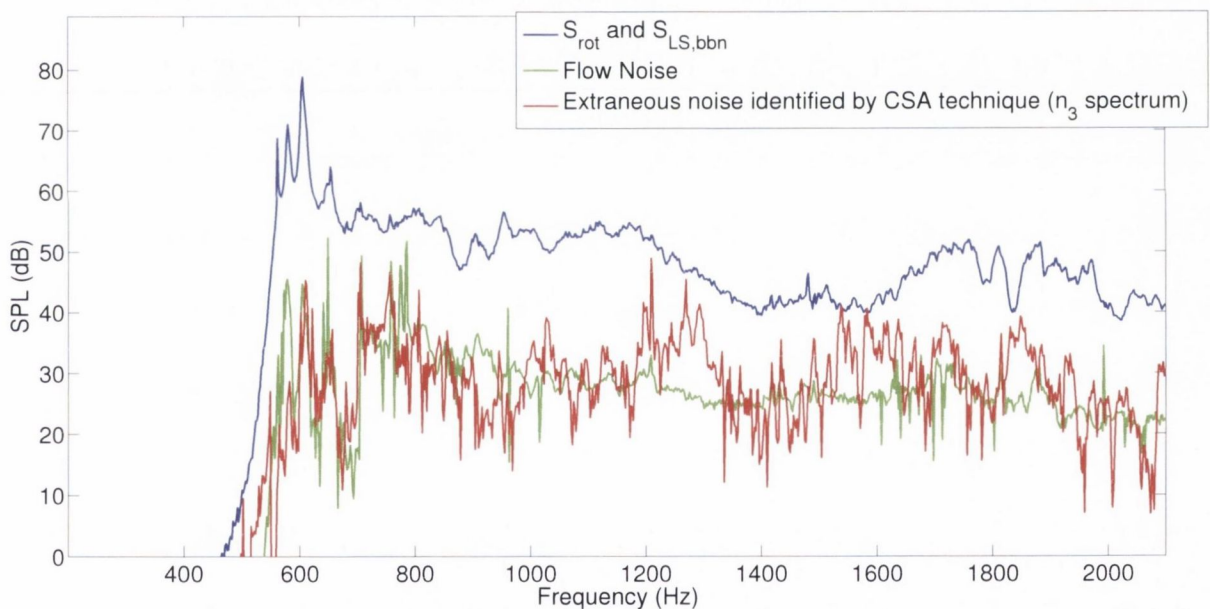
Figure 4.35: Spectra of the $A_{2,0}^-$ mode when both S_{rot} and $S_{LS,bbn}$ are present, shown in the blue spectrum (G_{y3y3}). The green spectrum shows the noise spectrum found by subtracting the flow-noise removed SPL spectrum from the raw SPL spectrum when S_{rot} is present in isolation. The red spectrum shows the extraneous noise contribution to the amplitude of this mode order identified when both sources are present (G_{n3n3}).

4.4 Discussion

In this chapter, previously published techniques of noise-source identification which apply the coherence function between a number of sensor measurements have been investigated for their applicability to turbomachinery noise-source identification using experimental data. These techniques are pre-existing in the literature, but are applied here for a specific ducted two noise-source region scenario. It was demonstrated that the five-microphone CSA technique was best suited to the scenario tested, as it is required to decouple both noise sources using a partial coherence formulation. This technique is applied in two stages; the first stage is performed by applying the coherent output technique, the second stage applies a partial coherence formulation of the signal enhancement technique on the residual.

A novel modal CSA technique was also developed in this chapter, and tested using this same experimental data. This technique enhances the original five-microphone CSA technique by allowing the specific contribution of both noise-sources to the modal content decomposed at the duct inlet to be identified. This is a significant advancement on the existing techniques, accurately identifying the contributions of two correlated noise-sources containing both broadband and tonal noise by combining the techniques of modal analysis with traditional partial coherence methods. A modal-based signal enhancement technique was also investigated which can be applied when a single correlated noise-source is present, in order to isolate the contribution of uncorrelated extraneous noise from the measured modal amplitudes.

All noise-source identification techniques investigated in this chapter apply the coherence function between a number of input and output acoustic measurements in order to assess causal links between the noise measured at the output measurements and one or several noise sources. All such coherence measurements make a fundamental assumption of there being a linear propagation path between each source and receiver. If this assumption were to be violated, an erroneous conclusion of causality will result from application of the ordinary coherence function. In the small-scale TEENI test campaign, both tonal and narrowband noise was generated using one or more loudspeakers in the mode generator array, which then propagates through a rotating rotor-stator stage. It was found

that in some cases that the noise observed in spectral measurements was scattered at sum and difference frequencies relative to the incident noise. This noise is scattered at frequencies of plus or minus multiples of the rotor blade-pass frequency. Examples of this scattering of noise are shown in the upstream and downstream spectral measurements shown in Figures 4.36 and 4.37 for both tonal and narrowband (NBN) tests respectively. In both cases, noise was generated by all 16 loudspeakers in the mode generator. For the tonal noise case the rotor is rotating at 3000rpm and for the narrowband case the rotor was rotating at 1500rpm, giving BPFs at $1210Hz$ and $605Hz$ respectively. There is zero phase difference between each loudspeaker in the mode generator array, and so the $m = 0$ mode has been targeted in both cases (see Section 3.2 for more on targeted azimuthal mode generation).
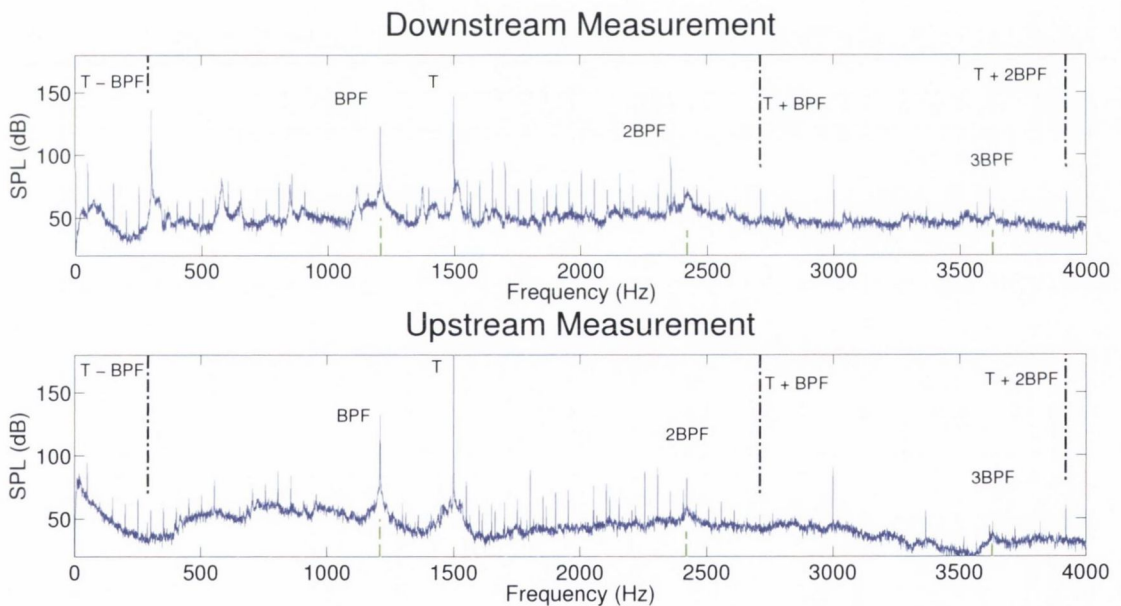
Figure 4.36: Sound-pressure level measurements from two microphones located upstream and downstream of the rotor. The rotor is rotating at 3000rpm, giving a BPF of $1210Hz$. A tone is generated at $1500Hz$ by sixteen loudspeakers in a single ring in the mode generator array.

This sum and difference scattering of noise had previously been observed by Bennett and Fitzpatrick [6] who suggested that this noise was generated by the quadratic interaction between the rotating rotor and the incident noise, as generated by the mode generator in this case. A non-linear coherence function was also developed in this study.
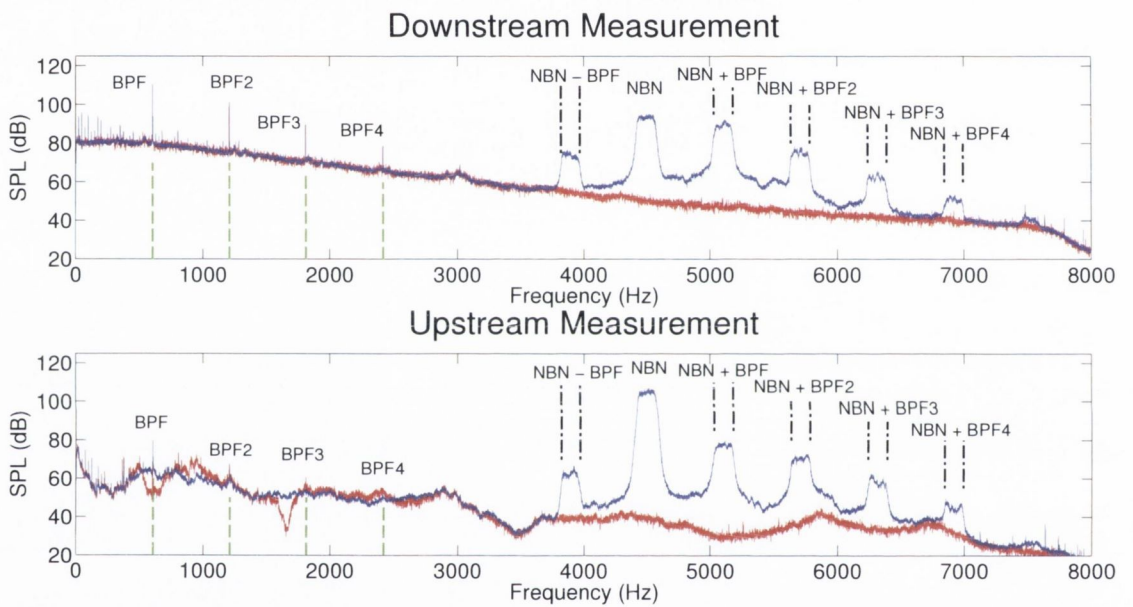
Figure 4.37: Sound-pressure level measurements from two microphones located upstream and downstream of the rotor. The rotor is rotating at 1500rpm, giving a BPF of $605Hz$. Narrowband noise centred at $4500Hz$ with a bandwidth of $150Hz$ is emitted from sixteen loudspeakers in a single ring. These auto-spectra are superimposed onto the plots for the test point where the narrowband noise is turned off and hence the rotor is the only noise-source, as shown in the red spectra.

This non-linear coherence function has been applied to the results shown in Figures 4.36 and 4.37 in Figures 4.38 and 4.39, as well as the ordinary coherence function. Further results and discussion are presented in an additional paper [62]. These results show that the noise scattered at sum and difference frequencies is measured with low ordinary coherence, and the high quadratic coherence show that the reason for this drop in ordinary coherence is the non-linear relationship between measurements of this noise upstream and downstream of the rotor/stator stage.
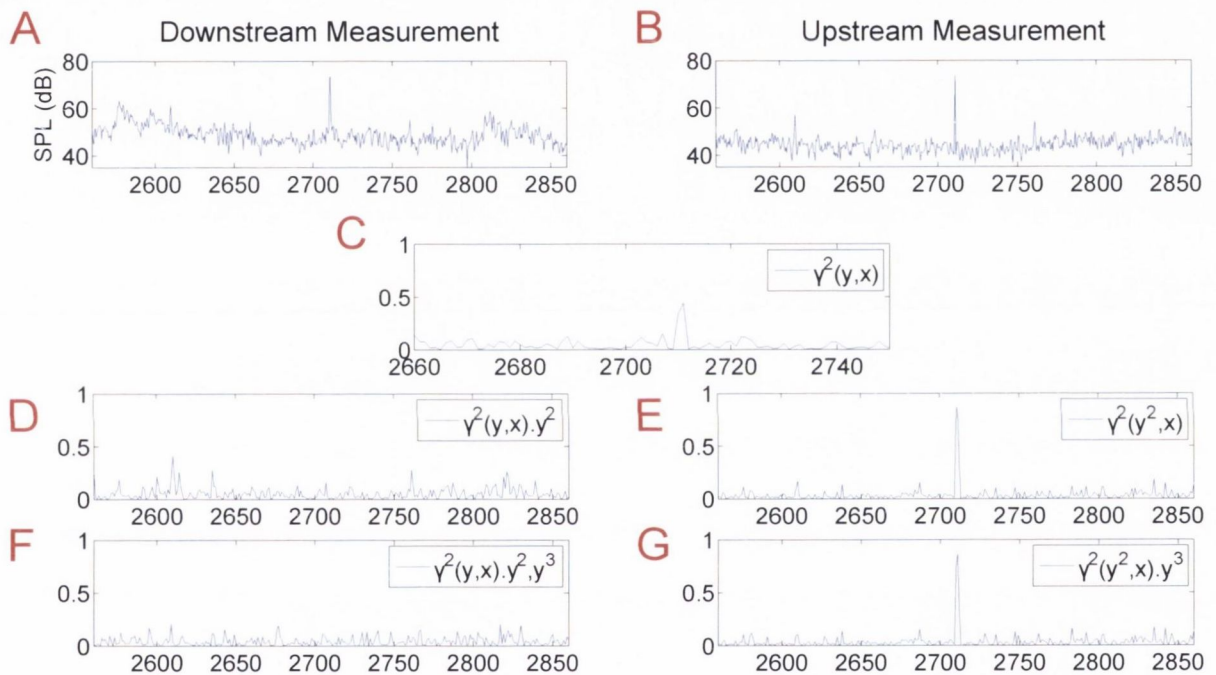
Figure 4.38: A and B show close-ups of the autospectra for both measurements made downstream and upstream of the rotor. These close-up spectra are centred at a single scattered tone. The ordinary coherence calculated between the upstream and downstream measurements is shown in C. The linear and enhanced linear coherence functions are shown in D and F respectively. The quadratic and enhanced quadratic coherence functions are shown in E and G respectively.

The exact conditions that cause this scattering of noise to occur are unknown. Sum and difference scattering was observed at certain incident noise test frequencies, but not others. Figure 4.40 shows the spectra measured by a single microphone for several narrowband noise tests, with sum and difference scattering only evident at higher source frequencies. It is proposed that the reason that noise scattering occurs above a critical frequency is linked to the cut-on frequencies of certain mode orders, however no work is present in the
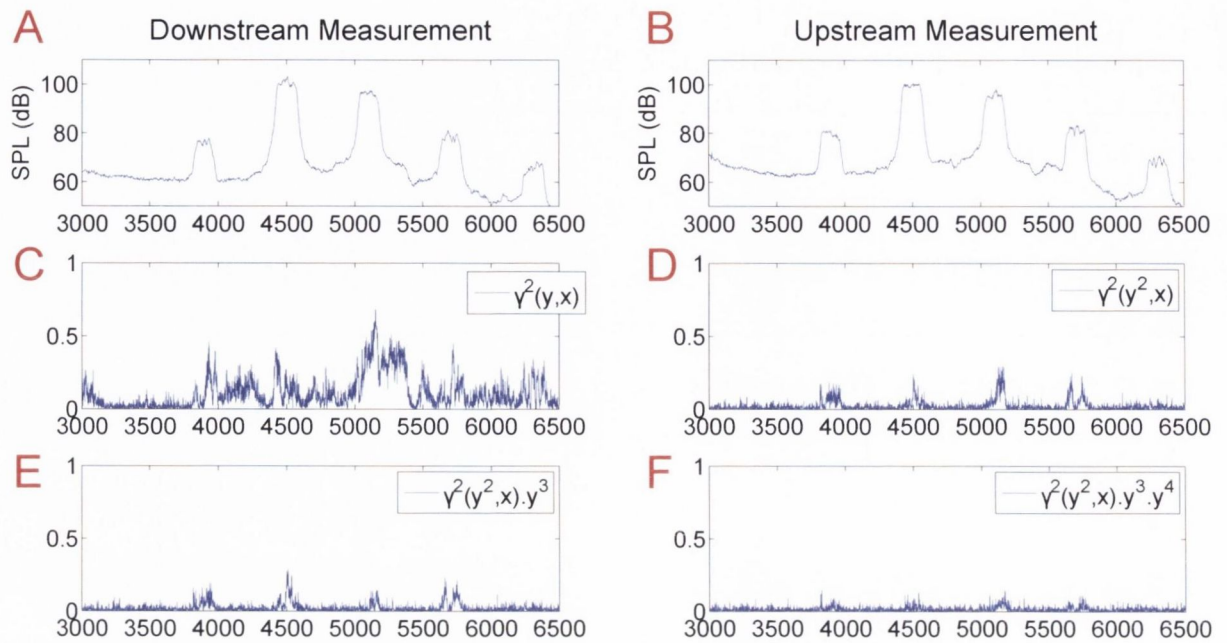
Figure 4.39: A and B show the autospectra for both measurements made downstream and upstream of the rotor. These spectra show the incident narrowband noise generated at $4500Hz$ as well as noise scattered at several additional frequencies. The ordinary coherence calculated between the upstream and downstream measurements is shown in C. The quadratic and enhanced quadratic coherence functions are shown in D–F.

literature to investigate this scattering of noise in detail. It was not possible to investigate the modal content of both the source narrowband noise generated by the loudspeaker and any scattered noise in the small-scale TEENI tests due to the limited frequency range in which modal analysis could be performed. The frequency resolution between source frequencies was also insufficient for a detailed investigation. The objective of the next chapters in this thesis are to design an experimental set-up to investigate this sum and difference scattering of noise, as well as undertaking a review of the existing relevant literature which may offer clues to the causes of this scattering of noise.
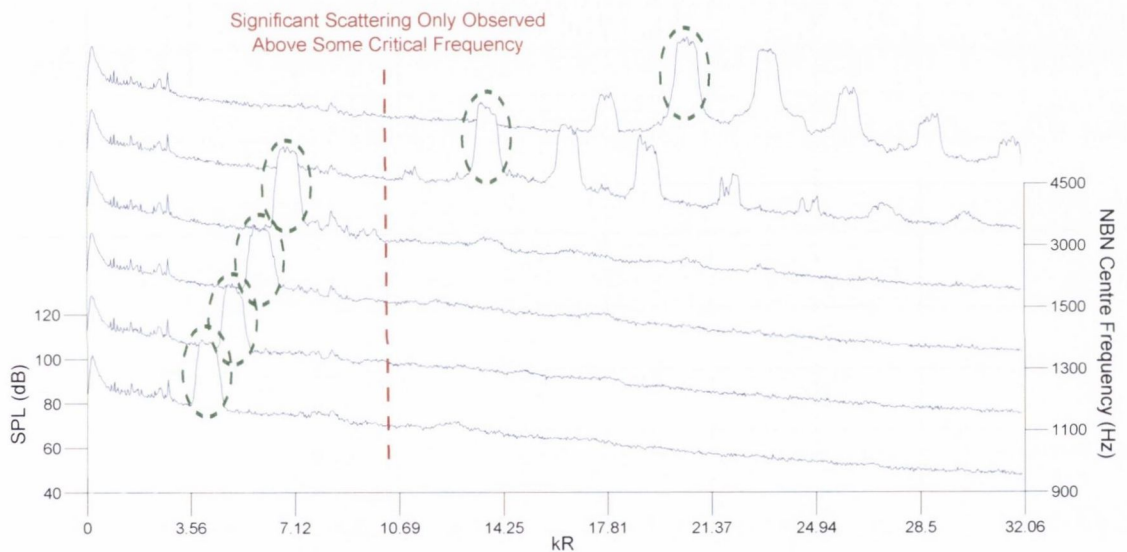
Figure 4.40: Waterfall plot of several test cases similar to that shown in Figure 4.37. The x-axis shows the dimensionless frequency range and the y-axis shows the sound pressure level of the measured noise. Each spectra shows a different test case where NBN has been generated by the loudspeaker array at a different centre frequency, as denoted in the z-axis. The NBN generated by the loudspeaker array is circled in green in each case.

Chapter 5

Sum and Difference Scattering of Noise Through a Fan/Rotor Stage – Background and Experimental Set-Up

5.1 Theory and Background

In Chapter 4, an experimental investigation was undertaken into noise-source identification for an experimental rig which was designed as a simplified representation of a real turboshaft engine. The aim of these tests was to assess the efficacy of existing coherence-based noise-source identification techniques for the identification of the contributions of various noise sources within a real turboshaft engine to the noise radiated from the engine exhaust.

It was observed in Section 4.4 that scattering of both tonal and narrowband noise propagating downstream in a duct can occur on interaction with a rotating rotor. Acoustic energy may be scattered at sum and difference frequencies from the incident noise under certain test conditions. This phenomenon is only observed when the incident noise is generated at relatively high frequencies. Bennett and Fitzpatrick [6] proposed that the reason scattering is only observed at higher frequencies is linked to the cut-on of certain acoustic modes in the duct. However, to date not enough experimental data has been gathered to make an in-depth quantitative study in order to ascertain the exact conditions which cause scattering to occur at these sum and difference frequencies.

In this section, a review of the existing literature concerning scattering of noise by a fan/rotor is presented. Scattering of the incident noise can occur, which will cause the modal content of the incident noise to be affected by interaction with the rotating fan or stationary stator as some modal content is reflected or scattered. Sum and difference scattering of noise can also affect the spectral and modal distribution of acoustic energy at frequencies other than the incident noise frequencies. Having reviewed the literature, a strategic design process is outlined in order to investigate sum and difference scattering of noise experimentally. The results of this experimental investigation are then discussed in Chapter 6.

5.1.1 Transmission of Noise Through Rotating Turbomachinery

Kaji and Okazaki [63] considered a spiral wave, as generated by the interaction of a rotor-stator at the rotor BPF for example, entering a cascade of blades. They consider the near-field region of the rotor as a semi-actuator disk *i.e.* a plane layer whose acoustic

impedance differs from the surrounding air. As the impedance changes, some sound will be reflected and some will be transmitted through the blade row. As the blade camber and thickness are not factored into the analysis, and an assumption is made of infinitesimal blade spacing, the problem case is one-dimensional. It was found that Mach flow and angle of incidence have a large impact on the transmission of waves through the cascade; as both are increased, sound transmission decreases. Increasing the stagger angle also decreases the transmissibility of the cascade.

Amiet and Sears [64] also investigated this scenario of sound propagation through a fan stage, under a different assumption that draws upon a classical, steady-flow lattice for an estimate of the forces on the blades using quasi-steady Prandtl-Glauert theory, and drew similar conclusions. Kaji and Okazaki [65] factored blade spacing in an additional study, and concluded that when the product of the free-field wavenumber and the blade spacing (ks) became large, many circumferential modes propagate as the transmitted wave. At high Mach numbers, blade spacing has little impact in the reflection and transmission curves found in the their earlier actuator disk analysis. Muir [66] extended the analysis of Kaji and Okazaki [63] to include a three-dimensional sound field at inlet, and the results show good agreement. In a companion paper [67], Muir expands this analysis for multiple blade rows which may be stationary (stator) or rotating (rotor) under the assumption of small blade spacing relative to the wavelength of the sound. Koch [68] also showed good agreement with the findings of Kaji and Okazaki in a study which applied the Wiener-Hopf technique to estimate the reflection and transmission properties of a cascade of blades.

Hanson [69] studied the effects of rotor/stator interaction noise caused by spinning modes from the rotor and the interaction of the rotor wakes with the stator blades downstream. Classical analysis methods had been applied to this problem previously [70, 71] which modelled the rotor-stator stage with 3 interface planes between the inlet, rotor, stator, and outlet. No transmission losses or reflections from other acoustic elements were assumed. Hanson treated each acoustic element in isolation using a simple input/output relationship, with the output from one element as the input for the next. The method used applies modal transmission and reflection coefficients to each element, coupled at the interface planes by solving a system of linear equations. Most relevantly for this study, Hanson's study also includes scattering into frequencies (BPF harmonic order) and modes

that are different from the input waves. Blade row scattering behaviour was computed with an adaptation of Smith's [72] flat plate cascade theory. It was observed that stators scatter input waves into many modes at the same frequency whereas rotors scatter on frequency and mode order.

Hanson highlights cases where the rotor reflection coefficient is greater than unity, and a mode at the rotor BPF travelling from the stator with unit sound power is reflected by the rotor with more than unit power at the second and third BPF harmonics. This phenomenon of mode trapping demonstrates that a fundamental BPF acoustic mode could be trapped in the swirl region between a rotor and stator, scatter into higher multiples of the BPF, and be amplified and released. Logue and Atassi [73] investigated the effect of blade geometry on these trapped modes and found that increasing the blade camber increases the bandwith of the trapped modes, and that trapped modes can be scattered on radial mode order through a stator.

The literature discussed in this sub-section has demonstrated that the modal content of incident noise is affected as it is transmitted through rotor-stator stage by both the rotor blades and stator vanes. This effect is largely dependent on the angle between each incident azimuthal mode and the angle of incidence of the blades/vanes. This needs to be a consideration for any experimental tests undertaken to investigate sum and difference scattering; any attempts to draw relationships between the SPL levels and modal content of any incident and scattered noise must also factor in the possibility that the modal content and SPL levels at the incident noise frequencies will be affected by the rotor-stator stage.

5.1.2 Scattering of Incident Noise at Sum and Difference Frequencies

Barry and Moore [74], in a general discussion of subsonic rotor alone noise, studied the spectral content of the noise emitted from one or several rotor stages and how it is conceived of as having a pure tone content at the blade pass frequency and its harmonics superimposed on a broadband spectrum. Tones may also be present at sum and difference frequencies relative to the blade-pass frequency tone and its harmonics. Possible sources of this modulation include blade vibration, rotor speed fluctuation, variations in

boundary layer thickness with position and/or time, irregularly positioned blades, blade-to-blade variations in tip clearances or stagger angle, and rotating intake distortions. It is this last point which is of interest for this current study. Barry and Moore consider the interaction of a particular intake distortion, which rotates with a steady circumferential speed, with a rotating rotor. This produces noise at frequencies of:

$$f_{scatt} = f + q f_{BPF} \tag{5.1}$$

where f is the frequency of the intake distortion, q is a non-zero integer denoting the scattering harmonic and f_{BPF} is the blade-pass frequency of the rotor. The modal content at each scattered frequency is predicted as being

$$m_{scatt} = m + qB \tag{5.2}$$

where q is again the scattering harmonic, B is the number of rotor blades and m is any azimuthal mode carrying energy by the incident noise. This assumes that there is little or no irregularity between blade forces and the interaction results in scattered noise with a supersonic phase velocity *i.e.* m_{scatt} is cut-on at the scattered frequency. If the incident noise was a downstream-travelling rotor BPF tone generated by an upstream rotor-stator, m will be restricted to Tyler-Sofrin values (see Section 2.4). If the incident noise were generated by an upstream mode generator (see Section 3.2 for more on targeted azimuthal mode generation), m will be restricted to the specific azimuthal mode excited by the mode generator.

Cumpsty [8] observed that when two rotor stages are present, as in a compressor for instance, tonal noise is apparent at sum and differences frequencies of the rotor blade-pass frequencies in downstream spectral measurements. Cumpsty studied this effect of frequency scattering by considering the variation of the time-domain acoustic pressure with respect to the circumferential coordinate, θ. Radial and axial effects were omitted. The author considered first a rotor with B_1 blades rotating at an angular velocity Ω_1 interacting with an inflow distortion of the form $\cos(m_i\theta)$. This inflow distortion is in the form of an azimuthal mode of order m_i, which spins as it propagates in the axial-direction. It was shown that rotor acoustic modes took the form:

$$p(\theta, t) = a_{m1} \exp(i(m_1\theta - h_1 B_1 \Omega_1 t)) \tag{5.3}$$

where $m_1 = n_1 B_1 - m_i$ and h_1 is the rotor blade-pass harmonic.

The author then demonstrates how, if this scattered pressure field were to propagate downstream and through a second rotor stage having B_2 blades rotating at Ω_2, the pressure pattern generated by the blades of this second rotor will be given by:

$$p(\theta, t) = B_2 a_m \exp(i[m\theta - (h_1 B_1 \Omega_1 \pm h_2 B_2 \Omega_2)t + \Phi_m]) \tag{5.4}$$

where the values for m are restricted to $m = \pm h_2 B_2 + m_1 = \pm h_2 B_2 + h_1 B_1 - m_i$.

Holste and Neise [45] also discuss the interaction case of two rotors and the subsequent scattered modes and frequencies, and made the same conclusions regarding predicted scattering frequencies and mode orders. Enghardt *et al.* [9] expanded for the case of two rotors and two stators, and suggested that scattering would occur and be measured at frequencies:

$$f_{scatt} = h_1 f_{BPF,1} + q f_{BPF,2} \tag{5.5}$$

with the modal content at each scattered frequency given by:

$$m_{scatt} = h_1 B_1 \pm q B_2 - k_1 V_1 - k_2 V_2 \tag{5.6}$$

where h_1 and $f_{BPF,1}$ are the blade-pass harmonic and blade-pass frequency of the upstream rotor, q is a non-zero integer denoting the scattering harmonic, $f_{BPF,2}$ is the blade-pass frequency of the downstream rotor, B and V are the number of blades and vanes at each rotor-stator stage and both k_1 and k_2 can take any integer value. The $\pm$ value in the modal scattering equation will be positive if the rotors are rotating in the same direction or negative if the rotors are counter-rotating.

5.1.3   Non-Linearity of Sum and Difference Scattering

Bennett and Fitzpatrick [6] undertook an investigation into the application of coherence-based noise-source identification techniques for the identification of combustion noise through a ducted system. The underlying assumption made with these identification

techniques is that the propagation path from source (*e.g.* combustor can) to receiver is linear. The authors considered non-linearities which may arise which would cause these techniques to fail to correctly attribute noise at a receiver location to its corresponding noise source. Siller *et al.* [75] noted a drop in coherence between acoustic pressure measurements at a combustor can and measurements at the exit plane of an aero-engine when the rotational speed of the rotor was increased. An interpretation of this result is that, as jet noise is low, combustion noise is a significant contributor to noise in the near field. As jet noise is increased, however, the relative contribution of the combustor is low and hence the coherence drops. This interpretation assumed a linear frequency response function between the combustor can and the exit plane of the engine. If there were non-linearities present, however, this could also explain the relative drop in coherence observed at higher rotor speeds.

The authors considered the case where fluctuating pressure propagates through a rotating turbine stage in an aeroengine. Such a pressure pattern could be tonal noise, such as that generated at the BPF of a second turbine located upstream of the turbine of interest, or narrowband (band-limited broadband) noise generated at a combustor upstream of the turbine of interest. The authors considered the possibility of interactions between the downstream propagating noise and the turbine, and that additional inputs to the system as shown in Figure 5.1, due to non-linearities, could cause the drop in coherence as measured by Siller *et al.*. In a non-linear system, a drop in coherence may occur when there is no change in the power of the linear noise sources. Without non-linear analysis the conclusion could be made that core noise is less significant than it is in reality, and hence be ignored in the development of acoustical treatment. It was demonstrated by the authors using basic trigonometric identities how quadratic interactions result in a doubling of frequency from self-interaction, and sum and difference frequencies from combination interactions.

Having proposed a non-linear interaction that could arise when downstream-going noise propagates through a rotor stage, the authors showed that energy scattered into sum and difference frequencies would not be identified using classical ordinary coherence-based techniques. They highlighted this by generating synthetic data representing a non-linear interaction between combustor noise and fan noise, as shown conceptually in Figure 5.2.
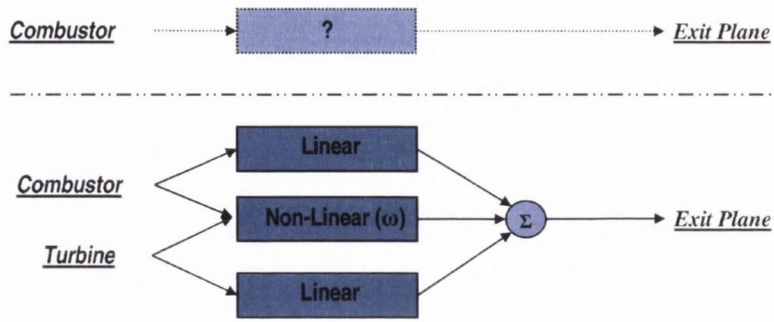
Figure 5.1: Frequency response function between the combustion noise and the pressure measured at the exit plane when some rpm dependent non-linearity is included in the model (from Bennett and Fitzpatrick [6]).

(a) Incident pressure upstream   (b) Incident pressure downstream
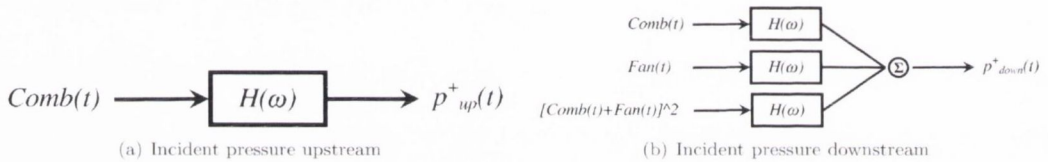
Figure 5.2: Incident pressure models accommodating a quadratic non-linear term (from Bennett and Fitzpatrick [6]).

Having concluded that non-linear interactions are not identified using the ordinary coherence function between noise measurements upstream and downstream of the rotor stage, the authors proposed a technique for identifying the non-linear component of the coherence between two such measurements, and hence separating the non-linear contribution from the linear contribution. By considering the model shown in Figure 5.3, where the underlying non-linear phenomenon is quadratic in nature, it was shown that the non-linear part of the output could be isolated by taking the ordinary coherence between the square of the input and the output.

A further consideration was then made by the authors to enhance non-linear coherence-based identification by conditioning out the linear effects between signals i and j, assuming that i and j are composed of at least two components each, one of which is the correlated linear effect r. Using the technique of Rice and Fitzpatrick [76], the partial coherence function between the two signals with the linear effects r removed can be isolated. This technique uses the partial coherence function, given by:

$$\gamma_{ij \cdot r}^2 = \frac{|G_{ij \cdot r}|^2}{G_{ii \cdot r} G_{jj \cdot r}} \quad (5.7)$$

where

$$G_{ij \cdot r} = G_{ij} - \frac{G_{ir} G_{rj}}{G_{rr}} \quad (5.8)$$

and

$$G_{ii \cdot r} = G_{ii} - \frac{|G_{ri}|^2}{G_{rr}} \quad (5.9)$$

which provides the input conditioned on the square of the input, *i.e.* the linear contribution.
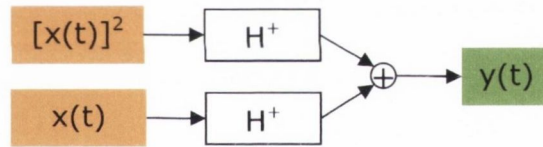
Figure 5.3: Inputs into upstream and downstream measurements modelled showing linear and non-linear parts (from Bennett and Fitzpatrick [6]).

This technique for identifying non-linear interaction was further enhanced by Bennett *et al.* [77] who proposed the enhanced non-linear coherence technique. From analysis of the expansion of $x^3(t)$ it was found that multiples of the same correlated terms appear which are also present in the expansion of $x^2(t)$. The proposal for an enhanced non-linear coherence technique was to condition the $x^3(t)$ contribution from $x^2(t)$ to removed these partially-coherent terms. As the expansion of $x^4(t)$ contains further terms not included in the $x^2(t)$ term, it was proposed that the partial coherence function was applied to condition $x^4(t)$ from $x^3(t)$, and then conditioning this result from $x^2(t)$.

The possibility of sum and difference scattering being the result of a non-linear (quadratic) interaction between the incident noise and the rotor has been observed in Section 4.3 using the non-linear coherence functions outlined above.

5.1.4   Research Questions

Previous research has indicated that sum and difference scattering occurs when noise (tonal or non-tonal) interacts with a downstream rotor stage. It was demonstrated that periodic noise generated by upstream rotors and tonal and broadband noise generated by loudspeakers may be scattered in this way.

Scattering through a single rotor-stator will be investigated in the following bench-top experimental test campaign. For this test set-up, the theory presented from the literature in Section 5.1.2 predicts that an incident tone will scatter at sum and difference frequencies:

$$f_{scatt} = f + q f_{BPF} \qquad (5.10)$$

with a dominant modal content given by:

$$m_{scatt} = m + (qB - kV) \qquad (5.11)$$

where q is a non-zero integer denoting the scattering harmonic. The modal content of these tones has not previously been studied experimentally. Unless the rotor blade count (B) is low or the frequency of modal decomposition is high (requiring many microphones), these scattered modes are predicted to occur outside the range of modal decomposition. The current literature therefore leaves many issues related to sum and difference scattering open for further experimental study, such as:

1. How do the magnitudes of the scattered tones compare with the magnitude of the tone at the incident frequency?

2. Previous experimental tests have observed that sum and difference scattering of tones and narrowband noise does not occur below a critical frequency. What is the explanation for this? Is this critical frequency linked to the cut-on frequency of certain mode orders as theory predicts?

3. It has been demonstrated that narrowband noise can also be scattered at sum and difference frequencies of the incident centre frequency. Is there a limit on the band-with of this effect for narrowband noise?

4. If the predicted scattering modes in Equation 5.11 are cut-on, do they dominate at these frequencies as predicted?

5. What is the modal content of these sum and difference tones when the predicted scattering modes are not cut-on at the corresponding sum and difference frequencies? Does any scattering occur in such conditions?

6. Does scattering occur through a stator stage as expected?

7. The results discussed in Section 4.3 and in the work by Bennett and Fitzpatrick [6, 23] have raised the possibility that sum and difference scattering arises as the result of a non-linear interaction between the incident noise and the rotor. Is this further verified in a more thorough experimental investigation?

The design of a bench-top experimental rig at TCD to answer these questions in presented in the rest of this chapter, and the subsequent experimental results discussed in Chapter 6.

5.2   Design of the Experimental Rig

The quadratic-interaction frequency scattering at source frequencies plus or minus the rotor BPFs, as introduced and discussed in Section 5.1, was clearly in evidence during the experimental tests from the TEENI test campaign in Berlin as outlined in Section 4.4. It would therefore seem like an excellent source of data to answer some of the questions outlined in Section 5.1.4. However, there are some issues with the set-up of the Berlin test campaign which make do not allow many of these questions to be answered.

During the TEENI test campaign, the amplification factor for the tonal tests where only the loudspeakers were present (the rotor was not rotating) was different to the amplification factor of the equivalent test where the rotor was also present. This higher amplification was necessary to ensure the tones were of sufficient magnitude to dominate above the higher broadband noise floor present when the rotor is rotating. This means that these two test scenarios cannot be investigated in order to compare the tonal energy when no scattering is occurring to the tonal energy when scattering is occurring, as the magnitudes of the tones generated will differ between tests.

Sum and difference scattering also occurred outside the range of modal decomposition in the TEENI tests, which may be linked to the dependence of the scattered modes on the number of rotor blades. The rotor used had 24 blades which would result in scattering into very high-order azimuthal modes (according to Equation 5.11), which will only propagate above cut-on at high frequencies.

In order to investigate the scattering of noise through a rotor stage, a new bench-top experimental rig was designed at TCD. The experimental rig was designed with the following parameters in mind, in order to avoid the issues which prevented an in-depth analysis using the TEENI test data:

- As in the Berlin test set-up, the new experimental rig consists of two noise-source regions; a rotor or rotor-stator stage and a loudspeaker array (mode generator).

- The new experimental rig has a rotor-stator stage which contains a lower number of rotor blades/stator vanes than were present in the Berlin experimental rig in order to minimise the scattered modal orders (m_{scatt}) to within a range for modal decom-

position. This assumes that the modal scattering model put forward in Equation 5.11 holds, and therefore m_{scatt} is dependent on both the number of fan blades and the modal content of the incident noise.

- In order to investigate any possible stator effects, the stator stage will be changeable.

- A reasonably constant source amplification will be maintained for all tests, so direct comparisons can be made between test points where the rotor is rotating or not.

- When investigating tonal noise scattering, tests will be undertaken for a wide range of frequencies, with a constant change in source frequency between tests. This change in frequency will be small enough to accurately observe the critical frequency above which sum and difference scattering occurs.

- The bandwidth of the narrowband noise (*i.e.* the bandwidth of the band-pass filter applied to broadband noise which is used to generate a narrowband signal) will be adjustable, and for each bandwidth a number of tests will be run for a range of centre frequencies to accurately estimate the previously observed [6, 62] critical frequency above which sum and difference scattering occurs.

In order to rectify the issues which prevented a thorough investigation of the sum and difference scattering phenomenon in the Berlin tests, the experimental parameters were carefully selected. The duct diameter was set at $0.1m$ to match a fan with the required low number of blades. A key design concern for the new rig was the number of microphones at the receiver bank and the number of loudspeakers located in the mode generator. An experimental rig requiring large numbers of either would be unfeasible as the required number of DAQ channels, microphones and loudspeakers increases. This limitation meant that the azimuthal mode order targeted by the loudspeaker array should be as low as possible, as higher-order modes require a larger number of loudspeakers to successfully target and excite (see Section 3.2).

Furthermore, the azimuthal mode order of any scattered modes should be as low as possible as higher order modes require more sensors to analyse; the azimuthal order m of any mode to be decomposed must also be less than or equal to $s/2$, where s is the number of acoustic sensors per axial ring. Figure 5.4 shows the modal cut-on frequencies for a

$0.1m$ diameter duct, assuming standard conditions for temperature and pressure and a quiescent fluid.
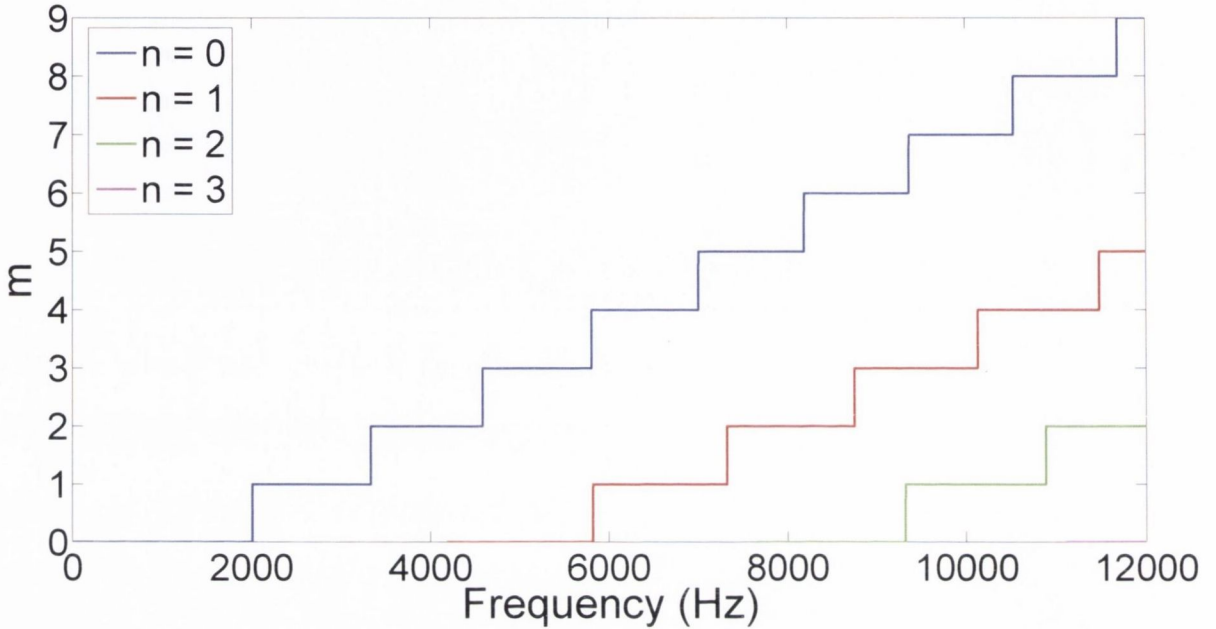
Figure 5.4: Modal cut-on frequencies for a $0.1m$ diameter circular duct. m is the azimuthal mode order index and n is the radial mode order index.

In order to extend the frequency range of possible modal decomposition, it was decided to use a single ring of all twenty-five available microphones. This allows an azimuthal modal analysis to be performed up to the $m = \pm 12$ azimuthal modes, but without the ability to separate out the incident and reflected components and the specific radial modes. In order to verify that an accurate modal analysis could be undertaken using a single ring of microphones, an experimental study was undertaken in Section 3.3. Provided the modal reflections were kept low, a single-ring of sensors could estimate the azimuthal modal amplitudes with a good degree of accuracy. Twenty-five electret microphones were available. Extending the range of modal decomposition to as broad a frequency range as possible is desirable as noise scattering is predicted to occur across several higher-order mode orders.

A mode generator has been installed in order to generate a tone at a specific frequency, with a specific targeted azimuthal mode dominating the acoustic pressure field at this frequency. This is analogous to the generation of a BPF tone by a rotor, where the azimuthal modal content of the generated tone is limited to azimuthal modes predicted

by Tyler-Sofrin theory [14]. This is achieved using a circumferentially-spaced array of five loudspeakers at a single axial location of the test duct. Each loudspeaker is housed in its own waveguide. Tonal noise propagates from each acoustic driver through the waveguide and into the main test duct through a hole in the duct wall. Assuming the noise is planar, the noise will radiate out equally in all directions, simulating a monopole source at the duct wall. By adjusting the phase between the loudspeakers, a specific azimuthal mode can be targeted by effectively adjusting the phase of these virtual monopole sources as per the following equation:

$$l = 0, 1, \cdots, S-1$$

$$q(\theta_l) = q_m e^{im\frac{2\pi l}{S}} \quad \text{where} \tag{5.12}$$

$$\theta_l = \frac{2\pi l}{S}$$

The theory of targeted mode generation is described in Section 3.2. The mode generator design and performance is discussed in further detail in Section 5.3.

The final experimental design is shown in Figure 5.5. The design of the experimental rig is similar to that used for the Berlin test campaign. The experimental duct is made of PMMA with an internal diameter of $0.1m$ with a wall thickness of $0.01m$. Semi-anechoic terminations were located at both ends of the duct in order to reduce end reflections. As outlined at the start of this section, the experimental rig was designed with two source regions; an array of five loudspeakers which mounted in a mode generator array, and an axial-fan-stator stage. The rotor used was a five-bladed EBM-PAPST standard vane-axial-fan which induces a flow in the positive x-direction when rotating. The stator stage adjacent to the fan has eight vanes. An additional fan with an alternative five-vane configuration which has been manufactured in-house using rapid prototyping was also available, in order to investigate stator scattering effects.

Full details of each aspect of this experimental set-up are discussed in the following sections. Section 5.3 discusses the design and performance of the mode generator. Both numerical simulations and experiments are performed, demonstrating the efficacy of the mode generator design. Section 5.4 discusses the vane-axial-fan used, and the characteristics of the noise generated by the fan for both stator configurations. Finally, the design
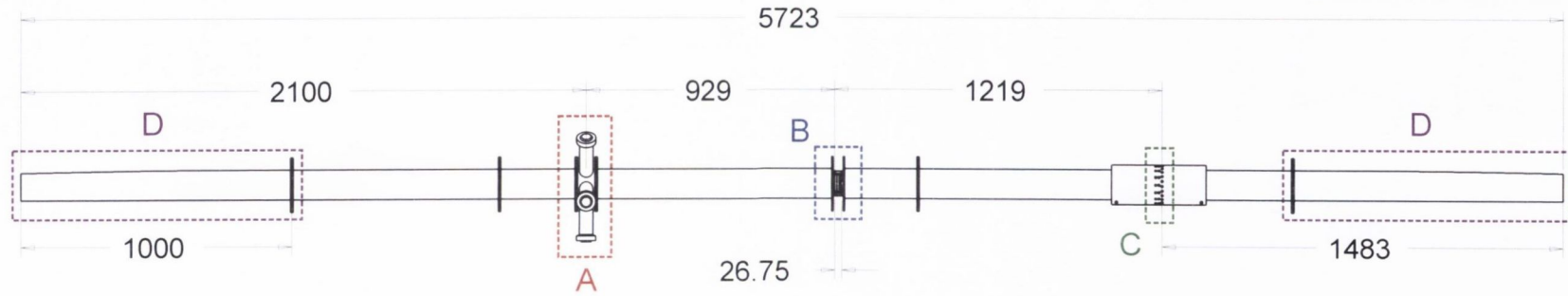
A = Mode Generator

B = Fan-Stator Stage

C = Microphone Array

D = Semi-Anechoic Terminations
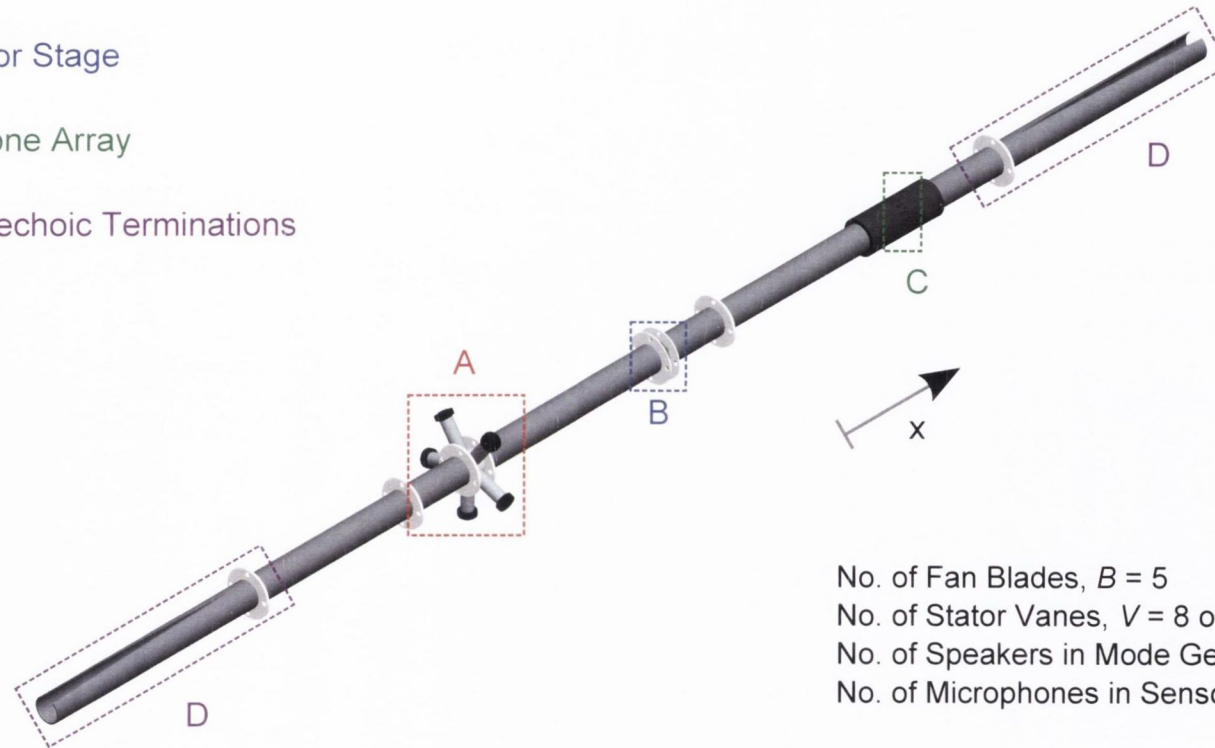
No. of Fan Blades, B = 5
No. of Stator Vanes, V = 8 or 5
No. of Speakers in Mode Generator = 5
No. of Microphones in Sensor Array = 25

Figure 5.5: Experimental rig used to investigate frequency and modal scattering at sum and difference frequencies (all distances shown in *mm*).

and performance of the semi-anechoic terminations located at both ends of the test duct
are discussed in Section 5.5.

Spectral analysis of the data from the data gathered during the experimental test
campaign will be limited by constraints such as the sampling frequency of the DAQ
system, the upper-limit of modal decomposition for the number of sensors used, and the
effective frequency range of the loudspeakers in the mode generator array. These frequency
constraints are collated in Table 5.1. Other frequencies of interest such as the rotor BPF
and its harmonics at the rotational speed investigated in Chapter 6, and the cut-on of the
three azimuthal modes targeted by the mode generator, are also presented.

The upper frequency of noise generation by the mode generator was set at $11kHz$.
This frequency was selected as $13kHz$ represents the upper limit of spectral analysis for
the sampling rate used, and sum and difference scattering is anticipated to occur at sum
and difference frequencies of $1083Hz$ (the fan BPF) relative to the noise generated by the
mode generator. Above $11kHz$, most of the noise scattered at sum frequencies relative
to the mode generator tone would therefore fall outside the range of spectral analysis.

Table 5.1: Key frequencies of interest for the bench-top experimental rig used to investigate sum and difference scattering of noise

Limits of Spectral Analysis	kHz
Data Acquisition Sampling Rate, f_{samp}	26
Nyquist Frequency for Data Acquisition, f_{nyq}	13
Upper Limit of Modal Analysis	18.583
Rotor BPF and Harmonics at 13000rpm	**kHz**
BPF1	1.083
BPF2	2.166
BPF3	3.249
BPF4	4.332
Effective Range of Mode Generator	**kHz**
$m = 0$ Mode is Cut-on	0
$m = 1$ Mode is Cut-on	1.998
$m = 2$ Mode is Cut-on	3.335
Effective Range of Speakers	$2 - 30$
Upper Limit of Noise Generation	11
Upper Limit of Waveguide Design (see Sec. 5.3.1.1.)	11.549

5.3   Mode Generator Design and Performance

In order to facilitate the investigation of azimuthal mode scattering through a fan stage, it is necessary that any incident noise propagating through the fan stage has clearly defined modal content, with a single azimuthal mode dominating. This allows clear relationships to be found between the modal content at any scattering frequencies and the incident modal content. The mode generator is an array of loudspeakers, each of which is housed in its own waveguide. Each waveguide allows the sound to radiate from the loudspeaker and into the main test duct through a hole in the test duct wall. The sound should radiate through this hole in a planar fashion with as little azimuthal or radial distortion as possible, therefore simulating a spherical source or monopole.

The waveguides are equi-azimuthally spaced at a single axial location of the main test duct. By generating sine waves at a desired frequency f using all loudspeakers, with a phase difference ϕ between each loudspeaker and its neighbours, a specific azimuthal mode can be excited by the array of the mode generator at frequency f as per Equation 3.7. Therefore a tone at frequency f will propagate in the main test duct with a prescribed azimuthal mode dominant at this frequency. Further information on the theory of the mode generator operation, as well as analytical validations of the technique, can be found in Section 3.2.

Each loudspeaker mounting (waveguide) is required to support the acoustic driver and allow sound to radiate from the driver into the test duct. The key design issues which must be overcome are:

- the mounting must be designed so that the five loudspeakers used can physically fit around the periphery of $0.01m$ diameter duct. This will constrain the length and diameter of the mounting.

- the diameter of the opening of the mounting at the loudspeaker end must be such that it matches the diameter of the loudspeaker membrane (1" or $25.4mm$).

- the flange diameter at the loudspeaker end must match the mounting of the loudspeaker end.

- no higher-order modes can be cut-on inside the mounting at the highest test frequency of $11kHz$. This limits the inner diameter of the waveguide.

- if a simple cylindrical duct design is used, harmonics of the longitudinal resonance frequencies must be accounted for. This will constrain the length of the duct.

- the mounting must be strong enough the support its own weight and the weight of the loudspeaker, and must be rigidly fixed at both loudspeaker and duct ends so that vibration does not occur and cause acoustic resonances in the test duct.

Each loudspeaker is housed at one end of a waveguide which connects the loudspeaker to the test duct. A conical, exponential or catenoidal shaped horn design would have been desirable as they better match the impedance of the loudspeaker membrane with the fluid as well as improving the transmissibility at the interface between the waveguide and the main test duct. However, due to space constraints a circular cross-sectioned design was used. The final waveguide design consists of two circular cylinders of different diameters connected end-to-end to each other. The cylinders' diameters are set by two design constraints: the waveguide must match the loudspeaker voice coil diameter, but must also be constrained such that no higher-order acoustic modes are cut-on inside the waveguide for the test frequencies planned.

In order to prevent higher-order modes being cut-on inside the waveguide, the diameter of the waveguide must be set below a maximum value such that the Helmholtz number, kR, does not exceed 1.83 at the highest test frequency planned ($11kHz$). A kR value of 1.83 corresponds to the cut-on frequency of the first higher-order acoustic mode. As this corresponds to a critical diameter which is less than the diameter of the loudspeaker voice coil, the waveguide must step from a larger diameter to a smaller diameter. The final waveguide design is shown in Figure 5.6.

BMS 4540ND neodymium compression drivers were selected as the acoustic drivers for each waveguide. This acoustic driver had been selected due to its linear response for a wide frequency range ($2kHz$–$30kHz$), its low weight (0.53 kg), compact design and high power capacity (60W). This driver is also threaded, allowing the waveguides to be designed with a tapped open end so that the loudspeaker can simply be screwed into each waveguide.
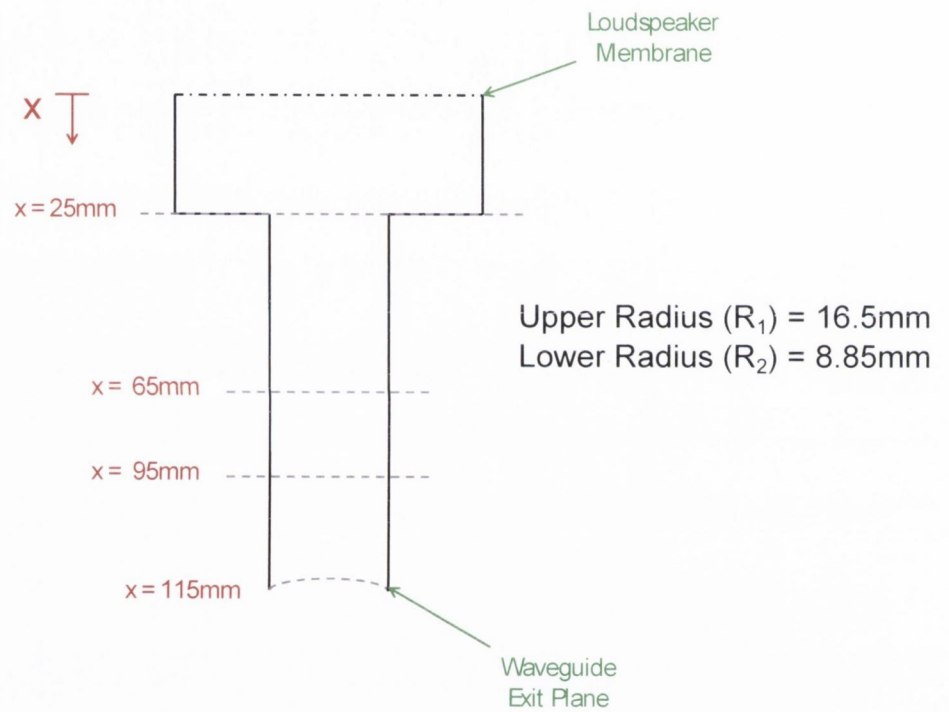
Figure 5.6: Schematic of waveguide design. The cross-sectional geometry is circular throughout. In the prototype design microphone holes were located at $x = 65mm$ and $x = 95mm$.

5.3.1 Numerical Simulations

In order to investigate the acoustic performance of the proposed waveguide design shown in Figure 5.6, as well as a mode generator consisting of five such waveguides in an array, a series of numerical simulations were performed. The numerical scheme used was the WEM (Wave Element Method), a full-domain discretisation technique which allows acoustic analyses to be performed on non-homogeneous geometries subject to a range of boundary conditions by solving of the Helmholtz equation. A detailed description of this technique can be found in Appendix A. The Wave Element Method had previously been applied to duct acoustics investigations by Bennett *et al.* [78] and shown to perform very well in comparison to analytical methods.

5.3.1.1 Single Waveguide

To simulate a loudspeaker membrane, a Neumann (velocity) boundary condition was applied at the $x = 0$ plane of the waveguide design shown in 5.6. Each source node is in phase with each other. The volume was meshed with a tetrahedral mesh with a maximum mesh spacing of $2mm$, ensuring that 8 nodes are located per acoustic wavelength at the highest test frequency of $18kHz$.

The objective of investigating the pressure field generated inside the waveguide is to ensure that no higher-order acoustic modes are cut-on inside the narrow section of the waveguide, and that sound propagates from the loudspeakers to the test duct as plane waves. If the sound radiating from the interface between the waveguides and the test duct is planar, the sound will radiate out equally in all directions, best approximating a monopole source.

Figure 5.7 demonstrates the pressure field generated in the waveguide when a Neumann boundary condition is applied at $x = 0$ for a range of frequencies. The test Helmholtz numbers kR are taken with the main test duct geometry as reference, giving $R = 0.05m$. Inside the waveguide the radii are far smaller. The radius at the wider portion of the waveguide, R_1, is $0.0165m$. The radius of the narrower section of the waveguide, R_2, is $0.00865m$. A comparison of the Helmholtz numbers for each test frequency is shown in Table 5.2. This means that higher-order modes can be cut-on inside the main test duct, therefore allowing higher-order modes excited using the mode generator array to

propagate in the main test duct without these higher-order modes being cut-on inside the waveguides themselves. However, there is a possibility that higher-order modes could be cut-on inside the wider section of the waveguide but not the narrower section. At a test Helmholtz number $kR = 7$, for example, this is the case; the Helmholtz number inside the wider section of the waveguide is $kR_1 = 2.31$, which is above the cut-on frequency of the ($\pm$1,0) modes. Since these modes are not cut-on inside the narrower section, it is anticipated that they will rapidly decay with axial distance, and the pressure field will still be planar at the interface between the waveguide and the main test duct. The visualisation of the pressure field generated inside the waveguide shown in Figure 5.7 would seem to indicate that the pressure field is planar inside the narrow section of the waveguide for each frequency tested.

Table 5.2: Helmholtz numbers in the main test duct (kR), the wider section of the waveguide (kR_1) and the narrower section of the waveguide (kR_2) for the numerical simulations shown in Figures 5.7 – 5.9.

kR	kR$_1$	kR$_2$
3.5	1.155	0.595
5	1.65	0.85
5.55	1.83	0.94
7	2.31	1.19

In order to provide strong evidence that the noise propagating in the narrow section of the waveguide remains planar for all test frequencies up to the cut-on of the first higher-order mode at $kR_2 = 1.83 = 11549 Hz$, a modal decomposition was performed using the numerical data. Sixty-four nodes are located in four axial rings, with each containing sixteen circumferentially-spaced nodes. The complex pressures measured at each of these nodal locations were used to perform a radial modal decomposition of the pressure field inside the narrow section of the waveguide, as per the modal decomposition technique applied by Bennett [23] and outlined in Section 3.1. The axial locations of the rings of sensors inside the narrow section of the waveguide at $x = 0.08m, 0.1m, 0.12m, 0.14m$.

Pressure field simulations were made across a wide range of kR values and the modal amplitudes were determined for each test frequency. The resulting modal amplitudes are plotted in Figure 5.8. The (0,0) mode is plotted in red. These results clearly show that the (0,0) mode is dominant inside the narrow section of the until the cut-on of the ($\pm$1,0)

modes inside the narrow section, at a Helmholtz number $kR_2 = 1.83$ inside the narrow section of the waveguide and $kR = 10.76$ inside the main test duct.

In the numerical tests discussed above, a Neumann boundary condition was applied at the $x = 0$ plane with all source nodes in phase. This is a best case scenario for modelling the loudspeaker membrane, in that it acts as a vibrating piston at the top of the waveguide, an action that would intrinsically target the (0,0) mode as the source membrane acts as a vibrating plane. In order to offer a "worst-case" scenario, a simulation model was used wherein all source nodes are phase adjusted such that the first azimuthal mode is targeted at the source plane. This would cause a stronger generation of the (1,0) mode in the wider section of the waveguide above its cut-on at $kR = 5.55$, which would increase the likelihood of this higher-order mode not decaying in the narrower section of the waveguide, and hence radiating into the main test duct, reducing the efficacy of the waveguide design.

In order to ensure that the waveguide design operates suitably in this scenario, the method undertaken to measure the modal amplitudes shown in Figure 5.8 was repeated for this alternative Neumann boundary condition. Changing the Neumann boundary condition does lead to a marked increase in the amplitude of the (1,0) mode above cut-on, as shown in Figure 5.9. The effective cut-on of the (1,0) mode does decrease slightly, showing that the stronger generation of the (1,0) mode in the wider section of the waveguide does cause the higher-order mode to propagate at lower than expected frequencies in the narrow section. This shift in cut-on is very minor however, of the order of $30Hz$, and therefore the waveguide still performs well in the event that the (1,0) mode is somehow strongly excited by the loudspeaker membrane.

5.3.1.2 Full Speaker Array

The waveguide design shown in Figure 5.6 and investigated numerically in Section 5.3.1.1 was shown to perform as intended, with plane wave radiation for all test frequencies of interest. In order to assess the suitability of the waveguide design for use in a mode generator array, a full array of five waveguides connected to a $0.7m$ length section of main test ducting was meshed for investigation using WEM. Five waveguides were used as no more could be fit around the periphery of the test duct. As in the single waveguide tests,
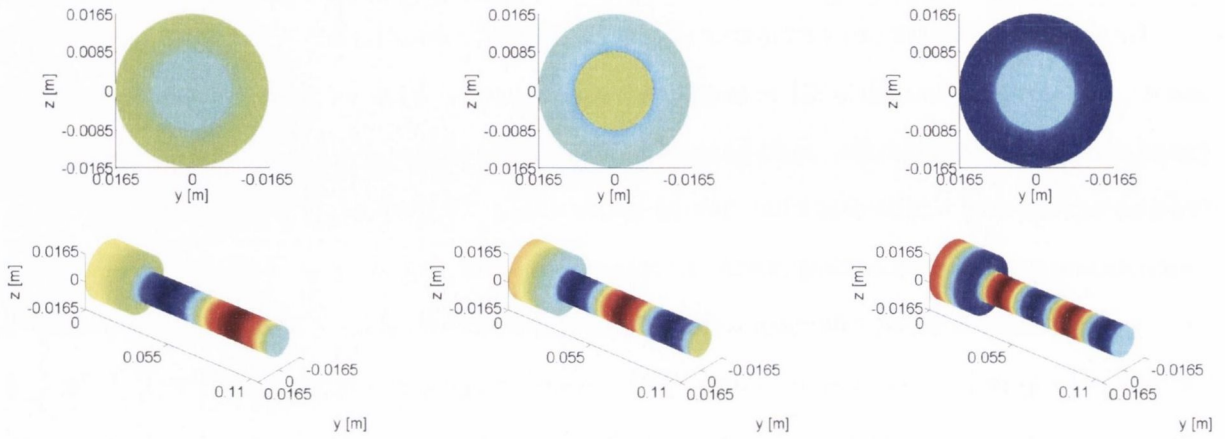
Figure 5.7: Real part of pressure fields generated in a single waveguide by a simulated loudspeaker membrane at the $x = 0$ plane. From left to right the test frequencies are $kR = 3.5, 5, 7$. The top sub-figures shown an end-view of the waveguide, the bottom figures shown an oblique view. All source nodes at $x = 0$ are in phase with each other.
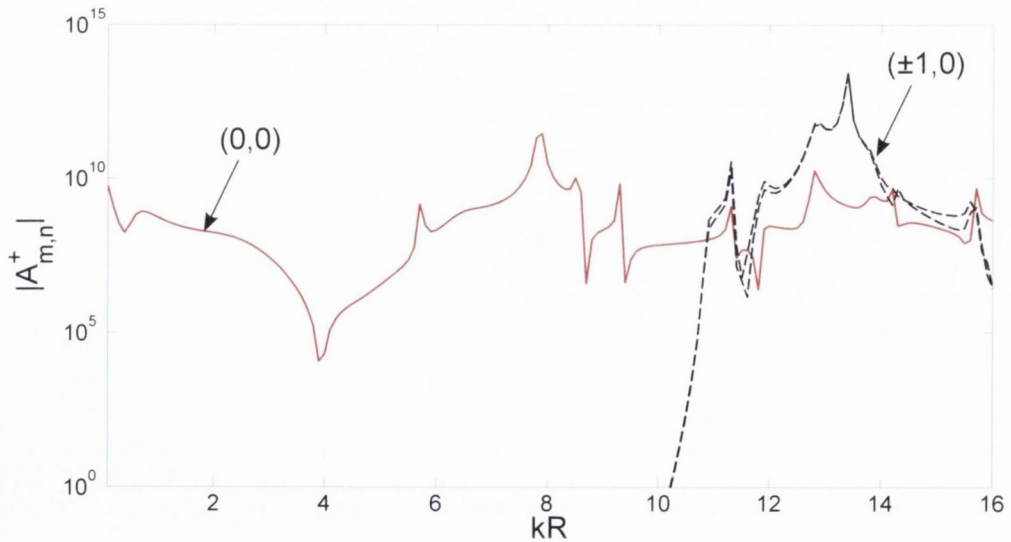
Figure 5.8: Radial modal analysis performed using 64 sensors in an array, located in the narrow part of the waveguide (R_2). A simple Neumann condition has been applied at the $x = 0$ plane with all source nodes in phase.
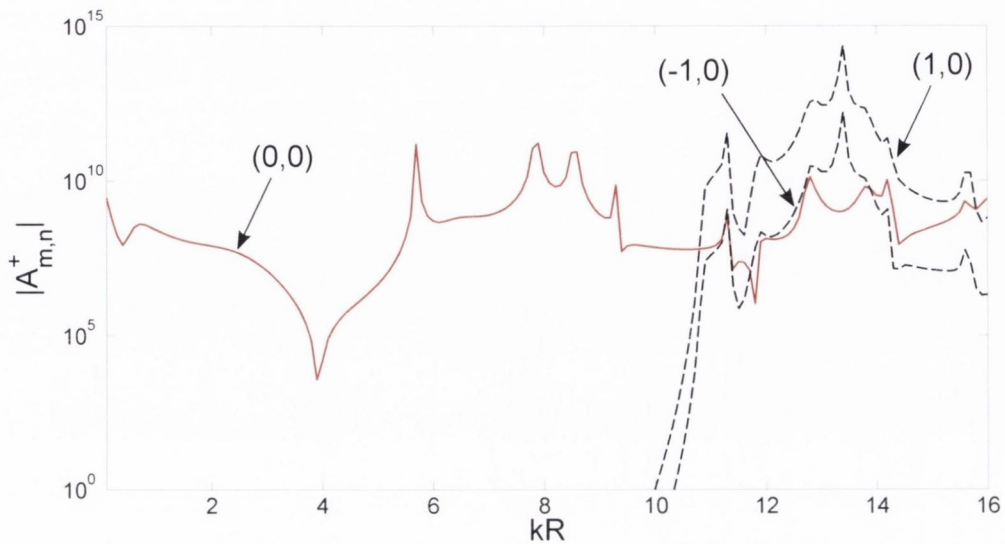
Figure 5.9: Radial modal analysis performed using 64 sensors in an array, located in the narrow part of the waveguide (R_2). An alternative Neumann condition has been applied at the $x = 0$ plane, targeting the $m = 1$ mode.

a Neumann boundary condition was applied at the entrance plane of each waveguide, and the source nodes within each waveguide are in phase with each other. However, a phase difference was set between each of the five source planes in accordance to Equation 3.7. This means that the sound radiating out of each of the waveguides can be set out of phase with the neighbouring waveguides. This sound radiates out the waveguides as plane waves, and therefore the interfaces between the test duct and the exits of the waveguides simulate monopole sources. By applying this phase difference between the five monopole sources, specific azimuthal modes can be targeted and therefore excited in the main test duct. These targeted modes should dominate the acoustic pressure field inside the main test duct.

Figure 5.10 demonstrates this concept. In each sub-figure noise has been generated by Neumann boundary conditions applied at the entrance plane to each of the waveguides at a frequency $kR = 3.5$. Different phase relationships were applied between the loudspeakers in each case, targeting three different azimuthal modes. The amplitude and phase plots of the pressure fields clearly show that the targeted modes dominate, with a planar acoustic field evident when the $m = 0$ azimuthal mode has been targeted and spiral-patterned pressure fields evident when higher-order azimuthal modes have been targeted.

An investigation of the efficacy of the mode generator array over a range of test

frequencies was conducted by performing a radial mode decomposition inside the main test duct, in order to deduce the modal amplitudes and therefore asses the dominance of the targeted modes. The analytical study undertaken in Section 3.2 showed that in order target a specific azimuthal mode in a duct, $N_{SRC} = (2 \times \text{TAM}) + 1$ sources are required to successfully excite the targeted azimuthal mode (TAM) at cut-on. For the targeted mode to dominate at higher frequencies beyond cut-on, an additional source must be added per additional cut-on azimuthal mode.

Figures 5.11 – 5.13 show the results from a radial modal decomposition performed using sixty-four nodes located in four axial rings located at $x = 0.4m, 0.42m, 0.44m, 0.46m$ over a range of test frequencies for three targeted azimuthal modes. The targeted azimuthal modal amplitudes are shown in red in each case. The analytical study would suggest that given $N_{SRC} = 5$ and $\text{TAM} = 0$, the targeted mode will dominate for all frequencies up until the cut-on of the $m = 5$ azimuthal mode at $kR = 6.32$. The numerical test results shown in Figure 5.11 generally corroborate the analytical simulation results, however the numerical results suggest that the $m = 0$ mode will in fact dominate at some frequencies above the frequency range in which analytical simulations predicts it will be effective. This is also the case for the $m = 1$ and $m = 2$ modes; when targeted, they dominate the acoustic pressure field for several frequencies beyond the maximum frequencies anticipated in Figure 3.7. A marked decrease in performance is generally observed for higher frequencies however.

The numerical simulations have demonstrated that the mode generator design is effective for a wide range of possible test frequencies, and is therefore likely to be effective for use in the experimental study undertaken in Chapter 6. One key limitation to these tests has been that the effect of a mean flow in the test duct has not been accounted for, despite the fact that a mean flow will be present in the experimental tests. As well as generating flow noise which will lower the signal-to-noise ratio of any acoustic pressure measurements and affecting the modal cut-on frequencies through modification of the axial wavenumbers, inducing a flow in the duct will also affect the directivity of the sound field radiating from each waveguide. This will in turn affect the assumption of equal sound being radiated in every direction from each waveguide exit, which will lower the efficacy of the mode generator as the assumption that a monopole source is simulated at each waveguide exit is violated.
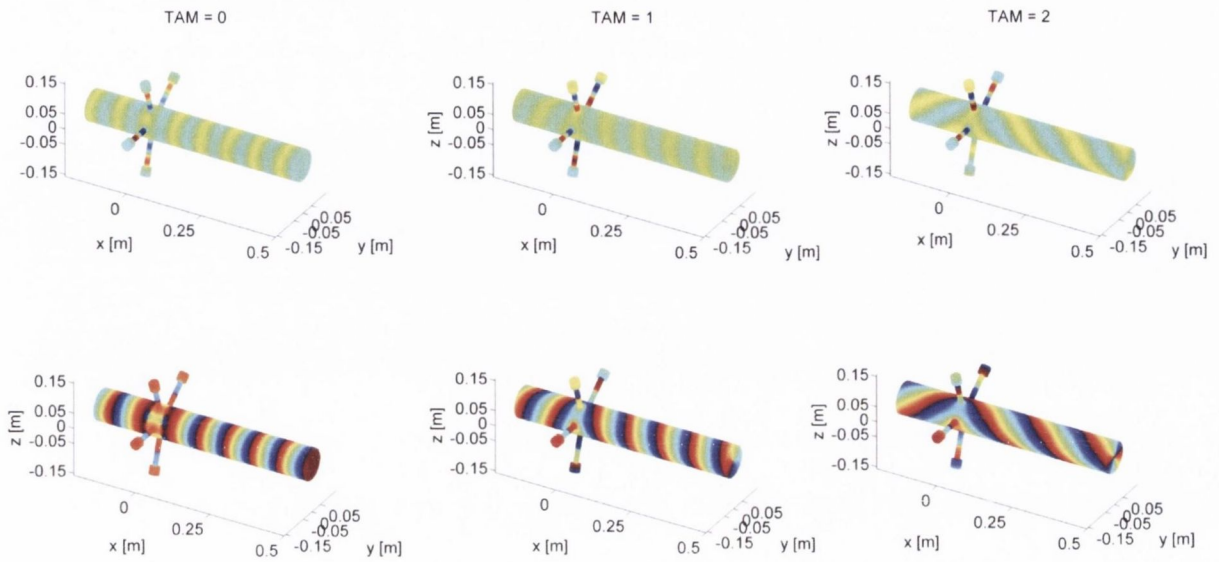
Figure 5.10: Amplitude (top) and phase (bottom) plots of WEM generated pressure field in a cylinder by five simulated loudspeaker membranes, each at the end of a waveguide, located at $x = 0$. Test frequency, $kR = 3.5$. Different azimuthal modes are targeted by adjusting the phase relationship between the sources.
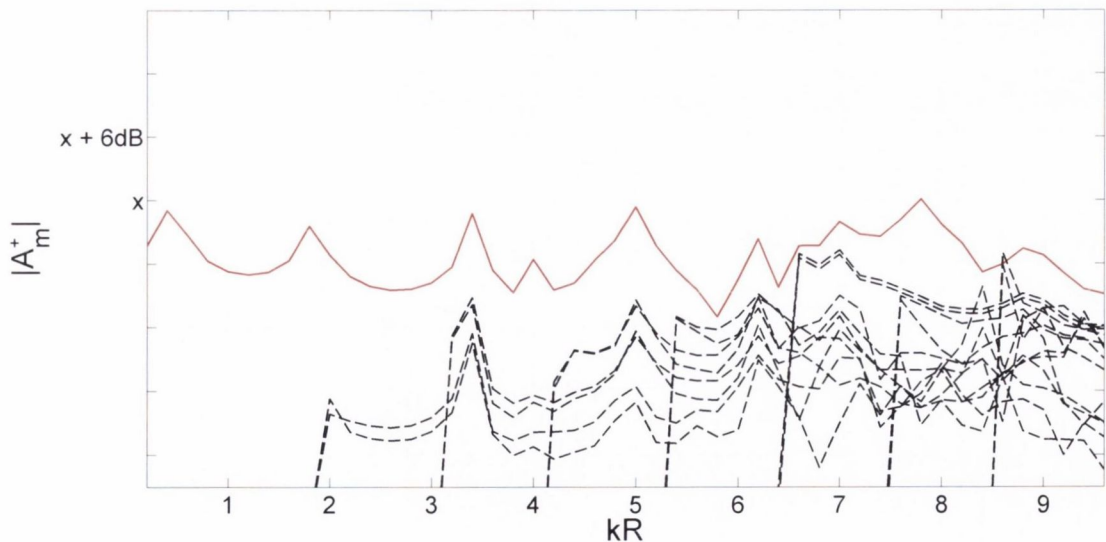
Figure 5.11: Azimuthal modal amplitudes estimated using a radial mode analysis performed using a four rings of 16 virtual receivers each. The receivers located at the wall of the test cylinder shown in Figures 5.10. The ring of sensors is located at $x = 0.4m, 0.42m, 0.44m, 0.46m$. The $m = 0$ mode has been targeted by the mode generator.
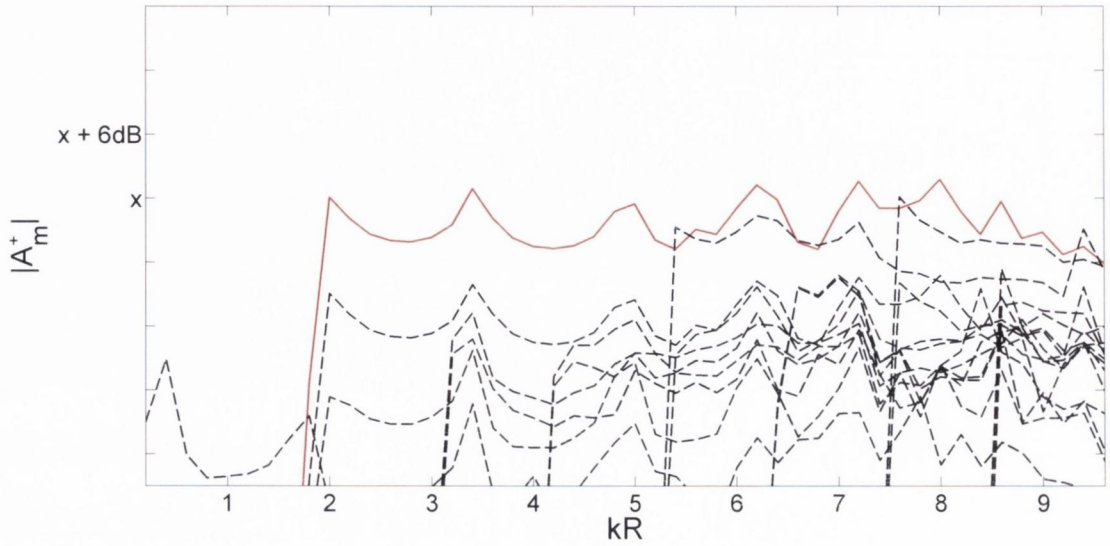
Figure 5.12: Azimuthal modal amplitudes estimated using a radial mode analysis performed using a four rings of 16 virtual receivers each. The receivers located at the wall of the test cylinder shown in Figures 5.10. The ring of sensors is located at $x = 0.4m, 0.42m, 0.44m, 0.46m$. The $m = 1$ mode has been targeted by the mode generator.
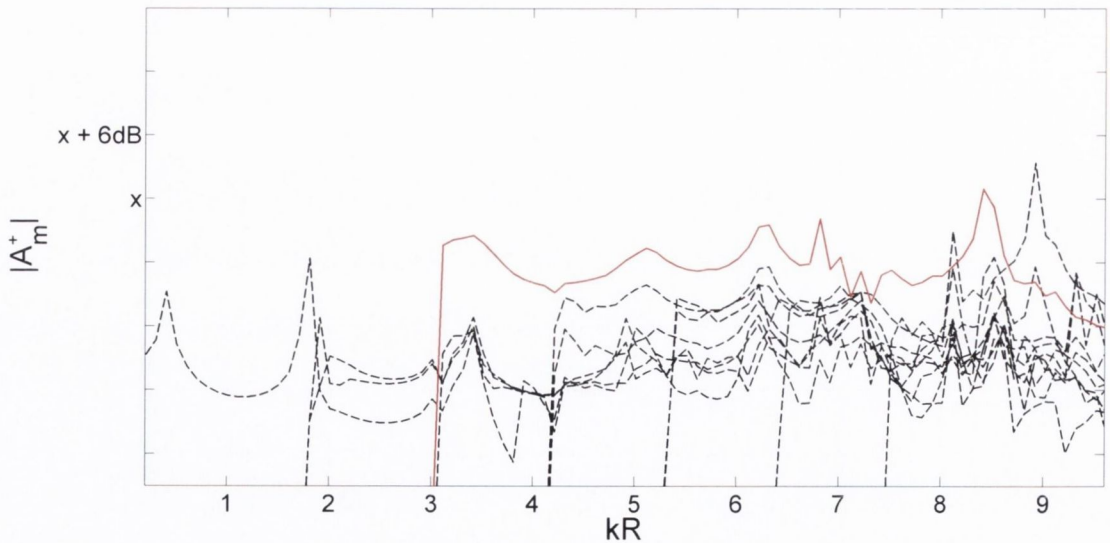
Figure 5.13: Azimuthal modal amplitudes estimated using a radial mode analysis performed using a four rings of 16 virtual receivers each. The receivers located at the wall of the test cylinder shown in Figures 5.10. The ring of sensors is located at $x = 0.4m, 0.42m, 0.44m, 0.46m$. The $m = 2$ mode has been targeted by the mode generator.

5.3.2   Waveguide Prototype Tests

As shown in Figure 5.6, the prototype design of the waveguide has two microphone holes at the same azimuthal location with an axial-distance of $30mm$ between each hole. The prototype design consists of the final waveguide design connected to a short section of duct ($0.1m$ in length) with the same radius as the main test duct to be used in the noise scattering test campaign ($0.05m$). The duct is open at both ends. A BMS 4540ND loudspeaker was mounted at one end of the waveguide and generates broadband noise. If no higher-order modes are present, the estimated transfer function between two microphone measurements in the waveguide should be linear phase, with little or no distortion evident in the magnitude or phase of the transfer function. This is the case as the distribution of acoustic pressure in the waveguide is planar, with the acoustic pressure only changing in the axial direction. Above the cut-on frequency of the first azimuthal mode, some distortion of the magnitude and phase of the transfer function is expected, as the distribution of acoustic pressure in the duct becomes more complex than simply planar. Data was acquired at a sample rate of $40kHz$. Broadband noise is generated by the loudspeaker at all frequencies below $20kHz$.

The transfer function can be used to assess the accuracy of the assumption that no higher modes are cut-on in the waveguide. The transfer function can also be used to assess other acoustic properties in the waveguide, such as the reflectivity, transmissibility and impedance of the passive end of the waveguide, using the theory outlined in Seybert [79] and Chung and Blaser [80]. The assumption is made that the random excitation at the active end of the waveguide is a stationary random process.

The magnitude and phase of the transfer function of the waveguide is shown in Figure 5.14. In this test scenario the small section of test duct has been packed with rock wool. Rock wool absorbs acoustic energy, and therefore reflections from the waveguide will be minimised. The magnitude of the transfer function between measurements made at two axial locations is predicted as being unity for all frequencies if end reflections are eliminated. The magnitude of the measured transfer function is close to unity, but fluctuates slightly, most likely due to the rock wool not acting as a perfect acoustic damper. The anticipated cut-on frequency of the first higher-order acoustic mode within the narrow
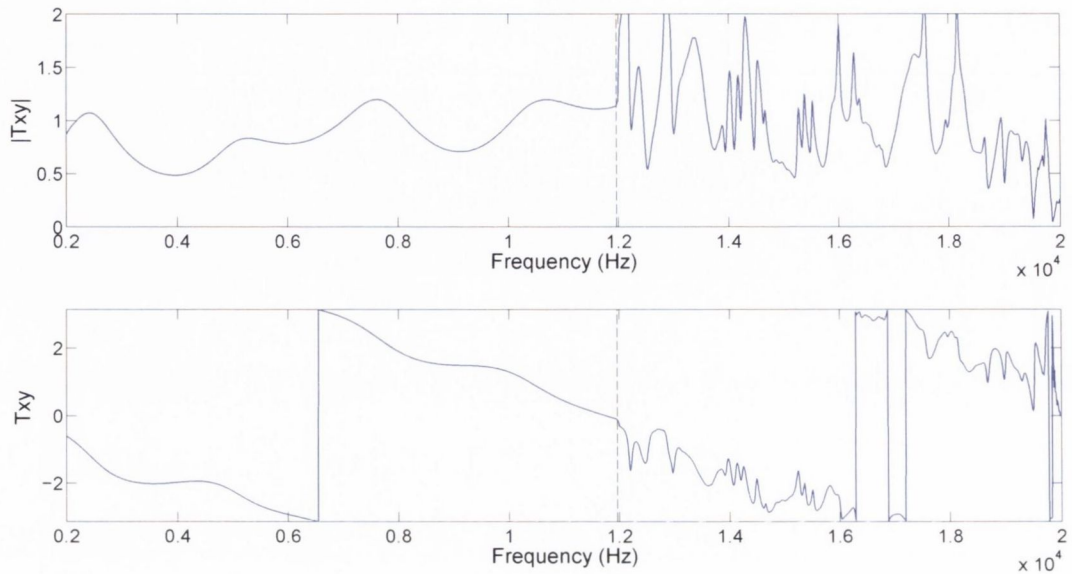
Figure 5.14: Transfer function measured between two microphones located at $x = 65$mm and $x = 95$mm, flush-mounted to the inside of the prototype waveguide, at the locations shown in Figure 5.6. The black-dashed line at around $11.8kHz$ corresponds to the cut-on of the first higher-order acoustic mode.

section of the waveguide is shown using a black dashed line. Up to this frequency, the phase of the transfer function is linear phase, as expected for a planar pressure distribution inside the waveguide with low/no reflections.

It is clear that the characteristics of the magnitude and phase of the transfer function both change significantly at the cut-on frequency, with the onset of large amounts of distortion beyond this frequency. This would imply that beyond this frequency, higher-order modes will be present in the waveguide, and the distribution of pressure at the waveguide exit will not be planar. This would result in a non-uniform distribution of acoustic pressure at the exit plane, which would not act as a spherical source at the wall of the test duct. It is therefore anticipated that the mode generator will not operate effectively above this frequency. Up to this frequency however the lack of significant distortion in the magnitude and phase of the measured transfer function is positive, strongly suggesting that acoustic transmission from the narrow section of the waveguide and into the test duct is planar, which will best simulate a monopole at the interface between the waveguide and the test duct.

5.3.3   Experimental Mode Generator Performance

The final mode generator assembly is shown in Figure 5.15. It consists of five waveguides, each of the design shown in Figure 5.6 (without microphone holes) mounted on a short section of flanged duct. This duct is connected to other sections of duct as part of the final experimental rig design shown in Figure 5.5. This modular design was used as it would allow the mode generator's axial location to be changed easily, as well as allowing the mode generator to be re-used in future test configurations.
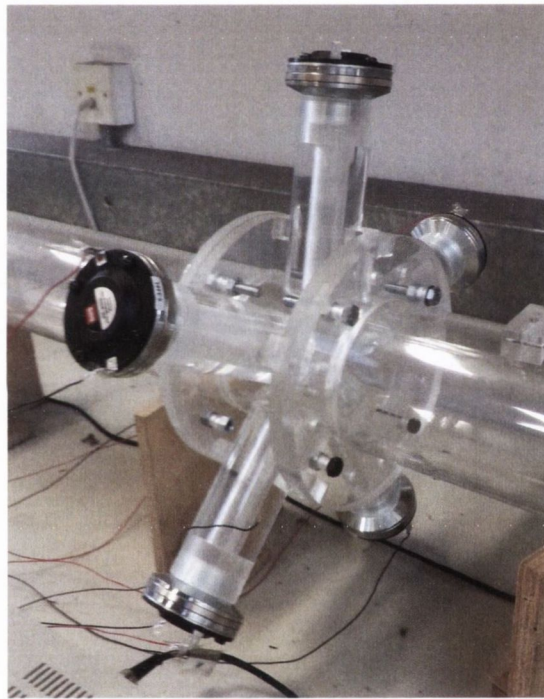
Figure 5.15: Mode generator array consisting of five loudspeakers in individual waveguides connected to a section of the main test duct.

In order to assess the effectiveness of the mode generator, a simple experimental procedure was undertaken. The mode generator was designed such that the targeted azimuthal mode (TAM) generated at the loudspeaker array could dominate inside the test duct. The effectiveness of the mode generator is defined as the dominance (in amplitude) of the azimuthal mode targeted at the mode generator above any other azimuthal modes which are present (cut-on) at the test frequency examined. The experimental rig was set up with the mode generator, vane-axial-fan and sensor array in place, as per Figure 5.5. The fan was in place but not rotating. At each test point a tone was generated at the mode generator

with a specific phase relationship between each loudspeaker. The 25 microphones in the sensor array measure the resulting acoustic pressure at a single axial location in the duct for 10 seconds at a sampling frequency of $26kHz$. This test procedure was repeated for the targeting of three different azimuthal modes ($m = 0, 1, 2$). These three test points were repeated at a range of tonal frequencies from $2kHz$ up to $10kHz$, with a $50Hz$ resolution between tests.

Figure 5.16 shows the results of an azimuthal modal analysis performed at the sensor array when different azimuthal modes are targeted at the mode generator array. Two test frequencies are shown; one at a relatively low frequency ($4000Hz$) where only the modes being targeted are cut-on, shown as sub-figure a). The mode generator performs well at this frequency with each targeted mode dominant by around $10dB$. The other test point, shown in sub-figure b), is at a higher test frequency of $5600Hz$ where the $m = \pm3$ azimuthal modes are also cut-on. The mode generator is shown to be effective at this frequency also despite the presence of several higher-order modes. This demonstrates that even at frequencies above which other higher-order modes are cut-on the mode generator can still operate effectively.
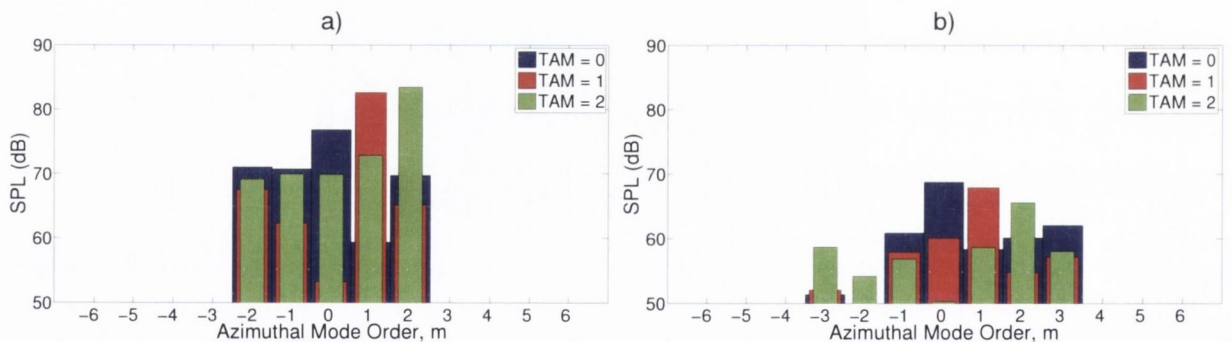
Figure 5.16: Azimuthal modal analysis of mode generator tone generated at two test frequencies; a) $4kHz$, b) $5.6kHz$

The dominance of each targeted mode with non-dimensional frequency (kR) is plotted in Figures 5.17 – 5.19. The blue spectra show the dominance in amplitude (denoted Λ_{TAM}) of each targeted mode above the second most dominant mode present at each corresponding test point. At the points where this dominance drops below zero, the targeted mode is not the dominant mode. In these cases the plot shows how many dB the amplitude of the targeted mode falls *below* the amplitude of the most dominant mode

at that test frequency. The higher horizontal black-dashed line in the plot corresponds to a dominance level of $6dB$, which corresponds to the point at which the amplitude of the targeted mode is double that of the next most dominant mode present at the corresponding test frequency.

It is desirable that each targeted mode dominate by at least $6dB$ at as many frequencies as possible. The purpose of the mode generator is to "prescribe" a known acoustic pressure distribution in the duct by exciting a specific azimuthal mode at a given frequency. Viable test frequencies for testing the effect of modal scattering through the fan stage will therefore correspond to test frequencies where several modes targeted at the mode generator are dominant by at least $6dB$. Figures $5.17 - 5.19$ show that several such test frequencies exist. However, as the test frequency is increased the performance of the mode generator generally decreases. This has been anticipated by both the analytical study in Section 3.2 and the numerical study of the mode generator design undertaken in Section $5.3.1.2$. For example, the decrease in effectiveness when targeting the $m = 0$ mode above the cut-on of the $(5,0)$ mode is in line with both the previous analytical and numerical studies.

Tapken and Nagai [81] discuss possible causes of spill-over modes $i.e.$ modes excited by a mode generator other than the targeted mode. Such effects could include variations in loudspeaker impedance with frequency, variations in the transmissibility of the waveguides with frequency, the curvature at the interface between the waveguide and the main test duct, and any distortion of the acoustic source at each waveguide exit which will affect the validity of the monopole assumption (as caused by axial-flow distortion, for example).

The red spectra in Figures $5.17 - 5.19$ show the Λ_{TAM} values measured when the mode generator targets a specific azimuthal mode, and the fan is rotating at 13000rpm. As discussed in Section $5.1.1$, the modal content of the noise generated by the mode generator array will be modified, with variations in the transmission and reflections coefficients depending on the angles of incidence of the noise, the Mach number of the flow and other factors. The axial mean-flow will also affect the modal cut-on frequencies by modification of the axial wavenumbers. These spectra show that although the presence of a rotating fan does affect the performance of the mode generator, this impact is not significant and the range of effective frequencies is not greatly reduced.
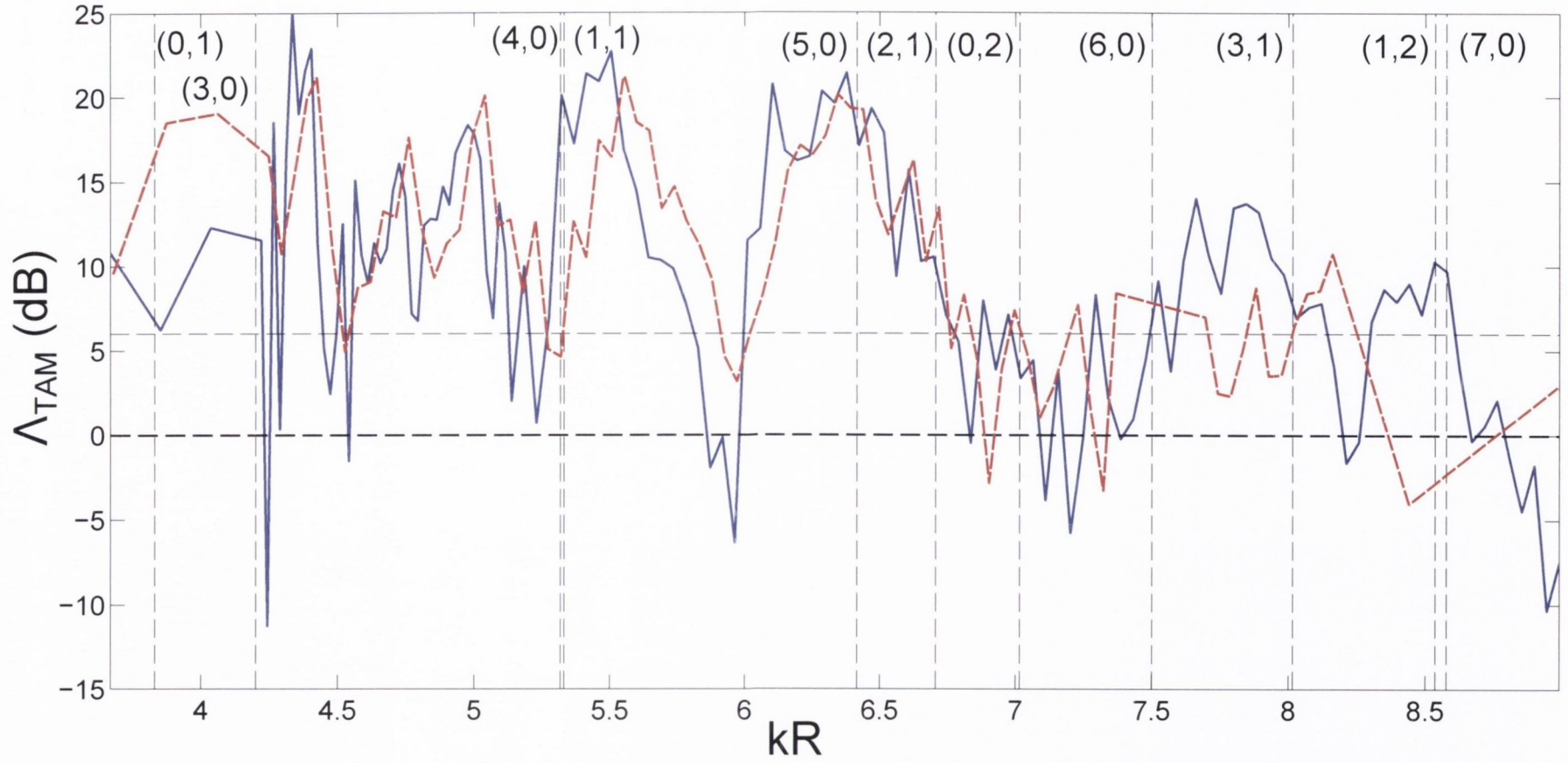
Figure 5.17: Performance of the mode generator for a range of test frequencies with the $m = 0$ mode targeted. For the case in blue, the fan is not rotating. For the case in red, the fan is rotating at 13000rpm.
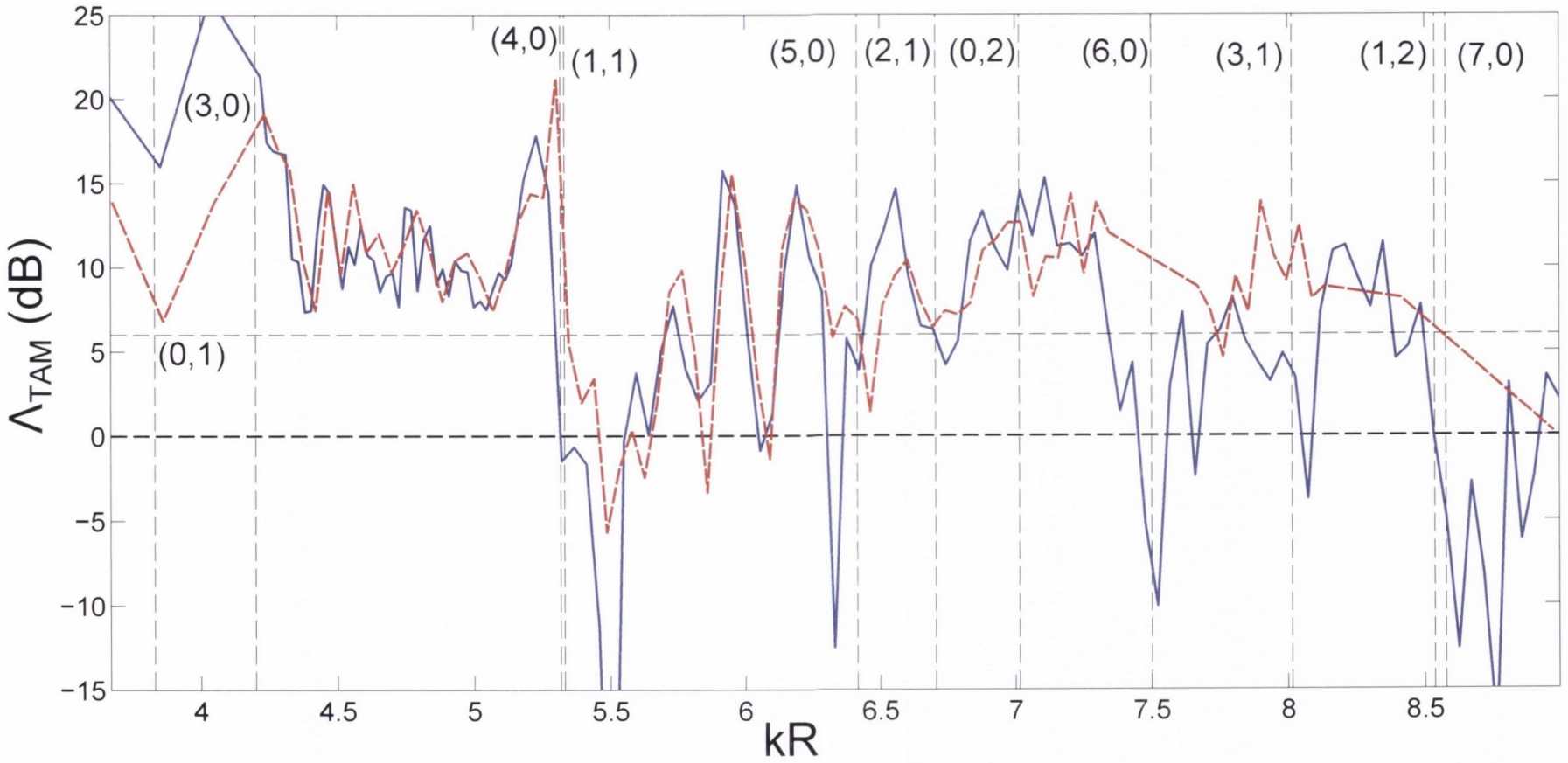
Figure 5.18: Performance of the mode generator for a range of test frequencies with the $m = 1$ mode targeted. For the case in blue, the fan is not rotating. For the case in red, the fan is rotating at 13000rpm.
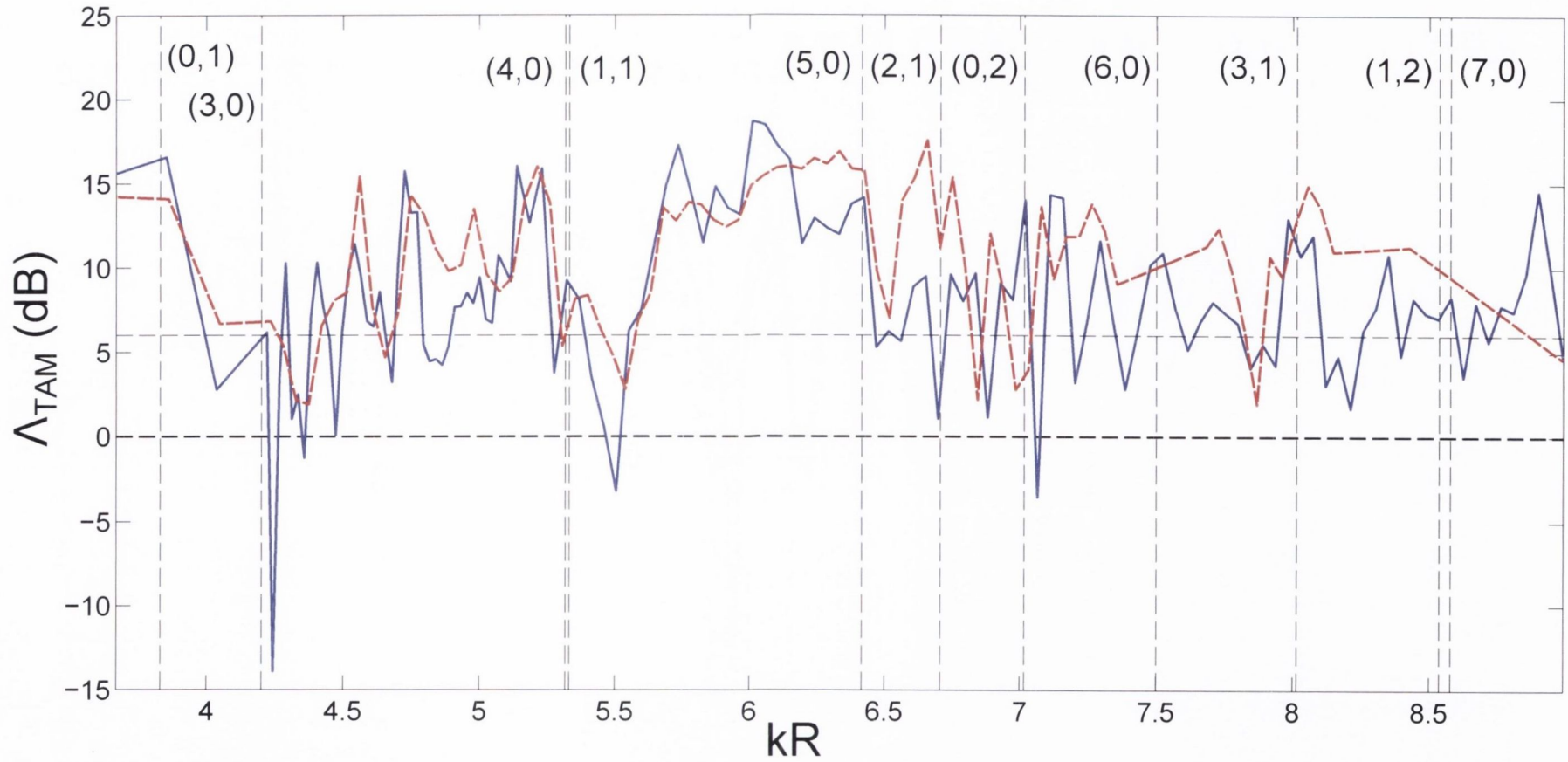
Figure 5.19: Performance of the mode generator for a range of test frequencies with the $m = 2$ mode targeted. For the case in blue, the fan is not rotating. For the case in red, the fan is rotating at 13000rpm.

5.4   Axial-Fan Noise

The EBM-PAPST standard vane-axial-fan used in the noise scattering experiments has 5 fan blades and 8 stator vanes. Its rotational speed can be set anywhere between 4000 and 13000rpm. At 13000rpm an axial-flow of Mach number $M_x = 0.036$ is induced through the duct. A second EBM-PAPST fan was also used with an alternative five-stator vane design. The casing for this alternate fan was manufactured in-house using rapid prototyping.

Fan noise generally consists of periodic tonal noise at blade-pass frequencies superimposed on a broadband noise floor. Some tonal noise is also generated at shaft frequencies of the fan, which will become more significant as the tip speed of the fan approaches supersonic levels. For a $0.05m$ radius fan, a rotational speed of at least 65508rpm is necessary to reach supersonic tip speeds. Figures 5.20 and 5.21 show the spectra of the fan noise measured by a microphone in the sensor array at a range of fan rotational speeds. The experimental set-up is as shown in Figure 5.5. Three harmonics of the BPF are identified in each case. The BPF is important to note, as it indicates at what frequencies any scattered tones are predicted to occur in the scattering tests relative to the frequency of the tone generated by the mode generator.

The dominant modal content at each h harmonic of the fan BPF is predicted by Tyler-Sofrin [14] theory as:

$$m = -hB - kV \tag{5.13}$$

where h in the blade-pass harmonic, k is any integer, B is the number of fan blades and V is the number of stator vanes. It should be noted that the fans rotate counter-clockwise, but the azimuthal modes have been decomposed with the clockwise direction being taken as being positive, hence the negative sign preceding Equation 5.13. The dominant modes predicted at the first three harmonics of the fan BPF are shown in Tables 5.3 and 5.4. The actual modal content of the blade-pass harmonics, as decomposed using the sensor array, are shown in Figures 5.22 and 5.23 as a function of fan speed (and hence BPF frequency).

For the standard fan configuration, only the $m = 0$ mode is cut-on in the duct for all rotational speeds tested at the fan BPF, and therefore no Tyler-Sofrin predicted modes
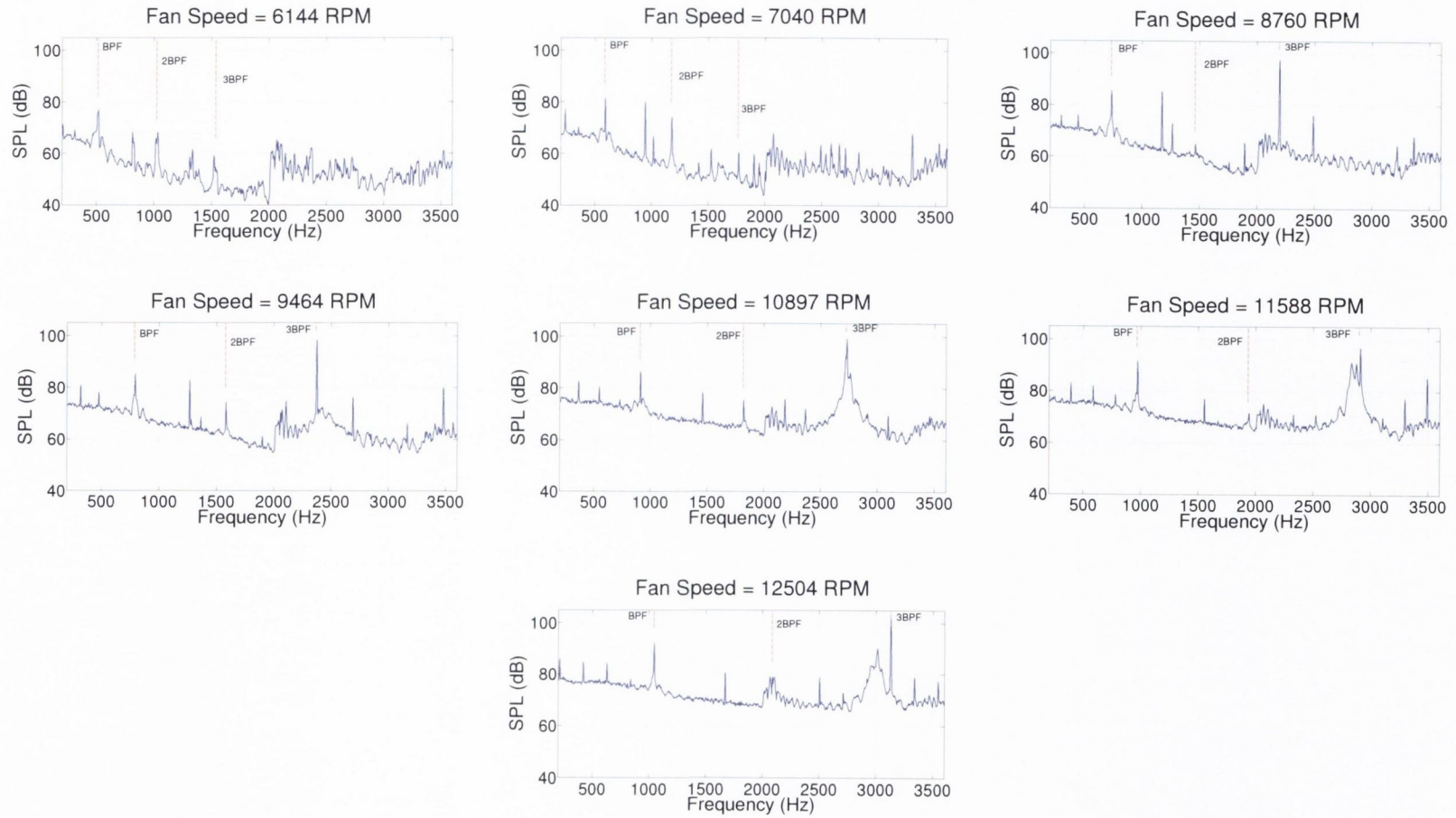
Figure 5.20: Fan spectra at a range of rotational speeds, standard eight-vane configuration
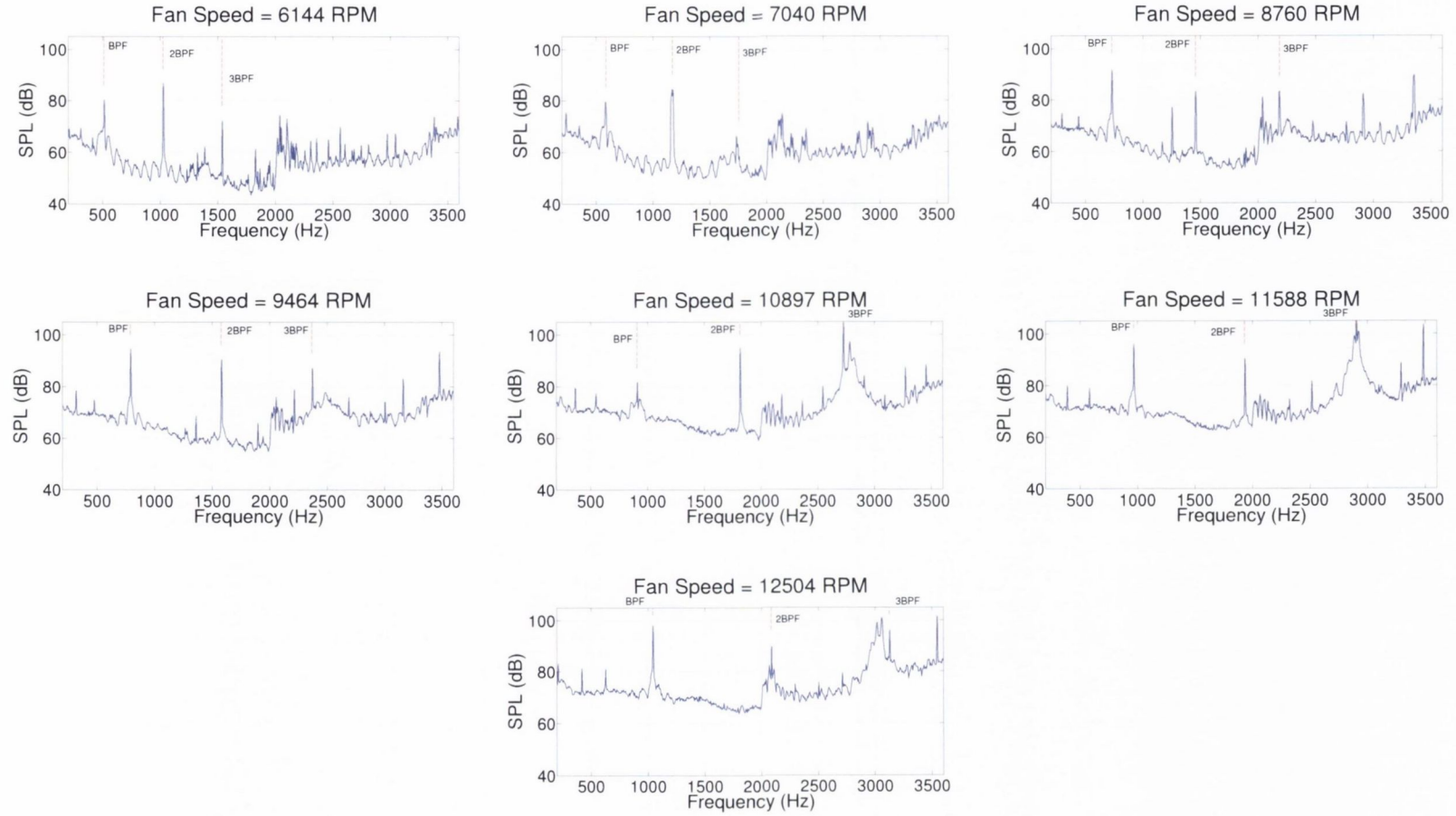
Figure 5.21: Fan spectra at a range of rotational speeds, alternative five-vane configuration

Table 5.3: Tyler-Sofrin predicted azimuthal modes at fan BPF tones for the eight-vane fan-stator configuration, as per Equation 2.25.

BPF ($h = 1$)		BPF2 ($h = 2$)		BPF3 ($h = 3$)		BPF4 ($h = 4$)	
k	**m** $= -5 - 8k$	**k**	**m** $= -10 - 8k$	**k**	**m** $= -15 - 8k$	**k**	**m** $= -20 - 8k$
-1	3	-2	6	-2	1	-3	4
0	-5	-1	-2	-1	-7	-2	-4

Table 5.4: Tyler-Sofrin predicted azimuthal modes at fan BPF tones for the five-vane fan-stator configuration, as per Equation 2.25.

BPF ($h = 1$)		BPF2 ($h = 2$)		BPF3 ($h = 3$)		BPF4 ($h = 4$)	
k	**m** $= -5 - 5k$	**k**	**m** $= -10 - 5k$	**k**	**m** $= -15 - 5k$	**k**	**m** $= -20 - 5k$
-2	5	-3	5	-4	5	-5	5
-1	0	-2	0	-3	0	-4	0
0	-5	-1	-5	-2	-5	-3	-5

shown in Table 5.3 are cut-on. In fact, for almost all BPF harmonics shown no predicted Tyler-Sofrin modes are cut-on for this fan configuration. The only exception to this is the third harmonic of the BPF, where the $m = 1$ mode cuts-on at higher fan speeds. The cut-on of this mode corresponds to a sharp increase in the magnitude of this BPF tone shown in Figure 5.22.

For the alternative five-vane configuration, Table 5.4 indicates that the $m = 0$ mode is predicted as being generated by the fan-stator stage at the fan BPF and each of its harmonics. Figure 5.23 demonstrates a far stronger generation of the fan BPF and the three higher harmonics shown than was observed for the standard eight-vane fan, with the $m = 0$ mode dominating in almost all cases as predicted.

These results show that when Tyler-Sofrin predicted modes are cut-on, they dominate the noise generated by both fan-stator configurations at the BPF and its harmonics. Furthermore, a much stronger BPF excitation is observed when these modes are cut-on. The BPF energy also increases with increasing fan rotational speed. However significant BPF excitation is still observed in cases when such modes are not cut-on, due to the fact that the fans tested are "non-ideal", with some blade-to-blade variations and shaft imbalances to be expected.
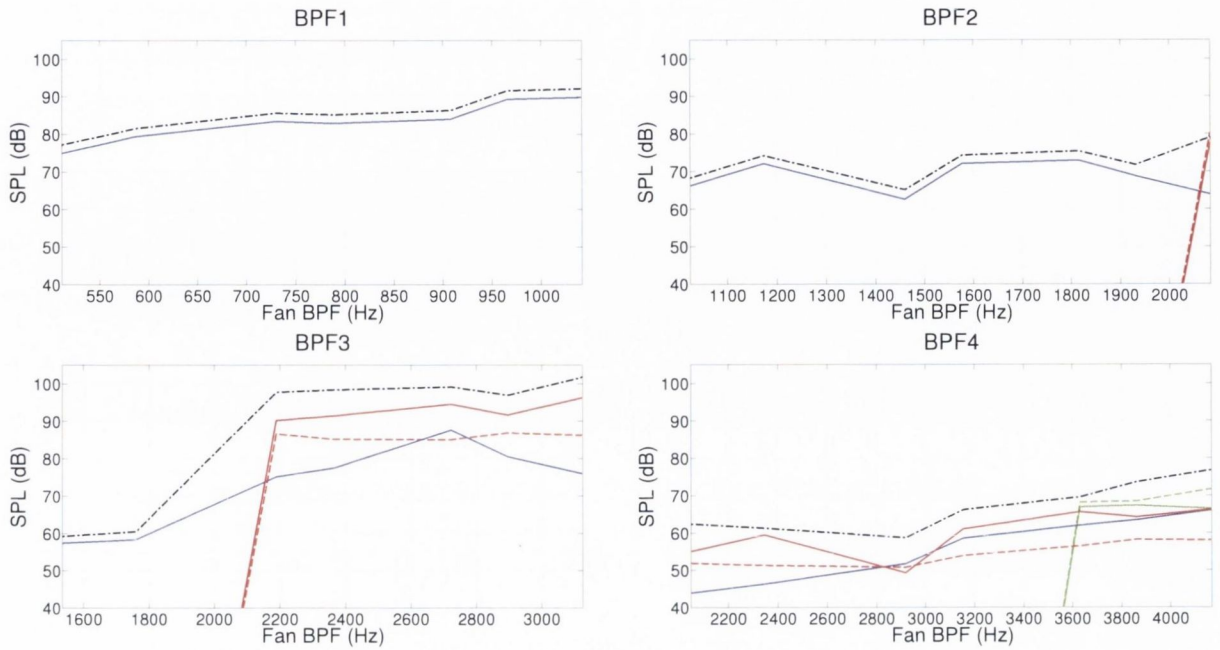
Figure 5.22: Modal amplitudes at fan BPF harmonics at a range of rotational speeds, standard eight-vane configuration. The black-dashed lines shows the SPL spectra measured at a single microphone. The blue, red and green lines shows the SPL spectra of the $m = 0$, $m = \pm1$ and $m = \pm2$ azimuthal modes respectively. Broken lines indicate negative mode orders.
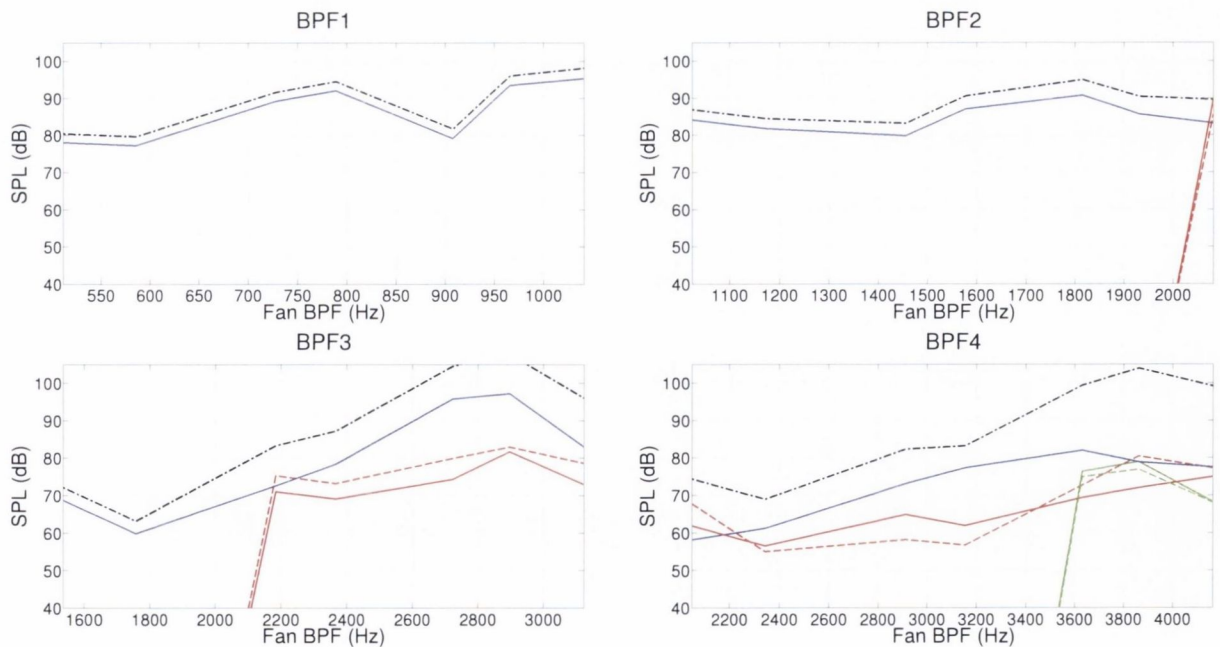
Figure 5.23: Modal amplitudes at fan BPF harmonics at a range of rotational speeds, alternative five-vane configuration. The black-dashed lines shows the SPL spectra measured at a single microphone. The blue, red and green lines shows the SPL spectra of the $m = 0$, $m = \pm1$ and $m = \pm2$ azimuthal modes respectively. Broken lines indicate negative mode orders.

5.5   Semi-Anechoic Termination Performance

Both the single-microphone and microphone array techniques applied in the noise scattering tests in Chapter 6 cannot discriminate between incident and reflected components, as all microphones are located at the same axial location. Due to this limitation, any acoustic reflections at either end of the main test duct will contaminate any attempts to draw quantitative conclusions from such techniques. Such reflections must also be eliminated in order to conclude causal relationships from any correlation estimates between microphone measurements made upstream and downstream of an in-duct noise-source. Semi-anechoic terminations are therefore located at both ends of the main test duct in order to reduce the influence of reflections as much as possible.

Both end sections of PMMA ducting are $1m$ in length and have a triangular section removed. These terminating duct sections will be referred to as semi-anechoic rather than anechoic unless it is proven that they completely eliminate reflections from the end of the duct. The design of the triangular slot is given in an ISO standard on the determination of sound power radiated into a duct by fans and other air-moving devices [82] and is shown in Figure 5.24. The hypothesis behind the design is that the impedance is slowly changed from the in-duct characteristic impedance to that of the surrounding environment, therefore preventing a sudden change in impedance at the duct ends which leads to high reflections. The mesh material placed over the removed notch is acoustically transparent but resistant to any air flow, thus ensuring a smooth flow of air through the end duct sections.

The two-microphone transfer function method of Chung and Blaser [80] can be used to asses the reflection coefficient and the specific acoustic impedance of the main test duct. Broadband noise is generated which propagates in the duct and is measured by two axially-spaced microphones, and the transfer function estimated between the two microphones can be used to assess the duct acoustic properties. This method was applied in the waveguide tests in Section 5.3.2. However, this technique may only be performed under the assumption of plane wave transmission in the test duct. This means that the duct acoustic properties can only be assessed up to the cut-on frequency of the first higher-order mode, which occurs at around $2kHz$ for the test duct geometry investigated
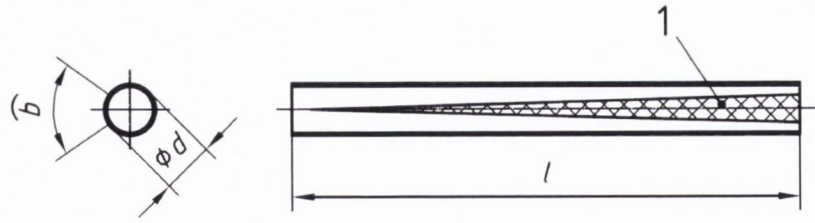
Key

1   triangular slot

$l = 9d$, $b = 0,6d$, covered with porous material

NOTE 1   Flow resistance equals approximately 400 N·s/m^3 ($\approx \rho c$).

NOTE 2   Tested for $d \leqslant 0,3$ m

Figure 5.24: Design of the anechoic termination used in the experimental set-up shown in Figure 5.5, as given in standard BS EN ISO 5136:2003.

herein.

Since the noise scattering tests planned using this experimental set-up focus on the transmission and measurement of several higher-order modes, an analysis of the duct acoustic properties which only extends such a low frequency range is unsuitable. It is instead proposed that the incident and reflected acoustic modal amplitudes be identified using an array of microphones in two axial rings. Since 24 microphones are available, they are split into two rings of 12 microphones each. Having less microphones in each axial ring will reduce the maximum frequency of modal decomposition, but allow a higher-order radial mode procedure to be performed which will output the incident and reflected complex modal amplitudes $A_{m,n}^{+}$ and $A_{m,n}^{-}$. As the noise scattering experiments focus on an azimuthal modal decomposition, it is not necessary in this analysis to discriminate on radial mode order, so each azimuthal modal amplitude is found by summing up the higher-order radial modes as follows:

$$|A_m^{\pm}| = \sum_{n=0}^{N} |A_{m,n}^{\pm}| \tag{5.14}$$

where N is the maximum radial mode order cut-on in the frequency range tested. The magnitude of the reflection coefficient for each azimuthal mode is then found by:

$$|R_m| = \frac{|A_m^-|}{|A_m^+|} \tag{5.15}$$

The basic experimental set-up used to assess the reflection coefficient was the same as shown in Figure 5.5 for the noise scattering tests. Broadband noise was generated by each of the five loudspeakers in the mode generator array at all frequencies below $12kHz$. The broadband noise emanating from each loudspeaker is uncorrelated with each additional speaker. The resulting sound field was then measured by all microphones in the sensor array for 30 seconds at a sampling rate of $26kHz$. Data was analysed using averaging blocks of 2048 points in an ensemble with zero overlap, giving 380 independent averages and a frequency resolution of $12.7Hz$ in any frequency-domain estimates. This test procedure was repeated for four modifications of the experimental rig shown in Figure 5.5 in order to assess the impact of the semi-anechoic terminations on the modal reflection coefficients:

1. Both semi-anechoic termination sections were removed and each replaced by circular cross-sectioned ducting of length $1100mm$. This extends the total length of the test ducting, L, by $200mm$, and represents a simple open/open-ended boundary condition.

2. As in 1, with the ducting added at $x = 0$ replaced by a semi-anechoic termination (S.A.T.) section.

3. As in 1, with the ducting added at $x = L$ replaced by a semi-anechoic termination (S.A.T.) section.

4. Semi-anechoic terminations are located at $x = 0$ and $x = L$ i.e. the experimental rig was exactly as shown in Figure 5.5.

The sound pressure level spectra recorded by all microphones are shown for all four test set-ups in Figure 5.25. These spectral measurements were averaged across all sensors in each axial ring. These broadband noise measurements give information on the propagation characteristics from the loudspeakers and through the waveguides, the main test duct, and the stationary fan-stator stage to the microphone array. This explains why the flat

spectral source signals do not propagate from the speakers to the microphones with equal amplitude across all measured frequencies. Any noise propagating in the main test duct will also be reflected at both duct ends, and the characteristics of this reflection will be impacted by the change in end termination. The "spikey" nature of the measured spectra is likely linked to the low fundamental longitudinal standing wave frequency of the duct of around $15Hz$, and therefore any higher standing wave harmonics will be closely spaced together in the frequency-domain, as well as the peaks and troughs in the transmissibility of the mode generator waveguides with frequency. Interestingly, the averaged sound pressure levels at both axial locations drop as the unmodified duct ends are replaced by semi-anechoic termination sections, particularly when a semi-anechoic section is located at $x = L$. This drop in sound pressure level would strongly suggest that more noise is being radiated from one or both ends of the test duct, meaning less noise is being reflected at the duct ends, reducing the measured sound pressure levels.
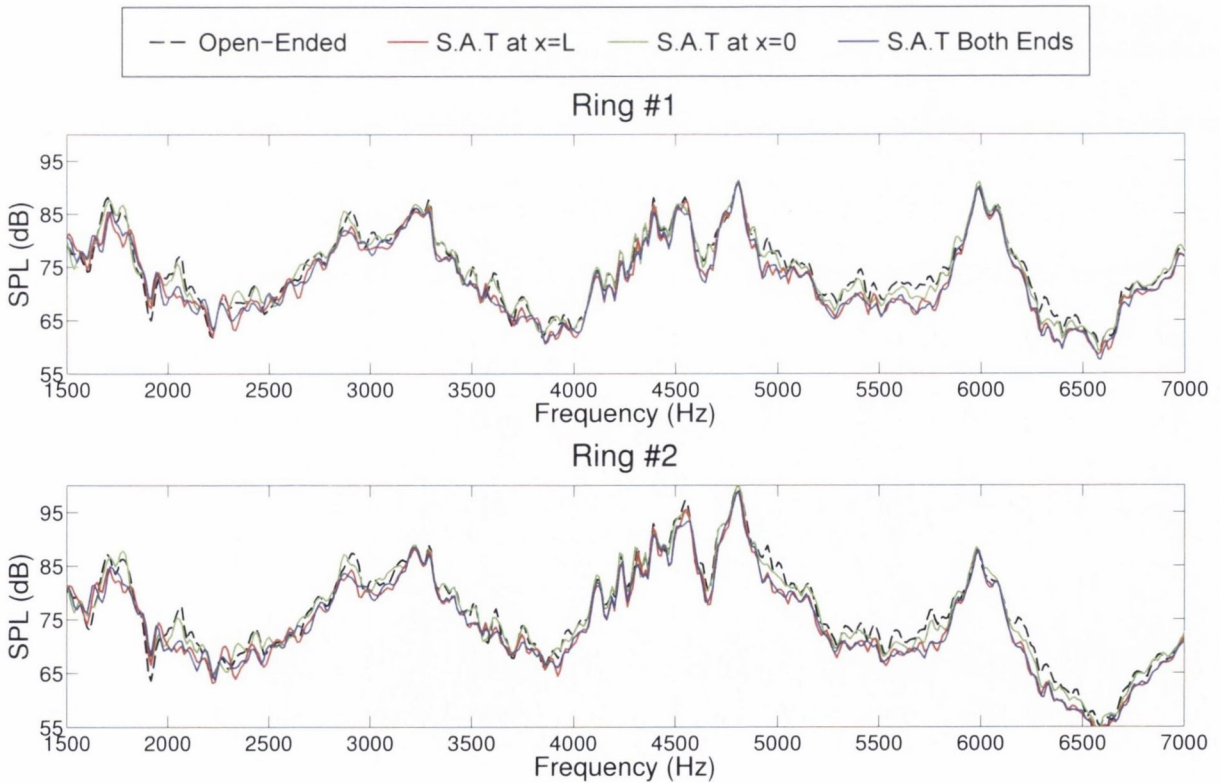
Figure 5.25: Broadband noise levels measured at the sensor array and averaged across both rings of sensors for four duct end conditions. Mutually uncorrelated broadband noise has been generated by five loudspeakers at the mode generator array.

Although examining the overall sound pressure levels gives some indication of the

performance of the semi-anechoic terminations, an azimuthal modal analysis performed using all sensors in the array as described at the beginning of this section gives a far more complete overview of the individual modal reflections and therefore a more complete overview on their performance. The results for such an analysis for the four experimental rig modifications are presented in Figures 5.26 and 5.27. Each subplot shows, for a given azimuthal mode order, the measured modal reflection coefficients as per Equation 5.15 against Helmholtz number, kR. Each azimuthal mode has been plotted well above their respective cut-on frequencies. Focusing first on the $m = 0$ mode, it is clear that the reflection coefficient stays reasonably high when the main test duct is open at both ends at around 0.4–0.5. A large peak in the reflection coefficient is observed at a kR value close to 3.81, which corresponds to the resonance frequency expected at the cut-on of the (0,1) mode. Other peaks are assumed to be attributable to other azimuthal and modal cut-on resonances as well as resonances at longitudinal standing wave frequencies. It is unknown why, in some cases, the reflection coefficients exceed a unity value. This occurs at a kR values of 4.4–4.6 for the $m = 1$ mode and a kR values of 2.1–2.3 for the $m = -1$ mode. This would indicate noise generation in the negative x-direction relative to the sensor array, where no noise-source is located. This is as yet unexplained.

When a semi-anechoic termination section is located at $x = L$, a significant drop is observed in the modal reflection coefficients (around 0.2–0.25) for all azimuthal modes across all frequencies. This demonstrates that locating the semi-anechoic termination further down the propagation path from noise-source to receiver effectively increases the transmission through the end of the test duct and into the surrounding environment. This reduction is best achieved at the resonance frequencies commented on previously. Interestingly, locating a semi-anechoic termination at $x = 0$ also reduces the reflection coefficient slightly, despite not being located past the propagation path between the noise-source array and the measurement location. This reduction is again best seen at spikes in the reflection coefficient. This positive result may be attributed to the semi-anechoic termination acting to reduce standing wave resonances by increasing sound transmission at this end of the duct.

These semi-anechoic termination tests have demonstrated that the chosen design operates favourably, significantly reducing if not quite eliminating the influence of reflections

on any analysed results in Chapter 6. This is important so that an accurate modal analysis can be undertaken using a single-ring of sensors, as any reflections will result in erroneous quantitative modal amplitude estimates as a single-ring analysis cannot separate out the incident and reflected components.
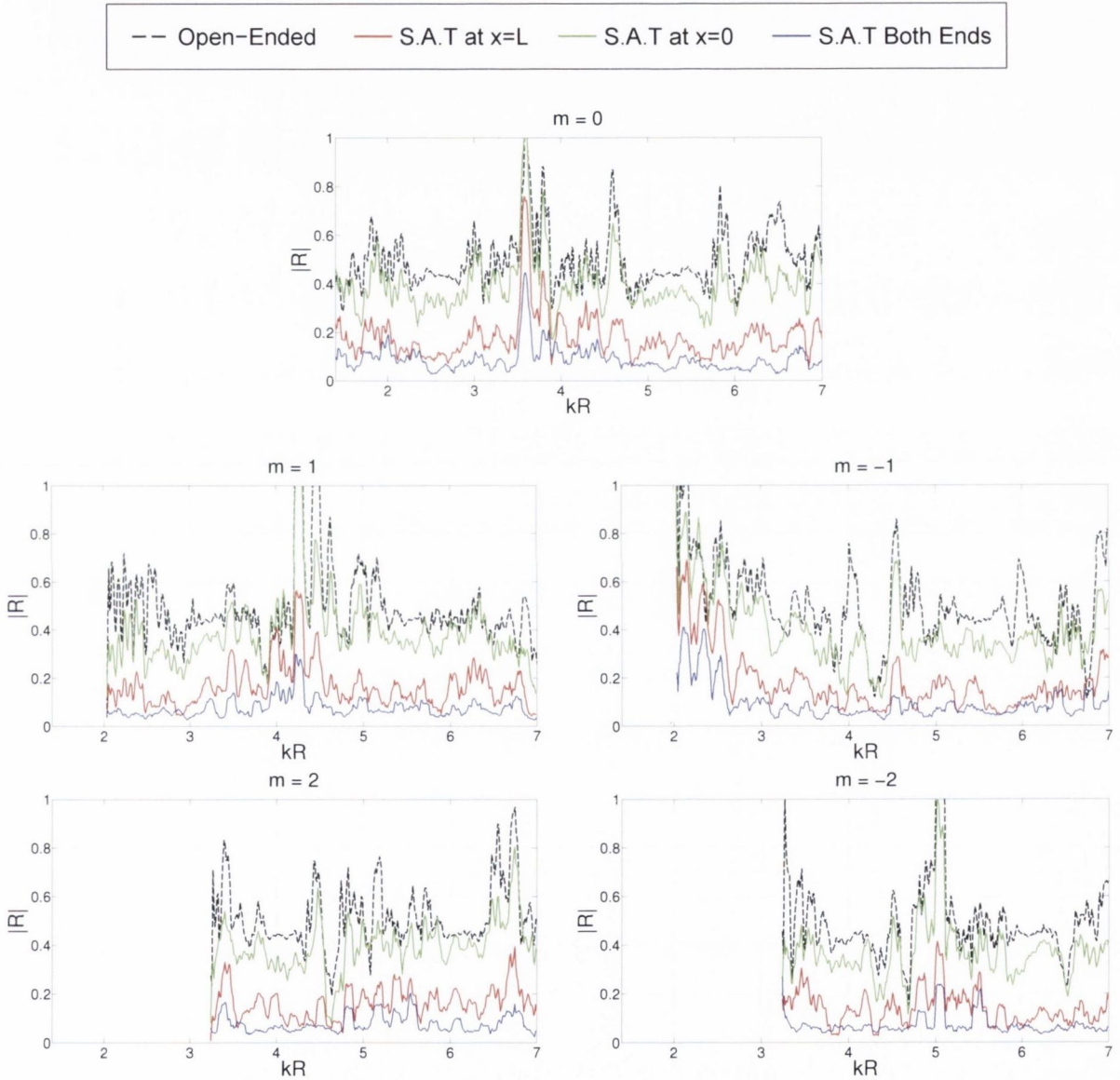
Figure 5.26: Reflection coefficients of azimuthal modes estimated at the sensor array plotted against Helmholtz number. Mutually uncorrelated broadband noise has been generated by five loudspeakers at the mode generator array for four duct end conditions.
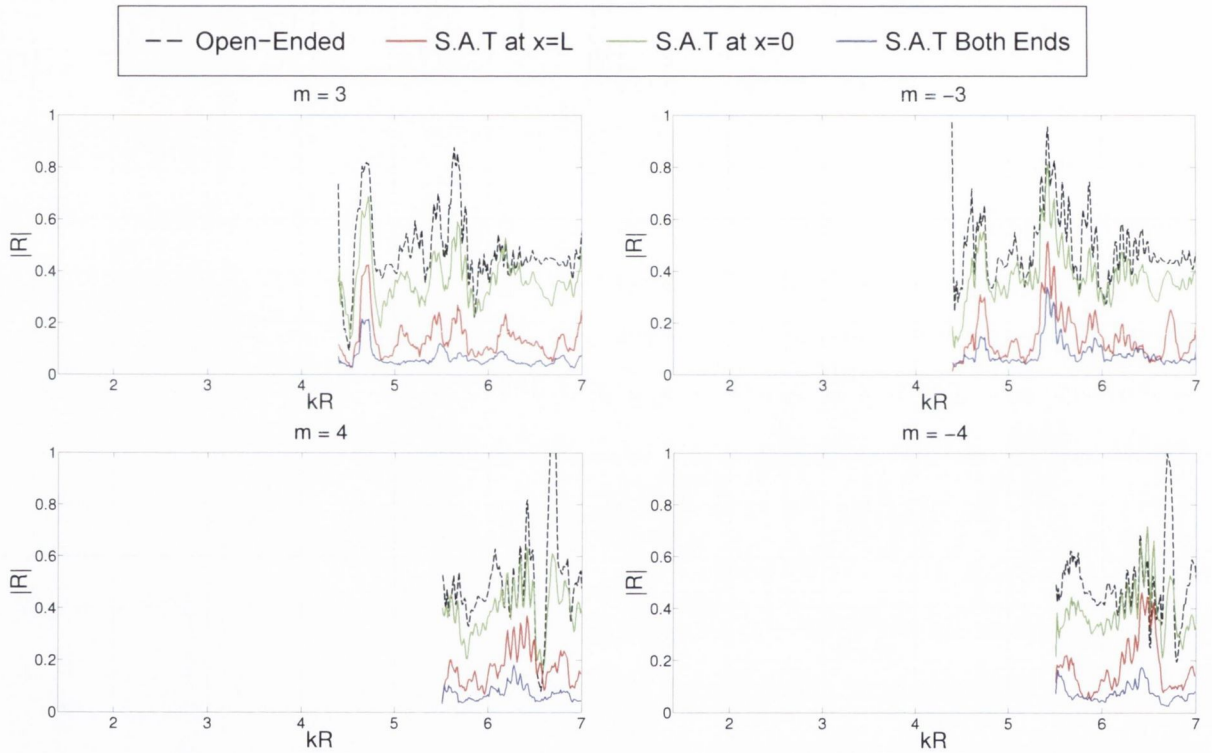
Figure 5.27: Reflection coefficients of azimuthal modes estimated at the sensor array plotted against Helmholtz number. Mutually uncorrelated broadband noise has been generated by five loudspeakers at the mode generator array for four duct end conditions.

Chapter 6

Sum and Difference Scattering of Noise Through a Fan/Rotor Stage – Results of Experimental Investigation

6.1   Tonal Scattering Results

In Section 5.3.3, an experimental testing procedure was outlined whereby a tone was generated at the mode generator array and a specific azimuthal mode was excited at this tone by adjusting the phase relationship between the loudspeakers in the array. This was repeated for a range of targeted modes and tonal frequencies. Any noise generated by the mode generator array which propagates downstream in the main test duct towards the fan-stator stage will be referred to through-out this chapter as the *incident noise*. The fan was not rotating in this case. In Section 5.4, the characteristics of the noise generated by the vane-axial-fan were discussed.

The aim of this section is to overview the results obtained when both the fan is rotating and the mode generator is operating, in order to investigate the phenomenon of sum and difference scattering of tones. Both the incident tones which are generated at the mode generator, and any scattered tones which are caused by the interaction between the rotating fan and the incident tones, are of interest. Primarily, the modal content and amplitude of the scattered tones, and their relationship with the modal content and amplitudes of the incident tones, will be examined.

Suitable test points for study occur at frequencies where:

- the mode generator is effective *i.e.* any targeted modes are dominant by $6dB$ or more (see Section 5.3.3).

- the mode generator tone is not generated at a frequency which corresponds to a periodic noise generation frequency at the fan, *e.g.* the fan BPF or its harmonics.

- any sum and difference scattered tones do not occur at frequencies which correspond to a periodic noise generation frequency at the fan.

- both the incident and scattered modes fall within the frequency range of signal processing (see Table 5.1). Tones will not be generated above $11kHz$ due to the limitations of the mode generator design, and data cannot be analysed beyond $13kHz$ as this corresponds to the Nyquist limit for the sampling rate used.

Data was acquired by each microphone at a sampling rate of $26kHz$ for 30 seconds. When processing the time-domain signals, each averaging block contained 16384 points,

giving an ensemble of 47 averaging blocks and a frequency resolution of $1.59Hz$ in any spectral estimates. A low number of averages was considered acceptable as this study is focused on deterministic, tonal data, and therefore the influence of variance errors will be low in any spectral estimates. The high frequency resolution was selected in order to reduce peak-resolution bias errors/spectral leakage, and all microphones have been cross-calibrated for both magnitude and phase to reduce systematic errors in any results. For the modal analyses performed in Section 6.1.2, data was analysed by means of the zoom-transform procedure discussed in Appendix C.3.

6.1.1 Single Microphone Spectral Analysis

It is anticipated that scattering of tonal energy will occur at mode generator source tone frequencies (T) plus or minus multiples of the BPF of the fan (see Section 5.1.2). In the following test campaign the fan was rotating at 13000rpm, giving a BPF of $1083Hz$.

Figures 6.1 and 6.2 show the SPL (sound-pressure level) spectra measured at a single microphone in the sensor array (located at $\theta = 0°$), acquired over 30 seconds, for a variety of test points. The fan is rotating at 13000rpm and the mode generator generates a tone at a test frequency T. The test frequencies shown were selected as the mode generator is effective for each frequency for each targeted azimuthal mode tested.

The spectra at frequency ranges close to the incident mode generator tone T and several possible scattering frequencies $T + (q{\times}BPF)$ are shown in each column. The scattering harmonic q can take any non-zero integer value. The black spectrum shows the noise measured when the fan is rotating, and no noise is generated by the mode generator. The blue, red and green spectra show the noise measured by this same microphone when the fan is rotating, and tonal noise is generated at the test frequencies noted on each row of plots. For the test case recorded in the red spectrum, the $m = 0$ mode was targeted. The $m = 1$ and $m = 2$ modes were targeted in the test cases recorded in the green and blue spectra respectively. Existing theory on sum and difference scattering predicts that the onset of significant scattering is linked to the cut-on of specific azimuthal modes, and thus the cut-on frequencies of all modes within the range of data analysis are collated in Table 6.1. It should be noted that the actual cut-on frequencies will diverge from these tabulated values slightly due to the presence of a mean-flow in the duct as well the

Table 6.1: Cut-on frequencies in Hz (with the corresponding kR values in brackets) of acoustic modes for a $R = 0.05m$ circular duct, assuming standard conditions for temperature and pressure and zero mean-flow.

m↓ n→	0		1		2	
0	0	(0)	4183	(3.83)	7660	(7.02)
1	2010	(1.84)	5821	(5.33)	9320	(8.54)
2	3335	(3.05)	7322	(6.71)	10885	(9.97)
3	4587	(4.20)	8751	(8.02)	12388	(11.35)
4	5806	(5.32)	10135	(9.23)	13846	(12.68)
5	7005	(6.42)	11486	(10.52)	15271	(13.99)
6	8190	(7.50)	12812	(11.73)	16670	(15.27)
7	9365	(8.58)	14120	(12.93)	18047	(16.53)
8	10533	(9.65)	15411	(14.12)	19406	(17.77)

temperature within the test facility differing from standard values. The effects of these variations from an idealised quiescent fluid at standard temperature will be very small however, affecting the modal cut-ons by less than $10Hz$.

It is clear from this figure that tonal energy is scattered at frequencies of $T + (q \times BPF)$ for some test frequencies, but not others. Above certain critical frequencies, energy *is* scattered at these sum and difference frequencies. Furthermore, once the onset scattering occurs it generally continues to occur for all higher test frequencies above this critical frequency. This critical frequency varies, depending on both the scattering harmonic q and the dominant azimuthal mode of the incident tone. This would suggest a link between the onset of frequency scattering and the cut-on of certain modes. Identifying the critical frequency at which this scattering occurs, for each q scattering harmonic, is vital to understanding the conditions necessary for frequency scattering to occur.

Focusing on the $q = 1$ scattering harmonic, and thus a scattering frequency of $T + (1 \times BPF)$, significant scattering is observed for all test frequencies when the $m = 2$ mode has been excited by the mode generator. Little or no scattering is observed when the $m = 0$ or $m = 1$ have been targeted by the mode generator up until $T = 5200Hz$. At this test frequency, scattering of noise is observed at $T + (1 \times BPF)$ when the $m = 1$ mode has been targeted, and noise scatters at this scattering harmonic for all higher test frequencies. Scattering is observed when the $m = 0$ is targeted at test frequencies greater than $T = 5600Hz$.
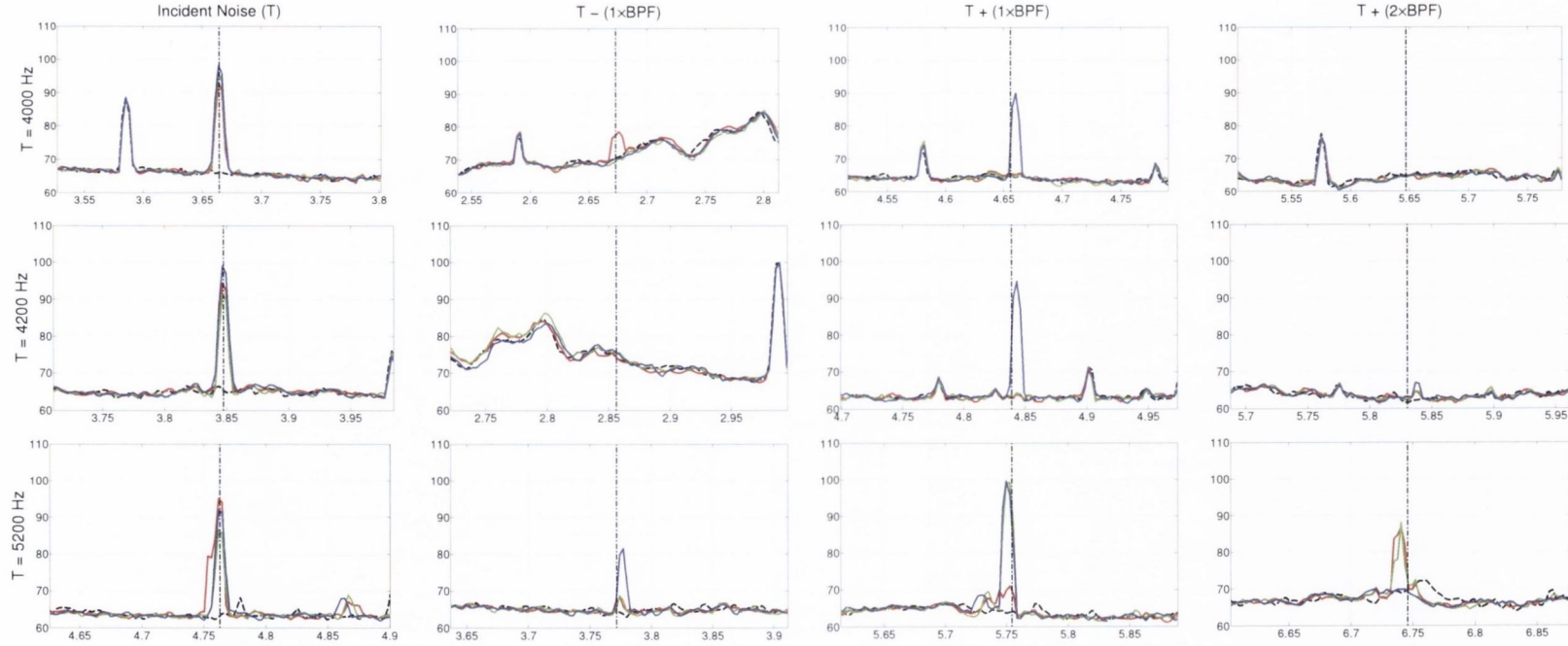
Figure 6.1: SPL spectra (in dB) measured against Helmholtz number (kR) by a single microphone for several test frequencies. The black-dashed spectrum was measured when the standard fan is rotating at 13000rpm. The red, green and blue spectra were measured when both the fan is rotating and the mode generator is generating a tone. The $m = 0$, $m = 1$ and $m = 2$ modes were targeted for the test cases recorded in the red, green and blue spectra respectively. Fan BPF $= 1083Hz$.
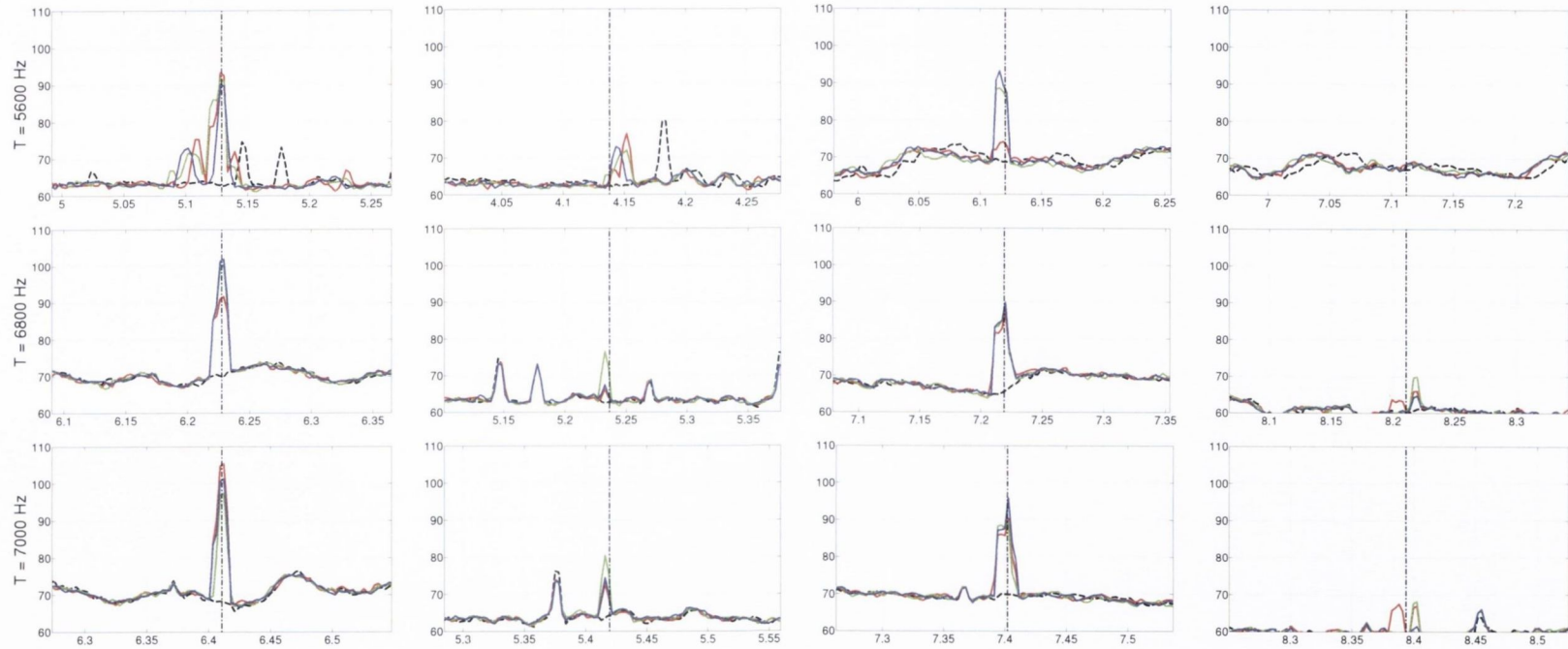
Figure 6.2: SPL spectra (in dB) measured against Helmholtz number (kR) by a single microphone for several test frequencies. The black-dashed spectrum was measured when the standard fan is rotating at 13000rpm. The red, green and blue spectra were measured when both the fan is rotating and the mode generator is generating a tone. The $m = 0$, $m = 1$ and $m = 2$ modes were targeted for the test cases recorded in the red, green and blue spectra respectively. Fan BPF = $1083Hz$.

For frequency scattering to occur at $T + (q \times BPF)$, the azimuthal mode order of the scattered tone, caused by the interaction of the mode generator tone and the rotating fan, is predicted by the theory discussed in Section 5.1.2 as:

$$m_{scatt} = m - qB \tag{6.1}$$

where the integer q denotes the scattering harmonic which can take positive or negative non-zero integer values. A negative sign precedes qB due to the fact that the fan rotates counter-clockwise, but the modal analysis undertaken herein takes clockwise rotating modes as being positive. As a stator is present, this equation is modified by a stator scattering term, as factored into the analysis by Enghardt *et al.* [9]. The scattered modal content of an incident mode due to the presence of a rotating fan and stationary stator is therefore predicted to be:

$$m_{scatt} = m - (qB - kV) \tag{6.2}$$

Each mode excited at the incident tone will be scattered in this way. This equation would suggest that if the dominant mode order of the tone generated at the mode generator is changed, scattering may occur above a different critical frequency. Furthermore, scattering could occur at several mode orders, as the variable k can take any integer value. Tables 6.2 – 6.4 summarise the potential scattering modes when the $m = 0, 1, 2$ azimuthal modes are dominant in the incident tone (using targeted azimuthal mode generation) for a range of scattering harmonics, q. The corresponding cut-on frequencies of these modes are also shown, and the scattered modes that are cut-on in the range of test frequencies shown in Figures 6.1 and 6.2 are highlighted.

Returning to the analysis of the $q = 1$ scattering harmonic, Equation 6.2 would predict significant scattering into the $m_{scatt} = TAM - 5$ mode at a frequency of $T + (1 \times BPF)$, where TAM is the targeted azimuthal mode which dominates the pressure field at the incident tonal frequency T and $k = 0$ in Equation 6.2. When $TAM = 2$, it is predicted that significant scattering will occur into the $m = -3$ mode which is cut-on at $kR = 4.2$. For all T tested, the scattering frequency $T + (1 \times BPF)$ is above this cut-on frequency. However, when $TAM = 1$ the corresponding predicted scattered mode is $m = -4$, which

is only cut-on at $kR = 5.32$ at $T + (1 \times BPF)$ for test frequencies of $T \geq 5200Hz$. The onset of significant scattering in the experimental results corresponds to this modal cut-on. Finally, when $TAM = 0$ mode is excited by the mode generator, significant scattering is anticipated into the $m = -5$ mode which has a cut-on of $kR = 6.42$, and significant scattering is indeed only observed at $T + (1 \times BPF)$ when this frequency falls above the cut-on frequency of the $m = \pm 5$ modes.

Some modulation is observed in any tonal noise measured at scattered frequencies relative to the exact predicted scattered frequencies shown by the vertical black dash-dot lines. This modulation is small (no more than $6Hz$) and is caused by slight variations in the fan rotational speed (and hence BPF) between tests.

Using the data presented in Tables 6.2 – 6.4 in conjunction with the experimental data presented in Figures 6.1 and 6.2, it may be possible to further assess whether or not the scattering mechanism predicted by Equation 6.2 occurs in practise. However, the relationship between modal scattering and the onset of frequency scattering is complicated by the fact that each incident mode can be scattered into several other mode orders, and the magnitude of the incident tone varies with frequency. Furthermore, it is necessary to take into account the magnitude of each individual mode, and the dominance of the targeted mode at the incident tone in particular, into account. Hence clear relationships can only be drawn when the modal amplitudes at the incident frequencies and the modal content at any scattered frequencies are known. In the following section, the results of an azimuthal modal decomposition performed at the sensor array are presented.

6.1.2   Modal Analysis at Incident and Scattered Frequencies

In Section 6.1.1, analysis of spectra acquired from a single microphone in the sensor array suggested a link between the onset of sum and difference scattering at a range of scattering harmonics $(T + (q \times BPF))$ and the cut-on frequency of the predicted scattered mode given in Equation 6.2. Using an array of 25 microphones in a single axial ring, the specific azimuthal modal amplitudes of the pressure field at that axial location can be found. This modal decomposition technique allows the azimuthal content at this location to be investigated without directional information *i.e.* without being able to separate out the incident and reflected components, and without the ability to discriminate between

Table 6.2: Scattered modes predicted as per Equation 6.2, with the $m = 0$ mode dominant at the incident tone. $B = 5$, $V = 8$.

	Scattered Mode Order (m_{scatt})						Cut-On Frequency of m_{scatt} (Hz)				
q	$k = -2$	$k = -1$	$k = 0$	$k = 1$	$k = 2$	q	$k = -2$	$k = -1$	$k = 0$	$k = 1$	$k = 2$
-1	-11	-3	5	13	21	-1	14004	4587	7005	16299	25390
1	-21	-13	-5	3	11	1	25390	16299	7005	4587	14004
2	-26	-18	-10	-2	6	2	31027	21993	12851	3335	8190

Table 6.3: Scattered modes predicted as per Equation 6.2, with the $m = 1$ mode dominant at the incident tone. $B = 5$, $V = 8$.

	Scattered Mode Order (m_{scatt})						Cut-On Frequency of m_{scatt} (Hz)				
q	$k = -2$	$k = -1$	$k = 0$	$k = 1$	$k = 2$	q	$k = -2$	$k = -1$	$k = 0$	$k = 1$	$k = 2$
-1	-10	-2	6	14	22	-1	12851	3335	8190	17442	26519
1	-20	-12	-4	4	12	1	24259	15153	5806	5806	15153
2	-25	-17	-9	-1	7	2	29901	20858	11695	2010	9365

Table 6.4: Scattered modes predicted as per Equation 6.2, with the $m = 2$ mode dominant at the incident tone. $B = 5$, $V = 8$.

	Scattered Mode Order (m_{scatt})						Cut-On Frequency of m_{scatt} (Hz)				
q	$k = -2$	$k = -1$	$k = 0$	$k = 1$	$k = 2$	q	$k = -2$	$k = -1$	$k = 0$	$k = 1$	$k = 2$
-1	-9	-1	7	15	23	-1	11695	2010	9365	18583	27648
1	-19	-11	-3	5	13	1	23127	14004	4587	7005	16299
2	-24	-16	-8	0	8	2	28775	19722	10533	0	10533

higher-order radial modes.

Several azimuthal modal analyses performed for a range of test frequencies are shown in Figures 6.3 and 6.4. These figures show bar charts of the SPL (in dB) of the modes estimated from an azimuthal modal analysis performed using all microphones in the sensor array. The x-axis shows the azimuthal mode orders cut-on at each frequency. The y-axis shows the amplitude of each cut-on mode as measured by the microphone array.

As in the single-microphone SPL spectra figures, each row corresponds to a different test frequency and each column corresponds to the incident tone (on the left) and three possible scattering frequencies (to the right). The red bars indicate the SPL of the modal amplitudes measured when the $m = 0$ mode has been targeted by the mode generator. The green and blue bars show the modal amplitudes measured when the $m = 1$ and $m = 2$ modes have been targeted. For each of the incident tone bar charts shown in the left column of sub-figures, it is clear that the targeted modes dominate the acoustic pressure field. All the test points shown in these figures correspond to the same test points as shown in Figures 6.1 and 6.2.

Focusing on a single test frequency of $T = 5200Hz$, and a single scattering frequency of $T + (1{\times}BPF)$, it can be seen in Figure 6.1 that significant energy was being scattered at a frequency of $T + (1{\times}BPF)$ when the $m = 1$ and $m = 2$ modes were targeted at the mode generator, but this was not the case when the $m = 0$ mode was targeted. Figure 6.3 demonstrates that this result is most likely linked to the cut-on of the predicted scattering modes given in Equation 6.2 for $k = 0$. The modal amplitudes shown in the second column from the left are the azimuthal modal amplitudes at a frequency of $T + (1{\times}BPF) = 6280Hz$ measured for these same test points. For the case where the $m = 0$ mode is targeted, no azimuthal mode order is clearly dominant at the scattered frequency. However, when the $m = 1$ mode is targeted, it clear that the $m = -4$ mode is dominant at this scattered frequency. The $m = 1$ mode is dominant by $12dB$ at the incident tonal frequency, and the $m = -4$ mode is dominant by $12dB$ at the scattered frequency. The amplitude of the $m = -4$ mode at the scattered frequency matches closely to the magnitude of the $m = 1$ mode at the incident frequency. Examining Figure 6.3, for the case where the $m = 2$ azimuthal mode is targeted, it is clear that the $m = -3$ mode is dominant at the scattered frequency. These match the theoretically expected results

collated in Tables 6.2 – 6.4, for the $k = 0$ column.

Interestingly, the predicted scattering modes in the $k = 1$ column do not generally appear to be dominant as expected. For example, the $m = 4$ mode is predicted as being of significant amplitude at the scattering frequency of $T + (1{\times}BPF)$ when the $m = 1$ mode is targeted at the incident tone, but this is not observed in the experimental test results. However, when the $m = 0$ mode is targeted, some scattering is observed into the $m = 3$ mode at this scattering frequency as predicted. At higher test frequencies where the $m = -5$ mode is cut-on, the $m = 0$ mode does scatter into the $m = -5$ mode at a frequency of $T + (1{\times}BPF)$ as predicted when $k = 0$ in Equation 6.2. This scattering is far more significant than the scattering observed into the $m = 3$ mode. This pattern is evident when comparing all the results shown in Figures 6.1, 6.2, 6.3 and 6.4 – significant scattering of noise occurs at frequencies $T + (1{\times}BPF)$ when the azimuthal modes predicted by Equation 6.2 are cut-on, with $k = 0$. Noise scattering is less evident at mode orders predicted by Equation 6.2 when $k{\neq}0$. Furthermore, no modes in the $k = 0$ column of Tables 6.2 – 6.4 are cut-on at other scattering harmonics for the test frequencies shown. What scattering of noise that does occur is of relatively low magnitude, of the order of $4dB$ above the noise floor of the fan. No mode order is consistently dominant across all test frequencies at these scattering harmonics.

The barcharts of the modal amplitudes presented in Figures 6.3 and 6.4 are effective at showing, at a single test frequency, how the modal amplitudes at the incident mode generator tone frequency compare with the modal amplitudes at a range of scattered frequencies. However, in order to give a better presentation of the experimental data across several test frequencies, many barcharts would be required. An alternative format of data presentation is to plot the scattered modal amplitudes against test frequency, and hence examine which modes are dominant for each test frequency. Simply plotting the absolute amplitude of each mode with frequency gives an incomplete picture however, as it does not separate out the contribution of the fan-stator broadband noise to this measured scattered noise. Accordingly, the difference in sound pressure levels between each azimuthal mode m measured when both the mode generator generates a tone and the fan is rotating, and the amplitude of this same mode m measured when the rotating fan is the only noise-source, was plotted. This difference in amplitude will be referred to
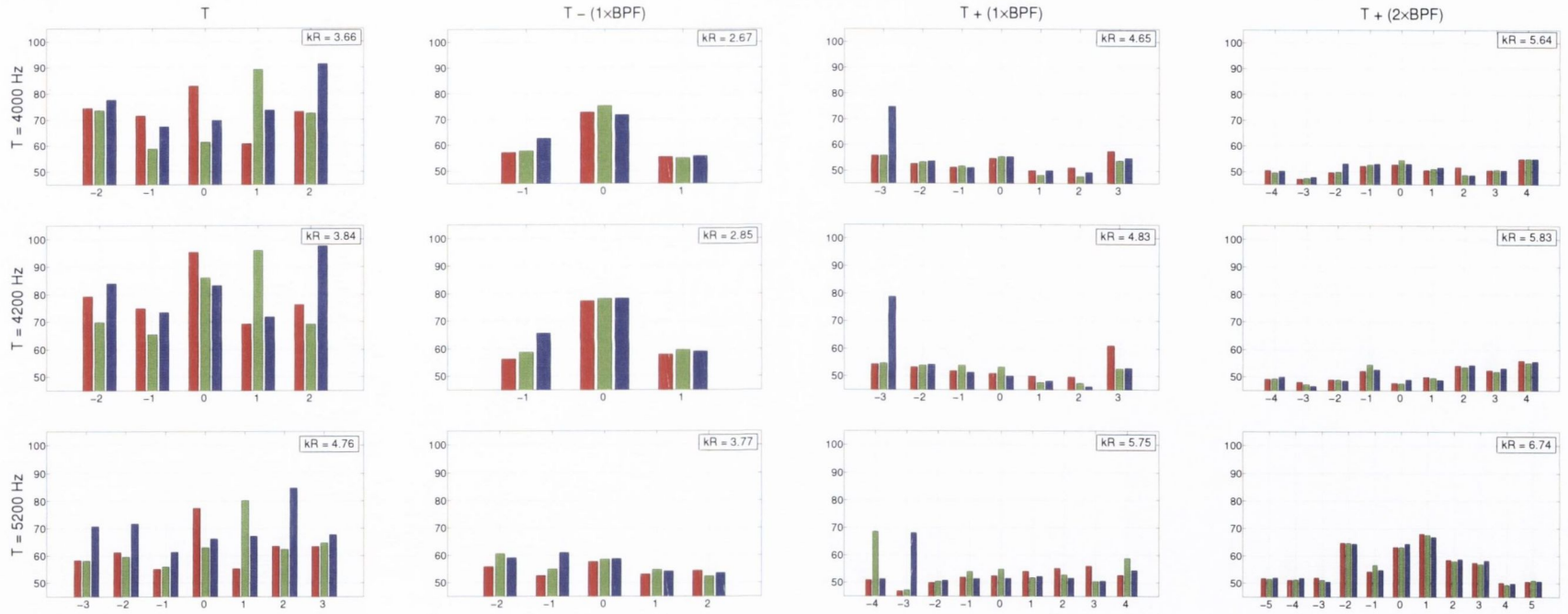
Figure 6.3: Bar charts of azimuthal modal amplitudes at incident and scattered frequencies; TAM = 0 in red, TAM = 1 in green, TAM = 2 in blue.
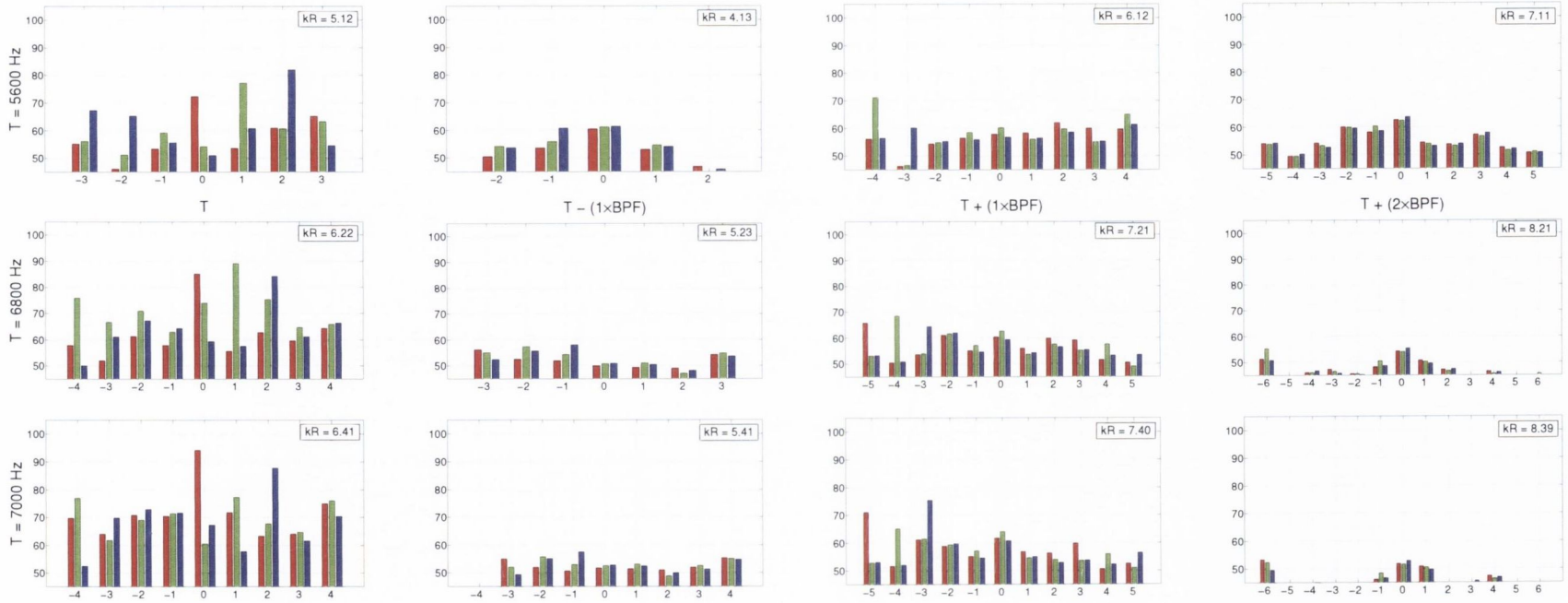
Figure 6.4: Bar charts of azimuthal modal amplitudes at incident and scattered frequencies; TAM = 0 in red, TAM = 1 in green, TAM = 2 in blue.

as Δ_{SPL}. This separates out the contribution to the modes estimated at a given frequency by the interaction between the incident tone and the rotating fan from the noise generated by the fan itself. An example of an estimate of this quantity is given in Figure 6.5.
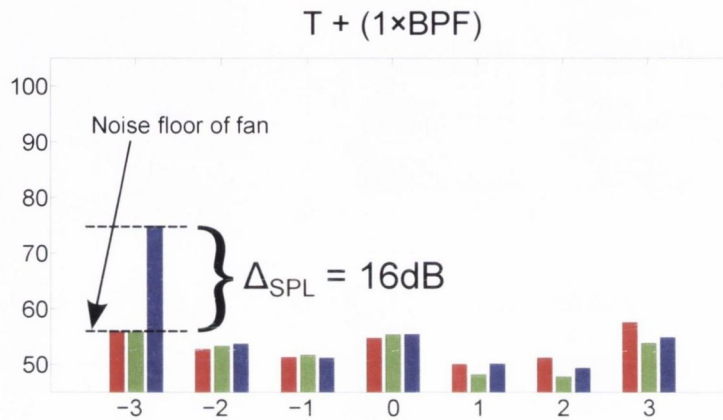
Figure 6.5: Example of the Δ_{SPL} quantity, shown here for the $m = -3$ mode.

Figures 6.6 – 6.14 show checkerboard plots of the relative sound pressure levels (in dB) of each azimuthal mode at three sum and difference frequencies when each azimuthal mode is targeted. The quantity plotted is Δ_{SPL}. This quantity was measured by calculating the difference in the azimuthal modal amplitudes between the test case where both the fan is rotating and the mode generator generates a tone and the test case where the fan is rotating and no noise is generated at the mode generator. Each figure plots the results for several tests when a specific azimuthal mode has been targeted by the mode generator and focuses on a specific scattering harmonic q. Each column of elements along the x-axis corresponds to a unique test frequency, and the values along this axis give the $T + (q{\times}BPF)$ frequencies at which modal analysis has been performed. The kR values of these test frequencies are given in the upper x-axis and the corresponding frequencies in Hz are given in the lower x-axis. The y-axis shows thirteen of the azimuthal modes measured by the sensor array, and the colour of each specific element gives the measured Δ_{SPL} value for each azimuthal mode at the given scattering harmonic, for a specific test frequency. In order to aid the interpretation of these results, the scattering modes predicted by Equation 6.2 and tabulated in Tables 6.2 – 6.4 have been circled in each figure. The colour of each circle corresponds to a k value inserted into Equation 6.2. A legend of how each specific k value corresponds to a specific circle colour is tabulated in

Table 6.5.

Table 6.5: Legend for coloured circles in Figures 6.6 – 6.23. Each colour corresponds to specific k values inserted into Equation 6.2.

k	Colour of Circle
0	Red
±1	Green
±2	Blue
±3	Orange

The density of elements along the x-axis indicates the number of viable test frequencies in a given frequency range. Using Figure 6.6 as a reference, a high density of elements is observed up to a frequency of around $T + (1 \times BPF) = 8kHz$. This means that the mode generator array was effective for many frequencies in this range. However, beyond this frequency, a single column of elements is plotted from $8.2kHz – 9.3kHz$. This is due to the fact that the mode generator was not effective (see Section 5.3.3) for any test frequencies T in this frequency range. Therefore frequency ranges with more densely packed elements are more informative.

Focusing first on the scattering harmonic of $T + (1 \times BPF)$, it is evident that significant modal scattering occurs as predicted in Tables 6.2 – 6.4. In particular, modal scattering occurs according to the following solutions to Equation 6.2:

$$
\begin{aligned}
m_{scatt} &= TAM - ((1)(B) - (0)(V)) \\
&= TAM - 5
\end{aligned}
$$

$$
\begin{aligned}
m_{scatt} &= TAM - ((1)(B) - (1)(V)) \\
&= TAM + 3
\end{aligned}
$$

This would mean, for example, that the $m = 0$ mode scatters into the $m = -5$ and $m = 3$ modes. These results show that significant modal scattering occurs into the $TAM - 5$ mode in particular. This goes further to prove the point suggested by the results in Figures 6.3 and 6.4; that the onset of frequency scattering is linked to the cut-on of

certain acoustic modes, which can be predicted with knowledge of the fan geometry and the modal content of the incident noise. For significant sum and difference noise scattering to occur at a given sum or difference frequency, significant acoustic energy must be carried by an azimuthal mode at the incident tonal frequency whose predicted scattered mode orders are cut-on at the scattered frequency.

Equation 6.2 predicts an infinite number of possible scattering modes for each scattering harmonic q, however the results presented herein strongly suggest that modal scattering occurs for solution to Equation 6.2 for small values of k. Modal scattering is not observed in any of the results in Figures 6.9 – 6.14 for solutions of Equation 6.2 where $k > 1$ or $k < -1$. This is not overly surprising given that as $|k|$ gets larger, the scattered mode order generally increases. Therefore it is more likely that this scattered mode will not be cut-on in the duct, and so will decay exponentially as it propagates in the axial-direction if excited by the interaction between the incident tone and fan stage. The results presented here demonstrate that modal scattering is stronger into azimuthal modes predicted by Equation 6.2 where $k = 0$ than for non-zero values of k, suggesting that stator scattering is less significant than scattering by the rotating fan for the fan-stator design used in these experimental tests.

The results also show that scattering into all cut-on modes increases as the test frequency is increased. This is to be expected; as more modes are cut-on at the incident tone as the test frequency is increased, a wider range of potential scattering modes in Equation 6.2 will be cut-on at all scattering harmonics.

The Δ_{SPL} quantity plotted in these results has proven to be very effective for isolating the influence of sum and difference scattering on the azimuthal modal amplitudes at the scattered frequencies. This demonstrates the key benefits of this bench-top experimental rig, which has been designed and controlled in a way which allows such a quantity to be estimated, revealing specific characteristics of the scattered noise which would not be easily observed otherwise.

Figure 6.6: Δ_{SPL} of modal amplitudes of scattered tones above the noise floor of the fan, at a frequency of $T + (1 \times BPF)$. The $m = 0$ mode is targeted in this case.

Figure 6.7: Δ_{SPL} of modal amplitudes of scattered tones above the noise floor of the fan, at a frequency of $T + (1 \times BPF)$. The $m = 1$ mode is targeted in this case.

Figure 6.8: Δ_{SPL} of modal amplitudes of scattered tones above the noise floor of the fan, at a frequency of $T + (1 \times BPF)$. The $m = 2$ mode is targeted in this case.

Figure 6.9: Δ_{SPL} of modal amplitudes of scattered tones above the noise floor of the fan, at a frequency of $T - (1 \times BPF)$. The $m = 0$ mode is targeted in this case.

Figure 6.10: Δ_{SPL} of modal amplitudes of scattered tones above the noise floor of the fan, at a frequency of $T - (1 \times BPF)$. The $m = 1$ mode is targeted in this case.

Figure 6.11: Δ_{SPL} of modal amplitudes of scattered tones above the noise floor of the fan, at a frequency of $T - (1 \times BPF)$. The $m = 2$ mode is targeted in this case.

Figure 6.12: Δ_{SPL} of modal amplitudes of scattered tones above the noise floor of the fan, at a frequency of $T + (2{\times}BPF)$. The $m = 0$ mode is targeted in this case.

Figure 6.13: Δ_{SPL} of modal amplitudes of scattered tones above the noise floor of the fan, at a frequency of $T + (2{\times}BPF)$. The $m = 1$ mode is targeted in this case.

Figure 6.14: Δ_{SPL} of modal amplitudes of scattered tones above the noise floor of the fan, at a frequency of $T + (2 \times BPF)$. The $m = 2$ mode is targeted in this case.

6.1.3 Effect of Changing Stator Vane Count

In Sections 6.1.1 and 6.1.2 it was demonstrated that frequency and modal scattering behaviour is dependent on the modal content of the incident noise as well as the fan-stator blade and vane counts. An eight-vane stator was located adjacent to a five-blade fan in these tests. In order to further investigate the veracity of Equation 6.2, the eight-vane stator stage was swapped for an alternative five-vane stator, and the test procedure repeated. Tables 6.6 – 6.8 collate the solutions to Equation 6.2 for the alternative fan-stator configuration investigated in the following test results.

As the number of fan blades and stator vanes is equal to 5 for the alternative fan-stator set-up, any modal scattering is predicted to occur into modes $m_{scatt} = \text{TAM} \pm 5u$, where u is a positive integer. Figures 6.15 – 6.23 show (for a range of test frequencies, targeted azimuthal modes and scattering harmonics) the Δ_{SPL} levels for each azimuthal mode order measured at the sensor array. These results show that scattering again occurs according to Equation 6.2 for the different number of stator vanes, and that modal scattering occurs

Table 6.6: Scattered modes predicted as per Equation 6.2, with the $m = 0$ mode dominant at the incident tone. $B = 5, V = 5$.

	Scattered Mode Order (m_{scatt})						Cut-On Frequency of m_{scatt} (Hz)				
q	$k=-2$	$k=-1$	$k=0$	$k=1$	$k=2$	q	$k=-2$	$k=-1$	$k=0$	$k=1$	$k=2$
-1	-5	0	5	10	15	-1	7005	0	7005	12853	18584
1	-15	-10	-5	0	5	1	18584	12853	7005	0	7005
2	-20	-15	-10	-5	0	2	24261	18584	12853	7005	0

Table 6.7: Scattered modes predicted as per Equation 6.2, with the $m = 1$ mode dominant at the incident tone. $B = 5, V = 5$.

	Scattered Mode Order (m_{scatt})						Cut-On Frequency of m_{scatt} (Hz)				
q	$k=-2$	$k=-1$	$k=0$	$k=1$	$k=2$	q	$k=-2$	$k=-1$	$k=0$	$k=1$	$k=2$
-1	-4	1	6	11	16	-1	5806	2001	8190	14005	19723
1	-14	-9	-4	1	6	1	17444	11696	5806	2001	8190
2	-19	-14	-9	-4	1	2	23129	17444	11696	5806	2001

Table 6.8: Scattered modes predicted as per Equation 6.2, with the $m = 2$ mode dominant at the incident tone. $B = 5, V = 5$.

	Scattered Mode Order (m_{scatt})						Cut-On Frequency of m_{scatt} (Hz)				
q	$k=-2$	$k=-1$	$k=0$	$k=1$	$k=2$	q	$k=-2$	$k=-1$	$k=0$	$k=1$	$k=2$
-1	-3	2	7	12	17	-1	4587	3335	9365	15154	20860
1	-13	-8	-3	2	7	1	16300	10534	4587	3335	9365
2	-18	-13	-8	-3	2	2	21995	16300	10534	4587	3335

most strongly into azimuthal mode order predicted by Equation 6.2 when $k = 0$ and $q = 0$.

With the change of stator geometry, the solutions of m_{scatt} are affected when $k \neq 0$. However, the same modal scattering behaviour is predicted for both fan-stator configuration when $k = 0$, as highlighted using red circles in the Δ_{SPL} results for the $q = 1$ scattering harmonic. The lower stator count leads to more solutions to m_{scatt} in Equation 6.2 being cut-on for the five-vane stator set-up than for the eight-vane stator set-up. Solutions to Equation 6.2 for values of k as high as ± 3 are observed for the five-vane results which were not cut-on in any of the test results from the eight-vane stator investigation.

It is generally observed that stronger modal scattering occurs into the $k \neq 0$ solutions for Equation 6.2 than was observed for the eight-vane stator configuration. This may be linked to the stronger BPF generation observed for the five-vane stator stage in Section 5.4, which is caused by a stronger interaction between the periodic fan noise and the stator stage. It is possible that the noise scattered at the fan stage in frequency also interacts with the stator stage more strongly than was the case for the eight-vane stage.

Figure 6.15: Δ_{SPL} of modal amplitudes of scattered tones above the noise floor of the fan, at a frequency of $T + (1 \times BPF)$. The $m = 0$ mode is targeted in this case.

Figure 6.16: Δ_{SPL} of modal amplitudes of scattered tones above the noise floor of the fan, at a frequency of $T + (1 \times BPF)$. The $m = 1$ mode is targeted in this case.

Figure 6.17: Δ_{SPL} of modal amplitudes of scattered tones above the noise floor of the fan, at a frequency of $T + (1 \times BPF)$. The $m = 2$ mode is targeted in this case.

Figure 6.18: Δ_{SPL} of modal amplitudes of scattered tones above the noise floor of the fan, at a frequency of $T - (1 \times BPF)$. The $m = 0$ mode is targeted in this case.

Figure 6.19: Δ_{SPL} of modal amplitudes of scattered tones above the noise floor of the fan, at a frequency of $T - (1 \times BPF)$. The $m = 1$ mode is targeted in this case.

Figure 6.20: Δ_{SPL} of modal amplitudes of scattered tones above the noise floor of the fan, at a frequency of $T - (1 \times BPF)$. The $m = 2$ mode is targeted in this case.

Figure 6.21: Δ_{SPL} of modal amplitudes of scattered tones above the noise floor of the fan, at a frequency of $T + (2 \times BPF)$. The $m = 0$ mode is targeted in this case.

Figure 6.22: Δ_{SPL} of modal amplitudes of scattered tones above the noise floor of the fan, at a frequency of $T + (2 \times BPF)$. The $m = 1$ mode is targeted in this case.

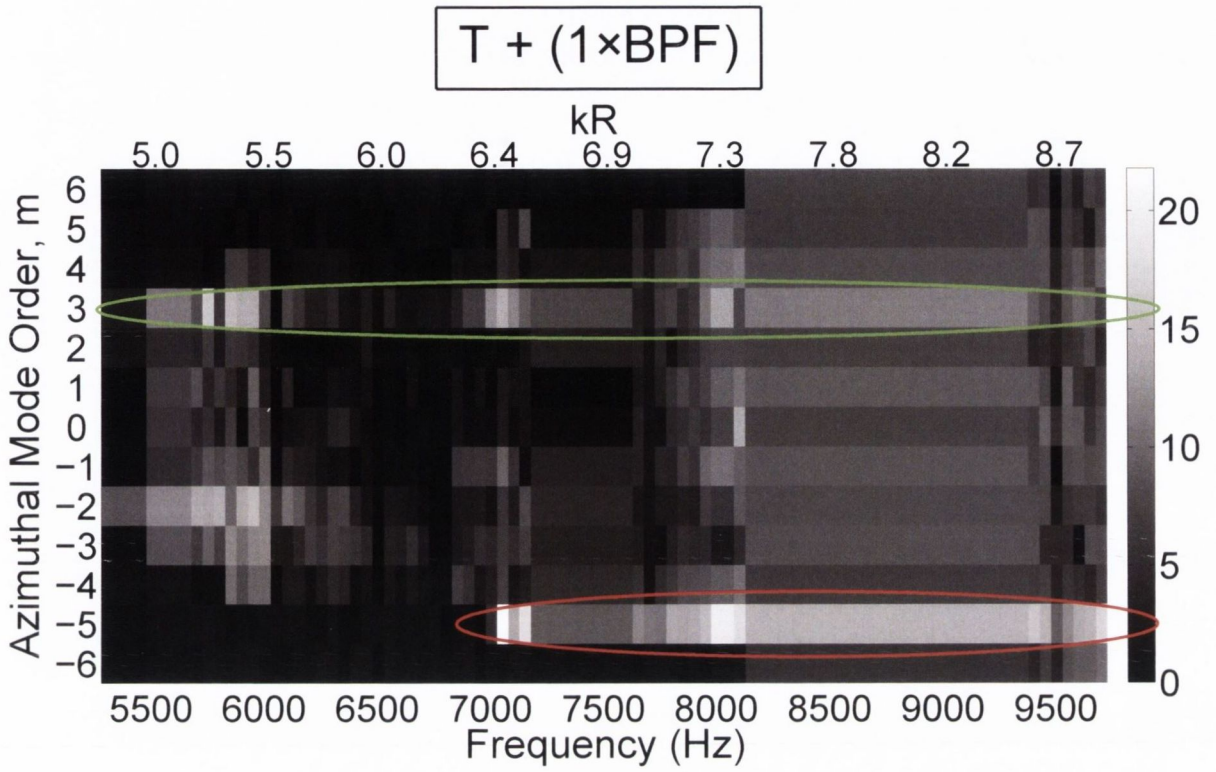**Figure 6.23:** Δ_{SPL} of modal amplitudes of scattered tones above the noise floor of the fan, at a frequency of $T + (2 \times BPF)$. The $m = 2$ mode is targeted in this case.
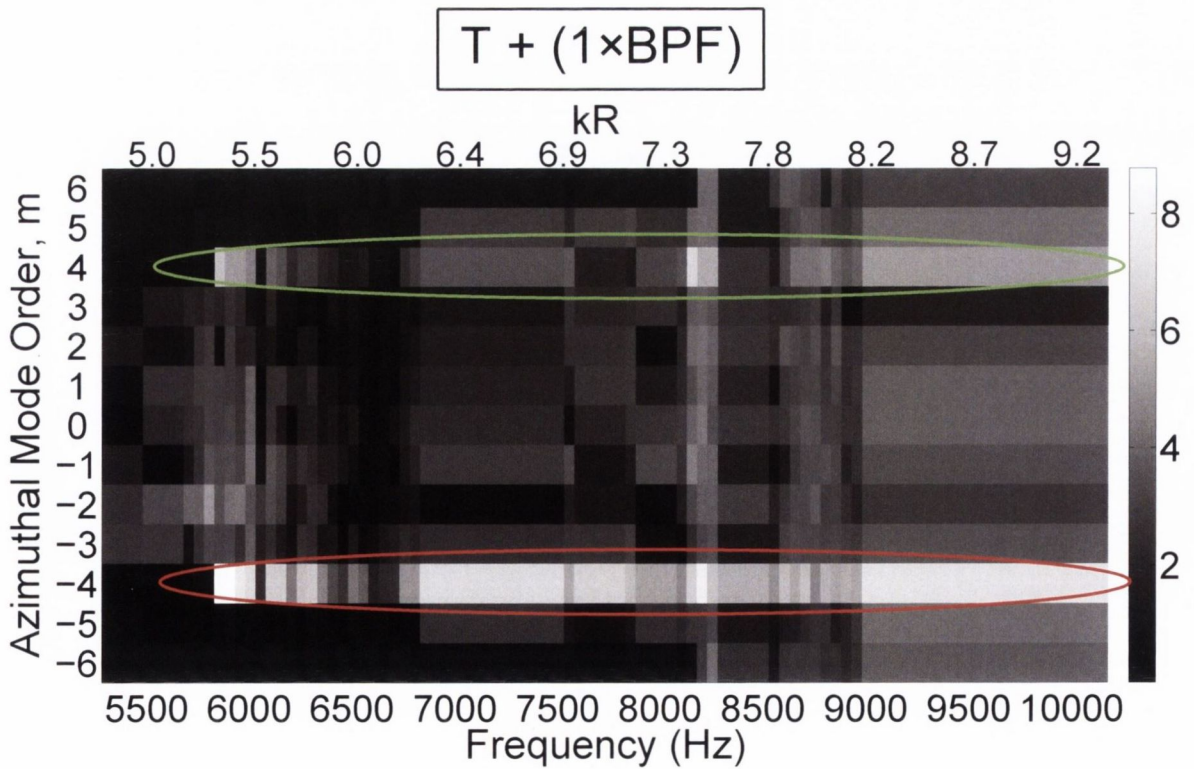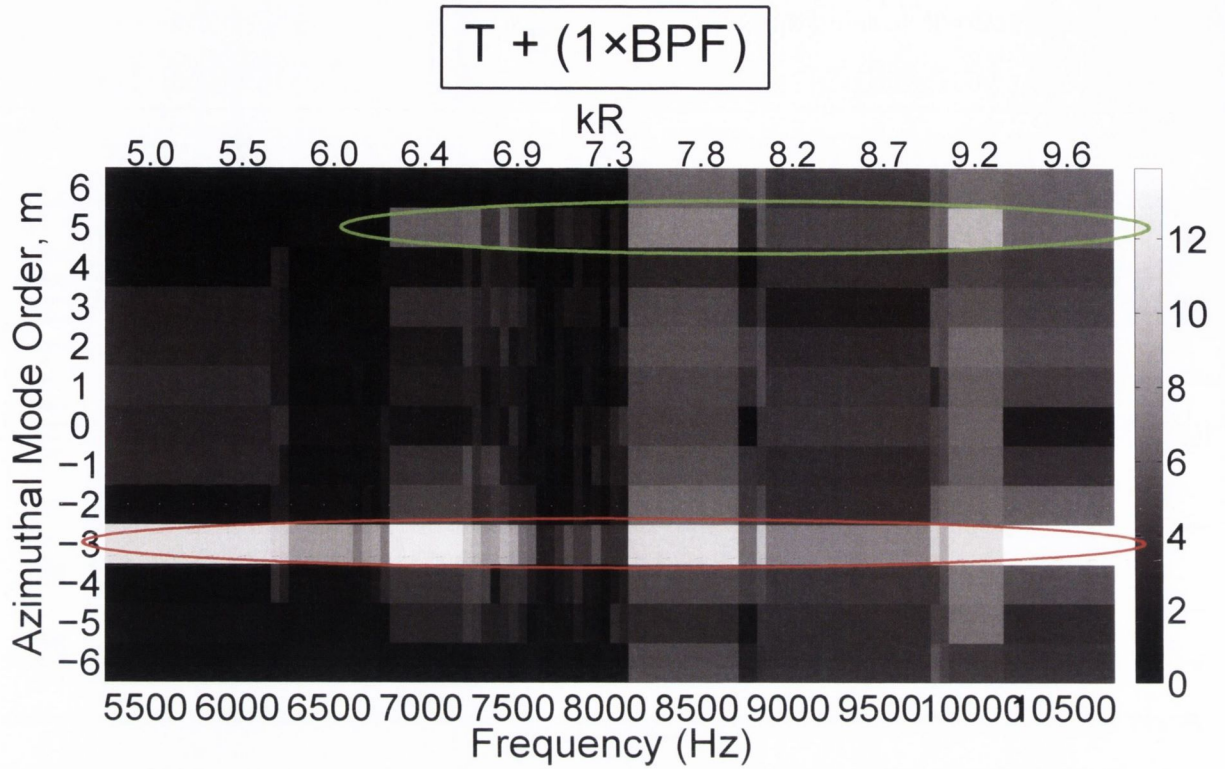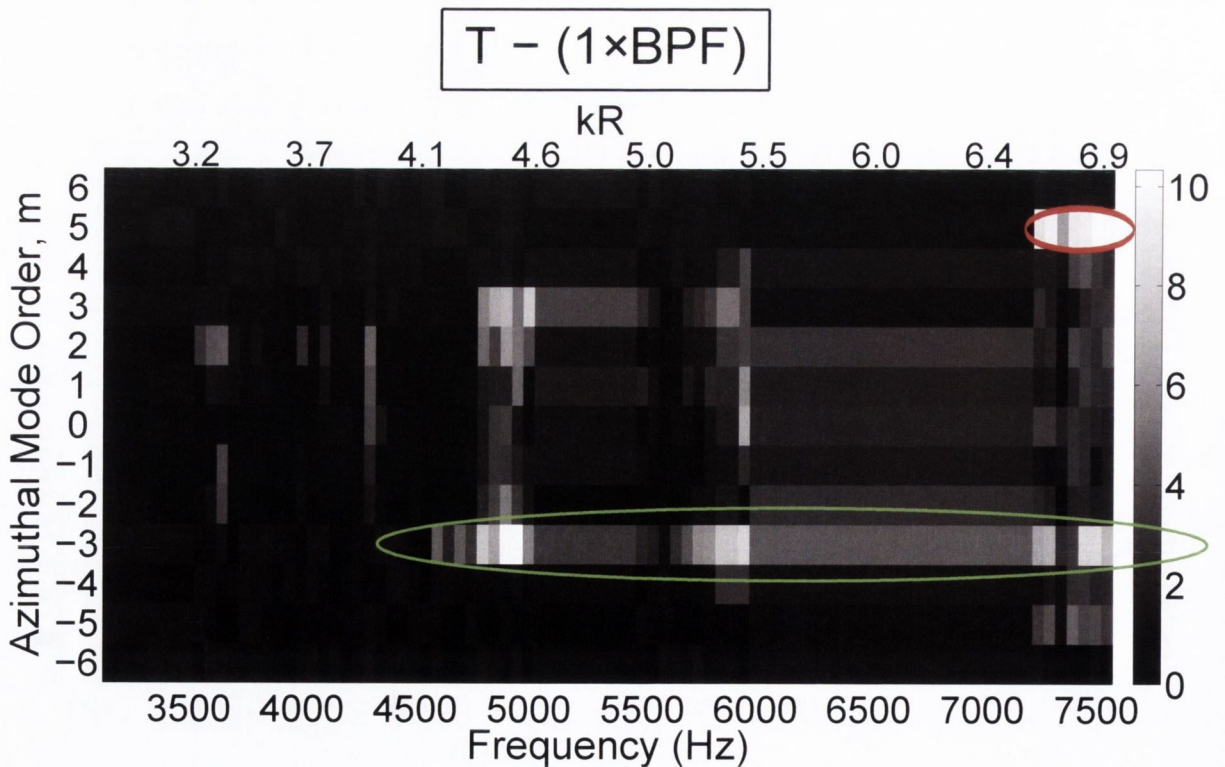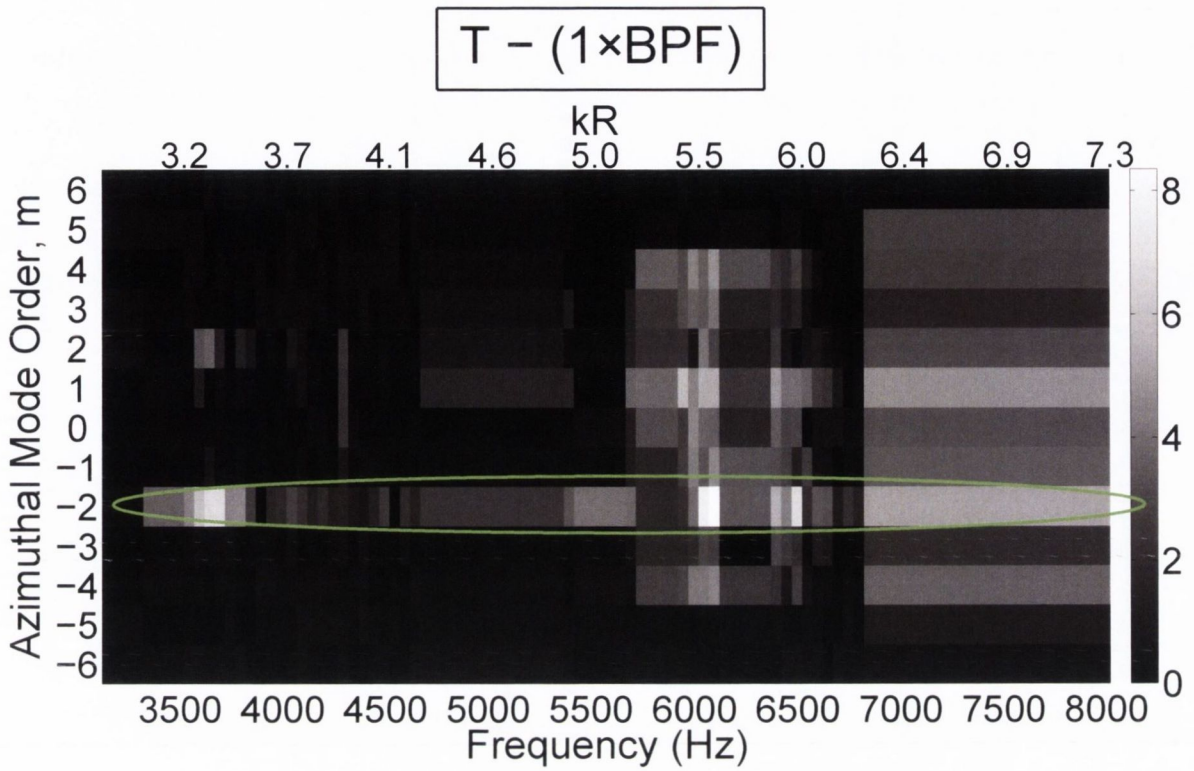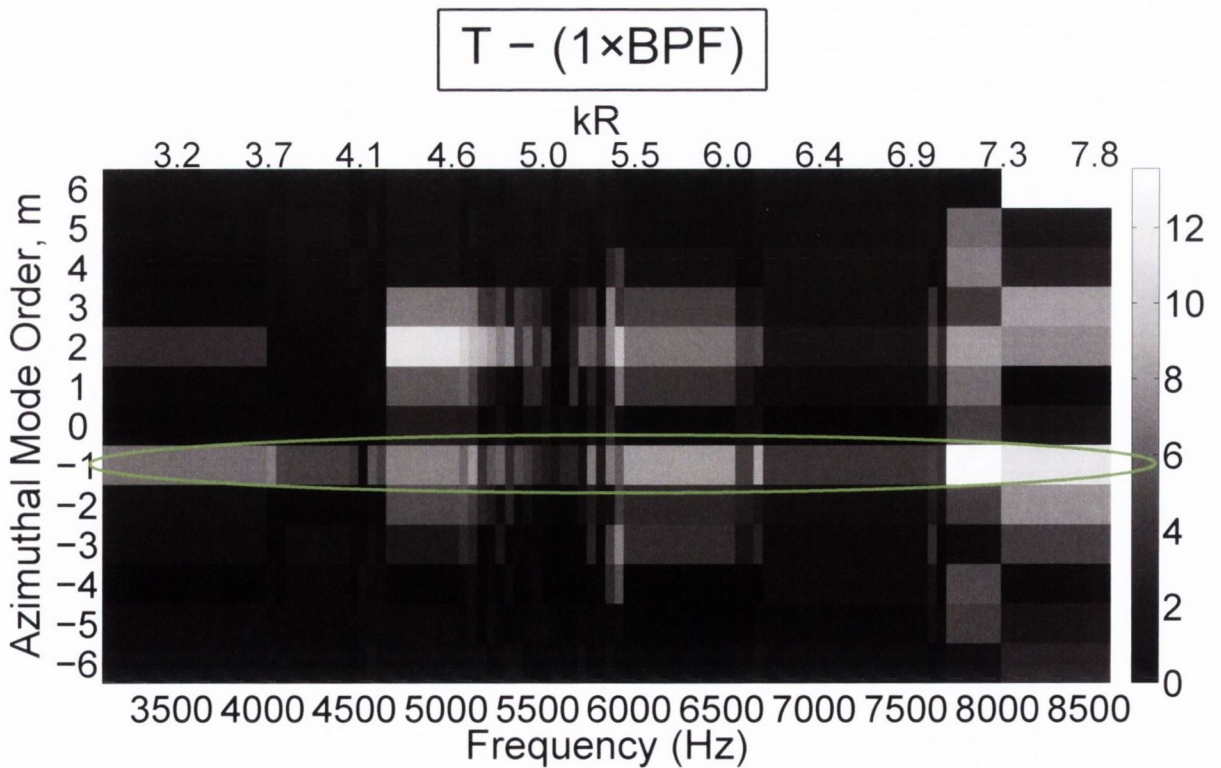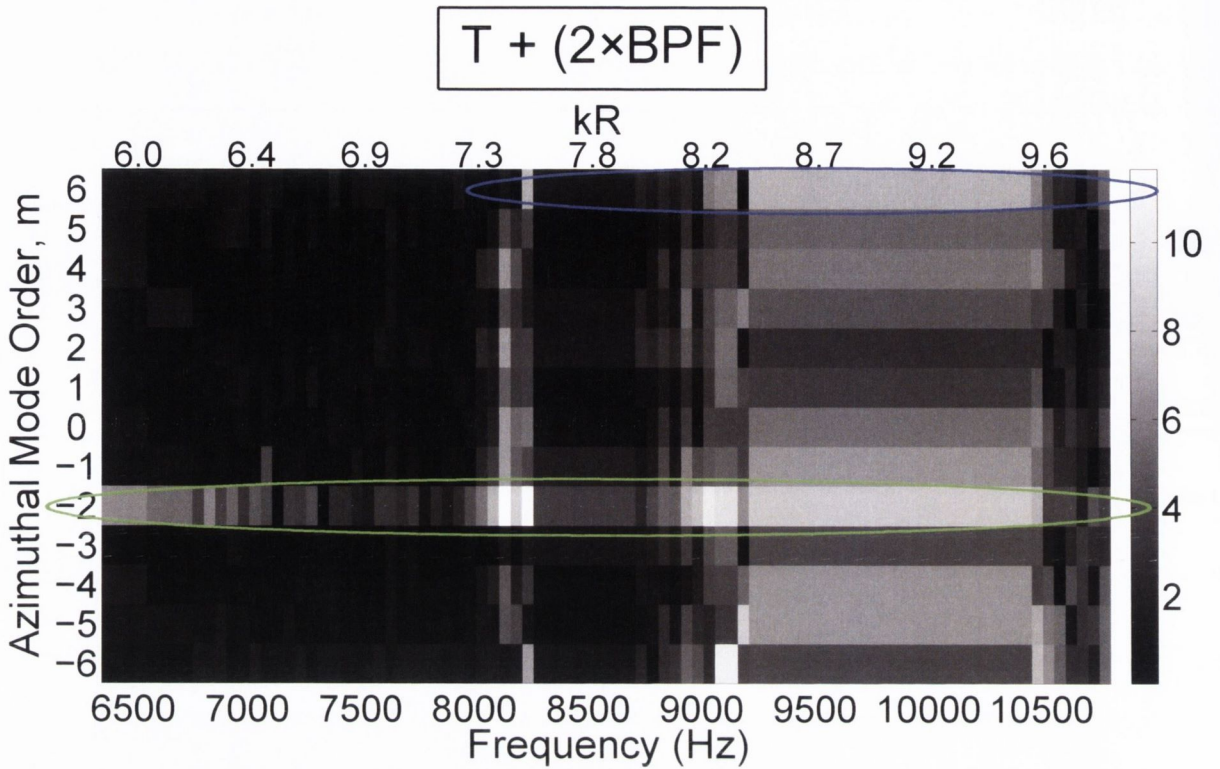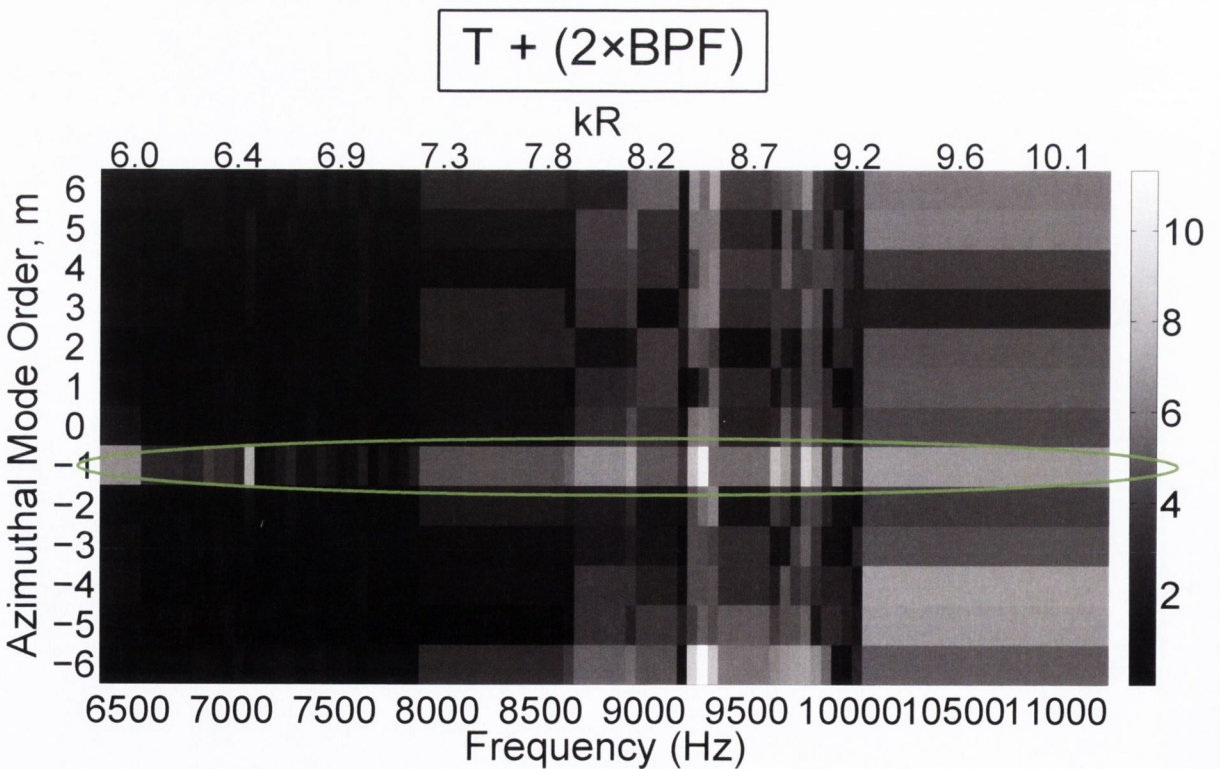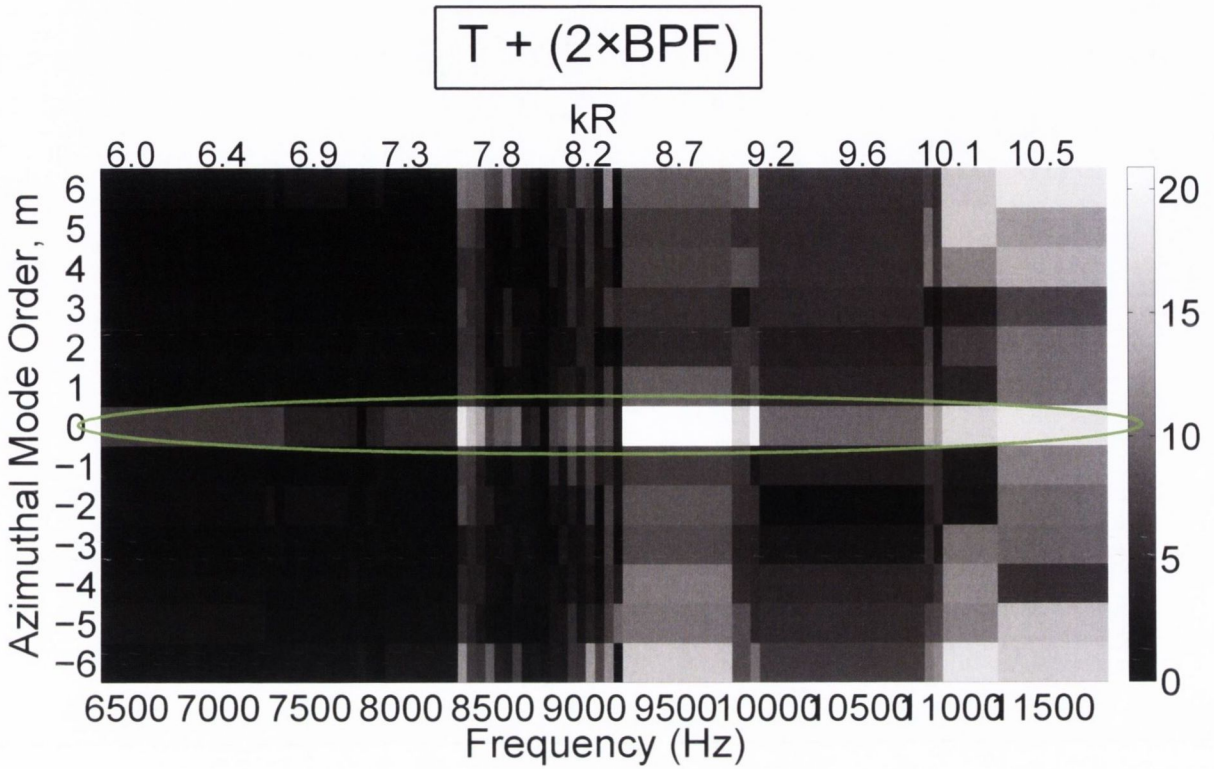
6.2   Narrowband Scattering Results

In Section 6.1, experimental tests were undertaken to investigate the sum and difference scattering of tonal noise through a fan stage. Studies by Bennett *et al.* [6, 62, 77] have shown that scattering of non-tonal noise is also possible. However, the focus is put on periodic noise in the existing literature as the propagation of fan BPF tones through rows of several rotor stages is commonly observed in aeroengine compressors.

The possibility of sum and difference scattering of semi-periodic or non-periodic noise is of great interest, as it can result in scattering of noise across a broad spectral range. Scattering of tonal noise is generally simply observed in any measurement spectra, as the sum and difference scattering frequencies can be predicted as $f_{scatt} = f + qf_{BPF}$, where q is a non-zero integer denoting the scattering harmonic and f_{BPF} is the fan blade-pass frequency. However, if noise is scattered across a broad spectral range, scattered and incident noise could potentially overlap in the measured spectra. This leads to a complex case, as scattered noise has been shown to be measured with low coherence between measurements upstream and downstream of the rotor stage (see Section 4.4). It is unknown how overlapping between the incident and scattered noise will affect these coherences. Furthermore, the scattering of modes at scattered frequencies due to interaction between the incident noise and a fan has been demonstrated in Section 6.1. If the incident and scattered noise overlap, the modal content at the overlapping frequencies could contain contributions from both the incident and scattered noise.

In order to investigate scattering of non-tonal noise, narrowband source signals were used to drive a single loudspeaker, located at one end of the duct. An example of a narrowband noise source signal is shown in Figure 6.25 in its time-domain and frequency-domain representations. Narrowband noise is generated by band-pass filtering random broadband noise. Both the centre frequency (CF) and bandwidth (BW) of the source noise can be adjusted between tests. The experimental rig used is a modification of the experimental rig outlined in Section 5.2 and shown schematically in Figure 5.5. The modified experimental schematic is shown in Figure 6.24. The mode generator and upstream semi-anechoic termination have been removed. A single BMS 4540ND loudspeaker has been placed at the entrance plane to the duct, located at the upstream open end. As

in Section 6.1, the test procedure is to analyse and compare both spectra from single microphones and azimuthal modal analysis results when:

- the fan is rotating;

- the loudspeaker generates narrowband noise;

- both the fan is rotating and the loudspeaker generates narrowband noise.

Azimuthal modal analyses at frequencies of interest were performed using the array of 25 microphones.

A = Single Loudspeaker

B = Fan-Stator Stage

C = Microphone Array

D = Semi-Anechoic Termination

E = Source Microphone
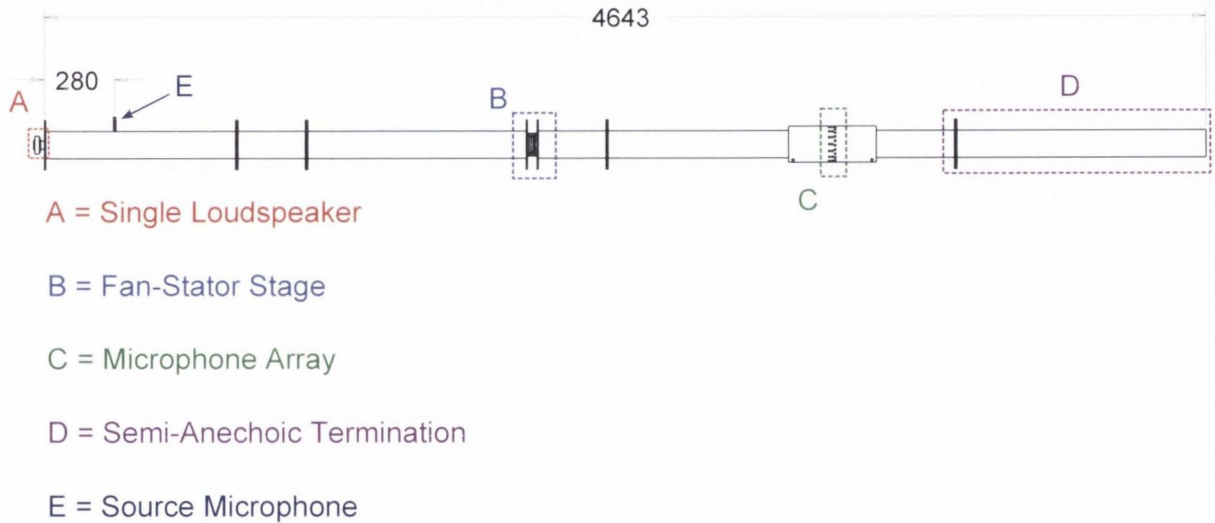
Figure 6.24: Experimental rig used to investigate narrowband frequency and modal scattering at sum and difference frequencies. All dimension in *mm*.

In order to draw clear relationships between the incident and scattered modes, it is beneficial to have a single azimuthal mode dominant at the incident noise frequencies. This was achieved using the mode generator array in the tonal test campaign. However, the mode generator array is not effective at targeting modes across a range of frequencies simultaneously. It was found however that narrowband noise generated by a single loudspeaker at the upstream end will propagate in the duct with the $m = 0$ mode dominant at many test frequencies, as demonstrated by results of a modal analysis undertaken when the loudspeaker generates narrowband noise shown in Figure 6.26. A possible explanation for this is that the loudspeaker membrane acts like a vibrating plane which
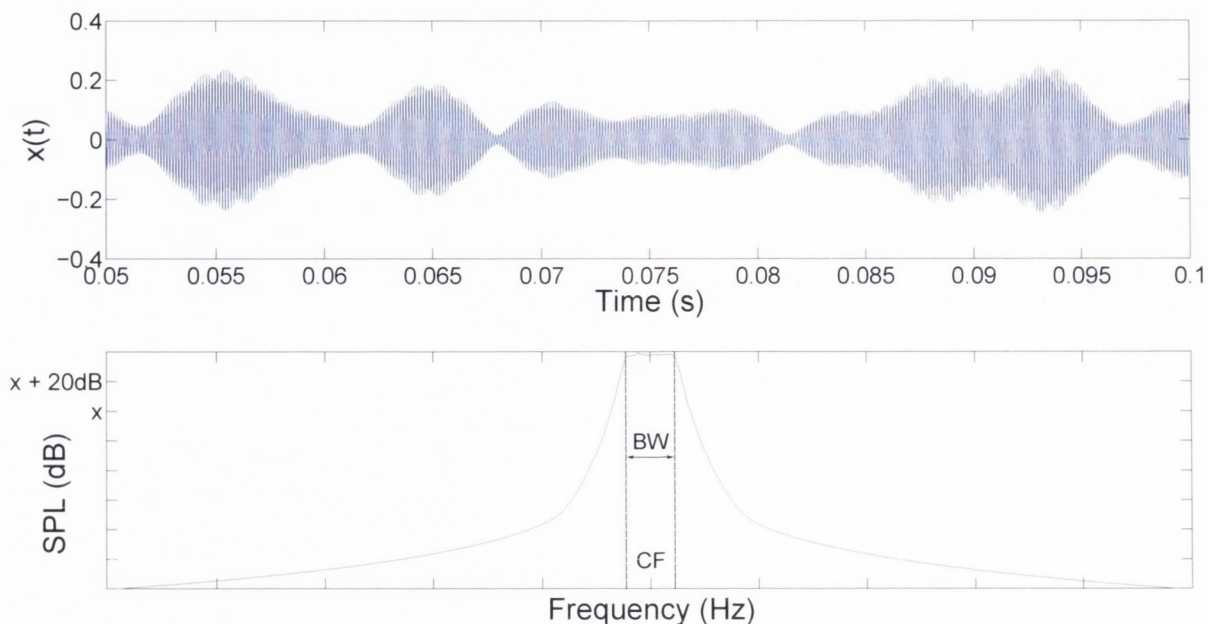
Figure 6.25: Time-domain representation (top) and auto-spectral density estimate (bottom) of a narrowband source signal of bandwidth BW and centre frequency CF. This signal was generated at a clock rate of $44100Hz$.

intrinsically excites a plane wave through the test duct. This means that it is possible to analyse modal scattering results without a mode generator, however being unable to target different azimuthal modes than the $m = 0$ mode limits the scope of the analysis.

Data was acquired at all microphones at a sampling rate of $26kHz$ for 40 seconds for each test point, allowing spectral analyses to be performed up to a frequency of $13kHz$. Azimuthal modal analyses could be performed using the microphone array up to the cut-on of the $(12,0)$ mode, which occurs at a frequency higher than the Nyquist frequency for the sampling rate used. Data was analysed using 252 blocks of time-domain data in an ensemble, each containing 4096 data points. This gives a frequency resolution of $6.34Hz$ in any spectral estimates.

6.2.1   Single Microphone Spectral Analysis

Narrowband tests were undertaken where a single loudspeaker generates a narrowband signal, and the resulting noise measured by a single microphone in the sensor array. For each test point the centre frequencies (CF) and bandwidths (BW) of the narrowband noise were changed. All tests were then repeated with both the loudspeaker generating
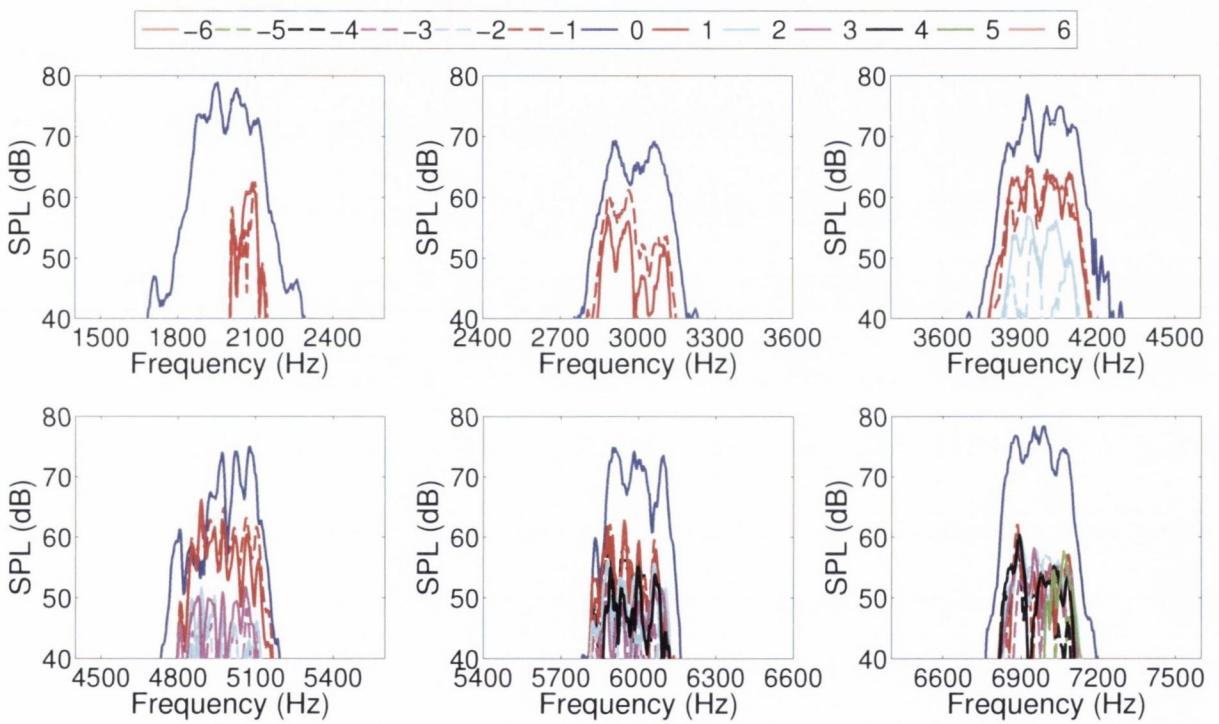
Figure 6.26: SPL spectra from an azimuthal modal analysis of narrowband noise gener-
ated by a single loudspeaker at a range of centre frequencies, BW = 200. The top legend
relates each coloured spectra to a specific azimuthal mode.

narrowband noise and the fan rotating at 13000rpm ($BPF = 1083Hz$) in order to isolate noise generated by the interaction between the incident narrowband noise and the fan-stator stage. Tests recording the fan-stator noise in isolation, without any noise generation at the loudspeaker, were also conducted.

Sound pressure level measurements when narrowband noise of bandwidth $200Hz$ is generated are shown in Figures 6.27 and 6.28 for a range of test centre frequencies. Each row of plots shows a different test frequency. Each column of plots centres on specific frequency ranges of interest, with the incident narrowband noise shown on the left and three potential scattering frequencies shown to the right. These figures centre on spectral ranges where interaction noise is anticipated to appear. The red spectrum shown the sound pressure level of the noise floor generated by the fan, the green spectrum shows the narrowband noise generated by the loudspeaker and the blue spectrum shows the spectrum measured when both the loudspeaker generates noise and the fan is rotating. Any acoustic energy measured in the blue spectrum not present in either the red or green spectra will have been generated by the interaction between the fan and the incident narrowband noise. All test frequencies were selected as the $m = 0$ mode was dominant at each narrowband source frequency, as demonstrated in Figure 6.26.

The investigation of tonal noise scattering undertaken in Section 6.1 demonstrated that for scattering of noise where the $m = 0$ was dominant at the incident tone, scattering of noise became apparent in the measurement spectra above the cut-on of the $m = 3$ mode at around $4587Hz$ at a frequency of $CF + (1 \times BPF)$. More significant scattering of noise was observed above the cut-on of the $m = -5$ mode at around $7005Hz$ at this same scattering harmonic. In the narrowband results shown in Figures 6.27 and 6.28, it was found that the onset of narrowband noise scattering at a frequency of $CF + (1 \times BPF)$ follows this same pattern. This is also the case for the other scattering frequencies, $CF - (1 \times BPF)$ and $CF + (2 \times BPF)$ – the onset of significant scattering of noise at these frequencies coincides with the cut-on of scattered modes predicted by Equation 6.2 and tabulated in Table 6.2. This would strongly suggest that the same rules governing the scattering of tonal noise are maintained for scattering of noise over a broader spectral range. Any noise scattered at sum and difference frequencies has a similar spectral shape as the incident noise, and for high test frequencies the noise scattered at $CF + (1 \times BPF)$ is of a similar

magnitude to the narrowband noise generated by the loudspeaker.

Further experimental test results are shown in Figure 6.29, again showing narrowband noise scattering as measured by a single microphone for a wider bandwidth source signal (BW = $400Hz$), in an alternative format. The frequency-axis is this case shows the kR values, more clearly illustrating the relationship between the cut-on of scattered modes predicted in Table 6.2 and the onset of significant sum and difference scattering.

As in the investigation of scattering of tonal noise, it is pertinent to undertake an azimuthal modal analysis of these experimental results in order to investigate this scattering of noise more deeply. In particular, modal analysis will allow links to be drawn between the modal content of the incident noise and the modal content of the scattered noise to confirm that the modal scattering mechanism which underlies the scattering of tonal noise also underpins the scattering of noise over a broader spectral range.

6.2.2   Modal Analysis at Incident and Scattered Frequencies

In Figures 6.27 – 6.29, spectral results were presented for a single microphone measuring the narrowband noise at both scattered and incident frequencies for a range of narrowband centre frequencies and bandwidths. Figures 6.30 – 6.31 present the azimuthal modal analyses for the test points shown in Figures 6.27 and 6.28 where narrowband noise was generated with a bandwidth of $200Hz$. Rather than simply plotting the absolute sound pressure levels of each azimuthal mode, the sound pressure levels of each mode above the noise floor of the fan are plotted instead. This gives the Δ_{SPL} of each mode, as applied in the analysis of the scattering of tonal noise in Section 6.1.2. This isolates the contribution of the noise generated by the interaction of the fan-stator and the incident noise to the azimuthal modal amplitudes at the scattered frequencies $CF + (q \times BPF)$.

Figures 6.30 and 6.31 show the Δ_{SPL} amplitudes of the azimuthal acoustic modes in a format similar to Figures 6.27 and 6.28. Modal scattering is shown in these results to occur in the same way as in the tonal noise tests, with significant scattering occurring into the modes predicted by Equation 6.2 and collated in Table 6.2. The corresponding azimuthal mode orders for each colour spectra are shown above Figure 6.30. The modal scattering patterns are the same as was observed for the tonal tests when the $m = 0$ mode was targeted at the mode generator tone, showing for example significant scattering into
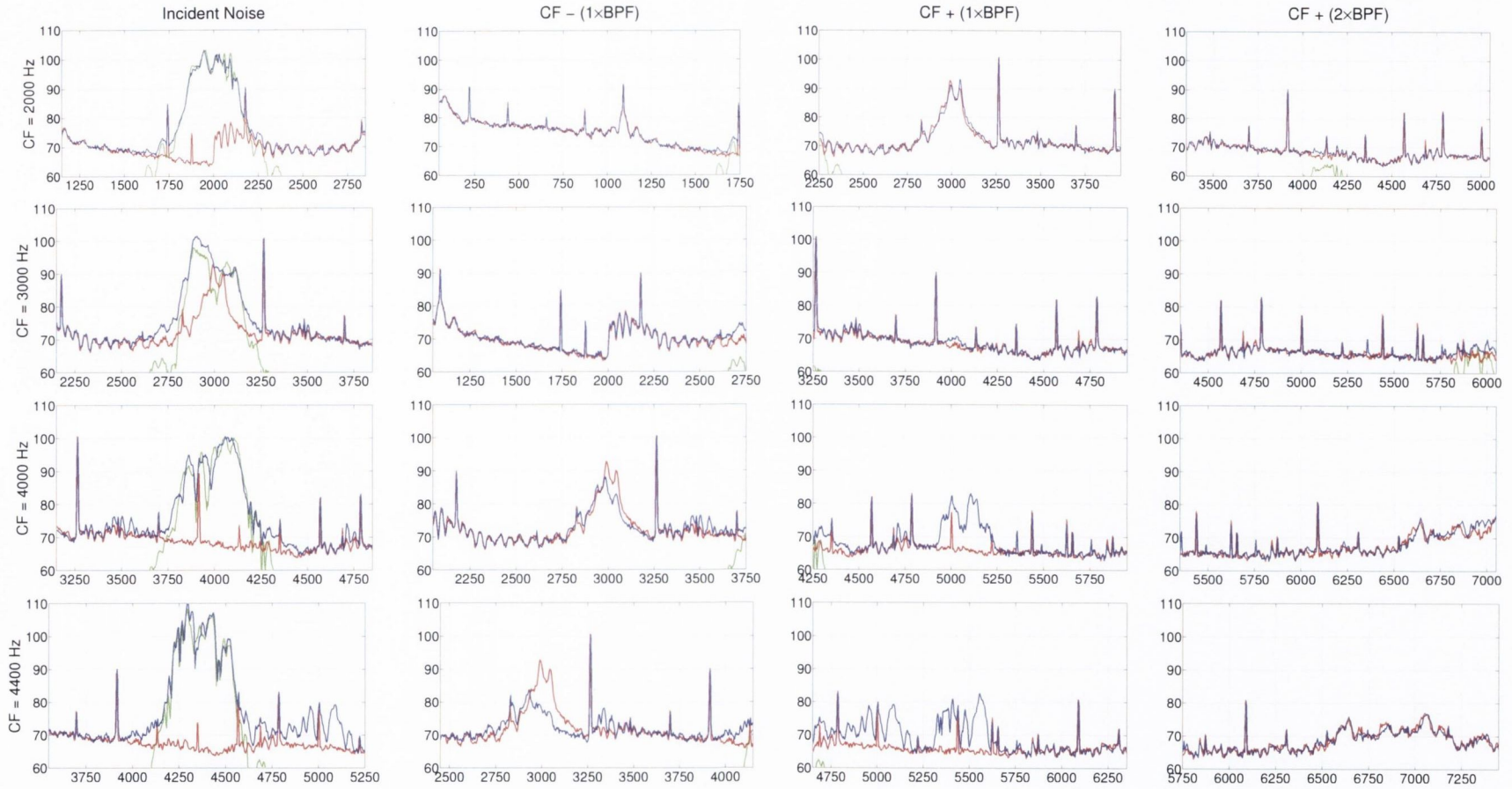
Figure 6.27: Auto-spectra estimated by a single microphone in the sensor array for a range of incident noise centre frequencies. The red spectrum was measured when the fan is rotating at 13000rpm. The green spectrum was measured when a single loudspeaker generates narrowband noise of bandwidth $200Hz$. The blue spectrum was measured when both the fan is rotating and a single loudspeaker generates narrowband noise, of bandwidth $200Hz$.
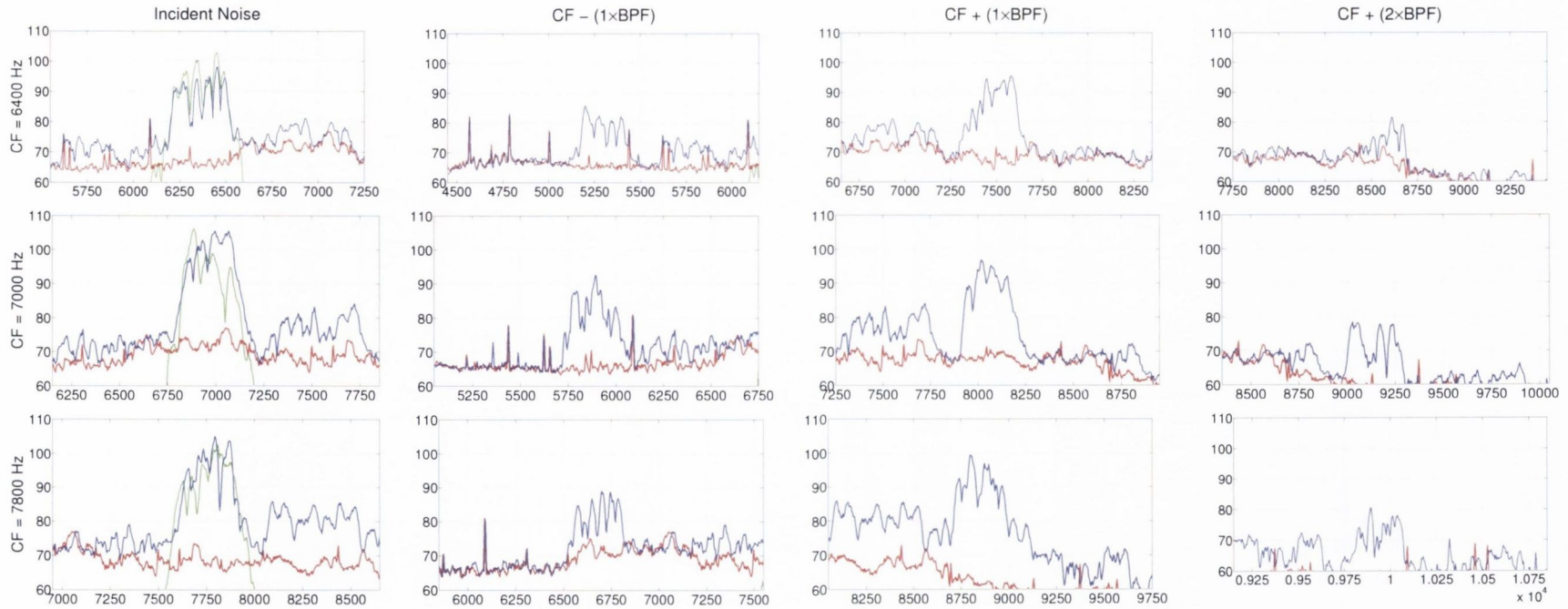
Figure 6.28: Auto-spectra estimated by a single microphone in the sensor array for a range of incident noise centre frequencies. The red spectrum was measured when the fan is rotating at 13000rpm. The green spectrum was measured when a single loudspeaker generates narrowband noise of bandwidth $200Hz$. The blue spectrum was measured when both the fan is rotating and a single loudspeaker generates narrowband noise of bandwidth $200Hz$.
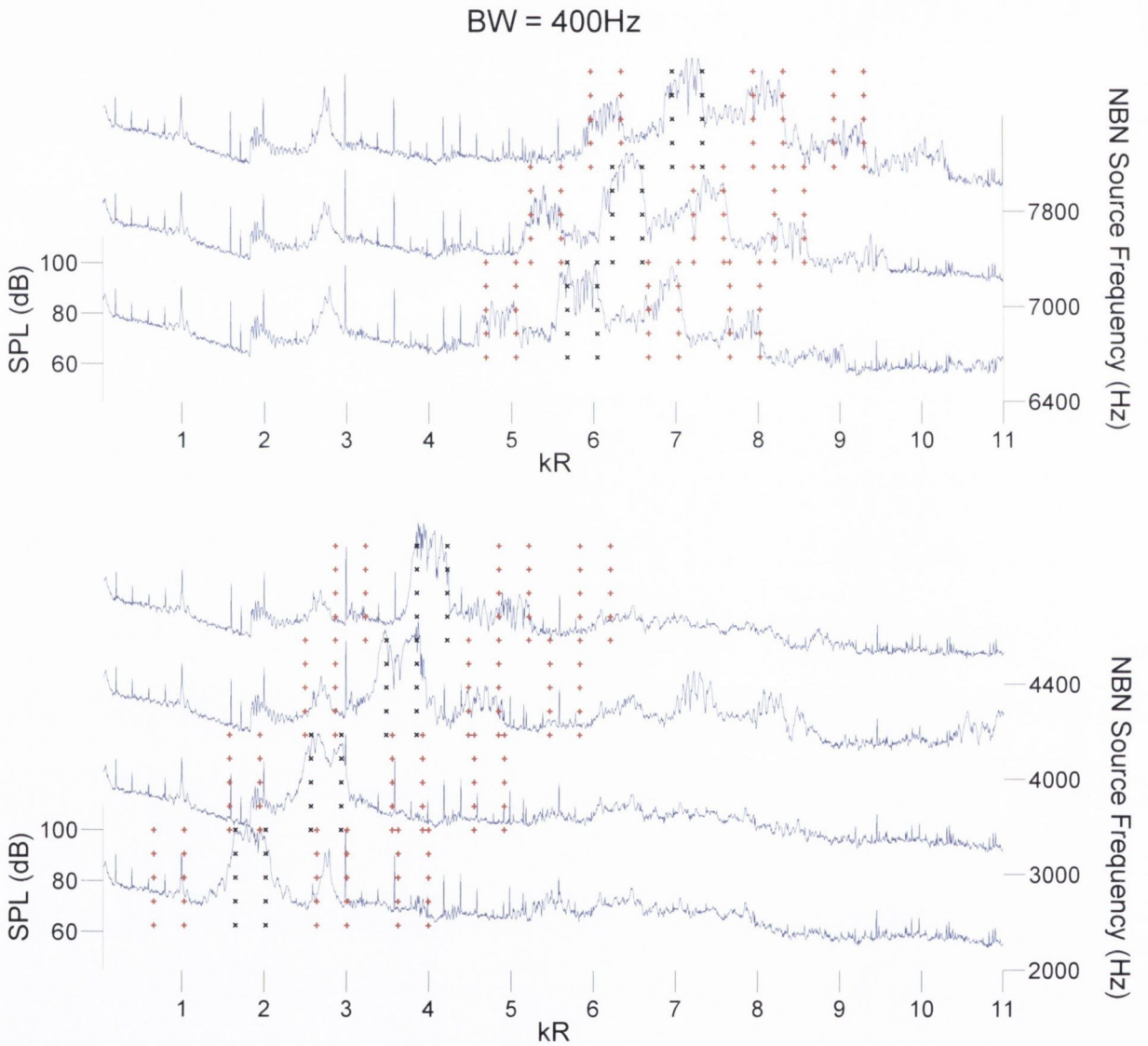
Figure 6.29: Waterfall plots of narrowband scattering observed for several test frequencies, BW = $400Hz$.

the $m = -5$ mode at a frequency of $T + (1 \times BPF)$, and also lower amplitude yet still significant scattering into the $m = 3$ mode. The scattering observed into the $m = -3$ mode at a frequency of $T - (1 \times BPF)$ and the $m = 2$ mode at a frequency of $T + (2 \times BPF)$ also matches the scattering modes predicted by Equation 6.2.

6.2.3 Spectral Overlapping of Incident and Scattered Noise

The narrowband scattering results presented thus far have focused on the sound pressure levels of the acoustic modes at both the incident and scattered frequencies, and the relationships between these acoustic modes. The bandwidths of the narrowband signals used to generate the loudspeakers were smaller than the fan BPF $(1083Hz)$, and therefore no overlapping of the noise at incident and scattered frequencies was observed. The possibility of such overlapping is interesting, as the acoustic pressure field in the overlapping frequency range could contain contributions of both the incident and scattered noise. As sum and difference scattering is a result of a quadratic interaction between the incident noise and the rotating fan, this also raises the possibility that the coherence between acoustic measurements made upstream and downstream of the fan could drop in this overlapping frequency range, due to the addition of a non-linear contribution to the system equation between both input and output measurements.

In Figure 6.32 the sound pressure level spectra from a single microphone in the sensor array are presented for three test points: the fan rotating at 13000rpm (BPF $= 1083Hz$); the loudspeaker generating narrowband noise of bandwith $1600Hz$ centred at $7000Hz$; and a third test with the previous two noise-sources both present. The bandwidth of the source narrowband noise generated by the loudspeaker is shown in A. The bandwidth of the anticipated scattered noise for the $q = 1$ scattering harmonic is shown in B.

Focusing on the $q = 1$ scattering harmonic, it is apparent in this figure that noise at a frequency of $CF + (1 \times BPF)$ is being scattered into the spectral range of the incident noise, as evident by the increase in the sound pressure levels in the overlapping region between A and B when both fan and loudspeaker are present. In order to isolate the contribution of this sum scattering to the total noise for this test point, and also ensure that the noise measured in this scattered frequency range is not merely the contribution of fan broadband self-noise, the sound pressure levels of the fan only and loudspeaker
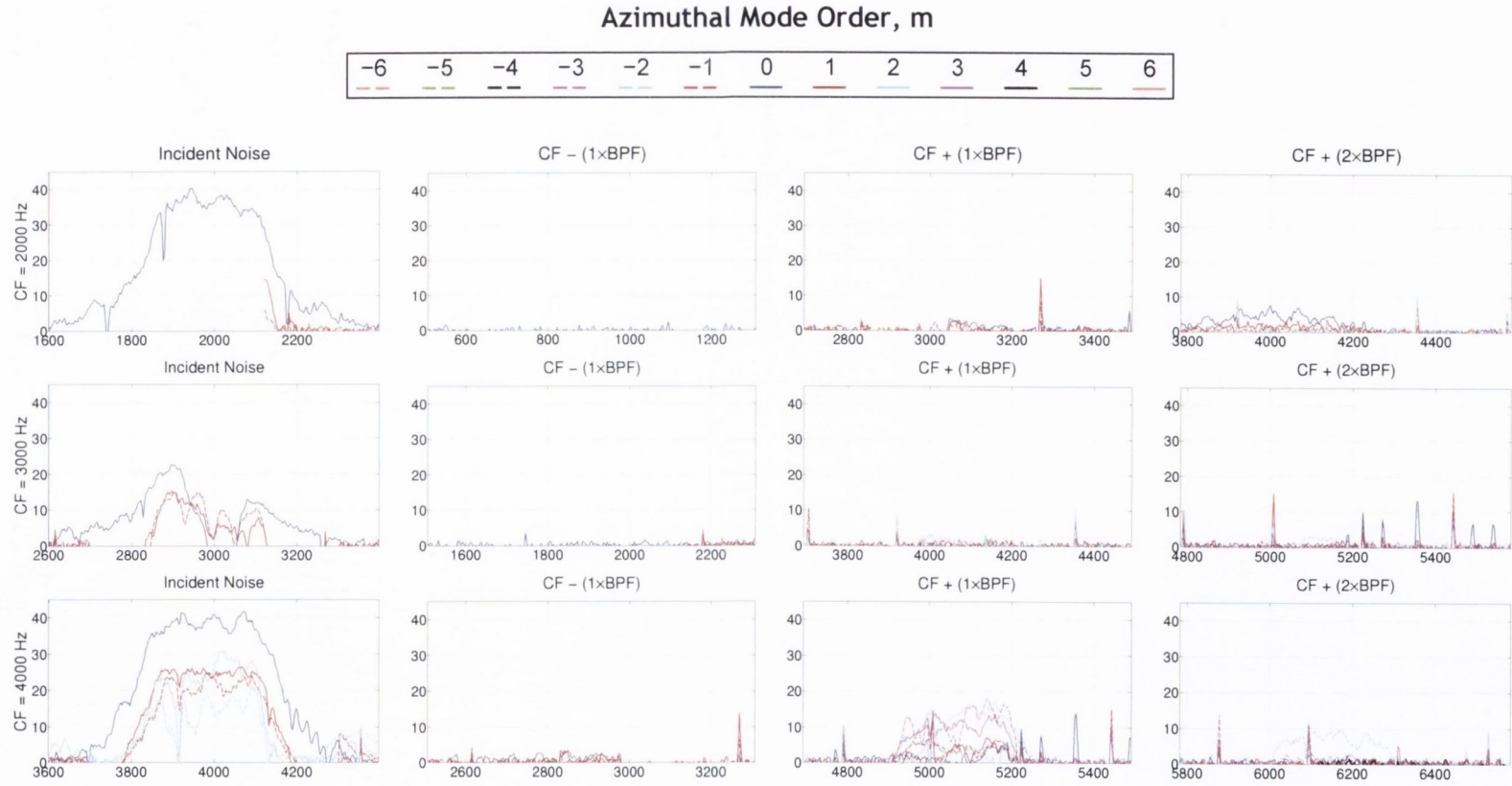
Figure 6.30: Azimuthal modal analysis performed at the sensor array. A single loudspeaker generates narrowband noise of bandwidth $200Hz$ and the fan is rotating at 13000rpm. Each spectrum plots the Δ_{SPL} levels (in dB) of each azimuthal mode with frequency.
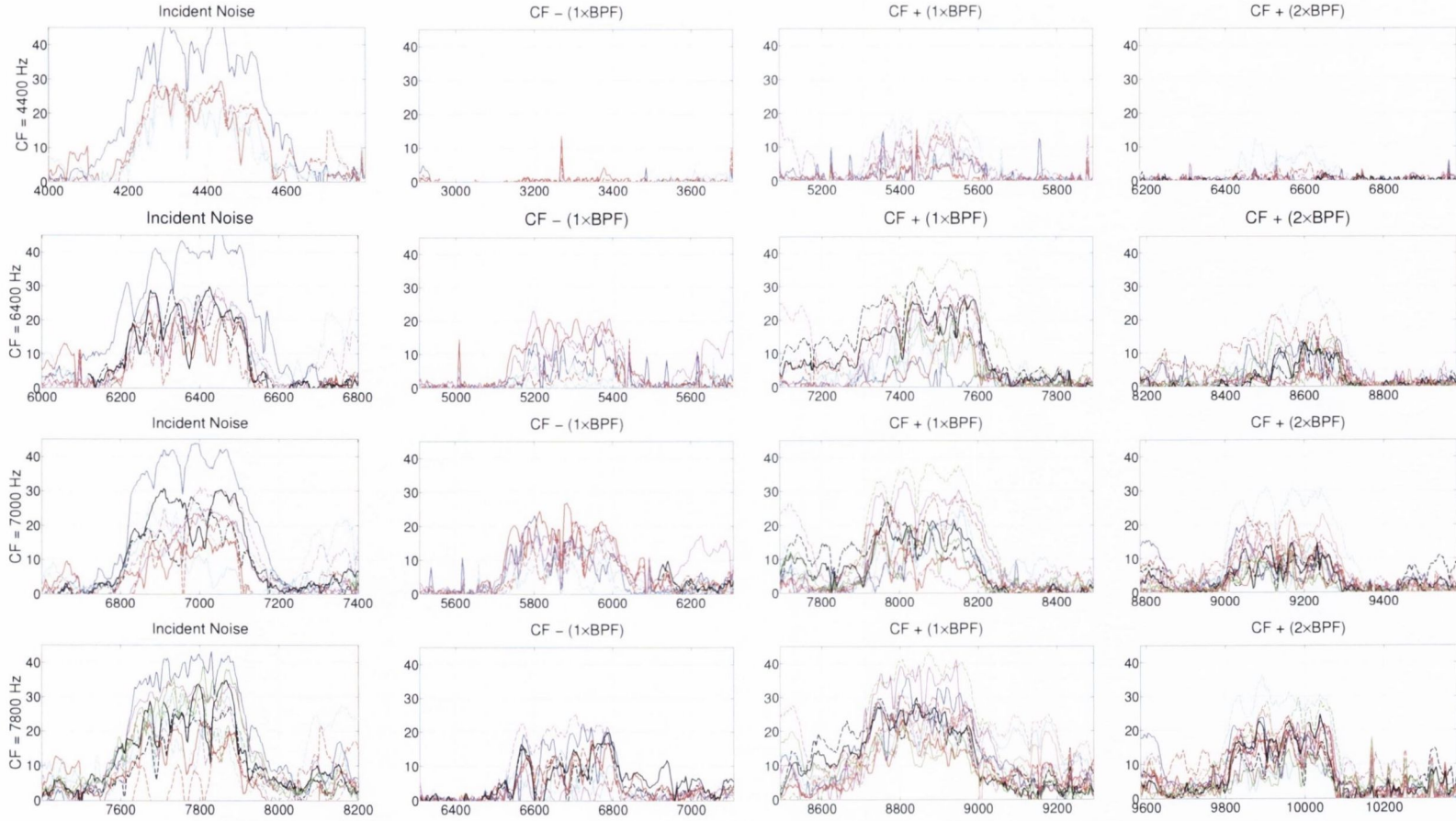
Figure 6.31: Azimuthal modal analysis performed at the sensor array. A single loudspeaker generates narrowband noise of bandwidth $200Hz$ and the fan is rotating at 13000rpm. Each spectrum plots the Δ_{SPL} levels (in dB) of each azimuthal mode with frequency.

only tests were summed (in Pa), and the difference in sound pressure level between this summation and the sound pressure levels measured when both noise-sources are present simultaneously was then calculated. The resulting measurement, which isolates the contribution of sum and difference interaction to the total noise measured when both noise-sources are present, is shown in Figure 6.33. This more clearly demonstrates that significant noise is scattered at a frequency of $CF + (1 \times BPF)$ which overlaps with the incident noise, increasing the sound pressure levels by around $5dB$ in this frequency range. The spikey tonal nature of this spectra is a result of periodic fan noise which has modulated slightly between tests due to small variations in fan rotational speed.

Figure 6.34 shows the difference in modal sound pressure levels measured for the "NBN Only" and "Fan Only" cases, hence showing the sound pressure levels of the modal amplitudes excited by the loudspeaker above the broadband noise floor of the fan. As in the narrower bandwidth studies, the $m = 0$ mode dominates the incident noise.

The Δ_{SPL} quantity estimated in Sections 6.1.2 and 6.2.2 was calculated for the "NBN and Fan" test case shown in Figure 6.32. However, the Δ_{SPL} quantity is estimated differently in this case. The quantity was calculated by measuring the difference between the modal sound pressure levels measured for the "NBN and Fan" test case, and the summation of the sound pressure levels measured for the "Fan Only" and "NBN Only" test cases. This is essentially the same procedure as was used to estimate the spectrum shown in Figure 6.33 from the spectra in Figure 6.32, but on a modal basis. The resulting Δ_{SPL} estimate is plotted in Figure 6.35, and isolates the modal sound pressure levels of the scattered noise from the contributions of the NBN source and fan broadband noise.

The $m = -5$ and $m = 3$ modes dominate the scattered noise for the $q = 1$ scattered harmonic shown in Figure 6.35. These are the dominant scattering modes predicted for Equation 6.2 when the $m = 0$ mode dominates the incident noise generated by the upstream loudspeaker. This further demonstrates, as was observed in Figure 6.2.2, that modal scattering behaviour is accurately predicted by Equation 6.2.

By examining the results plotted in Figures 6.34 and 6.35 together, it can be concluded that the overlap region between the incident noise and scattered noise will contain contributions from both the acoustic modes excited by the incident noise and the scattered noise. This is an interesting test case, as it illustrates that broader-band noise could be

scattered and hence overlap spectrally downstream of rotating turbomachinery, with the acoustic pressure field possibly containing contributions of:

1. broadband fan noise;

2. periodic fan noise;

3. noise generated upstream of the fan (the loudspeaker in this case);

4. the characteristics of the noise generated upstream of the fan being modified as it propagates through the fan by the mechanisms described by Kaji *etc.* in Section 5.1.1;

5. noise scattered at sum and difference frequencies by the interaction between the noise generated upstream of the fan and the fan itself.

Scattering of broadband noise therefore results in a very complex case, where the noise in a given frequency range could contain contributions from multiple scattering mechanisms and noise-sources. This may not be anticipated in the design of acoustic liners at the engine inlet and outlet, or in the application of noise-source identification techniques. The possibility that sum and difference scattering could be caused non-linear interaction will further detrimentally affect such techniques. While the non-linear nature of this interaction was observed in the results discussed in Section 4.4 for the Berlin small-scale experimental tests, an additional study is presented in the following section for the narrowband experimental tests undertaken using the bench-top experimental rig at TCD.
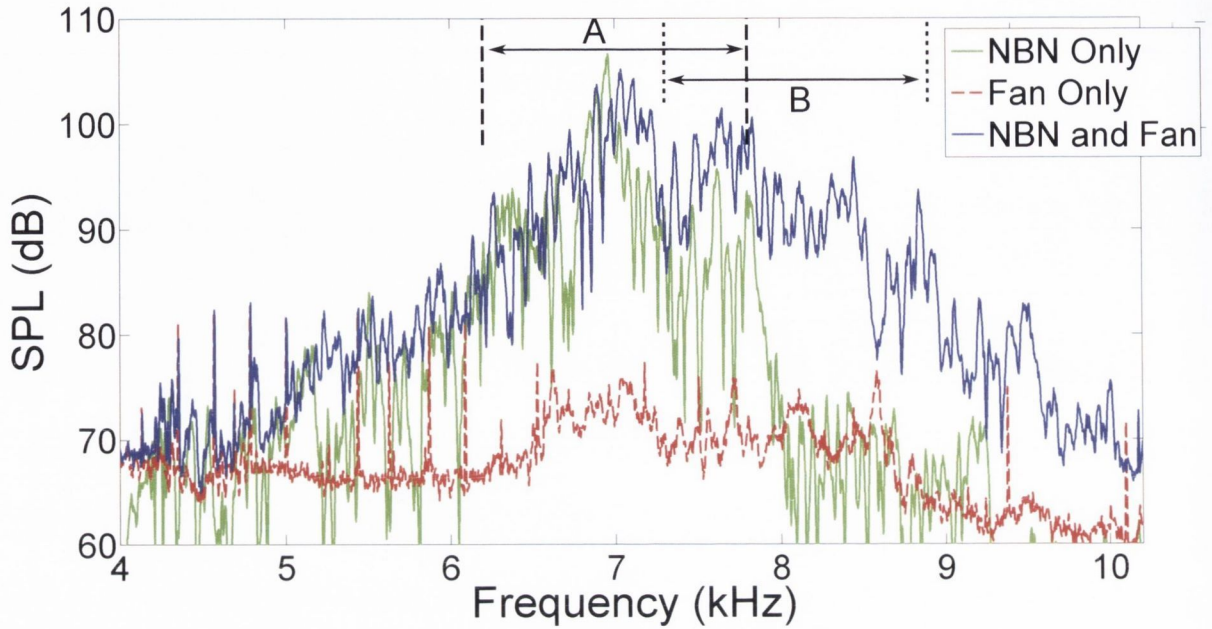
Figure 6.32: Sound pressure levels measured at a single-microphone for three narrow-band noise test points, BW = $1600Hz$.
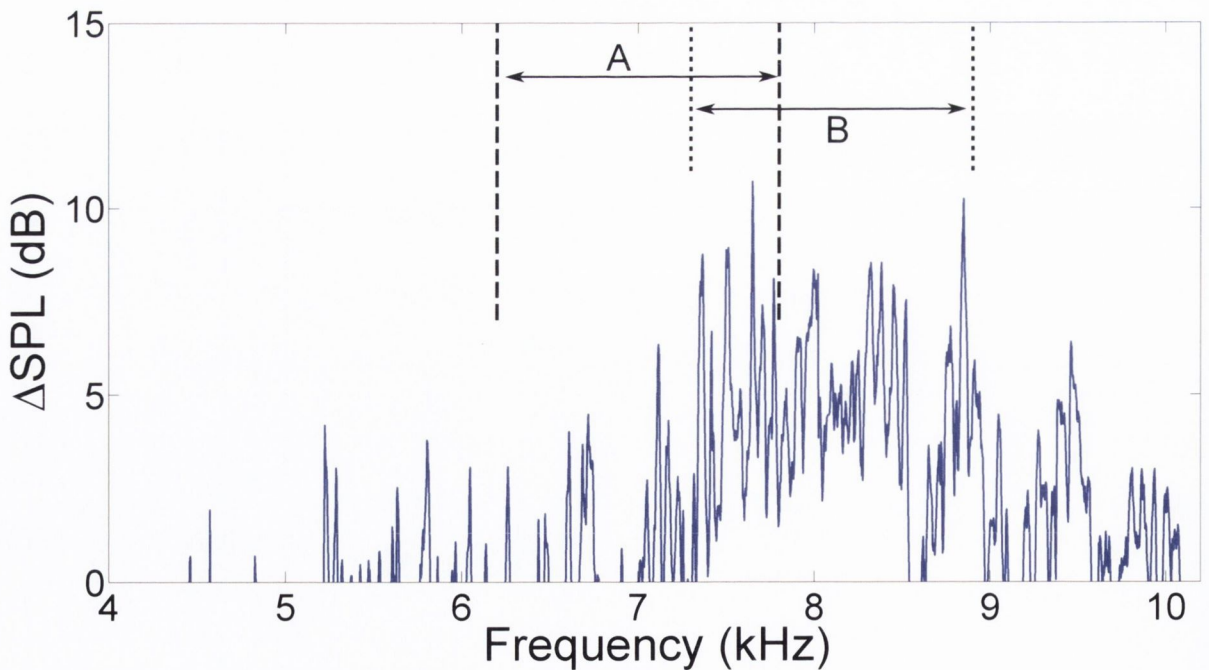
Figure 6.33: Difference in sound pressure levels measured for the "NBN and Fan" test case plotted in Figure 6.32 and the sum of the sound pressure levels measured for the "Fan Only" and "NBN only" test cases.
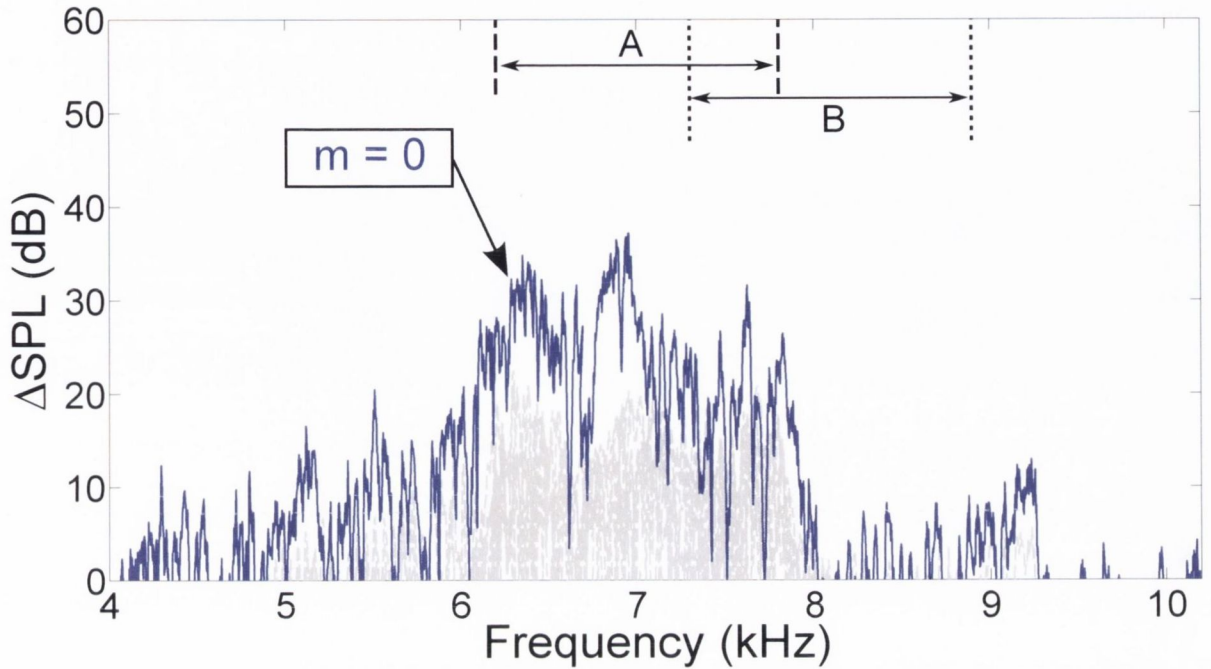
Figure 6.34: Sound pressure levels of the azimuthal modes excited by the loudspeaker when it is the only noise-source above the modal sound pressure levels measured when the fan is the only noise-source.
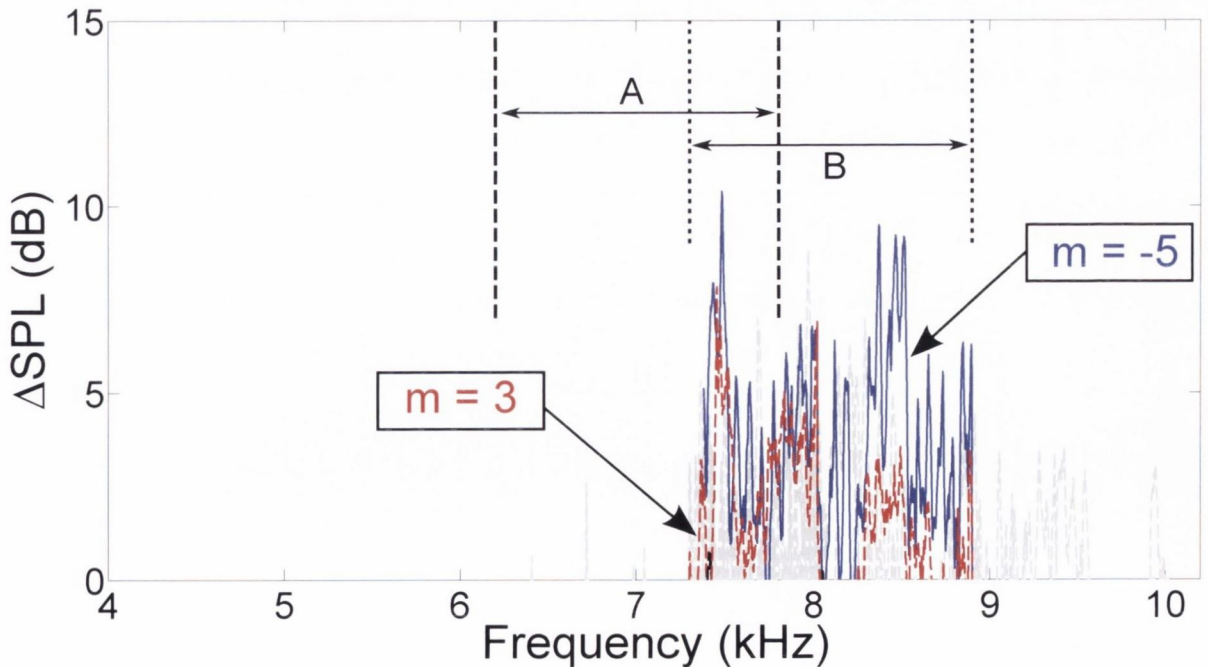
Figure 6.35: Sound pressure levels of the measured azimuthal modes of the scattered noise isolated in Figure 6.33.

6.2.4   Coherence Analysis of Incident and Scattered Noise

The analysis of narrowband noise scattering has so far been limited to sound pressure level spectra of both microphone and acoustic modal measurements. As discussed in Section 5.1.3, scattering of noise has previously been suggested as being caused by a quadratic interaction between the downstream-propagating noise and the rotating rotor. Sum and difference frequency scattering could arise, for example, as a result of the following quadratic trigonometric identity:

Noise from
Upstream Noise-
Source   Rotor BPF

$$[A\cos(\omega_1 t) + B\cos(\omega_2 t)]^2 = \frac{1}{2}A^2[1 + \cos(2\omega_1 t)] + \frac{1}{2}B^2[1 + \cos(2\omega_2 t)]$$
$$+ AB\cos(\omega_1 + \omega_2)t + AB\cos(\omega_1 - \omega_2)t$$

$\omega_1 = 2\pi f_1$ = Angular frequency of upstream tonal noise

f_1 + BPF f_1 - BPF

$\omega_2 = 2\pi f_2$ = Angular frequency of rotor BPF

Figure 6.36: Trigonometric identity showing how sum and difference frequency scattering could be the result of a quadratic interaction between incident noise and the rotating rotor.

The presence of such a quadratic non-linear interaction occurring at a rotor stage can be identified using the non-linear coherence function, defined as $\gamma^2_{x^2 y}$, where x and y are measurements made upstream and downstream of the rotor stage. In order to demonstrate how the quadratic coherence function allows the presence of quadratic interaction to be identified, we first consider the noise measured by an upstream sensor:

$$x = T + BPF + (T + BPF)^2 \tag{6.3}$$

where T is the upstream noise (generated by the loudspeaker in this experimental investigation) and BPF is the blade-pass frequency of the rotor. Expanding the square of this input:

$$((T + BPF) + (T + BPF)^2)^2 = \underline{T^2 + 2(T \times BPF) + BPF^2} + 6(T^2 \times BPF) + 6(T \times BPF^2)$$
$$+ 4(T^3 \times BPF) + 6(T^2 \times BPF^2) + 4(T \times BPF^3) + 2T^3 + 2 \times BPF^3 + T^4 + BPF^4$$

$$(6.4)$$

The quadratic contribution to the total input measurement (underlined) is maintained in this expansion. Therefore taking the ordinary coherence between the square of the input $(x^2(t))$ and some output $(y(t))$ will identify the non-linear components of the output measurement.

This technique has been applied in previous experimental tests (see Section 4.4) to estimate both linear and non-linear coherence functions between upstream (input, x) and downstream (output, y) measurements. These experimental results showed very low measurements of the linear coherence and relatively high non-linear coherence at sum and difference scattered frequencies, which would confirm the hypothesis that such scattering is indeed the result of a quadratic interaction. Further enhanced linear and non-linear coherence function were formulated using partial coherence methods, in order to condition out the influence of non-quadratic higher-order terms from the quadratic coherences. Enhanced linear coherence functions were also tested, which condition quadratic and other higher-order terms from the linear coherence measurements. These partial coherence formulations are discussed further in Section 5.1.3.

The possibility of sum and difference scattering being caused by a non-linear interaction is of interest, as such a violation of the assumption of a linear propagation path from source to receiver will reduce the effectiveness of coherence-based methods of noise-source identification. By adding non-linear effects to the system equation between two measurements, the measured ordinary coherence will drop, even if the contribution of linear effects to this system equation is unchanged [6]. It is therefore prudent to investigate coherence measurements further using the current experimental rig, which allows more detailed and accurate causal conclusions to be obtained from coherence measurements than for the small-scale DLR rig experiments due to the reduced reflections at the downstream end of the test duct.

For this coherence investigation, most signal processing parameters were maintained

from the results discussed in Sections 6.2.1 – 6.2.3, however the data acquisition time for each test case was increased to 120 seconds. This increases the number of time-domain blocks in the averaging ensemble to 761. The number of blocks was increased in order to increase the accuracy of any coherence function estimates by reduction of the associated mean error, which is dependent on the number of averaging blocks used (see Appendix C).

The sound pressure level spectra measured by a single microphone in the sensor array for three test cases is shown in Figure 6.37. In the "NBN Only" case, narrowband noise has been generated by the loudspeaker, centred at $6400Hz$ with a bandwidth of $200Hz$. In the "Rotor Alone" case, the rotor rotates at 13000rpm. In the "NBN and Rotor" case, both the rotor rotates and the speaker generates narrowband noise. A significant amount of noise has been scattered into each of the three scattering frequencies displayed in this figure. It therefore presents an interesting test case in order to investigate the linear and quadratic coherence measured between the source microphone and a microphone in the sensor array.

The ordinary coherence estimated between the source microphone (as the input x, shown with label E in Figure 6.24) and a microphone in the sensor array (as the output y) is plotted in Figure 6.38. The linear coherences conditioned by the square and third power of the input are also plotted in this figure. The measured ordinary coherence is high (≈ 1) for most frequencies for the incident noise, and remains high when conditioned of the higher powers of the input. The dips in the coherence match dips in the sound pressure level spectra in Figure 6.37. This demonstrates that the frequency response function, describing the propagation path from source (loudspeaker) to receiver (output microphone), is linear for the incident noise.

At the three scattered frequencies shown in Figure 6.38, the ordinary coherence drops significantly when compared with the incident noise, peaking at levels of ≈ 0.5. Unlike the incident noise, the coherence at the scattered frequencies drops significantly when conditioned of the square of the input, and further again when additionally conditioned of the third power of the input.

Figure 6.39 shows the quadratic coherence estimated between the source and output microphone measurements, as well as the quadratic coherence conditioned of the third
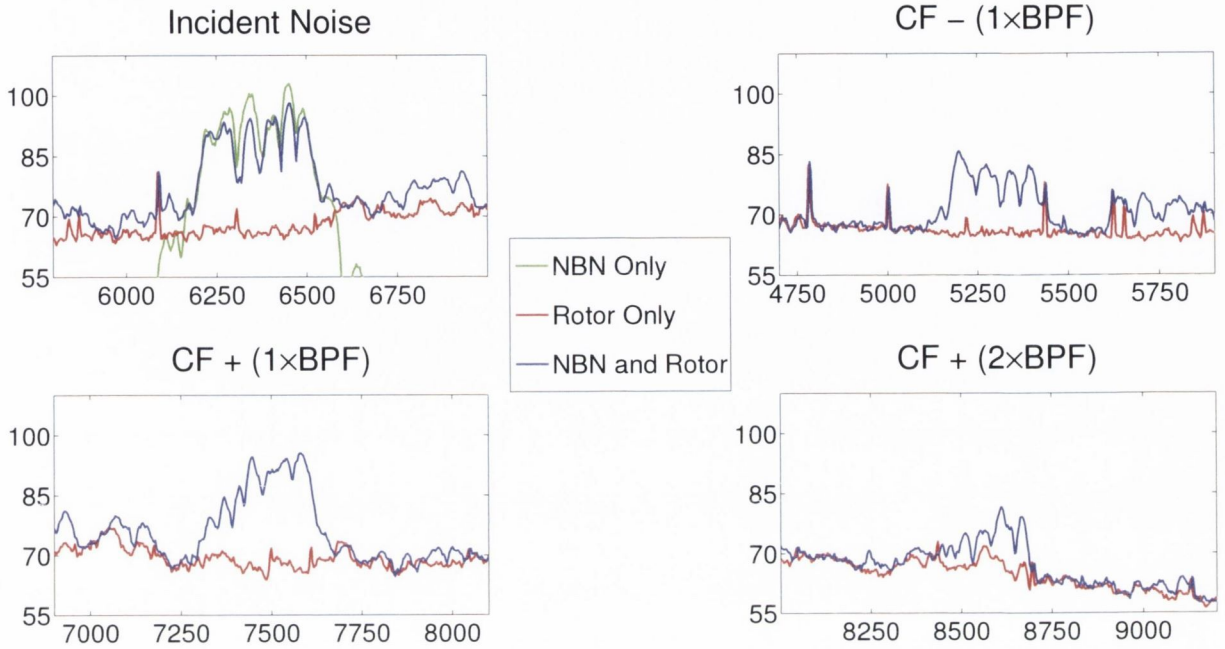
Figure 6.37: Spectra of narrowband noise (SPL (dB) against Frequency (Hz)) centred at the incident noise at $6400Hz$ (top left) and three possible scattering frequencies.
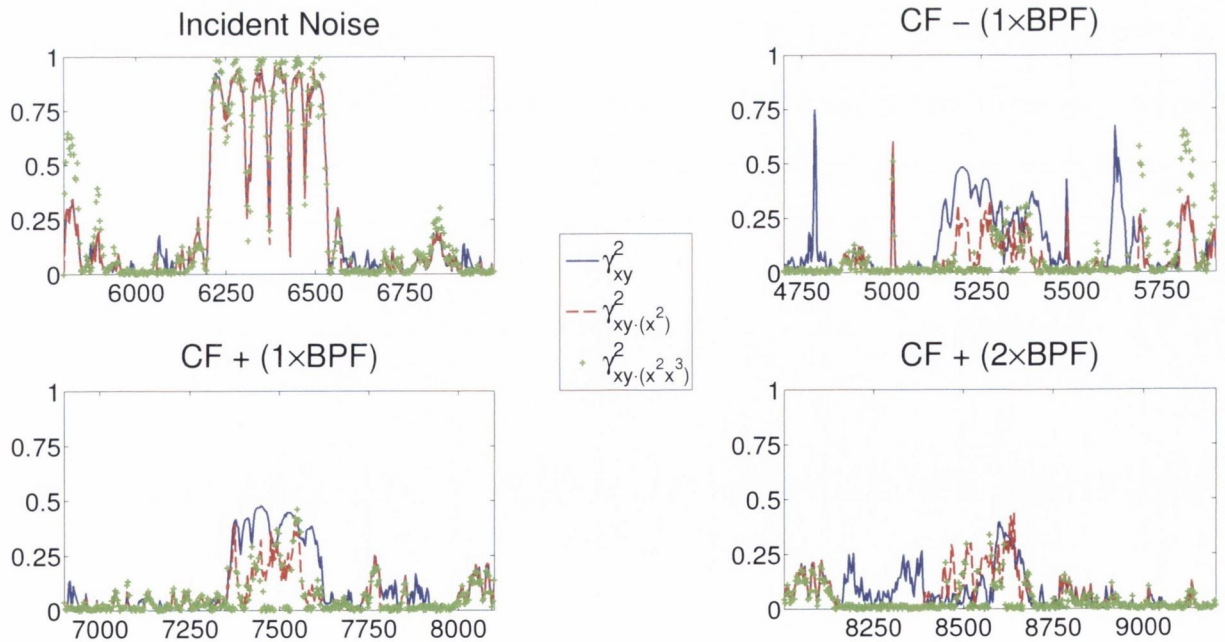
Figure 6.38: Linear coherence estimated between measurements made upstream (x) and downstream (y) of the rotor plotted against frequency for the "NBN and Rotor" test case shown in Figure 6.37.

power of the input. In both estimates, the quadratic coherence is very low at the incident noise frequencies, further demonstrating that the propagation path between the speaker source and output receiver is linear. The quadratic coherences estimated at all scattered frequencies are far higher however, generally of the order of 0.5 but peaking at a value of almost 1 at the scattered frequency $CF + (2 \times BPF)$. The quadratic coherence remains high when conditioned of the third power of the input.
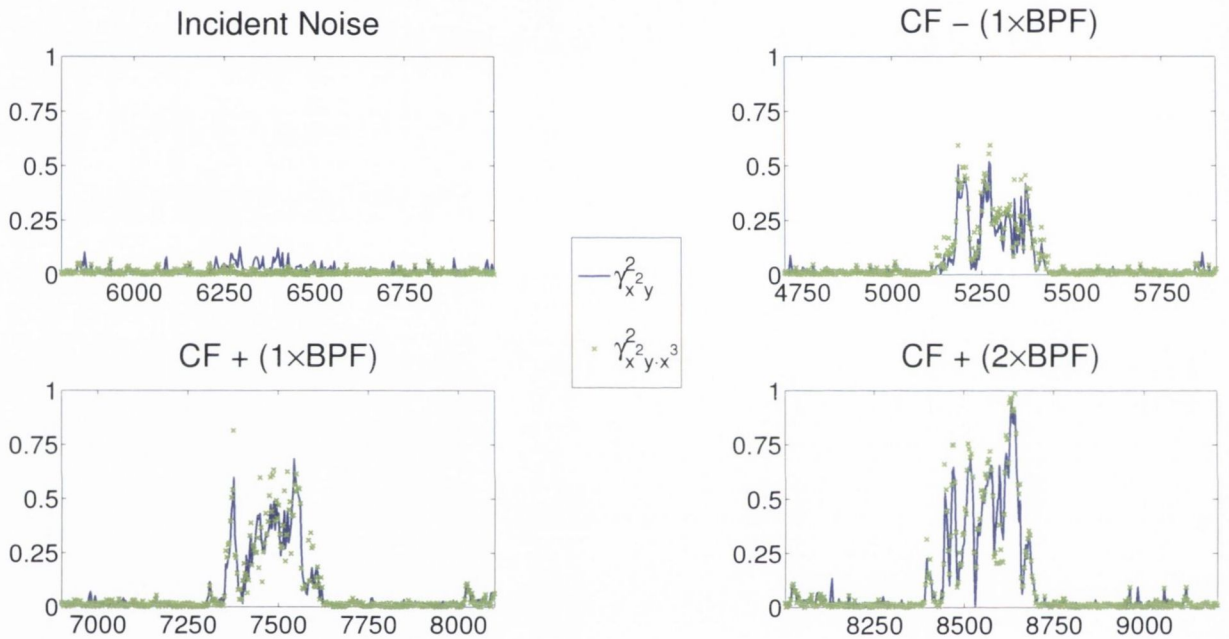
Figure 6.39: Quadratic coherence estimated between measurements made upstream (x) and downstream (y) of the rotor plotted against frequency for the "NBN and Rotor" test case shown in Figure 6.37.

The results shown in Figures 6.38 and 6.39 demonstrate that the system describing the propagation path of the narrowband noise generated by the speaker to the output microphone located in the sensor array is linear. When this noise propagates through the rotor, significant noise is scattered at sum and difference frequencies, as observed in Figure 6.37. The high quadratic coherences at these scattered frequencies would strongly suggest that the scattering mechanism is quadratic in nature, however significant linear coherences are also observed. These results would suggest that sum and difference scattering is caused by a combination of both quadratic and linear interactions between the incident noise and the rotating rotor. The observed linear coherence is also higher than was observed in the results discussed in Section 4.4.

6.2.5   Alternative Interaction Mechanism

In Figure 6.36, an interaction model was outlined (as originally proposed by Bennett and Fitzpatrick [6]) which shows how a quadratic interaction between the rotor/fan and the incident noise could cause the frequency scattering observed in this chapter. Although the coherence analysis performed herein would suggest that this model is accurate, the model itself does not describe the physics of the scattering mechanism. Furthermore, the previously published analytical studies discussed in Section 5.1.2 accurately predict frequency and modal scattering behaviour using simple linear kinematic theory. The significant amount of linear coherence observed at scattered frequencies in the preceding experimental study is also not explained by the quadratic scattering model.

An alternative interaction mechanism which could lead to sum and difference scattering of noise is the presence of a time-varying boundary condition. A possible model demonstrating this is shown below:

$$A\cos(\omega_1 t) + B\cos(\omega_2 t) = \frac{A}{2}[\cos(\omega_1 - \omega_2)t + \cos(\omega_1 + \omega_2)t] + B\cos(\omega_2 t) \qquad (6.5)$$

where ω_1 is the frequency/frequencies of the incident noise, ω_2 is the fan BPF, and $A = A\cos(\omega_2 t)$ i.e. the amplitude of the incident noise is time-varying and linked to the rotor rotational speed. While this time-varying boundary condition model does not explain the high quadratic coherence levels observed in the experimental results presented in this subsection, it does demonstrate that a linear interaction model with a time-varying boundary condition will also predict sum and difference frequency scattering.

In order to validate which model best describes the real interaction observed in these experimental results, further parametric testing is required. Specifically, experimental tests must be undertaken where the amplitude of the noise generated at the speaker is varied between tests. It is also possible that the actual scattering mechanism is best approximated by a combination of both linear and quadratic models. This could perhaps explain the significant levels of both linear and quadratic coherences observed in the experimental results herein.

6.3   Discussion of Noise Scattering Results

In Section 5.1.4, several research question were put forward that have thus far not been answered by the current literature. The experimental test campaign undertaken in this chapter has sought to answer some of these outstanding questions. Following these experimental results, several conclusions can be reached:

1. How do the magnitudes of the scattered tones compare with the magnitude of the tone at the incident frequency?

   Although some qualitative observations on the magnitudes of any scattered noise relative to the incident noise can be made from the experimental results presented herein, quantitative conclusions cannot be made. This is due to the fact that the magnitude of the incident noise will be affected as it propagates through the fan-stator stage by the mechanisms discussed in Section 5.1.1 as well as by the sum and difference scattering interaction investigated herein. Therefore the modification of the incident noise magnitude by the sum and difference mechanism cannot be isolated. Generally the magnitude of the scattered noise is lower than the incident noise, although in some cases the scattered noise is of similar amplitude to the incident noise when scattered at a frequency of $F + (1 \times BPF)$, where F is the frequency range of the incident noise. The largest magnitude scattering was observed when m_{scatt} values predicted by Equation 6.2 are cut-on for $k = 0$.

2. Previous experimental tests have observed that sum and difference scattering of tones and narrowband noise does not occur below a critical frequency. What is the explanation for this? Is this critical frequency linked to the cut-on frequency of certain mode orders as theory predicts?

   The results shown through out this chapter have confirmed that the onset of significant levels of sum and difference scattering is linked to the cut-on of specific azimuthal acoustic modes, and these azimuthal modes can be predicted by the theory in Section 5.1.2. Acoustic energy is scattered into these predicted azimuthal modes at each scattered frequency.

3. It has been demonstrated that narrowband noise can also be scattered at sum and

difference frequencies of the incident centre frequency. Is there a limit on the band-with of this effect for narrowband noise?

Significant levels of noise scattering was observed at a frequency $CF + (1 \times BPF)$ for the highest bandwidth tested (BW = 1600Hz). This scattering of noise with a bandwidth greater than the fan BPF (1083Hz), which results in overlapping of incident and scattered noise. These results would strongly suggest that scattering of broadband noise can occur, which will greatly increased the complexity of the acoustic pressure field as the incident and scattered noise will overlap.

4. If the predicted scattering modes in Equation 5.11 are cut-on, do they dominate at these frequencies as predicted?

   The modal analysis undertaken for both tonal and narrowband noise experimental tests have verified that this equation accurately predicts the modal content of sum and difference scattered noise. This was validated over a range of targeted azimuthal modes, test frequencies, scattering harmonics and stator vane counts.

5. What is the modal content of these sum and difference tones when the predicted scattering modes are not cut-on at the corresponding sum and difference frequencies? Does any scattering occur in such conditions?

   Very little scattering was observed when m_{scatt} modes predicted by Equation 5.11 were not cut-on. As the mode generator (for the tonal test cases) and single speaker (for the narrowband test cases) do not only excite a single azimuthal mode, some scattering of other azimuthal modes is expected. If only a single azimuthal mode were to be excited by an idealised mode generator, no scattering would occur if no predicted m_{scatt} modes were cut-on.

6. Does scattering occur through a stator stage as expected?

   Stator scattering of azimuthal modes is accounted for in Equation 5.11. As this equation was shown to accurately predict the scattered modes for both stator vane counts investigated for the tonal tests, as well as for the narrowband noise tests, scattering through a stator stage has been shown to be accurately accounted for in this equation.

7. The results discussed in Section 4.3 and in the work by Bennett and Fitzpatrick [6, 23] have raised the possibility that sum and difference scattering arises as the result of a non-linear interaction between the incident noise and the rotor. Is this further verified in a more thorough experimental investigation?

The coherence-based investigation undertaken in Section 6.2.4 has investigated the quadratic nature of the interaction further. These coherence measurements have indicated that scattering arises due to a quadratic interaction between the incident noise and the rotating rotor, however significant levels of linear coherence are also observed in the results from the current test campaign. No conclusive explanation for this high linear and quadratic coherence is as yet offered, however this would appear to further validate the hypothesis that sum and difference scattering arises as a result of a quadratic interaction between the incident noise and a rotating rotor.

Further observation and conclusions can be made from these experimental results:

- The drop in measured ordinary coherences between upstream and downstream measurements at frequencies where scattered noise is measured, due to the quadratic nature of the interaction, means that it also adversely affects any noise-source identification which make assumptions of a linear system equation relating the two measurements.

- The higher the kR value at the incident tonal frequency, the more likely scattering is to occur at sum and difference frequencies, as more potential scattering mode orders are cut-on as the frequency is increased.

- The modal scattering which occurs at each scattered frequency and is predicted by Equation 5.11 essentially shifts the incident azimuthal mode orders of the incident noise by the Tyler-Sofrin mode orders predicted to be generated at the fan BPF harmonics. Interestingly however, modal scattering occurs even when the predicted Tyler-Sofrin modes are not cut-on at the incident BPF tones, as was the case for the eight-vane stator as demonstrated in Section 5.4. The results from the tonal scattering tests suggest that the strength of the rotor-stator interaction may also affect the magnitude of noise scattering into azimuthal modes predicted by Equation

5.11, with more significant scattering occurring into azimuthal modes predicted by this equation for $k{\neq}0$ when the five-vane stator was used than for the eight-vane stator. More work is needed to investigate this further however.

- In the incident noise contains equal energy per mode, scattering is more likely to occur at higher frequencies as more potential scattered modes are cut-on.

- In a real turboshaft or other aeroengine, the presence of many consecutive rotor-stator stages particularly at the compressor will cause scattering to occur in a way that would be very difficult to predict, as each incident acoustic mode can scatter into several other modes.

- A more complete analysis would be possible using a radial modal decomposition procedure which would require many more microphones, DAQ channels *etc.*, in order to investigate the possibility of scattering on radial mode order. None of the results observed in this test campaign would suggest scattering on radial mode order, as would have been observed had significant scattering behaviour occurred above a frequency corresponding to the cut-on of a radial mode.

- In order for incident noise to be scattered at frequencies of $F - (h{\times}BPF)$, where h is a positive integer, the incident noise frequency/frequencies F must be above the rotor BPF. If the difference between F and BPF were small, noise could be scattered to a very low frequency range. This raises an interesting possible scenario for aeroengine core noise radiated from the engine exhaust. Provided at least one solution for m_{scatt} were cut-on at the low frequency range, high frequency broadband turbine noise could be scattered through a second turbine stage into a low frequency range. This noise could then be falsely attributed to some other low-frequency core noise-source *e.g.* direct or indirect combustor noise. This possible noise scattering scenario is shown graphically in Figure 6.40. The frequency ranges of the turbine broadband and BPF noise were roughly approximated from the far-field measurement spectra of turboshaft engine exhaust noise shown in Figure 1.1. This effect could be predicted if the modal content of the turbine broadband noise and BPF were known, however given that this noise is generated at very high frequencies,

many microphones would be required for such a modal analysis.
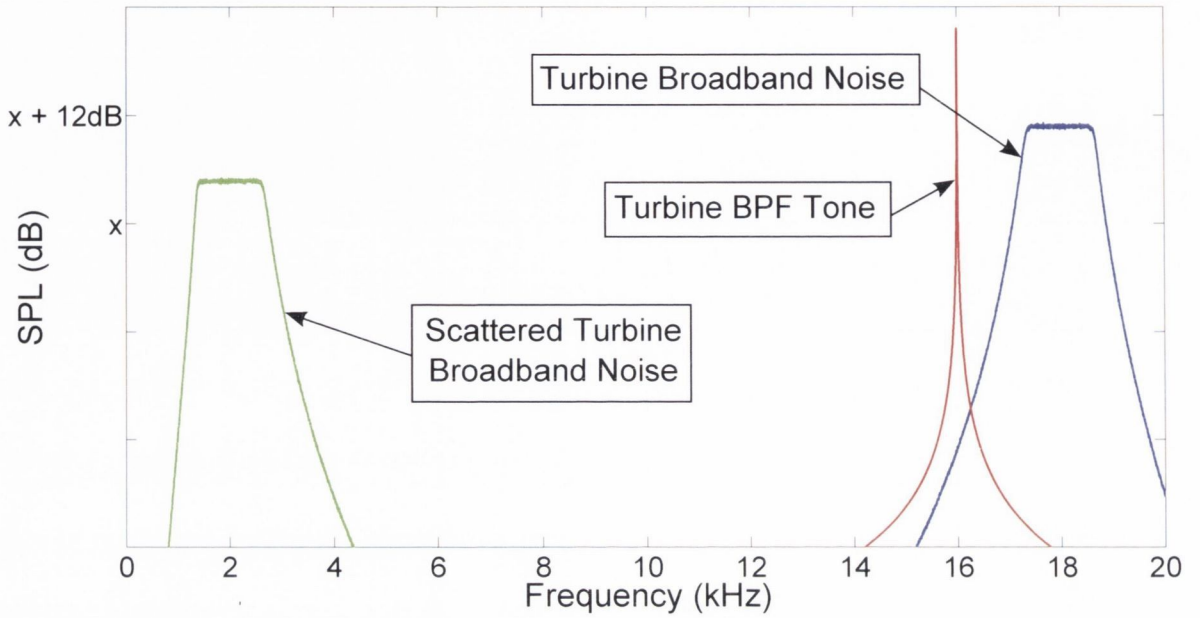
Figure 6.40: Possible difference frequency noise scattering of turbine broadband noise through a second turbine stage into a low frequency range.

Chapter 7

Conclusions

Both pre-existing and novel coherence-based noise-source identification techniques have been tested on a small-scale rig, designed as a simplified analogy to a real turboshaft engine. This experimental test campaign was undertaken as part of the E.U. FP-7 project TEENI. This experimental rig has two noise-source regions: a rotor-stator stage (representing a turbine stage) and a loudspeaker array (which can simulate a range of core noise sources). The objective of this experimental investigation was to assess the efficacy of the existing techniques for use in a real turboshaft engine, as well as to develop and test novel modal-based techniques.

It was found that more sophisticated techniques, using five microphones, were better suited to the model tested due to their ability to decorrelate the two noise-sources' contributions to the output measurement of interest. However, these techniques using many microphones require great care in their application, as statistical errors propagate in the combinations of many cross-spectral estimates used in their formulation. A novel technique was developed and found to effectively assess the contribution of both noise-sources to the modal amplitudes identified at a given axial location in the test duct. These modal amplitudes are estimated using a modal decomposition technique applied using an array of wall-flush-mounted microphones distributed at several azimuthal and axial locations. This novel technique enhanced with modal analysis is a significant advancement on existing noise-source identification techniques, which could be applied in a full-scale test rig to better identify the specific contributions of the various core noise-sources within the engine to the specific acoustic modal content of the sound radiated out the engine exhaust.

Sum and difference scattering of noise was observed in the previous tests under certain test conditions. This scattering can sometimes arise when noise propagating through a duct interacts with rotating turbomachinery. It was observed that this scattering only occurred above a certain critical frequency, which previous studies had suggested as being linked to the cut-on of specific acoustic modes. However, the small-scale experimental set-up was not designed such that a modal investigation could be performed at the high frequencies at which this scattering was observed. Coherence function estimates between upstream and downstream measurements also suggested that this interaction is non-linear (quadratic) in nature. As there has been little investigation of this scattering of noise in

the literature, a new bench-top experimental rig was designed at TCD specifically to undertake a more detailed study. Specific research questions were proposed, such as: What are the relationships between the acoustic modes of the incident (source) noise and the scattered noise? Do these predicted scattered modes match existing analytical predictions? Are the critical frequencies of noise scattering linked to the cut-on of these modes?

The design of this new experimental rig was described in detail in Chapter 5. Each element of the rig was tested to ensure that it performed as desired. Such elements include a rotor-stator stage, semi-anechoic terminations to reduce end reflections, and an array of five loudspeakers used as a mode generator. A mode generator allows specific azimuthal modes to be targeted at a specific frequency, allowing tones to be generated with a prescribed modal content. This is a key element of the experimental rig and was thus investigated in detail, both numerically during the design process and experimentally following its construction. This mode generator was located upstream of the rotor-stator, and an array of microphones located downstream so that a modal analysis could be performed. By comparing the modal content of the incident noise from the mode generator with the modal content of any scattered noise, conclusions could be made on the conditions necessary for significant scattering to occur.

An investigation of sum and difference scattering of tones was first undertaken using the new experimental rig. Tones were generated using the mode generator, with one of three possible azimuthal modes excited by the array. This tone then propagated through the rotating rotor and stator stages where in some cases it was scattered at sum and difference frequencies. This scattered noise was compared with rotor alone tests in order to isolate the contribution of noise scattering to the total noise measured at the sensor array. This test procedure was repeated for a range of test frequencies, azimuthal modes excited by the mode generator, scattering frequencies and stator vane counts. Using both single microphone spectra and modal analyses it was found that pre-existing analytical theory accurately predicts the scattered mode orders at each scattered frequency. If these scattered mode orders are not cut-on, no significant scattering of noise will occur.

Following the tonal tests, an additional test campaign was undertaken to investigate scattering of narrowband noise. The experimental rig was modified, with the mode gener-

ator removed and replaced with a single loudspeaker at the upstream end of the duct. An additional source microphone was located close to the loudspeaker. The upstream semi-anechoic termination was also removed. Similar to the tonal tests, noise was generated by the speaker upstream of the rotor, which then propagated through and interacted with the rotating rotor. The resulting noise propagating downstream of the rotor is measured by an array of microphones. This test procedure was repeated for a range of narrowband centre frequencies and bandwidths. It was found from modal analysis that the analytical theory which accurately predicted tonal scattering also successfully predicts the scattered modal content and onset of sum and difference scattered broadband noise. A case was also highlighted where scattered noise overlaps with the source noise generated by the loudspeaker. Finally, coherence measurements between the source microphone and a microphone in the sensor array demonstrated the quadratic nature of the scattering mechanism, however the presence of significant levels of linear coherence were also observed.

This investigation has significantly advanced the current level of understanding of sum and difference scattering of noise. This understanding will allow a better prediction of the onset of noise scattering, as well as better consideration of its effect on the exhaust pressure field in aeroengines, and better mitigation through passive (acoustic liner design) or active (noise control system) attenuation. The coherence noise-source identification techniques which combine modal analysis methods with correlation estimates advanced in this study also represent a significant advancement on existing methods of noise-source identification which could be applied in a range of full-scale aeroengine exhaust or inlet noise studies.

7.1 Future Work

Following the results reported in this thesis, several new avenues of research and improvements in experimental methodology are identified:

- In the application of more sophisticated coherence-based noise-source identification techniques using many microphones, very long acquisition times are strongly recommended. Although data was acquired for 120 seconds in the tests in Chapter 4, it was found in Appendix C.5 that even this acquisition time could result in significant uncertainty in any spectral quantities estimated by these techniques.

- For all experimental test set-ups investigated herein, anechoic or semi-anechoic terminations were located at one or both ends of the test duct. While these terminating sections significantly reduce reflections, it is advisable in future tests to ensure that reflections are eliminated in order to make more accurate causal conclusions from correlation estimates. Ideally, tests would also be undertaken in an anechoic chamber.

- In the experimental test undertaken in Chapter 5 and 6, azimuthal modal analyses were performed using a single-ring of microphones. Using microphones located at a single axial and radial location does not allow a radial modal analysis to be performed, nor does it allow the specific incident and reflected contributions to the azimuthal modal amplitudes to be identified. Although no further microphones were available, it would be possible to move the axial location of the ring of microphones slightly, and then repeat each test with the microphones moved to this new axial location. This procedure could be repeated for as many axial locations as desired. Assuming the measurement signals are ergodic (see Appendix C.1), a radial modal analysis could be performed by combing together the microphone measurements of each of the repeated tests, effectively giving acoustic pressure data at a range of axial as well as circumferential locations. It should be noted however that the non-synchronous nature of this method would not allow correlation analyses to be performed using the resulting modal amplitudes.

- This thesis has focused on the identification of noise-sources and the scattering of noise through rotor-stator stages. Further study is required to adapt the output from this thesis into considerations for mitigation of noise from aeroengines using passive or active control methods.

- In order to advance the findings in this study regarding the scattering of noise through a rotor-stator stage, it is advised that a similar test procedure to that undertaken herein be repeated for a wide range of rotor (and stator) geometries. In particular, the exact linear/quadratic nature of the interaction needs further investigation, as it has a large impact on the application of any techniques which make assumptions of a linear propagation path from source to receiver. More advanced

signal analysis (such as bicoherence) may aid such an experimental investigation, and more advanced analytical modelling of the interaction may help to explain the cause of the measured linear/quadratic coherences.

Appendix A

Wave Element Method

The wave element method is a full-domain discretisation numerical technique which can be used to model the pressure field in a domain of interest. This can be used as a tool for simulating one or more point sources (monopoles) in a duct, as demonstrated in the work of Bennett *et al.* [78]. Other types of sources can be modelled by adapting the boundary conditions. Full domain discretisation techniques have the advantage over boundary element methods (BEM) in that inhomogeneities can be introduced in the propagation medium.

The computational cost of any full-domain discretisation technique is closely linked to the number of nodal points required per acoustic wavelength. Many full domain discretisation techniques require 5-6 points per wavelength in order to obtain sufficient accuracy in the solution of the Helmholtz equation. The wave element method reduced this requirement to around 2 points per wavelength, which coincides with the Nyquist sampling limit for DSP. The WEM is derived from the Green Function Discretisation Method (GFD) introduced by Caruthers *et al.* [83, 84]. The fundamental aspects of the technique are outlined below – a more detailed description of the technique may be found elsewhere in the literature [85–87].

The GFD technique is used to find the acoustic pressure, p, at a point in the domain, x_0, given the amplitude and phase data at M neighbouring points, x_m. The pressure at each point in the domain can be approximated by the superposition of N hypothetical sources of strength γ_n, located at a constant distance $R = |x_n - x_0|$ from the subject point x_0. The acoustic pressure at x_0 is therefore given as:

$$p_{(x_0)} = \sum_{n=1}^{N} \gamma_n G(x_0; x_n) \tag{A.1}$$

where $G(x_0; x_n)$ is the Green's function which relates the pressure at x_0 due to the harmonic force at x_n. Repeating for all neighbouring points:

$$p_{(x_m)} = \sum_{n=1}^{N} \gamma_n G(x_m; x_n) \qquad\qquad m = 1, 2, \ldots M \tag{A.2}$$

In matrix notation:

$$\mathbf{p} = \mathbf{G}\boldsymbol{\gamma} \tag{A.3}$$

where $\mathbf{p}$ and $\boldsymbol{\gamma}$ are $M \times 1$ and $N \times 1$ matrices respectively. $\mathbf{G}$ is an $M \times N$ matrix. By solving Equation A.3 for $\boldsymbol{\gamma}$, the pressure at x_0 can be found using Equation A.1. If $N > M$, an infinite set of possible solutions for $\boldsymbol{\gamma}$ can exist, all of which will give values for the pressure vectors $\mathbf{p}$ which will satisfy the Helmholtz equation exactly. In this case, the matrix $\mathbf{G}$ can be pseudo-inverted to find the least energetic solution by imposing a smoothness constraint on $\boldsymbol{\gamma}$.

Letting $\mathbf{g}$ represent a column vector with elements $\mathbf{g}_n(\mathbf{x}) = G(\mathbf{x}_0, \mathbf{x}_n)$, then:

$$p_0 = \mathbf{g}^T \mathbf{G}^+ \mathbf{p} \tag{A.4}$$

where $p_0 = p(\mathbf{x}_0)$.

As stated by Ruiz [85], any solution to the governing equation may be used to interpolate the desired field variable. The GFD method outlined above requires *a priori* knowledge of the location of each monopole source. Plane waves, which are the infinite radial approximation of the Green's function, can be used as an alternative solution to the governing equation. Plane waves are suitable for problems where the governing equations have a spatial dependency, whereas no Green's function exists for this case. This occurs in problems involving acoustic waves in inhomogeneous flows, for example. Aside from the use of plane waves instead of Green's functions, the formulation of the WEM is the same as that for the GFD technique. The pressure at each point in the cell can therefore be approximated using a combination of plane waves:

$$p(x_0) = \sum_{n=1}^{N} \gamma_n e^{-ik\mathbf{d}_n \cdot \mathbf{x}_0} \tag{A.5}$$

where $\mathbf{d}_n$ is the unit propagation direction vector of the nth plane wave with complex amplitude γ_n. Equation A.5 can be expressed in matrix notation as:

$$p_0 = \mathbf{h}(\mathbf{x}_0)\boldsymbol{\gamma} \tag{A.6}$$

where $p_0 = p(\mathbf{x}_0)$, $h(\mathbf{x}_0)$ is a $1 \times N$ row vector of plane wave functions evaluated at x_0, and $\boldsymbol{\gamma}$ is the column vector of the wave strengths. Applying the same approximation at other nodal points in the cell:

$$\mathbf{p} = \mathbf{H}\boldsymbol{\gamma} \tag{A.7}$$

where $\mathbf{p}$ is an $N \times 1$ vector of the acoustic pressures at each surrounding node $\{\mathbf{x}_m\}_{m=1}^{M}$, and:

$$\mathbf{H}_{mn} = e^{-ik\mathbf{d}_n \cdot \mathbf{x}_m} \tag{A.8}$$

By combining Equations A.6 and A.7, a computational template is formed:

$$p_0 = \mathbf{h}\mathbf{H}^{+}\mathbf{p} \tag{A.9}$$

This equation is referred to as the Wave Element Discretisation (WED).

Due to the flexibility of the WEM formulation, there is a a choice of methods of imposing boundary conditions. Three boundary condition types are of interest. Each can be implemented by imposing additional constraint on the assembled matrix equation:

- Dirichlet (prescribed acoustic pressure) – implemented by constraining rows of the assembled matrix equation.

- Neumann (prescribed acoustic velocity) – implemented by augmenting $\mathbf{H}$ in Equation A.3.

- Radiation – implemented by augmenting $\mathbf{H}$ using only outward propagating directions.

Each of these boundary conditions can be implemented readily into the WEM model. For details on the implementation of each boundary condition for a 3-D problem, see Chapter 3 of Ruiz [85].

Appendix B

Microphone Calibration

The twenty-five KE4 Sennheiser electret array microphones used in the experimental tests outlined in Chapter 5 and 6 were calibrated for both magnitude and phase using one of the microphones as a reference. Each microphone has a nominal outer diameter of $8mm$. This calibration was undertaken using a simple impedance tube of inner diameter $16.7mm$, which is slightly greater than two microphone diameters. A cap is placed at one open end of the tube, with two microphones inserted into the cap, as demonstrated in Figure B.1. One of these microphones is the reference microphone. A loudspeaker is placed at the other open end of the tube which generates broadband noise. By placing both microphones in the same axial plane along the impedance tube, and assuming plane wave transmission of sound in the tube, both microphones will measure the same acoustic pressure. Any offset in the magnitude and phase between the measurements made by both microphones can therefore be attributed to bias errors, and so each microphone can be calibrated against the reference microphone.

The assumption of plane wave transmission will hold until the cut-on of the first higher-order acoustic mode at a frequency of $11.93kHz$, assuming standard conditions for both pressure and temperature. Figure B.2 shows the experimentally measured offset in both magnitude and phase between the reference microphone and each additional microphone. Above the cut-on of the $(1,0)$ mode at approximately $11.93kHz$ calibrations cannot be applied between the microphones, as evident in the distortion in the transfer function measurements above this frequency. Some distortion is evident at discrete frequencies below this cut-on however, possibly caused by a drop in signal-to-noise ratio in the microphone measurements as an acoustic pressure node is located at the measure-

207

ment plane. A linear fit was made to both the magnitude and phase calibration plots for each microphone which interpolates for these frequencies where the transfer function is distorted.

For the experimental tests discussed in Section 3.3 and Chapter 4, the array microphones used were calibrated in-house by DLR.
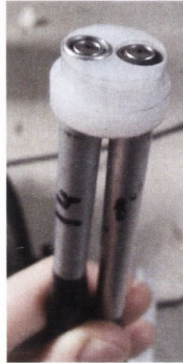
Figure B.1: End-cap for the impedance tube calibration of the microphones used in the experimental tests undertaken in Chapters 5 and 6. The cap is designed such that both microphones will be located in the same axial plane at the end of the impedance tube.
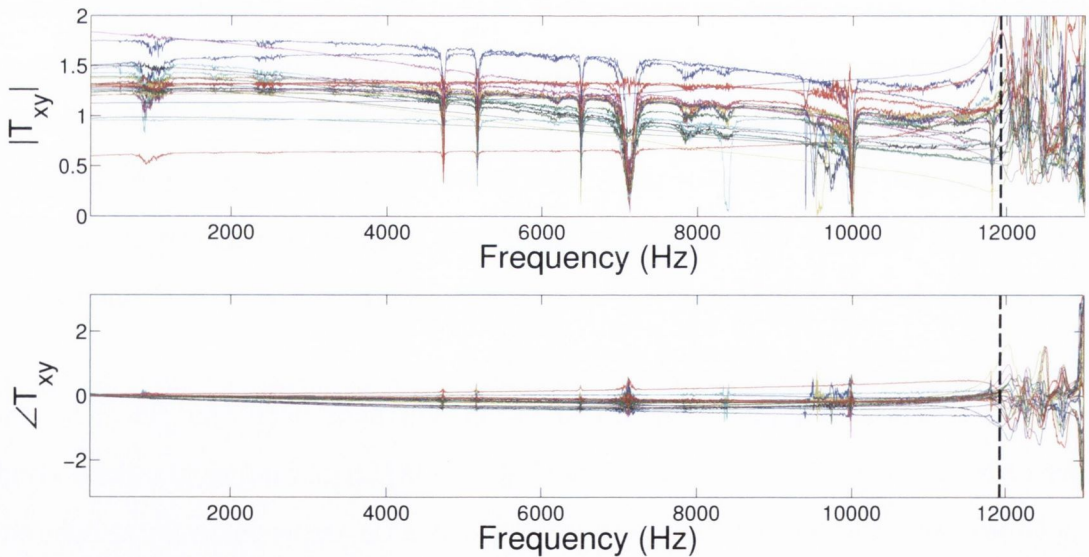
Figure B.2: Magnitude and phase calibration of microphones used in the experimental tests undertaken in Chapters 5 and 6.

Appendix C

Signal Processing of Ergodic Random Data and Associated Errors

The following appendix summarises the key concerns of digital signal processing acoustic time-domain data, with an aim to estimate spectral quantities using finite data records. Further reading can be found in the literature, with the books by Bendat and Piersol [61] and Newland [88] and the series of articles by Schmidt [89–93] of particular interest.

C.1   Characteristics of Random Data

In experimental noise studies, which generally involve data analysis of measurements made by several microphone, time-domain voltage signals are acquired at a given sampling rate for a finite amount of time. Each measured voltage time history is a known as a sample record. If another sample record were taken by the same microphone, a different time history would be measured. Such data measurements are therefore measurements of a stochastic or random process.

Random processes can be categorised as being stationary or non-stationary, and stationary random processes can be further categorised as ergodic or non-ergodic. Suppose we measure an ensemble of n_d sample records, all of which record the same random process. Each k-th time record in the ensemble of sample records $\{x(t)\}$ is denoted by $x_k(t)$. Statistical properties of the ensemble, such as the mean value (first moment) at time t_1, can be found by dividing the summation of all n_d sample measurements at time t_1 by the number of sample records, n_d:

$$\mu_x(t_1) = \lim_{n_d \to \infty} \frac{1}{n_d} \sum_{k=1}^{n_d} x_k(t_1) \tag{C.1}$$

Furthermore, the auto-correlation (joint moment) of the random process between the values at two times t_1 and $t_1 + \tau$ is given by:

$$R_{xx}(t_1, t_1 + \tau) = \lim_{n_d \to \infty} \frac{1}{n_d} \sum_{k=1}^{n_d} x_k(t_1) x_k(t_1 + \tau) \tag{C.2}$$

If the values of both $\mu_x(t_1)$ and $R_{xx}(t_1, t_1 + \tau)$ are invariant with changes in t_1, the random process $\{x(t)\}$ is said to be weakly stationary. Weakly stationary processes have constant mean values, and auto-correlation functions which depend only on the time delay between the two measurement times, τ. If all possible moments and joint moments are proven to be invariant with changes in t_1, the random process can be said to be strongly stationary. Generally, verification of a weakly stationary process is used to justify the assumption of strong stationarity [61]. Furthermore, if the statistical quantities such as the mean and auto-correlation values are the same for each sample record in the ensemble, as well as being equal to these same quantities averaged over the whole ensemble, the random process is said to be ergodic. Only stationary processes can be ergodic. Full details on tests for ergodicity and stationarity can be found in Chapter 5 of Bendat and Piersol [61].

Since random data is inherently non-deterministic, any properties inferred from ensembles of finite sample records must be considered statistical estimates of the true values. Under the assumption that the random data is both stationary (at least in the weak sense) and ergodic, it is possible to infer probabilistic estimates of the entire random process from ensembles of finite sample records. As these properties are statistical estimates of the true values for the random process, they are subject to statistical errors. Such properties of interest could include auto- and cross-correlations in the time-domain. Generally, for acoustic measurements in environmental noise studies it is the spectral properties in the frequency-domain which are of interest, as acoustic engineers are most interested in the distribution of acoustic energy with frequency as this can be related to perceived levels of annoyance for an observer. Such spectral properties include auto- and cross-spectral density functions, transfer functions and ordinary coherence functions. The procedure

for determining such properties from ensembles of sample records, and estimates for the associated errors, will now be discussed.

C.2 Signal Processing of Ergodic Random Data

Suppose that an ergodic random process is measured for T_{tot} seconds. The data is acquired by a data acquisition (DAQ) device, which samples the analogue voltage signal measured by the measurement instrument at a frequency of f_{samp}. The time step between each data measurement, $\Delta t = 1/f_{samp}$. The resulting discrete time-domain signal contains $T_{tot} \times f_{samp}$ data points. At least two sample points are required per cycle in order to uniquely define a given frequency component of any spectral measurements of this data, as given by the Nyquist-Shannon sampling theorem. Therefore the highest frequency that can be analysed in the frequency domain is $f_{samp}/2$, which is known as the Nyquist frequency. If any acoustic energy is present in the microphone measurements above this frequency, aliasing will occur in any spectral functions estimated from this data. This can be avoided by low-pass digital filtering the measured time-domain data prior to analysing in the frequency-domain.

In order to estimate spectral properties of the measured data, the data must be transformed into the frequency-domain by means of a Discrete Fourier transform (DFT). The FFT (Fast Fourier Transform) algorithm is a computationally efficient implementation of the DFT, which takes $N \log(N)$ operations, as opposed to N^2 operations for the computations of the DFT. While it is possible to simply take the FFT of the total signal, and analyse the resulting signal in the frequency-domain, it is more useful to divide the total time-domain signal into an ensemble of n_d blocks of data, each of length N points. Each of these blocks is then transformed into the frequency-domain by means of the FFT algorithm. The resulting ensemble $\{X(f)\}$ can be analysed by averaging spectral properties from the ensemble. For example, the two-sided auto-spectral density function can be estimated using the Fourier transforms of the ensemble as follows:

$$\hat{S}_{xx}(f_k) = \frac{1}{n_d N \Delta t} \sum_{i=1}^{n_d} |X_i(f_k)|^2 \qquad k = 0, 1, 2, \ldots, N-1 \qquad \text{(C.3)}$$

where $|X_i(f_k)|$ is the Fourier transform of the i-th block of data in the ensemble of time-domain data. The auto-spectral density is a real function which gives the distribution of acoustic energy with frequency, in units of Volts$^2/Hz$, from $0Hz$ up to $f_{samp}/2$, with the function mirrored around the Nyquist frequency. This is the Fourier transform of the auto-correlation function outlined in Equation C.2. The frequency resolution between each discrete frequency bin in the auto-spectrum is given by:

$$f_{res} = \frac{1}{N\Delta t} \tag{C.4}$$

so for each discrete frequency $f_k = kf_{fres}$. The corresponding one-sided auto-spectral density can be calculated as follows:

$$\hat{G}_{xx}(f_k) = \begin{cases} \dfrac{2}{n_d N\Delta t} \displaystyle\sum_{i=1}^{n_d} |X_i(f_k)|^2 & k = 1, 2, 3, \ldots, [(N/2) - 1] \\ \dfrac{1}{n_d N\Delta t} \displaystyle\sum_{i=1}^{n_d} |X_i(f_k)|^2 & k = 0, N/2 \end{cases} \tag{C.5}$$

It is possible to take the Fourier transform of the entire original signal, and calculate the auto-spectral density from this. The advantages of ensemble averaging over this method are:

- The power of the signal is enhanced.

- The residual spectral variance of any additive noise is reduced.

A comparison between the one-sided auto-spectra estimated by ensemble averaging with a range of n_d signal blocks is shown in Figure C.1. The data was acquired by a single microphone, recording narrowband noise in a duct which has been generated by a single loudspeaker. This illustrates the effect of increasing the number of signal blocks in the ensemble, improving the signal-to-noise ratio. Data was acquired with the following parameters: $f_{samp} = 26000$, $N = 8192$, $f_{res} = 3.17$, $T_{tot} = 30s$. Equation C.4 highlights the dependency of f_{res} on the number of points per signal block, and Figure C.1 shows the dependency of the signal-to-noise ratio on the number of signal blocks used in the averaging ensemble. Therefore, assuming T_{tot} and f_{samp} are constrained by

computational limitations of available memory and hardware clock speeds, there is a trade-off between the frequency resolution and signal-to-noise ratio of any spectral estimates. Further considerations must be made when random and bias errors of spectral estimates are accounted for, as the associated errors with any spectral estimates are dependent on n_d and f_{res}. These errors are discussed in Section C.4.
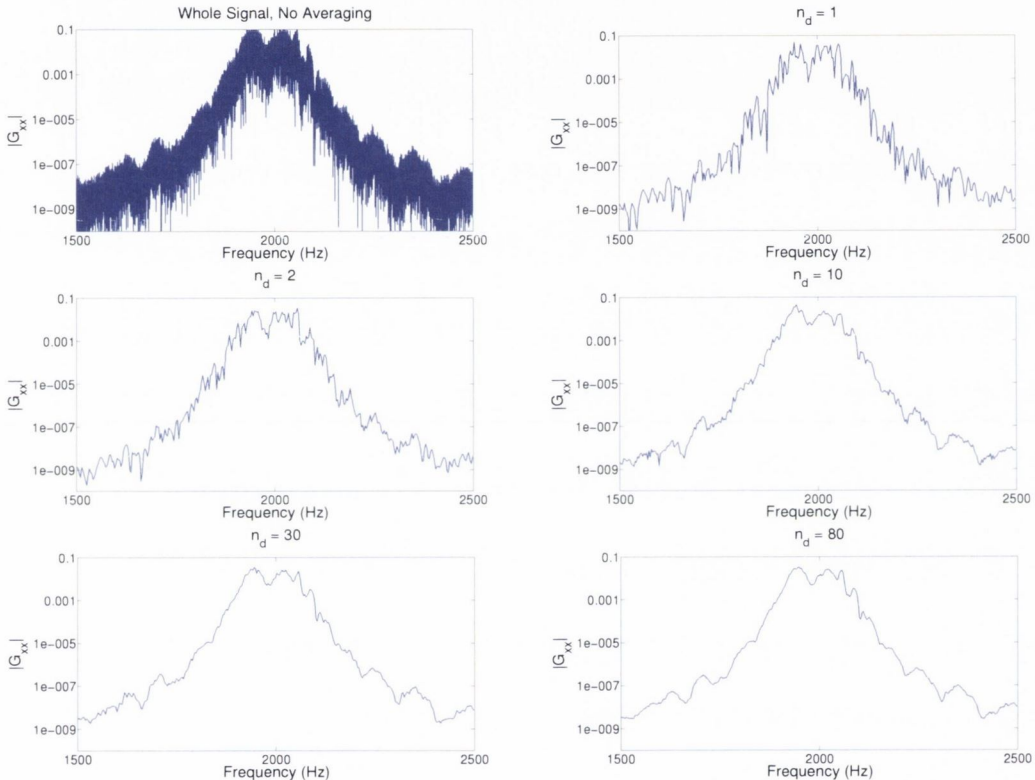
Figure C.1: Auto-spectral density measurements from a single microphone, showing the effects of ensemble averaging on the estimated spectra. Narrowband noise is measured at a centre frequency of $2kHz$ with a bandwidth of $100Hz$. n_d is the number of signal blocks used in the averaging ensemble in each case. The estimate of the auto-spectral density taken without dividing the time-domain signal into signal blocks is shown for comparison.

Another consideration when transforming time-domain data into the frequency-domain is spectral leakage due to side lobes which are inherent to the Fourier transform. These side lobes can be greatly reduced by applying a window function to the time-domain data, which tapers the data in order to remove discontinuities at both ends of the sample record. Many such window functions exist, however for many acoustic applications, the Hann (or Hanning) window is used due to its low aliasing. Further details on window functions, errors due to side lobes and spectral leakage, overlapping signal blocks, and other signal

processing concerns for random data can be found in the books by Newland [88] and
Lyons [94].

As well as auto-spectral density functions, estimates of cross-spectral density func-
tions, transfer functions and coherence functions between two signal measurements are of
interest in acoustic studies. These spectral functions can be used to analyse the propa-
gation characteristics between two measurements, identify source contributions to output
measurements in a SISO (single-input/single-output) system, and are used as the basis for
coherence-based noise source-identification techniques as outlined in Section 4.1. Suppose,
similarly to the example at the beginning of this section, two ensembles of data records
$\{x(t)\}$ and $\{y(t)\}$ are recorded by two different microphones. Each records a different
ergodic random process, which could be the noise measured at both microphone loca-
tions. The one-sided cross-spectral density function estimated between both microphones
is given by:

$$
\hat{G}_{xy}(f_k) = \begin{cases} \dfrac{2}{n_d N \Delta t} \displaystyle\sum_{i=1}^{n_d} [X_i^*(f_k) Y_i(f_k)] & k = 1, 2, 3, \ldots, [(N/2) - 1] \\[4mm] \dfrac{1}{n_d N \Delta t} \displaystyle\sum_{i=1}^{n_d} [X_i^*(f_k) Y_i(f_k)] & k = 0, N/2 \end{cases} \tag{C.6}
$$

The cross-spectral density function is of interest as it can be used to estimate both
the frequency response and coherence functions. The frequency response function can
be estimated for a SISO system from the cross- and auto-spectral density functions as
follows:

$$
\hat{H}_{xy}(f_k) = \frac{\hat{G}_{xy}(f_k)}{\hat{G}_{xx}(f_k)} = |\hat{H}_{xy}(f_k)| e^{-j\hat{\phi}_{xy}(f_k)} \tag{C.7}
$$

where $|\hat{H}_{xy}(f_k)|$ is the magnitude response function and $\hat{\phi}_{xy}(f_k)$ is the phase response
function. In fact, there are several methods for estimating the frequency response function
from auto- and cross-spectral function estimates. The form shown in Equation C.7 is
commonly used as it reduces the influence of noise on the output. However, alternative
forms of the frequency response estimator can be applied if, for example, noise is present
at the input measurement, in order to reduce bias errors [95].

The ordinary coherence function is estimated by the cross- and auto-spectral densities as follows:

$$\hat{\gamma}_{xy}^2(f_k) = \frac{|\hat{G}_{xy}(f_k)|^2}{\hat{G}_{xx}(f_k)\hat{G}_{yy}(f_k)} \tag{C.8}$$

which for all f_k will satisfy the Cauchy-Schwartz inequality:

$$0 < \hat{\gamma}_{xy}^2(f_k) \leq 1 \tag{C.9}$$

This function can alternatively be estimated using the two-sided spectral density functions. The ordinary coherence function is commonly applied to estimate the causality between an input measurement and an output measurement, assuming the system function is linear, and both measurements estimate random ergodic processes. If the system is non-linear, the coherence function will result in an erroneous interpretation of causality.

C.3 The Zoom-FFT

In order to analyse the data from experimental tests, an FFT (Fast-Fourier Transform) algorithm can be applied to an ensemble of time-domain data records. However, if only specific discrete frequencies are of interest, this can be inefficient, as the information at all other frequencies from $0Hz$ up to the Nyquist frequency will be discarded. A more efficient method would be to utilise a form of the FFT algorithm that can be applied only to a frequency band of interest (f_1 to f_2). This type of FFT is known as the zoom-FFT or the zoom transform, and was proposed by Yip [96] and developed by Hoyer and Stork [97]. It is performed using each N-point time history from an ensemble of time-domain data as follows:

1. Complex modulation is applied to the time-domain data, which has been acquired at a sampling frequency f_{samp}. This step is used to mix the lowest frequency of interest, f_1, down to the baseband. Complex modulation is applied by multiplying the data in the time-domain sequence $y(t)$ by a complex factor as follows:

$$y_{shift}(t) = y(t)e^{j2\pi f_1 t} \tag{C.10}$$

If a full-FFT is performed of the modulated sequence $y_{shift}(t)$, it would be identical to the full-FFT of the raw sequence $y(t)$, however the spectrum would begin at f_1 instead of $0Hz$.

2. The modulated data sequence is then passed through a low-pass filter (a Butterworth IIR filter was used), forming the data sequence $y_{filt}(t)$. This filter should be designed such that any data above the highest frequency of interest, f_2, is discarded. Therefore, only data from the baseband (f_1) to f_2 will remain. This will prevent aliasing at the decimation stage.

3. The data is decimated by a decimation factor, D. This means that only every D-th sample in the data sequence $y_{filt}(t)$ is kept, and the other samples discarded. The decimation factor is selected such that the decimation sampling frequency, $f_{samp,D} = f_{samp}/D$, is at least double the bandwidth of the frequency range of interest, $B = f_2 - f_1$, to avoid aliasing. This results in a sequence of length N/D.

4. An FFT is performed on the decimated signal, $y_{dec}(t)$. The resulting frequency-domain signal will contain the spectral information in the range $f_1 - f_2$, with the same frequency resolution obtained as would have been the case if the full-FFT technique were applied to the original data sequence $y(t)$.

The last step necessitates an N/D-point FFT, as opposed to an N-point FFT had the full-FFT technique been applied. Steps $1 - 4$ are illustrated in Figure C.2, which applies the zoom-FFT to the same narrowband data shown in Figure C.1. The computational savings of the zoom-FFT, given that an FFT of N data points will require $N \log(N)$ operations, are:

$$\text{Computational Savings} = D(\log_{N/D}(N))$$

It should be noted that this does not account for the extra computational work in filtering and decimating the data in order to perform the zoom-FFT. However, as the FFT
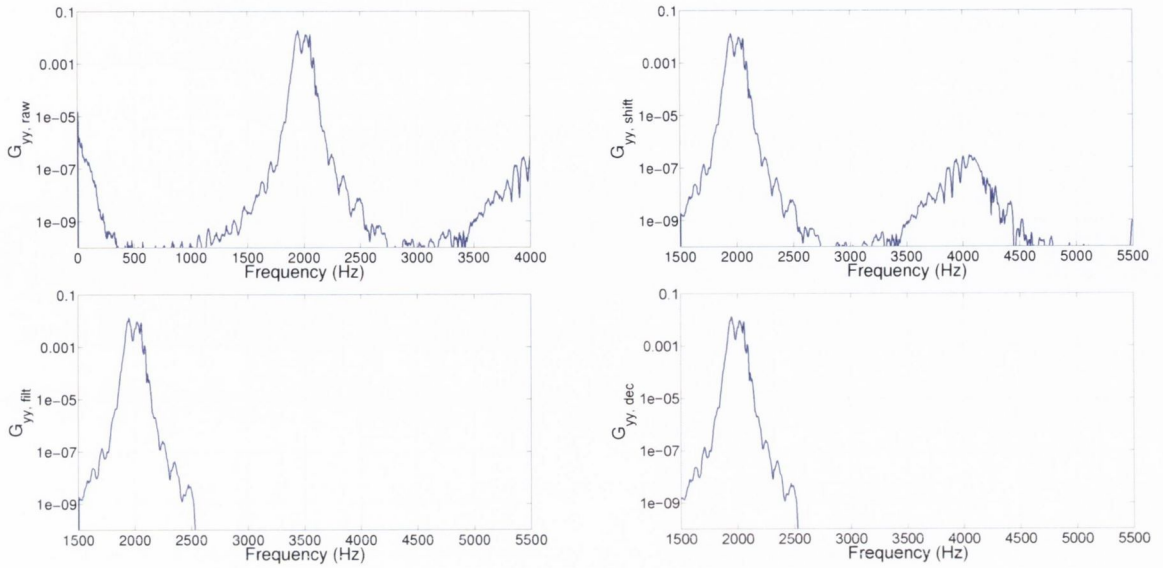
Figure C.2: Auto-spectral density estimates, calculated from measurements by a single microphone averaged over an ensemble of $n_d = 85$ time records. Narrowband noise is measured at a centre frequency of $2kHz$ with a bandwidth of $100Hz$. Each subplot shows the auto-spectral density estimated at different stages of the zoom-FFT: the original signal ($G_{yy,raw}$), the signal after frequency-shifting has been applied ($G_{yy,shift}$), the signal after being passed through a low-pass filter ($G_{yy,filt}$), and the signal after being decimated ($G_{yy,dec}$).

operation is so time consuming for large blocks of data, these operations are of minor computational cost in comparison. The computational benefits of the zoom-FFT are dependent on the decimation ratio, D. It is generally beneficial to choose D such that the decimated signal is of length 2^k, where k is a positive integer, as the FFT algorithm works most efficiently on signals of this length.

The zoom-FFT can also be applied as a means of decreasing the computational cost of increasing the frequency resolution in a spectral bandwidth of interest. For example, consider an N-point signal, acquired at a sampling frequency of f_{samp}, which is to be analysed in the frequency-domain. The resulting spectra from a full-FFT will have a frequency resolution of $f_{res} = f_{samp}/N$. However, suppose we are interested in the spectral content of a small bandwidth of the total signal, from f_1 to f_2. In order to decrease the frequency resolution by Z times in this frequency range of interest, and using the full-FFT, the user would have to increase the length of the signal to be Fourier transformed to $Z{\times}N$ points. However, assuming that the bandwidth of the frequency range of interest is such that:

$$B \leq \frac{f_s}{2Z} \tag{C.11}$$

an N-point zoom-FFT can be performed by first decimating the $(Z \times N)$-point signal by a decimation factor of Z. Therefore, for the computational cost of an N-point FFT, the frequency resolution can be increased to that of a $(Z \times N)$-point FFT, using the zoom-FFT method. If the condition outlined in Equation C.11 is not met, the resulting signal will not contain all the information in the frequency range of interest, and will instead contain information from f_1 to f_{end}, where $f_{end} < f_2$. This technique of "zooming" into a certain frequency range and increasing the frequency resolution has applications in seismic [98] and biomedical [99] studies, for example.

C.4 Statistical Errors in Spectral Estimates of Ergodic Random Data

The ensemble-averaging method of estimating spectral properties using finite time records of a random ergodic process, as outlined in Section C.1, is subject to errors as the estimated spectral functions are *statistical estimates* of the precise spectral functions. It is important to be able to put a measure on the errors inherent in these estimates. The accuracy of any estimated parameter can be described by the mean-square error:

$$\text{Mean square error} = E[(\hat{\phi} - \phi^2)] \tag{C.12}$$

where ϕ is the parameter being estimated, and $\hat{\phi}$ is the estimated value of this process. This equation can also be expressed in the following form:

$$\text{Mean square error} = E[(\hat{\phi} - E[\hat{\phi}])^2] + E[(E[\hat{\phi}] - \phi)^2] \tag{C.13}$$

which can be divided into a sum of variance and bias errors:

$$\text{Var}[\hat{\phi}] = E[(\hat{\phi} - E[\hat{\phi}])^2] = E[\hat{\phi}^2] - E^2[\hat{\phi}] \tag{C.14}$$

$$b^2[\hat{\phi}] = E[b^2\hat{\phi}] = E[(E[\hat{\phi}] - \phi)^2] \tag{C.15}$$

APPENDIX C. SIGNAL PROCESSING OF ERGODIC RANDOM DATA AND ASSOCIATED ERRORS

The variance error describes the random error of the estimate, and the bias error describes the systematic error of the estimate. Random errors can be thought of as scattering the estimated values in a function ϕ around the true values, distributed with a null arithmetic mean. Bias or systematic errors however are caused by a significant deviations between the arithmetic mean of the estimated values and the arithmetic mean of the true values. Systematic errors can be caused by errors in calibration of sensors for example, and lead to an under- or over-estimation of the quantity of interest.

Taking the square roots the equations for both variance and bias errors gives the errors in terms of units of the parameter ϕ being estimated:

$$\text{Random Error} = \sigma[\hat{\phi}] = \sqrt{E[\hat{\phi}^2] - E^2[\hat{\phi}]} \tag{C.16}$$

$$\text{Bias Error} = b[\hat{\phi}] = E[\hat{\phi}] - \phi \tag{C.17}$$

The total RMS error of the estimate is given by:

$$\text{RMS Error} = \sqrt{E[(\hat{\phi} - \phi)^2]} = \sqrt{\sigma^2[\hat{\phi}] + b^2[\hat{\phi}]} \tag{C.18}$$

Furthermore, it can be convenient to consider the normalised RMS error by dividing the RMS error by the quantity being estimated:

$$\text{Normalised RMS Error} = \epsilon = \sqrt{E[(\hat{\phi} - \phi)^2]} = \sqrt{\sigma^2[\hat{\phi}] + b^2[\hat{\phi}]} \tag{C.19}$$

Formulations of the normalised errors for both random and bias errors can be found by dividing Equations C.16 and C.17 by ϕ.

Tables C.1 and C.2 collate the normalised random and bias errors respectively for common spectral functions which are estimated in acoustic studies. It should be noted that in most cases these errors are first-order estimates only.

When a pair of microphones (or a combination of pairs) are being used to measure noise in a single-source system, any propagation delay due to the microphones being separated by some distance x relative to the direction of the propagation of sound will result in time-delay bias errors in any estimated spectral quantities. The propagation

Table C.1: Normalised Random Errors Associated with Estimates of Spectral Functions. Derivations for all equations can be found in Bendat and Piersol [61].

Estimated Spectral Function	Normalised Random Error, ϵ_r
$\hat{G}_{xx}(f), \hat{G}_{yy}(f)$	$\dfrac{1}{\sqrt{n_d}}$
$|\hat{G}_{xy}(f)|$	$\dfrac{1}{|\gamma_{xy}(f)|\sqrt{n_d}}$
$\hat{\gamma}_{xy}^2(f)$	$\dfrac{\sqrt{2}[1-\gamma_{xy}^2(f)]}{|\gamma_{xy}(f)|\sqrt{n_d}}$
$\hat{\gamma}_{xy\cdot L}^2(f)$	$\dfrac{\sqrt{2}[1-\gamma_{xy\cdot L}^2(f)]}{|\gamma_{xy\cdot L}(f)|\sqrt{n_d-1}}$
$|\hat{H}_{xy}(f)|$	$\dfrac{\sqrt{1-\hat{\gamma}_{xy}^2(f)}}{|\hat{\gamma}_{xy}(f)|\sqrt{2n_d}}$
$\hat{\Phi}_{xy}(f)$	$\sin^{-1}(\epsilon_r[|\hat{H}_{xy}(f)|])$

Table C.2: Approximated Normalised Bias Errors Associated with Estimates of Spectral Functions.

Estimated Spectral Function	Normalised Bias Error, ϵ_b
$\hat{G}_{xx}(f)$	$\dfrac{1}{24}B_e G_{xx}''(f)$ [a]
$|\hat{G}_{xy}(f)|$	$\dfrac{1}{24}B_e G_{xy}''(f)$
$\hat{\gamma}_{xy}^2$	$\dfrac{1}{n_d}(1-\hat{\gamma}_{xy}^2)^2$ [b]

[a] Second order approximation, assuming a continuous window. $B_e = 2f_{res}$ for a Hanning window [89].
[b] Only accurate for large n_d [100].

time delay τ_1 introduced due to propagation of sound at speed c_0 over this distance x is
estimated to a first-order degree of accuracy by:

$$\hat{G}_{xy}(f) = \left(1 - \frac{\tau_1}{T}\right) G_{xy}(f) \tag{C.20}$$

$$\hat{H}_{xy}(f) = \left(1 - \frac{\tau_1}{T}\right) H_{xy}(f) \tag{C.21}$$

$$\hat{\gamma}_{xy}^2(f) = \left(1 - \frac{\tau_1}{T}\right) \gamma_{xy}^2(f) \tag{C.22}$$

For a single-input system, this bias can be eliminated by shifting the output or input
signals in time, and putting the inputs and outputs in time coincidence. For multiple-
input systems *i.e.* multiple noise-sources at different spatial locations, this bias cannot be
eliminated so simply and should be factored into the uncertainty of any spectral analyses.
Schmidt [92] further factors in window effects in this bias error, and for a Hanning window
with approximated white noise at the input, the bias error is given by:

$$\hat{H}_R(f, T) \approx S_{uu}(\tau, T) e^{-j2\pi f\tau} \hat{H}_{0,u}(f, T) \tag{C.23}$$

$$\hat{\gamma}_R^2(f, T) \approx S_{uu}(\tau, T) e^{-j2\pi f\tau} \hat{\gamma}_{0,u}^2(f, T) \tag{C.24}$$

for $\tau << T$, where S_{uu} is the normalised auto-spectral density of the Hanning window
function. The $(0, u)$ subscript denotes the estimated function which would be obtained in
the measurement of the equivalent delay-free system.

C.5 Errors in Coherence-Based Noise-Source Identification Techniques

In Section 4.1, several coherence-based noise-source identification techniques are discussed.
These techniques aim to identify the contributions of one or more noise-sources, using a
combination of input and/or output noise measurements and formulations of auto-spectral
densities, cross-spectral densities and coherence functions between these measurements.
The statistical uncertainties inherent in estimating these spectral quantities will therefore

Table C.3: Propagation of Statistical Errors in Arithmetic Operations.

Function, Z	Relative Error, ϵ_Z
$Z = aX$	$\epsilon_Z = a\epsilon_X$
$Z = X \pm Y$	$\epsilon_Z = \dfrac{\sqrt{(\epsilon_X X)^2 + (\epsilon_Y Y)^2}}{Z}$
$Z = X \times Y$	$\epsilon_Z \approx \sqrt{\epsilon_X^2 + \epsilon_Y^2}$
$Z = \dfrac{X}{Y}$	$\epsilon_Z \approx \sqrt{\epsilon_X^2 + \epsilon_Y^2}$

propagate in the formulation of these techniques. Formulae for the propagation of normalised errors when arithmetic operations are applied to estimated functions are shown in Table C.3.

For the Coherent Output Power (COP) technique outlined in Section 4.1, an error analysis was performed in the original article by Halvorsen and Bendat [3]. For the estimated coherent output spectrum, the associated error is given as:

$$\epsilon[\hat{G}_{vv}(f)] = \sqrt{\epsilon^2[\hat{\gamma}_{xy}^2(f)] + \epsilon^2[\hat{G}_{yy}(f)]} \tag{C.25}$$

where ϵ is the estimated normalised RMS error (a combination of bias and variance errors, as per Equation C.19), $\hat{G}_{vv}$ is the estimated coherent output spectrum, $\hat{G}_{yy}$ is the estimated output auto-spectral density function, and $\hat{\gamma}_{xy}^2$ is the estimated coherence function between the input and output measurements.

An important result noted in this error analysis is that large errors in any of the spectral estimates will result in large errors in the estimation of the coherent output spectrum. In other words, any estimates of noise-source contributions using coherence-based noise source identification techniques will have high uncertainty if there is high uncertainty in *any* of the spectral functions used in its formulation.

For the signal enhancement technique, no error analysis was presented in the original article by Chung [4], but an uncertainty analysis was performed by Nance [58]. Nance investigated the impact of both coherence levels between the three microphone measurements used as outputs in the technique, and of the relative sound pressure levels of these

measurements, on the normalised error of the correlated and uncorrelated estimates found
from the signal enhancement technique. The conclusion reached was that uncertainty in
the signal enhancement technique is dependent on the relative coherence levels between
each microphone pair. The relative sound pressure levels at the three microphones and
the relative levels of the correlated and uncorrelated noise at each microphone do not
impact on this uncertainty.

An error analysis for the five-microphone conditional spectral analysis technique pre-
sented by Hsu and Ahuja [5], and applied in Chapter 4 of this thesis, was not performed in
the original report. Equations 4.6 and 4.7 utilise combinations of cross-spectral densities
to identify the contributions of two mutually uncorrelated noise sources to the noise mea-
sured at three microphones, each of which are measured with high correlation between
all three microphones, as well as any extraneous uncorrelated noise. Two additional mi-
crophone measurements are required which measure one of the correlated noise sources
and uncorrelated extraneous noise only. An analysis of the errors in the five-microphone
technique will now be presented, with focus on:

1. The effect of relative coherence levels between the three microphones which measure
   both correlated noise sources on the RMS error of the source measurements, by
   applying the error formulae in Tables C.1 and C.2 to the noise-source identification
   Equations 4.6 and 4.7. The effect of the number of data records used in the averaging
   ensemble will also be demonstrated.

2. The normalised RMS errors present for the experimental results presented in Section
   4.3 will be shown, to demonstrate the levels of uncertainty which can be expected
   in applying this technique.

Plots of the random errors for the estimation of the v spectra at each microphone
are shown in Figure C.3 for a range of coherence values between microphone pairs. The
equations for calculating this error are as follows (v_1 is shown only for brevity):

$$\epsilon[G_{v1v1}] = \sqrt{\epsilon[G_{y1y4}]^2 + \epsilon[G_{y1y5}]^2 + \epsilon[G_{y4y5}]^2} \qquad (C.26)$$

It is clear that the degree of uncertainty in each v_i estimate is dependent on the coher-
ence between microphone i and the other two microphones. As this coherence increases,

the random error asymptotically approaches an error floor. This error floor is dependent
on n_d; when more averaging blocks are used, the random error drops. Finally, for all esti-
mates of the v spectra, the degree of uncertainty is dependent on the coherence between
microphone 4 and 5 (γ_{y4y5}^2), as G_{y4y5} is used in each estimate.
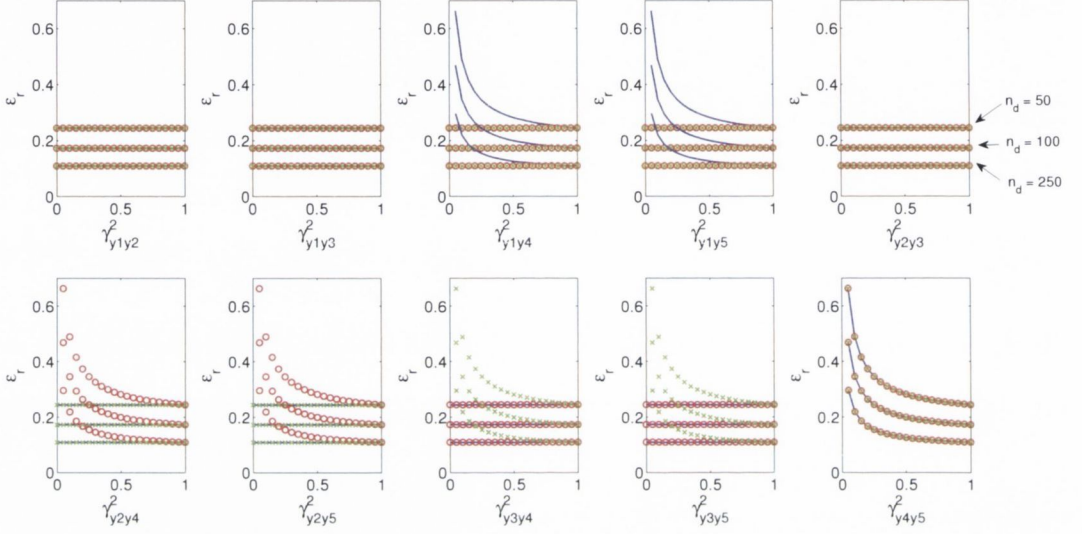
Figure C.3: Normalised random error in estimating the $\hat{G}_{vv}$ spectra for a range of values
for n_d and estimated coherences between microphone pairs. The blue spectra show the
effect of n_d and γ^2 on the random error for $\hat{G}_{k1k1}$, the red circles and green crosses show
this random error for $\hat{G}_{k2k2}$ and $\hat{G}_{k3k3}$ respectively.

Plotting the bias of the v and k spectral estimates is more complicated, as the bias
errors associated with auto- and cross-spectral densities are dependent on the second
derivative of these spectral estimates (see Table C.2). Furthermore, the random errors
associated the k estimates are also dependent on the relative levels of the cross-spectral
densities, as shown below:

$$\epsilon[G_{k1k1}] = \sqrt{A^2 + B^2 + C^2} \tag{C.27}$$

$$A = \frac{\sqrt{(|G_{y1y2}| \cdot \epsilon[G_{y1y2}])^2 + \left(\left|\dfrac{G_{y1y4} \cdot G_{y2y5}}{G_{y4y5}}\right| \sqrt{\epsilon[G_{y1y4}]^2 + \epsilon[G_{y2y5}]^2 + \epsilon[G_{y4y5}]^2}\right)^2}}{\left|G_{y1y2} - \dfrac{G_{y1y4} \cdot G_{y2y5}}{G_{y4y5}}\right|}$$

$$B = \frac{\sqrt{(|G_{y1y3}| \cdot \epsilon[G_{y1y3}])^2 + \left(\left|\dfrac{G_{y1y4} \cdot G_{y3y5}}{G_{y4y5}}\right| \sqrt{\epsilon[G_{y1y4}]^2 + \epsilon[G_{y3y5}]^2 + \epsilon[G_{y4y5}]^2}\right)^2}}{\left|G_{y1y3} - \dfrac{G_{y1y4} \cdot G_{y3y5}}{G_{y4y5}}\right|}$$

$$C = \frac{\sqrt{(|G_{y2y3}| \cdot \epsilon[G_{y2y3}])^2 + \left(\left|\dfrac{G_{y2y4} \cdot G_{y3y5}}{G_{y4y5}}\right| \sqrt{\epsilon[G_{y2y4}]^2 + \epsilon[G_{y3y5}]^2 + \epsilon[G_{y4y5}]^2}\right)^2}}{\left|G_{y2y3} - \dfrac{G_{y2y4} \cdot G_{y3y5}}{G_{y4y5}}\right|}$$

In order to demonstrate the magnitude of the normalised RMS error estimates for both the k and v spectra, including the impact of bias errors, real data of spectral density estimates must be used. The data from the experimental tests discussed in Section 4.3 was therefore investigated using Equations C.26 and C.27. The variance, bias, and RMS errors for these spectral estimates are shown in Figure C.4. It is assumed in estimating these errors that each microphone is well calibrated, and therefore systematic errors through magnitude and phase mismatch between microphone pairs has not been factored into the error analysis. Time-delay bias errors are also not factored into the analysis, as the propagation time between microphones is minimal. Data was acquired in these tests with the following parameters: $f_{samp} = 16000$, $N = 4098$, $n_d = 292$, $f_{res} = 3.9043$.

In all cases, random error is the dominant source of error in the analysis. Bias errors are generally insignificant at all frequencies aside from the blade-pass frequencies at 605 and $1200Hz$. The large spectral gradients at these tonal frequencies lead to these peaks in the bias error. The random error in all spectral estimates has a floor of $1/\sqrt{n_d} = 0.0585$. The spikiness of these error spectra is caused by peaks and troughs in the coherences measured between the pairs of microphones used in the technique. The random error for estimating the v spectrum is much lower than that for estimating the k spectrum, which is to be expected given that the formulation of the v spectrum uses fewer cross-spectral measurements. As more and more cross-spectral estimates are used to generate a spectral density estimate, more errors will propagate. As each k spectral estimate uses all possible combinations of cross-spectral densities between microphone pairs, the random error plots are identical in each case.

APPENDIX C. SIGNAL PROCESSING OF ERGODIC RANDOM DATA AND ASSOCIATED ERRORS

Generally, the RMS errors fall within $\pm 100\%$ of the estimate, *i.e.* the spectral density function estimates are good to within an order of magnitude of the real spectral densities. However, the peaks and troughs in the coherence between the measurements of microphone pairs used in five-microphone technique could lead to significant shifts in RMS error with frequency, and therefore the five-microphone technique is only suitable in experimental scenarios where the coherence between all microphone pairs is reasonably high for all frequencies of interest. It should be noted that these errors have been estimated for the power spectra; any amplitude spectra will have a significantly reduced error, and a $\pm 100\%$ error in the estimated power spectral densities will lead to an error of just $3.01 dB$ in the estimated sound pressure levels. This may explain why the technique performs so well when applied in Section 4.3, despite the significant error levels predicted in this uncertainty analysis.
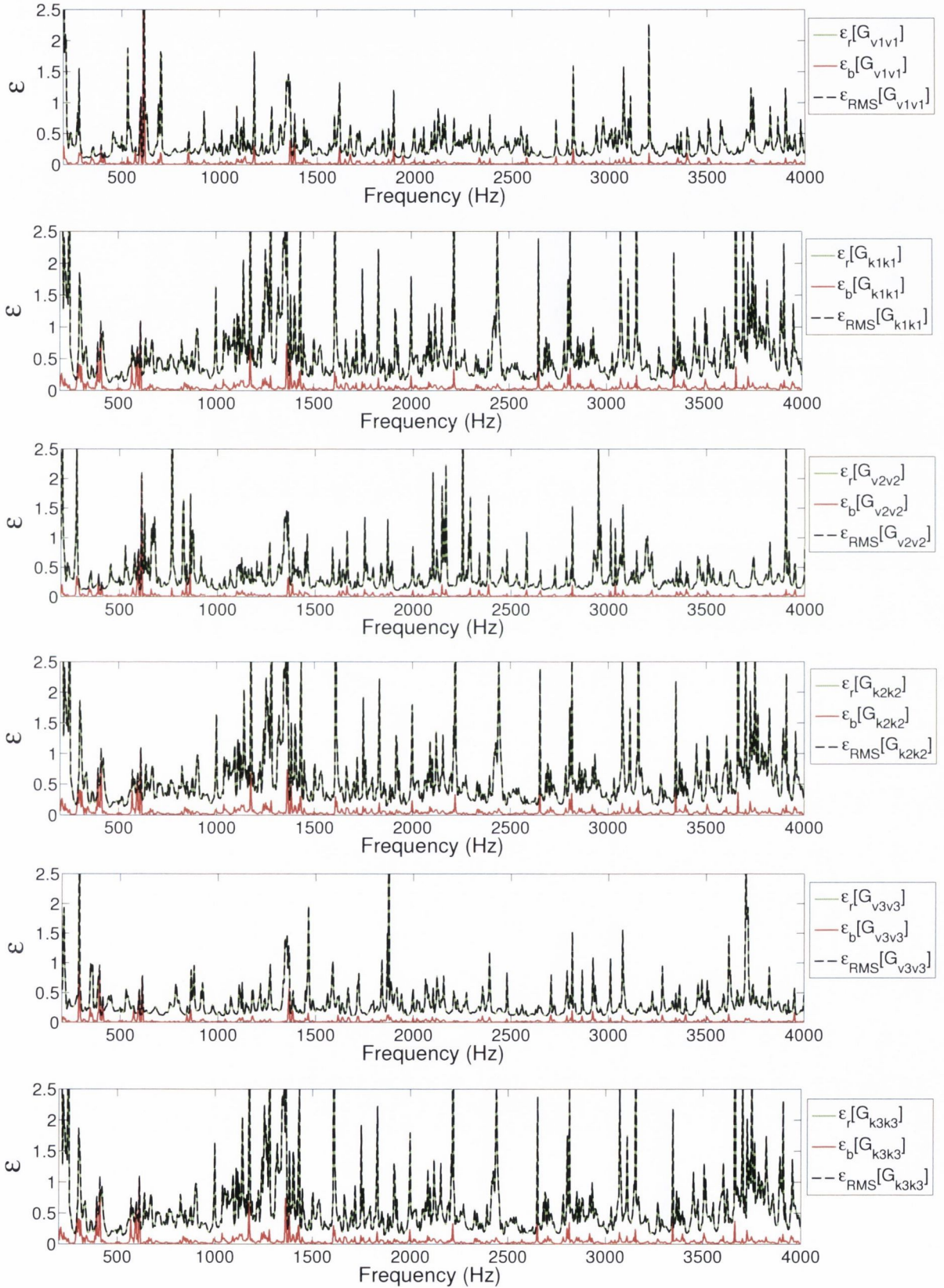
Figure C.4: Normalised errors for G_{kk} and G_{vv} estimates shown in Figures 4.27, 4.28 and 4.29.

C.6 Uncertainty in Modal Decomposition Technique

The azimuthal modal analysis (AMA) and radial modal analysis (RMA) techniques applied in the experimental studies throughout this thesis may be formulated using several transfer functions, estimated between several microphones and a microphone selected as a reference. As such, the main source of error in the application in the technique will arise from errors in these transfer function estimates. The random error in the transfer function estimation between a pair of microphones is given in Table C.1. The coherence between each microphone and the reference microphone is expected to be high, as the spacing between each microphone is relatively small, and modal decomposition is generally performed at frequencies of interest at which periodic signals are expected to dominate (for example, fan BPF tones, or tones generated by arrays of loudspeakers). As these coherences remain high, the anticipated random error is very small. Bias errors in the transfer function estimates are therefore of primary concern.

Bodén and Åbom [101] discuss the errors resulting in application of Chung and Blaser's two-microphone transfer function technique [80] to estimate acoustic properties in ducts. In considering the bias errors introduced by resonances in the duct, and other peaks and valleys in the auto-spectra measured by both microphones such as standing wave patterns, the authors estimated relationships between the microphone axial spacing s, the length of the duct L, the distance from the first microphone to the duct passive end ℓ, and the anticipated bias error. They concluded that bias errors are reduced if ℓ is kept small. Errors are further reduced when L is reduced if high reflections are anticipated at the duct passive end. However, any microphones used should be not located too close to the duct passive end or near-field effects will introduce errors into the transfer function estimation. Finally, large errors will arise when a pressure node is located at either of the microphones, as the signal-to-noise ratio approached zero. In using the two-microphone technique to estimate duct properties, the two-microphone technique is least sensitive to errors when $ks = \pi/2$. In order to keep error low, it is recommended that the technique is applied in the following interval only:

$$0.1\pi < \omega s/c < 0.8\pi \qquad \text{(C.28)}$$

where ω is the angular frequency and s is the spacing between each microphone. This equation assumes that there is no mean-flow is present in the duct. Åbom and Bodén [102] furthered this study to include the effect of a mean-flow, and modified the above equation as follows:

$$0.1\pi(1 - M^2) < \omega s/c < 0.8\pi(1 - M^2) \tag{C.29}$$

where M is the Mach number of the mean flow. It should be noted that the presence of a mean-flow will also introduce turbulence, attenuate sound waves, and reduce signal-to-noise ratios, all of which will increase errors in any spectral estimations. Equation C.29 can be applied to the microphones used in the modal decomposition technique in order to select a suitable azimuthal spacing between microphones. As the microphones are located in a circumferentially-spaced rather than an axially-spaced array, the above equation is applicable, but with s taken as the microphone spacing in the azimuthal direction. In this case, the Mach number M refers to the Mach number of the flow in the swirl direction. When applying the modal decomposition technique, this swirl velocity should be minimised by locating any microphone arrays as far from rotating turbomachinery elements as possible, and through use of stator vanes to straighten out the swirl these turbomachines produce. Flow swirl will also affect the cut-on frequencies of any higher-order acoustic modes as shown in Equation 2.16.

If a modal analysis is to be performed where the incident and reflected azimuthal modal amplitudes or specific radial modal amplitudes are of interest, several rings of microphones are required. Åbom [13] further considered the errors in using a transfer function method for performing a modal analysis using several rings of microphones, and formulated an additional range of parameters for microphone spacing in the axial-direction:

$$0.1\pi(1 - M^2) < \alpha_{mn}\omega s_x/c < 0.8\pi(1 - M^2) \tag{C.30}$$

where α_{mn} is defined in Equation 2.6.

APPENDIX C. SIGNAL PROCESSING OF ERGODIC RANDOM DATA AND ASSOCIATED ERRORS

Bibliography

[1] R.J. Astley, A. Agarwal, P.F. Joseph, R.H. Self, M.G. Smith, R. Sugimoto, and B.J. Tester. Predicting and reducing aircraft noise. In *14th International Congress on Sound and Vibration, Cairns, Australia, 9-12 July*, 2007.

[2] É. Bouty. TEENI Description of Work. Technical report, E.U. Seventh Framework Project, 2008.

[3] W.G. Halvorsen and J.S. Bendat. Noise source identification using coherent output power spectra. *Journal of Sound and Vibration*, 9(8):15–24, 1975.

[4] J.Y. Chung. Rejection of flow noise using a coherence function method. *The Journal of the Acoustical Society of America*, 62:388, 1977.

[5] J.S. Hsu and K.K. Ahuja. A coherence-based technique to separate ejector internal mixing noise from farfield measurements. In *4th AIAA/CEAS Aeroacoustics Conference, Toulouse, 2-4 June*, 1998.

[6] G. Bennett and J.A. Fitzpatrick. Noise source identification for ducted fan systems. *AIAA Journal*, 46:1663–1674, 2008.

[7] J.E. Piercey, T.F.W. Embleton, and L.C. Sutherland. Review of noise propagation in the atmosphere. *The Journal of the Acoustical Society of America*, 61:1403, 1977.

[8] N.A. Cumpsty. Sum and difference tones from turbomachines. *Journal of Sound and Vibration*, 32(3):383–386, 1974.

[9] L. Enghardt, U. Tapken, O. Kornow, and F. Kennepohl. Acoustic mode decomposition of compressor noise under consideration of radial flow profiles. *AIAA Journal*, 2833:23–25, 2005.

[10] M.L. Munjal. *Acoustics of ducts and mufflers*, volume 1. Wiley, 1987.

[11] A.R. Frey and L.E. Kinsler. *Fundamentals of acoustics*. Wiley, 1962.

[12] W. Eversman. *Aeroacoustics of Flight Vehicles: Theory and Practice. Volume 2: Noise Control*, chapter Theoretical models for duct acoustic propagation and radiation, pages 101–163. American Institute of Physics Publishing, 1991.

[13] M. Åbom. Modal decomposition in ducts based on transfer function measurements between microphone pairs. *Journal of Sound Vibration*, 135:95–114, 1989.

[14] J.M. Tyler and T.G. Sofrin. Axial compressor noise studies. *SAE Transactions*, 70:309–332, 1962.

[15] C.J. Moore. Measurement of radial and circumferential modes in annular and circular fan ducts. *Journal of Sound and Vibration*, 62(2):235–256, 1979.

[16] W. Eversman. Energy flow criteria for acoustic propagation in ducts with flow. *The Journal of the Acoustical Society of America*, 49:1717, 1971.

[17] E.J. Rice. Acoustic liner optimum impedance for spinning modes with mode cut-off ratio as the design criterion. In *3rd AIAA Aeroacoustics Conference, Palo Alto, CA*, page 8, 1976.

[18] V.V. Golubev and H.M. Atassi. Sound propagation in an annular duct with mean potential swirling flow. *Journal of sound and vibration*, 198(5):601–616, 1996.

[19] E. Envia. A high frequency model of cascade noise. Technical report, NASA, 1998.

[20] M. Nallasamy. Computation of noise radiation from fan inlet and aft ducts. *Journal of Aircraft*, 34(3):387–393, 1997.

[21] A. Karchmer. Acoustic modal analysis of a full-scale annular combustor. In *8th AIAA Aeroacoustics Conference, Atlanta, GA*, 1983.

[22] J.H. Miles. Restricted modal analysis applied to internal annular combustor autospectra and cross-spectra measurements. *AIAA Journal*, 45(5):988–999, 2007.

[23] G. Bennett. *Noise Source Identification For Ducted Fans*. PhD thesis, Trinity College Dublin, 2006.

[24] P.C. Morse. *Vibration and sound*, volume 2. McGraw-Hill New York, 1948.

[25] H. Levine and J. Schwinger. On the radiation of sound from an unflanged circular pipe. *Physical Review*, 73(4):383–406, 1948.

[26] T.F. Brooks, D.S. Pope, and M.A. Marcolini. Airfoil self-noise and prediction. Technical Report RP-1218, NASA, 1989.

[27] S.A.L. Glegg and C. Jochault. Broadband self noise from a ducted fan. In *3rd AIAA/CEAS Aeroacoustics Conference, Atlanta, GA*, 1997.

[28] S.A.L. Glegg. Airfoil self-noise generated in a cascade. *AIAA Journal*, 36(9):1575–1582, 1998.

[29] L. Enghardt. Selected final results of the European research project PROBAND on the improvement of fan broadband noise prediction, 2008.

[30] J.F. Groenweg, T.G. Sofrin, E.J. Rice, and P.R. Gliebe. *Aeroacoustics of Flight Vehicles: Theory and Practice. Volume 1: Noise Sources*, chapter Turbomachinery noise, pages 151–209. American Institute of Physics Publishing, 1991.

[31] W. Sears. Some aspects of non-stationary airfoil theory and its practical application. *Journal of Aeronautical Science*, 8:104–108, 1941.

[32] M.E. Goldstein. *Aeroacoustics*. McGraw-Hill International Book Company, 1976.

[33] R.K. Amiet. Compressibility effects in unsteady thin-airfoil theory. *AIAA Journal*, 12:252–255, 1974.

[34] M. Namba. Three-dimensional analysis of blade force and sound generation for an annular cascade in distorted flows. *Journal of Sound and Vibration*, 50(4):479–508, 1977.

[35] M.E. Goldstein and H.M. Atassi. A complete second-order theory for the unsteady flow about an airfoil due to a periodic gust. *Journal of Fluid Mechanics*, 74(04):741–765, 1976.

[36] R.K. Amiet. Airfoil gust response and the sound produced by airfoil-vortex interaction. *Journal of Sound and Vibration*, 107(3):487–506, 1986.

[37] I. Dyer. Measurement of noise sources in ducts. *The Journal of the Acoustical Society of America*, 30:833, 1958.

[38] C.L. Morfey. Rotating pressure patterns in ducts: their generation and transmission. *Journal of Sound and Vibration*, 1(1):60–87, 1964.

[39] B.D. Mugridge. The measurement of spinning acoustic modes generated in an axial flow fan. *Journal of Sound and Vibration*, 10(2):227–234, 1969.

[40] G.F. Pickett, T.G. Sofrin, and R.A. Wells. Method of fan sound mode structure determination. Technical report, NASA, 1977.

[41] E.J. Kerschen and J.P. Johnston. A modal separation measurement technique for broadband noise propagating inside circular ducts. *Journal of Sound and Vibration*, 76(4):499–515, 1981.

[42] J.P. Pasqualini, J.M. Ville, and J.F. de Belleval. Development of a method of determining the transverse wave structure in a rigid wall axisymmetric duct. *The Journal of the Acoustical Society of America*, 77:1921, 1985.

[43] M. Salikuddin and R. Ramakrishnan. Acoustic power measurement for single and annular stream duct-nozzle systems utilizing a modal decomposition scheme. *Journal of Sound and Vibration*, 113(3):441–472, 1987.

[44] P.D. Yardley. *Measurement of noise and turbulence generated by rotating machinery.* PhD thesis, University of Southampton, 1974.

[45] F. Holste and W. Neise. Noise source identification in a propfan model by means of acoustical near field measurements. *Journal of Sound and Vibration*, 203(4):641–665, 1997.

[46] L. Enghardt, Y. Zhang, and W. Neise. Experimental verification of a radial mode analysis technique using wall-flush mounted sensors. *The Journal of the Acoustical Society of America*, 105:1186, 1999.

[47] L. Enghardt, U. Tapken, W. Neise, F. Kennepohl, and K. Heinig. Turbine blade/vane interaction noise – Acoustic mode analysis using in-duct sensor rakes. In *7th AIAA/CEAS Aeroacoustics Conference, Maastricht, Netherlands, May 28-30*, pages 275–282, 2001.

[48] U. Tapken and L. Enghardt. Optimisation of sensor arrays for radial mode analysis in flow ducts. In *12th AIAA/CEAS-Aeroacoustics Conference, Cambridge, MA*, pages 8–10, 2006.

[49] M. Åbom. Modal decomposition in ducts based on transfer function measurements between microphone pairs. Technical report, TRITA-TAK-8702, Department of Technical Acoustics, Royal Institute of Technology, Stockholm, Sweden, 1987.

[50] F.O. Castres and P.F. Joseph. Mode detection in turbofan inlets from near field sensor arrays. *The Journal of the Acoustical Society of America*, 121:796, 2007.

[51] L. Enghardt, A. Holewa, and U. Tapken. Comparison of different analysis techniques to decompose a broad-band ducted sound field in its mode constituents. In *13th AIAA/CEAS Aeroacoustics Conference , Rome, Italy, May 21-23*, 2007.

[52] L. Enghardt, C. Lowis, and L. Neuhaus. Broadband sound power determination in flow ducts. In *10th AIAA/CEAS Aeroacoustics Conference, Manchester, United Kingdom, May 10-12*, 2004.

[53] I. Davis and G. Bennett. Experimental investigations of coherence-based noise-source identification techniques for turbomachinery applications – classical and novel techniques. In *17th AIAA/CEAS conference in Portland, Oregon, 5-8 June*, 2011.

[54] J.D. Risi, R.A. Burdisso, and C.R. Fuller. Analytical investigation of active control of radiated inlet fan noise. *The Journal of the Acoustical Society of America*, 99:408, 1996.

[55] A. Karchmer and M. Reshotko. Core noise source diagnostics on a turbofan engine using correlation and coherence techniques. *The Journal of the Acoustical Society of America*, 60:S112, 1976.

[56] A.M. Karchmer, M. Reshotko, and F.J. Montegani. Measurement of far field combustion noise from a turbofan engine using coherence functions. In *4th AIAA Aeroacoustics Conference, Atlanta, Georgia*, 1977.

[57] B.N. Shivashankara. High bypass ratio engine noise component separation by coherence technique. *Journal of Aircraft*, 20(3):236–242, 1983.

[58] D.K. Nance. *Separating contributions of small-scale turbulence, large-scale turbulence, and core noise from far-field exhaust noise measurements*. PhD thesis, Georgia Institute of Technology, 2007.

[59] T. Minami and K.K. Ahuja. Five-microphone method for separating two different correlated noise sources from far-field measurements contaminated by extraneous noise. In *9th AIAA/CEAS Aeroacoustics Conference, Hilton Head, South Carolina, May 1214*, pages 12–13, 2003.

[60] G. Bennett and J.A. Fitzpatrick. A comparison of coherence based acoustic source identification techniques. In *12th International Congress on Sound and Vibration, Lisbon, Portugal*, volume 11, page 14, 2005.

[61] J.S. Bendat and A.G. Piersol. Random data analysis and measurement procedures. *Measurement Science and Technology*, 11:1825–1826, 2000.

[62] G. Bennett, I. Davis, U. Tapken, and J. Mahon. Non-linear frequency scattering of broadband noise in turbomachinery. In *16th AIAA/CEAS Aeroacoustics Conference, Stockholm, 7-9 June*, 2010.

[63] S. Kaji and T. Okazaki. Propagation of sound waves through a blade row: 1 - analysis based on the semi-actuator disk theory. *Journal of Sound and Vibration*, 11(3):339–353, 1970.

[64] R. Amiet and W.R. Sears. Reflection and transmission of oblique sound waves by a blade row. In *Basic aerodynamic noise research: a conference held at NASA Headquarters, Washington, DC, July 14-15*, volume 207, page 223. Scientific and Technical Information Division, National Aeronautics and Space Administration; for sale by the Supt. of Docs., US Govt. Print. Off., 1969.

[65] S. Kaji and T. Okazaki. Propagation of sound waves through a blade row: 2 - analysis based on the acceleration potential method. *Journal of Sound and Vibration*, 11(3):355–375, 1970.

[66] R.S. Muir. The application of a semi-actuator disk model to sound transmission calculations in turbomachinery: 1 - the single blade row. *Journal of Sound and Vibration*, 54(3):393–408, 1977.

[67] R.S. Muir. The application of a semi-actuator disk model to sound transmission calculations in turbomachinery: 2 - multiple blade rows. *Journal of Sound and Vibration*, 55(3):335–349, 1977.

[68] W. Koch. Attenuation of sound in multi-element acoustically lined rectangular ducts in the absence of mean flow. *Journal of Sound and Vibration*, 52(4):459–496, 1977.

[69] D.B. Hanson. Acoustic reflection and transmission of rotors and stators including mode and frequency scattering. In *3rd AIAA/CEAS Aeroacoustics Conference, Atlanta, Georgia*, 1997.

[70] S. Kaji and T. Okazaki. Generation of sound by rotor-stator interaction. *Journal of Sound and Vibration*, 13(3):281–307, 1970.

[71] R.P. Dring, H.D. Joslyn, L.W. Hardin, and J.H. Wagner. Turbine rotor-stator interaction. *ASME Journal of Engineering for Power*, 104(3):729–742, 1982.

[72] S.N. Smith. Discrete frequency sound generation in axial flow turbomachines. *Aeronautical Research Council Reports and Memoranda*, 3709:1–56, 1972.

[73] M.M. Logue and H.M. Atassi. Scattering of acoustic waves by a rotor. In *14th AIAA/CEAS Aeroacoustics Conference, Vancouver, British Columbia, Canada, 5-7 May*, pages 2008–2989, 2008.

[74] B. Barry and C.J. Moore. Subsonic fan noise. *Journal of Sound and Vibration*, 17(2):207–208, 1971.

[75] H.A. Siller, F. Arnold, and U. Michel. Investigation of aero-engine core-noise using a phased microphone array. In *7th AIAA/CEAS Aeroacoustics Conference, Maastricht, The Netherlands, 28-30 May*, 2001.

[76] H.J. Rice and J.A. Fitzpatrick. A generalised technique for spectral analysis of non-linear systems. *Mechanical Systems and Signal Processing*, 2(2):195–207, 1988.

[77] G. Bennett, J. Mahon, and J.A. Fitzpatrick. Non-linear identification applied to broadband turbomachinery noise. In *12th CEAS-ASC Workshop on Turbomachinery Broadband Noise, Bilbao, Spain, 23-24 October*, 2008.

[78] G. Bennett, C.J. O'Reilly, H. Liu, and U. Tapken. Modelling multi-modal sound transmission from point sources in ducts with flow using a wave-based method. In *16th International Congress on Sound and Vibration (ICSV16)*, 2009.

[79] A.F. Seybert and D.F. Ross. Experimental determination of acoustic properties using a two-microphone random-excitation technique. *The Journal of the Acoustical Society of America*, 61(5):1362–1370, 1977.

[80] J.Y. Chung and D.A. Blaser. Transfer function method of measuring in-duct acoustic properties. i - theory. *The Journal of the Acoustical Society of America*, 68:907, 1980.

[81] U. Tapken and K. Nagai. Effects impairing the synthesis of acoustic duct modes with loudspeaker arrays. In *19th International Congress on Sound and Vibration, Vilnius, Lithuania, July 812*, 2012.

[82] BS EN ISO 5136: Determination of sound power radiated into a duct by fans and other air-moving devices, In-duct method, 2003.

[83] J.E. Caruthers, J.C. French, and G.K. Raviprakash. Green function discretization for numerical solution of the Helmholtz equation. *Journal of Sound and Vibration*, 187(4):553–568, 1995.

[84] J.E. Caruthers, J.C. French, and G.K. Raviprakash. Recent developments concerning a new discretization method for the Helmholtz equation. In *1st AIAA/CEAS Aeroacoustics Conference, Munich, Germany*, pages 819–826, 1995.

[85] G. Ruiz and HJ Rice. An implementation of a wave-based finite difference scheme for a 3-D acoustic problem. *Journal of Sound Vibration*, 256:373–381, 2002.

[86] G. Ruiz. *Numerical vibro/acoustic analysis at higher frequencies*. PhD thesis, Trinity College Dublin, 2002.

[87] L.B. Rolla. *A Forward Advancing Wave Expansion Method for Numerical Solution of Large-scale Sound Propagation Problems*. PhD thesis, Trinity College Dublin, 2006.

[88] D.E. Newland. *An Introduction To Random Vibrations and Spectral Analysis*. Longman Scientific and Technical, second edition, 1987.

[89] H. Schmidt. Resolution bias errors in spectral density, frequency response and coherence function measurements, i: General theory. *Journal of Sound and Vibration*, 101(3):347–362, 1985.

[90] H. Schmidt. Resolution bias errors in spectral density, frequency response and coherence function measurements, ii: Application to first-order systems (white noise excitation). *Journal of Sound and Vibration*, 101(3):363–375, 1985.

[91] H. Schmidt. Resolution bias errors in spectral density, frequency response and coherence function measurements, iii: Application to second-order systems (white noise excitation). *Journal of Sound and Vibration*, 101(3):377–404, 1985.

[92] H. Schmidt. Resolution bias errors in spectral density, frequency response and coherence function measurements, iv: Time delay bias errors. *Journal of Sound and Vibration*, 101(3):405–412, 1985.

[93] H. Schmidt. Resolution bias errors in spectral density, frequency response and coherence function measurements, v: Comparison of different frequency response estimators. *Journal of Sound and Vibration*, 101(3):413–418, 1985.

[94] R.G. Lyons. *Understanding Digital Signal Processing*. Prentice Hall, third edition, 2010.

[95] M. Åbom. A note on random errors in frequency response estimators. *Journal of Sound and Vibration*, 107(2):355 – 358, 1986.

[96] P.C.Y. Yip. Some aspects of the zoom transform. *IEEE Transactions on Computers*, 100(3):287–296, 1976.

[97] E. Hoyer and R. Stork. The zoom fft using complex modulation. In *Acoustics, Speech, and Signal Processing, IEEE International Conference on ICASSP'77.*, volume 2, pages 78–81. IEEE, 1977.

[98] L. Wang, J. Zhao, Z. Wang, and L. Pang. Application of zoom fft technique to detecting em signal of slf/elf. *Acta Seismologica Sinica*, 20(1):63–70, 2007.

[99] F.J. Taylor, A.S. Ramnarayan, and J. Wasserman. Non-invasive aneurysm detection using digital signal processing. *Journal of Biomedical Engineering*, 5(3):201–210, 1983.

[100] G.C. Carter. Coherence and time delay estimation. *Proceedings of the IEEE*, 75(2):236–255, 1987.

[101] H. Bodén and M. Åbom. Influence of errors on the two-microphone method for measuring acoustic properties in ducts. *The Journal of the Acoustical Society of America*, 79:541, 1986.

[102] M. Åbom and H. Bodén. Error analysis of two-microphone measurements in ducts with flow. *The Journal of the Acoustical Society of America*, 83:2429, 1988.

Summary

The exact contribution of each of the various core-noise sources within modern turboshaft engines to the noise radiated from the engine exhaust and into the surrounding environment is poorly understood. The E.U. FP-7 TEENI (Turboshaft Engine Exhaust Noise Identification) project aims to better characterise the specific contributions of each core noise-source to this exhaust noise. Sources of core noise include direct combustor noise generated by the unsteady heat release at the combustor stage, broadband turbine noise, periodic turbine noise and flow-noise. Core noise also contributes significantly to the exhaust noise in modern turbofan engines during approach.

One of the key avenues of investigation for the TEENI project was to assess the efficacy of various coherence-based noise-source identification techniques for application in a full-scale turboshaft engine. Such techniques require several acoustic measurements to be made at the noise-sources of interest. These techniques were first tested using a small-scale experimental rig constructed at the Department of Engine Acoustics at the German Aerospace Centre (DLR) in Berlin, Germany. The objective of these tests was to examine the effectiveness of both pre-existing and novel methods of noise-source identification, using the small-scale experimental rig as a simplified representation of a real turboshaft engine. The relative strengths and weaknesses of several pre-existing techniques are discussed, before a novel method of noise-source identification is introduced which identifies the relative contributions of two noise-sources to the specific acoustic modal content measured at a given axial location.

Additional experimental tests were undertaken using a bench-top rig at TCD to investigate sum and difference scattering of noise. Tests were undertaken applying both single-microphone spectral analysis and modal analysis in order to characterise both the incident and scattered noise. Scattering of tonal and narrowband noise was investigated, with parameters such as rotor-stator geometries, source frequencies, spectral bandwidth of the incident noise and the modal content of the incident noise modified between tests. These experimental tests not only validated the existing analytical theory, but also demonstrated scattering of non-tonal noise.

A relationship was found between the onset of significant scattering of noise and the cut-ons of certain acoustic mode orders. This was demonstrated for both tonal and narrowband noise, and it is shown that noise scattering can be predicted given the blade (and vane) counts of the rotor (and stator) stages, the rotational speed of the rotor, and the modal content of the incident noise. It is further demonstrated herein that incident noise and scattered noise can overlap if the spectral bandwidth of the incident noise is wide enough, raising the possibility of the distribution of acoustic energy across frequency and mode order being significantly affected for broadband noise propagating through a rotor.